MICRO-MACRO MODELING OF CHEMO-MECHANICAL DAMAGE AND HEALING IN ROCKS

A Dissertation
Presented to
The Academic Faculty

By

Xianda Shen

In Partial Fulfillment
of the Requirements for the Degree
Doctor of Philosophy in the
School of Civil and Environmental Engineering

Georgia Institute of Technology

December 2019

MICRO-MACRO MODELING OF CHEMO-MECHANICAL DAMAGE AND HEALING IN ROCKS

Approved by:

Dr. Chloé Arson, Advisor
School of Civil and Environmental Engineering
Georgia Institute of Technology

Dr. Susan E. Burns
School of Civil and Environmental Engineering
Georgia Institute of Technology

Dr. Sheng Dai
School of Civil and Environmental Engineering
Georgia Institute of Technology

Dr. Ken Ferrier
Department of Geoscience
University of Wisconsin Madison

Dr. Ting Zhu
School of Mechanical Engineering
Georgia Institute of Technology

Date Approved: October 9, 2019

ACKNOWLEDGEMENTS

First of all, I would like to express my sincere appreciation towards my Ph.D. advisor, Dr. Chloé Arson, for her patient guidance and endless support through out my Ph.D. life at Georgia Tech. Her remarkable erudition, insightful suggestions, and consistent encouragement always help me overcome research obstacles and make me enjoy my study. Her persistent enthusiasm on research and teaching motivate me, will continuously inspire me in my career.

I would like to acknowledge my Ph.D. thesis committee members including Dr. Susan Burns, Dr. Sheng Dai, Dr. Ken Ferrier, and Dr. Ting Zhu, for their insightful comments and suggestions that significantly improve the quality of this thesis. I am grateful to Dr. Burns for always being helpful and supportive. I want to thank Dr. Dai for sharing experience on experimental design and providing career advice. I appreciate Dr. Ferrier's great suggestions on my research from the geosciense aspect of view. I wish to thank Dr. Zhu for his invaluable suggestions on micromechanics and multi-scale study. I would like to take this opportunity to thank all other geosystems faculty members including Dr. David Frost, Dr. Leonid Germanovich, Dr. Haiying Huang, Dr. Jorge Macedo, and Dr. Paul Mayne for making such great study and research environment at Georgia Tech.

I am grateful for the valuable support from my research collaborators and friends: Dr. Fred Chester and Dr. Judith Chester at Texas A&M University; Dr. Nicole West at Central Michigan University; Dr. Sébastien Brisard at Université Paris-Est; Dr. Jihui Ding at Stanford University and Dr. Haoyan Zhai at Georgia Tech. Their instructive and insightful suggestions improve my research and help me to be a better researcher.

I am grateful for the help and support I received from my past and present lab members: Dr. Hao Xu, Dr. Cheng Zhu, Dr. Wencheng Jin, Dr. Pei Wang, Koochul Ji, L.

Fernando Patino Ramirez, Tingting Xu, and Haozhou He. I also want to thank all Geosociety members for sharing experience, jokes and progress, and bringing joy and happiness to my Ph.D. journey. I am thankful to the undergraduate research assistants involved in the Vertically Integrated Projects Program on Energy Geotechnology at Georgia Tech for valuable assistance and initiative research ideas.

I want to acknowledge the financial support from the School of Civil and Environmental Engineering at Georgia Tech and National Science Foundation, which makes my Ph.D. study at Georgia Tech possible.

Finally, I would like to thank Jiaqi Yang for for her everlasting understanding and love. I hope she will have a great Ph.D. journey. I am particularly indebted to my parents, Quanfa Shen and Jun Sun, for their supports and love at all times. I wish them have a sweet and enjoyable life.

TABLE OF CONTENTS

Acknowledgments iii

List of Tables vi

List of Figures vii

Chapter 1: Introduction and Background 1

1.1 Damage and healing processes in rocks 2

1.2 Continuum damage and healing mechanics 3

1.3 Fabric tensors and damage evolution 6

1.4 Micro-mechanics-based damage models 7

1.5 Homogenization theory 9

1.5.1 Eshelby's theory 10

1.5.2 Homogenization models based on Eshelby's theory 13

I Micro-Macro Damage Mechanics in Salt Rock **15**

Chapter 2: Fabric development and crack propagation in salt 19

2.1 Materials and Methods 20

2.1.1 Consolidation tests and cyclic compression tests 20

2.1.2 Grain morphology 23

2.1.3 Grain arrangement 24
2.2 Results 27
2.2.1 Grain morphology 27
2.2.2 Coordination orientation 31
2.2.3 Local solid volume fraction 33
2.2.4 Crack length and orientation 34
2.3 Discussion 35
2.3.1 Grain deformation 35
2.3.2 Normalization of fabric descriptors in the cyclic compression tests . 37
2.3.3 Categories of cracks 39
2.3.4 Fabric tensors 40
2.4 Conclusions 45

Chapter 3: Discrete Wing Crack Elasto-plastic Damage model 47

3.1 Tests and microstructure observations 49
3.1.1 Materials and methods 49
3.1.2 Summary of the results 51
3.1.3 Interpretation of the results 51
3.2 Theoretical formulation of the DWCPD model 52
3.2.1 The evolution of main cracks 52
3.2.2 The development of wing cracks 55
3.2.3 Micromechanics-based Gibbs free energy 57
3.2.4 Damage criterion and flow rule 59

3.2.5 Inelastic deformation 61
3.3 DWCPD model calibration 63
3.4 Sensitivity analyses 66
3.4.1 Influence of the frictional coefficient at main crack faces 66
3.4.2 Influence of the confinement 69
3.4.3 Damage evolution in predamaged salt rock 71
3.5 Summary 74

Chapter 4: Rate-dependent cyclic model of salt rock 77
4.1 Observations made during cyclic compression tests 80
4.2 Grain boundary sliding 82
4.2.1 Conceptual model 82
4.2.2 Thermodynamic model 84
4.3 Homogenization scheme 86
4.4 Model calibration 89
4.5 Sensitivity analysis 93
4.6 Energy dissipation 94
4.7 Conclusions 96

II Micro-Macro Chemo-Mechanical Damage 100

Chapter 5: Bedrock weakening by biotite weathering 102
5.1 Chemo-mechanical model of bedrock 105
5.1.1 Parameterization of biotite expansion during weathering 105
5.1.2 A crystal-scale model of biotite expansion 107

5.1.3 Damage model for the matrix . . . 110

5.1.4 A homogenization scheme for bedrock strain and damage at the REV scale . . . 111

5.1.5 Resolution algorithm for the homogenization scheme . . . 113

5.2 Simulation results . . . 114

5.2.1 Influence of boundary conditions . . . 115

5.2.2 Influence of biotite abundance . . . 121

5.2.3 Influence of biotite aspect ratio . . . 124

5.2.4 Influence of biotite orientation . . . 127

5.3 Discussion . . . 129

5.3.1 Sensitivity to boundary conditions . . . 131

5.3.2 Sensitivity to biotite abundance . . . 132

5.3.3 Sensitivity to biotite aspect ratio . . . 132

5.3.4 Sensitivity to biotite orientation . . . 133

5.3.5 Controls on biotite and matrix strains . . . 135

5.3.6 Model limitations . . . 135

5.4 Conclusions . . . 137

III Micro-Macro Chemo-Mechanical Healing 139

Chapter 6: Chemo-mechanical healing in salt . . . 141

6.1 Microscopic chemo-mechanical model . . . 142

6.1.1 Dissolution at grain contacts in salt rock . . . 142

6.1.2 Sphere inclusion model . . . 144

6.1.3 Ellipsoid inclusions . . . 153

6.2 Homogenization Scheme . . . 156
6.2.1 Averaging method . . . 156
6.2.2 Inclusion-matrix interaction model . . . 157
6.2.3 Upscaling calculations . . . 158
6.3 Model calibration against brine-saturated creep tests . . . 161
6.3.1 Macroscopic chemical creep of salt rocks and model calibration . . . 161
6.3.2 Sensitivity to the number of inclusions . . . 164
6.4 Influence of salt fabric . . . 165
6.4.1 Influence of initial inclusion size . . . 166
6.4.2 Influence of initial porosity . . . 169
6.4.3 Influence of the variance of the initial void radius distribution . . . 171
6.5 A generalized thermodynamic framework . . . 172
6.5.1 Helmholtz free energy . . . 173
6.5.2 Hydraulic mechanical coupling . . . 174
6.5.3 Chemical mechanical coupling . . . 176
6.5.4 Damage evolution . . . 176
6.5.5 Calculation procedure . . . 178
6.5.6 Preliminary simulations . . . 179
6.6 Conclusion . . . 181

Chapter 7: Damage and healing process in a salt cavern . . . 184

7.1 FEM modeling of CO_2 storage in a salt cavern . . . 184
7.2 Simulation results . . . 186

7.3 The influence of diffusion efficiency and grain size 189

7.4 Summary 190

Chapter 8: Conclusions and future work 192

8.1 Main Contributions 192

8.2 Plans for Future Research 195

References 217

Vita 218

LIST OF TABLES

2.1 Evolution of volumetric parameters in salt rock during the triaxial cyclic loading test. 38

3.1 Deformation modes of main cracks 53

3.2 DWCPD model parameters, calibrated against the cyclic triaxial test. 64

4.1 Parameters of the rate-dependent micro-macro model of salt calibrated against the results of the small loading cycles at 0% and 3.8% permanent axial strain. 91

5.1 Mechanical parameters in bedrock 115

6.1 Inclusion parameters in the isotropic and uniaxial creep tests 148

6.2 Model parameters found by calibration 162

6.3 Error made on the estimation of the final porosity, compared to the porosity estimated with 400 inclusions. 166

6.4 Microstructure parameters used in the sensitivity analysis 167

6.5 Parameters used in the THCM model of damage and healing 180

7.1 Damage parameters used for the excavation simulation 186

LIST OF FIGURES

1.1 Representative Elementary Volume (REV) in terms of porosity [87]. 10

2.1 Binary images of salt microstructure at several stages of consolidation tests. The blue scale bar represents 0.5 mm. The red inserts indicate the presence of intra-granular cracks (see Section 2.1.3). 21

2.2 Binary images of salt microstructure at several stages of cyclic compression tests. The blue scale bar represents 0.5 mm. The red inserts indicate the presence of cracks (see Section 2.1.3). The yellow areas represent grains that were removed by polishing. 22

2.3 Processed image of a grain, showing indentations on the contour. The image was taken at an axial strain of 0%, before the cyclic compression tests. . 23

2.4 The method to calculate the coordination vector of a grain. 25

2.5 The method to calculate grains' local solid volume fraction. The grey scale illustrates the differences in local solid volume fractions. The images were taken at an axial strain of 0%, before the cyclic compression tests. 26

2.6 Evolution of salt grains' shapes during the consolidation tests. 27

2.7 Evolution of salt grains' shapes during the cyclic compression tests. 28

2.8 Evolution of the orientation of the salt grains during the consolidation tests. 28

2.9 Evolution of the orientation of the salt grains during the cyclic compression tests. 29

2.10 Evolution of the solidity vector during the consolidation tests. 30

2.11 Evolution of the solidity vector during the cyclic compression tests. 30

2.12 Evolution of the distribution of grain indentations during the cyclic compression tests. 31

2.13 Evolution of the coordination orientation in the consolidation tests. 32

2.14 Evolution of the coordination orientation in the cyclic compression tests. . . 32

2.15 Evolution of the local solid volume fraction (LSVF) in the consolidation tests. 33

2.16 Evolution of the local solid volume fraction (LSVF) in the cyclic compression tests. 34

2.17 Orientation and length distributions of the cracks observed in the 2D images obtained at several stages of the cyclic compression tests. The number of cracks (n) is given for each loading stage. 35

2.18 Distribution of the void volume when ϵ_a reaches 7% in the cyclic compression tests. 36

2.19 Evolution of the coordination orientation after normalization in the cyclic compression tests. 39

2.20 Evolution of the magnitude of the local solid volume fraction during the cyclic compression tests. 39

2.21 Orientation and length distributions of the wing cracks observed in the 2D images obtained at several stages of the cyclic compression tests. n is the number of wing cracks. 41

2.22 Orientation and length distributions of the sliding cracks at several stages of the cyclic compression tests. n is the number of main cracks. 42

2.23 Axial and lateral components of fabric tensors in consolidation tests. Notation: F_{xx}, F_{zz}: lateral, axial components of fabric tensor $\boldsymbol{F}$. F: trace of $\boldsymbol{F}$: $F = F_{xx} + F_{zz}$. 43

2.24 Axial and lateral components of fabric tensors in cyclic compression tests. Notation: F_{xx}, F_{zz}: lateral, axial components of fabric tensor $\boldsymbol{F}$. F: trace of $\boldsymbol{F}$: $F = F_{xx} + F_{zz}$. 44

3.1 Microstructure of experimentally-deformed, granular salt rock after 7.3% axial strain (adapted after [129]). 52

3.2 The mechanisms of main crack propagation. Blue region: no slipping. Gray region: slipping. Mechanism 1: pure Mode I. Mechanism 3: modes I and II. Mechanism 4: pure Mode II. Mechanisms 2 and 5: no propagation. c is the cohesion at the main crack face. μ is the frictional coefficient. σ_n^m is the normal stress that applies on the faces of the main crack (tension stress). $\boldsymbol{\sigma}_t^m$ is the tensor of tangential stresses that apply on the faces of the main crack. 54

3.3 Schematic of wing crack propagation. Note: the sketch gives a 2D view, but the proposed model is in 3D. σ_n^m and $\boldsymbol{\sigma}_t^m$ are the normal stress and tangential stress that apply on the faces of the main crack respectively; σ_l^m is the normal stress applies on the faces of the wing crack induced by the stress of the REV. 56

3.4 stress-strain curve obtained during the confined cyclic triaxial tests: experimental results vs. DWCPD model predictions. 63

3.5 Evolution of damage during the triaxial cyclic tests (calibration of the DWCPD model). Ω_m is the main crack damage, Ω_w is the wing crack damage, and Ω is the sum of main crack damage and wing crack damage. 65

3.6 Damage propagation process: (1) Wing crack tensile opening; (2) Main crack slipping, inducing additional wing crack opening. 66

3.7 Influence of the frictional coefficient at main crack faces (stress-strain curve). μ is the frictional coefficient. 67

3.8 Influence of the frictional coefficient and the cohesion at main crack faces (damage evolution). μ is the frictional coefficient. 68

3.9 Influence of the cohesion at main crack faces (stress-strain curve). c is the cohesion. 70

3.10 Influence of the cohesion at main crack faces (damage evolution). c is the cohesion. 71

3.11 Influence of the confinement (stress-strain curve). p is the confinement. . . . 72

3.12 Influence of the confinement (damage evolution). p is the confinement. . . . 73

3.13 stress-strain curve - pre-damaged vs. undeformed salt rock. 74

3.14 Damage evolution - pre-damaged vs. undeformed salt rock. 75

4.1 Deformation map of damp halite. LT, low temperature; HT, high temperature; N-H, Nabarro-Hering. Adapted from [149] 77

4.2 Stress-strain curve obtained during cyclic compression tests under a 1 MPa confining pressure. Experimental protocol described in Chapter 3. 80

4.3 Plots of differential stress versus axial and radial strain for the first and last small loading cycles. ϵ_a is the axial strain. ϵ_r is the radius strain 81

4.4 Isolated brine pockets along grain boundaries in undeformed consolidated sample (5% porosity) [150]. 82

4.5 The concept of REV in the proposed rate-dependent model of salt rock. . . 84

4.6 Mechanism of shear displacement along a sliding plane filled with brine in a spherical inclusion 85

4.7 Model calibration against the results of the small loading cycles at a permanent axial strain ϵ_a = 0%. Solid lines: simulation results. Dashed lines: experimental results. 92

4.8 Model calibration against the results of the small loading cycles at a permanent axial strain ϵ_a = 3.8%. Solid lines: simulation results. Dashed lines: experimental results. 93

4.9 Local normal stress and chemical strain in a representative inclusion family. The orientation of crack plane is 25^o 94

4.10 Influence of crack thickness on stress/strain relationship. The total volume fraction of the inclusions, ϕ_c, is equal to 50%. The roughness angle α is set equal to 60^o. 95

4.11 Influence of crack subsurface angle on stress/strain relationship. The total volume fraction of sliding inclusions, ϕ_c, is equal to 50%. The crack thickness c was set equal to 4.8 μm. 96

4.12 Influence of the volume fraction of inclusions on stress/strain relationship. The roughness angle α was set equal to 60^o. The crack thickness c was set equal to 4.8 μm. 97

4.13 Influence of inclusions' crack thickness on energy dissipation. The roughness angle α is set equal to 60^o. The total volume fraction of the inclusions, ϕ_c, is equal to 50%. 98

4.14 Influence of the volume fraction of the inclusions on energy dissipation. The roughness angle α was set equal to 60^o. The crack thickness c was set equal to 4.8 μm. 99

5.1 Schematic of the crystal-scale weathering model. 108

5.2 Resolution algorithm for the proposed homogenization scheme. See the text for the definitions of the variables in this figure. 114

5.3 Schematic of the boundary conditions. 116

5.4 Influence of boundary conditions on strain and damage: effect of vertical stress. **a.** Biotite strain in the thickness direction c (ϵ_c) increases over time and shows negligible sensitivity to depth and boundary conditions (proportional stress vs. oedometric boundary conditions). **b.** Biotite strain in the transverse direction (ϵ_a) is $\sim$100 times smaller than ϵ_c. It exhibits contraction under the proportional stress condition, expansion under the oedometer condition, and negligible sensitivity to depth. **c.** Volumetric strain in the bedrock REV (ϵ_v) is small ($< 1\%$) and exhibits negligible sensitivity to depth and only minor sensitivity to boundary conditions. **d.** The time until damage initiation is noted as t_{lag}. Bedrock damage (Ω) initiates hundreds of years earlier under the oedometric condition than under the proportional stress condition, and exhibits minor sensitivity to depth. In each simulation, initial biotite abundance was 15%, initial biotite aspect ratio was 3, and the initial orientation of all biotite a-axes were 30° relative to the horizontal. . . 118

5.5 Effect of the stress coefficient (K) on strains and damage under the proportional stress boundary condition. **a.** Biotite strain in the thickness direction (ϵ_c) shows negligible sensitivity to K. **b.** Biotite strain in the transverse direction (ϵ_a) also shows negligible sensitivity to K. **c.** The REV volumetric strain (ϵ_v) is small ($< 1\%$) and exhibits negligible sensitivity to K. **d.** Bedrock damage (Ω) exhibits minor sensitivity to K. In each simulation, the initial biotite abundance was 15%, the initial biotite aspect ratio was 3, and the initial orientation of all biotite a-axes were 30° relative to the horizontal. 120

5.6 Effect of biotite abundance (AB) on strains and damage under the proportional stress boundary condition. **a.** Biotite strain in the thickness direction (ϵ_c) increases over time and shows negligible sensitivity to abundance until the initiation of damage. **b.** Biotite strain in the transverse direction (ϵ_a) exhibits larger contraction in rocks with lower biotite abundances. **c.** The REV volumetric strain (ϵ_v) increases with biotite abundance. **d.** Bedrock damage (Ω) initiates earlier at higher biotite abundances. In each simulation, the initial biotite aspect ratio was 3, the depth of the bedrock was 10 m, and the initial orientation of all biotite a-axes was 30° relative to the horizontal. 122

5.7 Effect of biotite abundance (AB) on strains and damage under the proportional stress boundary condition ("Prop") and the oedometric boundary condition ("Oedo"). **a.** Biotite strain in the thickness direction c (ϵ_c) increases over time and shows negligible sensitivity to abundance for both proportional stress and oedometric boundary conditions. **b.** Biotite strain in the transverse direction (ϵ_a) exhibits less contraction under oedometric boundary conditions. **c.** The REV volumetric strain (ϵ_v) increases slower under oedometric boundary conditions. **d.** Bedrock damage (Ω) initiates earlier under oedometric boundary conditions. In each simulation, initial biotite aspect ratio was 3, the depth of bedrock was 10 m, the overburden density was $\rho = 2000$ kg m^{-3}, and the initial orientation of all biotite a-axes were 30° relative to the horizontal. 123

5.8 Effect of biotite aspect ratio (AR) on strains and damage. **a.** Biotite strain in the thickness direction (ϵ_c) shows negligible sensitivity to aspect ratio. **b.** Biotite strain in the transverse direction (ϵ_a) exhibits minor sensitivity to aspect ratio. **c.** The REV volumetric strain (ϵ_v) exhibits slightly larger expansion at smaller aspect ratios. **d.** Bedrock damage (Ω) initiates earlier in rocks with biotites with smaller aspect ratios. In each simulation, initial biotite abundance was 15%, the depth of bedrock is 10 m, and the initial orientation of all biotite a-axes were 30° relative to the horizontal. 125

5.9 Effect of biotite aspect ratio (AR) on strains and damage under proportional stress and oedometric boundary conditions. **a.** Biotite strain in the the thickness direction c (ϵ_c) shows negligible sensitivity to aspect ratio under both proportional stress and oedometric boundary conditions. **b.** Biotite strain in the transverse direction (ϵ_a) is close to 0 under oedometric boundary conditions. **c.** The REV volumetric strain (ϵ_v) exhibits minor sensitivity to aspect ratio under oedometric boundary conditions. **d.** Bedrock damage (Ω) exhibits negligible sensitivity to aspect ratio under oedometric boundary conditions. In each simulation, initial biotite abundance was 15%, the depth of bedrock was 10 m, the overburden density was $\rho = 2000$ kg m^{-3}, and the initial orientation of all biotite a-axes were 30° relative to the horizontal. 126

5.10 Effect of biotite orientation (θ) on strains and damage. **a.** Biotite strain in the thickness direction (ϵ_c) exhibits minor sensitivity to orientation. **b.** Biotite strain in the transverse direction (ϵ_a) shows negligible sensitivity to orientation under proportional stress boundary conditions, and exhibits larger expansion in rocks with larger θ under oedometric boundary conditions. **c.** The REV volumetric strain (ϵ_v) exhibits minor sensitivity to orientation under the proportional stress boundary condition, and decreases with θ under the oedometric boundary condition. **d.** Bedrock damage (Ω) initiates earlier in rocks with larger θ under the oedometric boundary condition. In each simulation, initial biotite abundance is 15%, the initial biotite aspect ratio is 3, and the depth of the REV is 10 m under overburden with a density $\rho = 2000$ kg m^{-3}. 128

5.11 The effects of boundary conditions and biotite characteristics on damage initiation: simulation results obtained with proportional stress boundary conditions (filled circles), and with oedometric boundary conditions (open circles). In each simulation, the depth of the REV is 10 m with K = 0.5. . . 130

6.1 Pressure solution mechanisms 143

6.2 Schematic of an inclusion 145

6.3 REV of salt 145

6.4 Mass transfer governed by pressure solution, in contact plane XY 148

6.5 Evolution of inclusion geometry during an isotropic creep test 149

6.6 System of angles adopted to define the orientation of the inclusion relative to the loading axis in uniaxial creep tests 151

6.7 Evolution of inclusion geometry during a uniaxial creep test 152

6.8 Microstructure of an elliptical elementary inclusion (cell) 153

6.9 Time-dependent deformation of ellipsoid cells under isotropic stress conditions 154

6.10 Time-dependent deformation of ellipsoid cells under uniaxial stress conditions. Numbers into brackets indicate angular coordinates (θ, ϕ). 154

6.11 Process to update local and global strains from the local stress with the proposed homogenization scheme. 160

6.12 Calibration of the model against uniaxial creep tests (tests under 2.1 MPa are used for verification). 163

6.13 Graphical representation of the microscopic principal stresses 164

6.14 Principal stresses in each inclusion, for a uniaxial creep test under 1.1 MPa. 165

6.15 Evolution of the void radius and of the minor compressiver principal stress in 10 different inclusions during the creep test performed under an axial load of 1.1 MPa. 165

6.16 Sensitivity analysis on the number of inclusions considered in the REV . . . 166

6.17 Influence of grain size on creep rate 167

6.18 Principal stresses obtained during an oedometer test, for different grain sizes. 168

6.19 Effect of initial porosity on the evolution of porosity and void radius 169

6.20 Evolution of principal stresses in the inclusions for different initial porosities. 170

6.21 Influence of the void radius COV on the creep rate 171

6.22 Influence of void radius COV on the evolution of inclusion principal stresses. 172

6.23 Thermodynamic micro-macro model calculation procedure. 179

6.24 THCM loading path 180

6.25 Simulation results obtained at the material point with the THCM model of damage and healing. Subscript 33 indicates the axial loading direction. . . . 181

7.1 Dimensions and mesh of the FEM model 185

7.2 Halite damage after excavation 186

7.3 Minimum (compressive) principal stress distribution around the cavity (zone of dimensions 225 m $\times$ 300 m. 187

7.4 Evolution of damage at the cavern wall during the storage phase. 187

7.5 Evolution the deformation of the salt cavern during storage. 188

7.6 Effect of diffusive efficiency on cavern healing. 189

7.7 Effect of inclusion radius on cavern healing. 190

SUMMARY

In rock mechanics, damage and healing respectively refer to the degradation and recovery of stiffness and strength induced by the evolution of microscopic defects. The gap between microscopic and macroscopic models makes it difficult to bridge the defects characterization at the microscopic scale to the development of deformation and stiffness at the macroscopic scale. Therefore, the goal of this doctoral research work is to understand and predict damage and healing processes in rock, by coupling microstructural and poromechanical models.

In the first part of the thesis, we present micro-macro approaches to model the influence of micro-crack propagation on the accumulation of damage and irreversible deformation in salt rock. Consolidation tests and cyclic compression tests were conducted by our collaborators at Texas A&M University. Samples were taken out and sliced for microstructure observation at key stages of the loading paths. Based on statistical image analysis, the evolution of solidity, grain coordination, local solid volume fraction and crack volume exhibit the clearest trends. We use these fabric descriptors to relate microstructure evolution to macroscopic behavior. We found that deformation is dominated by grain rearrangement. In the consolidation tests, plastic deformation increases, grains are organized into horizontal layers, the size of the voids reduce and become more uniformly distributed, and salt rock becomes much denser laterally under compaction. In the cyclic compression tests, inter granular cracks mainly propagate in the axial direction, and grain-to-grain contact areas reduce. Large voids collapse into small and isolated voids, which, then, are connected by inter granular cracks and form large voids again. The evolution of the magnitude and orientation of the fabric descriptors correlates with the evolution of the Young's modulus and of the Poisson's ratio. During the cyclic compression tests, we also observed that macro-cracks form in two stages: (i) Wing cracks tensile opening; (ii) Main crack slipping, inducing ad-

ditional wing crack opening. Larger confinement and higher friction at the crack faces leads to higher strength of salt rock. This model shows that salt rock develops damage-induced anisotropy. This observation contradicts the common assumption made in a large number of models of salt rock, in which damage and healing induce isotropic stiffness changes. We formulated, calibrated and validated a micro-mechanical model coupled with elasto-plastic model that captures these phenomena, called a discrete wing crack elastoplastic damage (DWCPD) model. We also formulated a chemo-mechanical homogenization framework to understand the rate dependent behavior of salt rock observed in cyclic compression tests. A higher rate of pressure solution and/or a larger volume fraction of sliding cracks lead to larger chemical deformation, stiffness degradation and larger hysteresis. When the chemical strain rate at sliding cracks is too large, the development of hysteresis is restrained due to the quasi-instantaneous stress redistribution. Models presented in this part of the thesis can be used to guide the design of geological energy storage (i.e. Compressed Air Energy Storage), and enhance the efficiency of energy geotechnologies.

In the second part of the thesis, a micro-macro homogenization framework is established to understand the coevolution of chemical weathering of minerals and bedrock weakening. The proposed model quantifies the accumulation of damage in the matrix of bedrock driven by chemical weathering of minerals like biotite, which expand as they weather and create stresses sufficient to fracture rock. Our simulation results suggest that damage in the matrix of granite occurs earlier under higher biotite abundances and smaller biotite aspect ratios. Biotite orientation exerts a relatively weak effect on damage. The development of damage is also strongly influenced by the boundary conditions, and damage initiates earlier under laterally confined boundaries than under unconfined boundaries. This model shows that chemical weathering of minerals is the controlling mechanism of saprolite production.

In the last part of the thesis, a novel multi-scale homogenization model is presented to

simulate salt rock healing driven by pressure solution. Hollow sphere inclusions traversed by three inter-granular contact planes are modeled at the microscopic scale. Under sufficient normal stress, salt mineral is dissolved at grain contacts, diffuses along inter-granular crack planes, and precipitates on the pore walls. Pressure solution in the inclusions induces the accumulation of chemical strain and the recovery of stiffness of salt rock at the REV scale. The healing rate is faster in salt rock with uniformly distributed void sizes. The healing rate also increases with initial porosity, but the final porosity change is independent on the initial porosity of salt rock. We implemented the micro-macro model of healing in the Finite Element Method for simulating CO_2 storage in a salt cavern. Based on thermodynamic principles, a generalized thermodynamic thermo-hydro-chemo-mechanical framework is also proposed to model multiple processes of damage and healing.

The research presented in this thesis sheds light on the processes that can control damage and healing in rocks, and provides theoretical tools to guide the design of geological storage facilities.

CHAPTER 1
INTRODUCTION AND BACKGROUND

Damage in mechanics of materials refers to the degradation of stiffness and strength due to the propagation of cracks. Conversely, healing refers to the recovery of stiffness and strength due to the rebonding of microscopic defects. In rock mechanics, the gap between microscopic and macroscopic models makes it infeasible to uniquely characterize the pore and crack- scale mechanisms that control the evolution of deformation and stiffness upon damage and healing. The goal of this research is, therefore, to understand and predict damage and healing processes in rock, by coupling microstructural and poromechanical models.

Continuum Damage Mechanics (CDM) provides a theoretical framework to model damage in solids [1]. The fundamental idea is that crack propagation leads to a loss of potential strain energy. Thermodynamic conjugation relationships are used to express the field variables and calculate the damaged stiffness tensor. The stress-strain relationship is derived from the postulated expression of a thermodynamic potential, and the evolution of damage is related to phenomenological driving forces, such as the rate of energy release due to tensile strains [2, 3]. Under the assumption of crack non-interaction, the second-order crack density tensor, similar to the fabric tensor used in structural geology [4], is commonly defined as the damage variable [5, 6]. The damaged stiffness tensor can be expressed as a function of the elasticity tensor of the prestine material and of the fabric tensor, which is directly related to the distribution of cracks shape and orientation. In this thesis, we formulate CDM models that relate the evolution of microstructure to that of the mechanical properties of a Representative Elementary Volume (REV) or rock. In top-to-bottom models, the damage (or healing) variable is replaced by a fabric tensor, defined as a convolution of moments of probability of microstructure descriptors. In bottom-up models, the REV

mechanical properties are either calculated by averaging micro-mechanical equations derived from the theory of fracture mechanics, or by defining an inclusion-matrix problem that can be solved by Eshelby's theory.

In this chapter, we explain why damage and healing mechanics is relevant to rocks, and we provide the theoretical background which our proposed models build upon.

1.1 Damage and healing processes in rocks

Rock is a common host material for waste and energy storage (e.g., CO_2 sequestration, nuclear waste, and compressed air) [7, 8, 9, 6]. Under typical geotechnical stress conditions, energy in rock is dissipated predominantly by the nucleation and propagation of microscopic cracks. At the macroscopic scale of a typical rock sample, the occurrence of these microscopic defects leads to a nonlinear stress-strain relationship, an anisotropic degradation of stiffness and a decrease of strength. Rock damage is accompanied by stress concentration, which prompts the initiation of new microscopic cracks [10].

Damage can be triggered by viscoplastic deformation, when the local maximum principal microstress is larger than the tensile strength of rock [11]. Damage in rock can also be caused by dynamic loading, such as blasting [12, 13] and seismic loading [14, 15]. In addition to purely mechanical processes, the evolution of damage can be thermally, hydraulically, and/or chemically driven. For instance, the mismatch of the coefficients of thermal expansion among rock minerals induces intergranular compressive and tensile forces upon temperature variations [16]. In most rocks, heat treatment largely decreases the energy required for rock fracturing [17]. Chemical reactions in rock is usually accompanied by mineral volume changes, which induce stress redistribution and porosity enhancement [18, 19]. In porous rock, pressure sensitive elastoplastic deformation is typically coupled with hydraulic fracturing [20, 21, 22, 23].

Healing is the process by which a damaged material recovers mechanical stiffness and strength, and exhibits a permeability decrease. Internally or externally triggered healing

occurs in a broad range of geomaterials, including crystalline rock, salt, indurated clay, and plastic clay [24]. In salt rock, pressure solution is the driving mechanism of mechanical healing around excavation damage zone. The healing rate increases with the presence of brine [24, 25]. Many laboratory tests were conducted to study healing processes in salt rock. For example, Fuenkajorn [26] highlighted the significant influence of rock purity, fracture roughness and brine saturation on the healing process of salt rock under uniaxial and radial loading conditions. Healing decreases permeability. The reduction of permeability controlled by crack rebonding was studied by Chan's group [9]. Healing was observed in plastic clay at the Mont Terri underground laboratory in Switzerland [27]. The decrease of permeability is due to clay swelling and creep, which lead to crack closure.

1.2 Continuum damage and healing mechanics

Continuum Damage Mechanics (CDM) provides a solid theoretical framework to model the effects of damage evolution on the mechanical behavior of rock at the macroscopic scale [28, 29]. The evolution of damage is controlled by phenomenological driving forces derived from a thermodynamic potential, often expressed in terms of stresses and strains, e.g. Mises-equivalent stresses and strains or tensile stresses and strains [2, 30]. When coupled to an elasto-plastic framework, CDM can be used to predict the behavior of semi-brittle materials, including rocks that exhibit a transition from brittle to crystal-plastic behavior [31, 32, 33].

Broadly speaking, CDM models are either micro-mechanical or phenomenological. We will present micromechanical damage models in Section 1.4. In phenomenological CDM, the damage tensor is a phenomenological internal state variable that affects energy dissipation associated with stiffness and strength reduction. Phenomenological damage models are often formulated in terms of "effective stress" [34], which is equivalent to the stress undergone by the "effective" non-damaged part of the material. The concept of CDM effective stress is similar to that in soil mechanics: it is the stress supported by the skeleton

of the material, i.e., the solid part minus the pores (or cracks). The effective stress is used in the expression of the free energy of the solid skeleton to account for the loss of elastic strain energy [35]. The expression of the rock free energy is chosen so as to ensure certain stiffness properties, such as symmetry and positivity [35, 36, 37]. Damage grows when a damage criterion, similar to a plastic yield criterion, is exceeded. The damage evolution law can be associated or non associated, like in plasticity.

The first law of thermodynamics states that energy conservation is always satisfied [38]. The sum of the rate of the internal energy $\dot{U}$ and the rate of the kinetic energy $\dot{K}$ is the sum of the rate of external mechanical work $\dot{W}$ and the rate of heat exchange $\dot{Q}$ in a thermodynamic system Γ, as follows

$$\dot{U} + \dot{K} = \dot{W} + \dot{Q} \tag{1.1}$$

Equation 1.1 can also be written as:

$$\int_{\Gamma} \rho \dot{u} \mathrm{d}\Gamma + \int_{\Gamma} \rho \boldsymbol{a} \cdot \boldsymbol{v} \mathrm{d}\Gamma = \int_{\Gamma} \boldsymbol{b} \cdot \boldsymbol{v} \mathrm{d}\Gamma + \int_{\partial\Gamma} \boldsymbol{T} \cdot \boldsymbol{v} \mathrm{d}S + \int_{\Gamma} r \mathrm{d}\Gamma - \int_{\partial\Gamma} \boldsymbol{q} \cdot \boldsymbol{n} \mathrm{d}S \tag{1.2}$$

where ρ is density; $\dot{u}$ is the rate of the internal energy per unit mass; $\boldsymbol{a}$ is the acceleration vector; $\boldsymbol{v}$ is the velocity vector; $\boldsymbol{b}$ is the body force vector; $\boldsymbol{T}$ is the traction vector, which is equal to $\boldsymbol{\sigma} \cdot \boldsymbol{n}$; $\boldsymbol{n}$ is the outward unit normal vector of the boundary S of the system considered; r is the heat generation rate per unit surface; $\boldsymbol{q}$ is the heat flow vector.

Based on Gauss divergence theorem and the small strain assumption $\dot{\boldsymbol{\epsilon}} = \bigtriangledown \boldsymbol{v}$, Equation 1.2 is further simplified:

$$\int_{\Gamma} \left(\rho \dot{u} - \boldsymbol{\sigma} : \boldsymbol{\epsilon} - r + \bigtriangledown \cdot \boldsymbol{q} \right) \mathrm{d}\Gamma = \int_{\Gamma} \left(\bigtriangledown \cdot \boldsymbol{\sigma} + \boldsymbol{b} - \rho \boldsymbol{a} \right) \cdot \boldsymbol{v} \mathrm{d}\Gamma \tag{1.3}$$

Using the momentum balance equation, we have:

$$\rho\dot{u} - \boldsymbol{\sigma} : \dot{\boldsymbol{\epsilon}} - r + \bigtriangledown \cdot \boldsymbol{q} = 0 \tag{1.4}$$

The second law of thermodynamics states that the rate of entropy increase of a system is never less than the rate of entropy increase due to the heat exchange, which can be expressed as a function of the heat flux $\boldsymbol{q}$. Mathematically, the second law of thermodynamics is written as follows:

$$\int_{\Gamma} \rho\dot{s}\mathrm{d}\Gamma \geq \int_{\Gamma} \frac{r}{T}\mathrm{d}\Gamma - \int_{\partial\Gamma} \frac{\boldsymbol{q}}{T} \cdot \boldsymbol{n}\mathrm{d}S \tag{1.5}$$

where s is the entropy per unit mass and T is the absolute temperature. Combining the first and the second laws of thermodynamics, we have:

$$\rho T\dot{s} + \boldsymbol{\sigma} : \dot{\boldsymbol{\epsilon}} - \rho\dot{u} - \frac{\boldsymbol{q}}{T} \cdot \bigtriangledown T \geq 0 \tag{1.6}$$

The Helmholtz free energy per unit mass $\dot{\psi}$ is a measurement of the maximum work that can be done by a system, and is defined as follows:

$$\dot{\psi} = u - Ts \tag{1.7}$$

The Clausius-Duhem inequality is obtained by substituting Equation 1.7 into Equation 1.8:

$$\boldsymbol{\sigma} : \dot{\boldsymbol{\epsilon}} - \rho\dot{\psi} - \rho s\dot{T} - \frac{\boldsymbol{q}}{T} \cdot \bigtriangledown T \geq 0 \tag{1.8}$$

The Helmholtz free energy is a function of the state variables, for instance the elastic strains $\boldsymbol{\epsilon}^E$ and the temperature T, as well as the internal variables (in CDM, the damage variable $\boldsymbol{\Omega}$). Substituting the derivative of the Helmholtz free energy into the Clausius-Duhem

inequality, we have:

$$\left(\boldsymbol{\sigma} - \rho\frac{\partial\psi}{\partial\boldsymbol{\epsilon}^E}\right) : \dot{\boldsymbol{\epsilon}}^E + \boldsymbol{\sigma} : \left(\boldsymbol{\epsilon} - \boldsymbol{\epsilon}^E\right) + \rho\left(s + \frac{\partial\psi}{\partial T}\right) : \dot{T} - \rho\frac{\partial\psi}{\partial\boldsymbol{\Omega}} : \dot{\boldsymbol{\Omega}} - \boldsymbol{q}\cdot\frac{\bigtriangledown T}{T} \geq 0 \quad (1.9)$$

This inequality in Equation 1.9 holds in particular for reversible processes, for which it is actually an equality. From the equality for isothermal reversible processes, we get that stress is the the work-conjugate variable of the elastic deformation. From the equality for pure thermal reversible processes, we get that the reversible entropy is work-conjugate to temperature. These two statements can be expressed as:

$$\boldsymbol{\sigma} = \rho\frac{\partial\psi}{\partial\boldsymbol{\epsilon}^E} \qquad s = -\frac{\partial\psi}{\partial T} \quad (1.10)$$

Thermodynamics principles were used to formulate phenomenological models of damage and healing for crushed salt rock [39], thermoset polymers [40], shape memory polymers [41] and asphalt mixes [42]. A constitutive multi-mechanism deformation model was proposed by Chan [43, 44] to couple creep, fracture, and healing in salt rock: healing is controlled by the effective area reduction and influences the inelastic strain rate of salt rock.

1.3 Fabric tensors and damage evolution

A fabric tensor is typically a second-order symmetric tensor, equal to a moment of probability of a microstructure descriptor [45], such as crack orientation, grain aspect ratio, or branch length orientation, to cite only a few [46, 47].

Fabric descriptors such as projected areas, Feret diameters and effective grain diameters all characterize grain size [48, 49, 50]. Roundness [51, 52], aspect ratio [53] and sphericity [51, 54] describe grain shape. In addition to grain morphology, grain arrangement was measured by dedicated descriptors. For instance, the void ratio is a parameter measuring the packing density of granular materials at macroscopic scale. Based on the concept of void ratio, the local void ratio distribution was proposed to measure volumetric changes at

the microscopic scale [55, 56, 57]. Within a 2D image, the local void ratio is calculated over polygonal subdomains, in which polygon corners are grain centroids. The coordination number of a grain is equal to the number of grains that are in contact with that grain. It is usually defined as the average number of contacts per grain. Based on this definition of the coordination number, many contact fabric parameters were proposed to discriminate grains with less contacts [58, 59] or to measure the area of grain contacts [60, 46]. Distributions of directional descriptors are typically determined by stereological methods [61]. Descriptors of magnitude such as volumetric fraction, coordination number, grain size distribution, and crack density define the trace of fabric tensors [62, 45].

In granular materials, mechanical anisotropy is mainly due to the shape of pores and particles (grains) and to the distribution of the contact normal orientations [63]. Triaxial tests performed on Toyoura sand and rice grain samples [64] showed that stiffness anisotropy is more pronounced in specimens with elongated grains. Triaxial tests conducted on circular and elongated rods [45], and on natural sands [65] demonstrated the effects of grains' geometry and orientation on the anisotropy of strength in granular materials.

1.4 Micro-mechanics-based damage models

Micro-mechanical damage models are derived based on assumed distributions of microstructural features (i.e. micropores and microcracks). The displacement jumps (opening and sliding) at crack faces are internal variables that each affects the loss of elastic potential energy of the REV. The expression of displacement jumps of a single microscopic crack embedded in an infinite elastic homogeneous medium is derived from fracture mechanics principles [66, 67]. Considering a penny shaped micro-crack subjected to uniformly distributed tensile normal stress σ_n at its crack faces, the normal displacement u_n is expressed as:

$$u_n = 8\frac{1-\nu_0^2}{\pi E_0}\sigma_n\sqrt{a^2-r^2} \tag{1.11}$$

where ν_0 and E_0 are the Poisson's ratio and the Young's modulus of the infinite homogeneous media respectively; a is the radius of the crack. The averaged Crack Opening Displacement $< u_n >$ is:

$$< u_n >= \frac{16}{3} \frac{1-\nu_0^2}{\pi E_0} a\sigma_n \tag{1.12}$$

Similarly, considering a single crack embedded in an infinite elastic homogeneous medium and subjected to uniformly distributed tensile normal stress $\overrightarrow{\sigma_t}$ at its crack faces, the averaged shear displacement jumps is:

$$< \overrightarrow{u_t} >= \frac{32}{3} \frac{1-\nu_0^2}{\pi E_0(2-\nu_0)} a\overrightarrow{\sigma_t} \tag{1.13}$$

In rock with multiple non-aligned cracks, the distribution of cracks' orientation contributes to the mechanical behavior of the REV. Quite a few numerical 3-dimensional integration formulas for the crack distribution on the surface of a sphere were proposed [68, 69, 70]. The distribution of cracks' orientation can be discretized. Bažant derived the coefficients and the directions of integration on the unit sphere for various discretization schemes [71].

The rock free energy at the macroscopic scale is expressed as a function of cracks' distributions [72, 28]. The evolution of microstructure, due for instance to crack opening and propagation, dislocation, recrystallization, and boundary sliding, can be predicted by means of fracture mechanics or solid mechanics, at the scale of each relevant feature (e.g., crack plane, crystal, pore) [73, 74]. Damage can be a scalar equivalent to a crack volume fraction, a second-order tensor equivalent to a crack density tensor, or a higher-order tensor for more complex fabrics [75, 76, 77]. The second-order damage tensor is typically expressed as follows [5]:

$$\mathbf{\Omega} = \sum_{i=1}^{N} \phi_i \overrightarrow{n}_i \otimes \overrightarrow{n}_i \tag{1.14}$$

where $\mathbf{\Omega}$ is the damage variable, N is the total number of cracks, ϕ_i is the volume fraction of the i^{th} crack, and $\overrightarrow{n}_i$ is the i^{th} crack's direction. If cracks do not interact, it is sufficient

to formulate the model with the second-order crack density tensor to capture stress-induced anisotropy [5, 6, 78].

Stiffness is obtained by differentiating the damaged elastic energy potential, which yields a direct relationship between micro-crack distributions, the stiffness tensor and inelastic deformation. Crack closure is automatically accounted for, which allows capturing unilateral effects of damage on stiffness [79, 80]. The microscopic cracks that propagate in Mode I or Mode II have a significant impact on a homogeneous medium [81]. Fracture mechanics principles were applied to predict the development of micro-cracks in mixed-mode (e.g. wing cracks) [82, 83]. Wing cracks are defined as the tensile cracks that initiate at the edges of frictional defects present in the rock matrix [84].

1.5 Homogenization theory

Homogenization is a procedure that allows relating field variables at the micro-scale to those at the macro-scale [85] in order to calculate the effective mechanical properties of a composite at the macro-scale. The smallest material volume element of composite above which an effective property (such as porosity in Figure 1.1) does not vary with the position of the sample volume (for instance, the position of a core in a rock mass) is called the Representative Elementary Volume (REV) [86]. The REV size is not the same for all effective properties. For instance, the REV for permeability is typically larger than that for stiffness, since the permeability REV has to be statistically representative not only of defect distributions, but also, of defect connectivity distributions.

If all the elements of a composite are subjected to the same uniform strain, the Voigt approximation provides the upper bound of the composite's elastic stiffness [88]. If all the elements of a composite are subjected to the same uniform stress, the Reuss approximation provides the lower bound of the composite's elastic stiffness [89, 90]. A more general solution was established by Eshelby [91] to account for the disturbance caused by the presence of inhomogeneities.

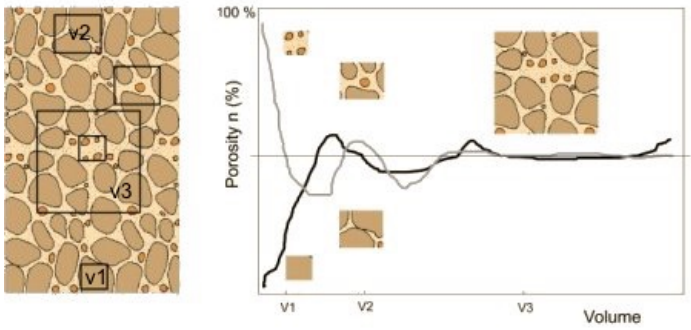

Figure 1.1: Representative Elementary Volume (REV) in terms of porosity [87].

1.5.1 Eshelby's theory

Let us consider inclusions $i = 1...N$, each with a stiffness $\boldsymbol{C}_i$, embedded in a continuum with stiffness $\boldsymbol{C}_0$, called the matrix of the composite. Using the 0 subscript for the matrix and the i subscript for inclusion i, we have:

$$\boldsymbol{\sigma}_0(\boldsymbol{x}) = \boldsymbol{C}_0 : \boldsymbol{\epsilon}_0(\boldsymbol{x}), \quad \boldsymbol{\sigma}_i(\boldsymbol{x}) = \boldsymbol{C}_i : \boldsymbol{\epsilon}_i(\boldsymbol{x}) \tag{1.15}$$

in which $\boldsymbol{\epsilon}_0$, $\boldsymbol{\sigma}_0$ and $\boldsymbol{\epsilon}_i$,$\boldsymbol{\sigma}_i$ are the strain, stress fields in the matrix and in inclusion i, respectively. The eigenstrain $\boldsymbol{\epsilon}^*(\boldsymbol{x})$ is defined as the strain field that is necessary to superpose to the inclusion strain fields to consider that the stiffness in all inclusions is equal to that of the matrix:

$$\boldsymbol{\sigma}_i(\boldsymbol{x}) = \boldsymbol{C}_0 : (\boldsymbol{\epsilon}_i(\boldsymbol{x}) - \boldsymbol{\epsilon}^*(\boldsymbol{x})) \tag{1.16}$$

$\boldsymbol{\epsilon}^*(\boldsymbol{x})$ is a so-called incompatibility eigenstrain, reflecting the difference of material properties between the matrix and the inclusions. It is equal to zero in the matrix. Additional eigenstrains have to be accounted for if inclusions are subjected to specific thermal strains or chemcial strains [92].

Consider that the composite is subjected to a uniform strain $\boldsymbol{E}_\infty$ in the far field (the reasoning is similar for an imposed stress field or for mixed boundary conditions). In the absence of inclusion, the strain field $\boldsymbol{\epsilon}(\boldsymbol{x})$ in the composite is equal to the strain imposed in

the far field, $\boldsymbol{E}_\infty$. The disturbance strain field $\boldsymbol{\epsilon}^d$ is introduced to account for the presence of heterogeneities, such that:

$$\boldsymbol{\epsilon}_i(\boldsymbol{x}) = \boldsymbol{E}_\infty + \boldsymbol{\epsilon}^d(\boldsymbol{x}) \tag{1.17}$$

Eshelby proved that if the eigenstrain field of an ellipsoidal inclusion is uniform, then the strain and stress fields in this inclusion are uniform, and the eigenstrain field is related to the disturbance field by the following relation [91]:

$$\boldsymbol{\epsilon}^d = \boldsymbol{S} : \boldsymbol{\epsilon}^* \tag{1.18}$$

where $\boldsymbol{S}$ is the Eshelby tensor. Note that since it is assumed that the eigenstrain field is assumed uniform, there is no dependence on the spatial variable $\boldsymbol{x}$ in the above equation. The Eshelby tensor is calculated as:

$$\boldsymbol{S} = \boldsymbol{P} : \boldsymbol{C}_0 \tag{1.19}$$

in which $\boldsymbol{P}$ is the so-called fourth-order "P tensor", which depends on the Green function. The Green function $G_{ij}(x - x')$ is the displacement component in direction i at point x induced by the unit body force in direction j at point x'. The expression of $G_{ij}(x - x')$ is as follows:

$$G_{ij}(x - x') = (2\pi)^{-3} \int_{-infty}^{\infty} N_{ij}(\xi) D{-}1(\xi) \exp\{i\xi \cdot (x - x')\} \mathrm{d}\xi \tag{1.20}$$

where N_{ij} and D are functions of the wave vector ξ, and $i = \sqrt{-1}$.

Substituting Equations 1.15, 1.16 and 1.18 into 1.17, the relation between the local strain $\boldsymbol{\epsilon}_i$ and the far field strain $\boldsymbol{E}_\infty$ is established, as follows:

$$\boldsymbol{\epsilon}_i = \boldsymbol{A}_\infty^i : \boldsymbol{E}_\infty \tag{1.21}$$

with:

$$\boldsymbol{A}_{\infty}^{i} = (\boldsymbol{I}_d + \boldsymbol{S}^i : \boldsymbol{C}_0^{-1} : (\boldsymbol{C}^i - \boldsymbol{C}_0))^{-1} \tag{1.22}$$

in which $\boldsymbol{I}_d$ is the fourth-order identity tensor.

A fourth-order concentration tensor $\boldsymbol{A}_i$ is used to relate the micro strain $\boldsymbol{\epsilon}_i$ and the macro strain $\boldsymbol{E}$ [92, 93], as follows:

$$\boldsymbol{\epsilon}_i = \boldsymbol{A}^i : \boldsymbol{E} \tag{1.23}$$

We have:

$$\boldsymbol{A}^i = \boldsymbol{A}_{\infty}^{i}(\sum \phi_i(\boldsymbol{I}_d + \boldsymbol{S}^i : \boldsymbol{C}_0^{-1} : (\boldsymbol{C}^i - \boldsymbol{C}_0))^{-1})^{-1} \tag{1.24}$$

in which ϕ_i is the volume fraction of phase i for $i = 0$ (matrix) to N ($i = 1...N$ inclusions). Due to strain compatibility and stress admissibility, the macroscopic strain $\boldsymbol{E}$ is the volume average of the local strains $\boldsymbol{\epsilon}_i$ and $\boldsymbol{\epsilon}_0$, and the macroscopic stress $\boldsymbol{\Sigma}$ is the volume average of the local stresses $\boldsymbol{\sigma}_i$ and $\boldsymbol{\sigma}_0$, as follows:

$$\boldsymbol{\Sigma} = \bar{\boldsymbol{\sigma}} = \overline{\boldsymbol{C} : \boldsymbol{\epsilon}} \tag{1.25}$$

Substituting 1.23 into 1.25, the expression of $\boldsymbol{\Sigma}$ is obtained as follows:

$$\boldsymbol{\Sigma} = \boldsymbol{C}^{hom} : \boldsymbol{E} \tag{1.26}$$

$$\boldsymbol{C}^{hom} = \overline{\boldsymbol{C} : \boldsymbol{A}} \tag{1.27}$$

where $\boldsymbol{C}^{hom}$ is the homogenized stiffness of the REV.

1.5.2 Homogenization models based on Eshelby's theory

Numerous models were developed to predict the effective properties of an inhomogeneous continuum with ellipsoidal inclusions based on Eshelby's solution [94, 95]. If the volumetric concentration of the inclusion is negligible, the interactions between inclusions are neglected and the dilute scheme is applied. In that case, the homogenized stiffness tensor of the REV is calculated from equations 1.27 and 1.24, with $\varphi \ll 1$ [96, 73].

In the Mori-Tanaka scheme, it is assumed that the average disturbance field in the matrix is zero, so that the average matrix strain is equal to the far field strain. Physically, interactions interact with a matrix subjected to a uniform strain in the far field (note: the reasoning is the same in the caes of stress or mixed boundary conditions) [97, 98, 99]. The Mori-Tanaka scheme has been widely used because of its accuracy and simplicity [100, 101], for instance, to predict voids' deformation and cracks' propagation in porous media [102]. Voids are regarded as inclusions, and the eigenstress in the matrix is related to the pore pressure in the voids. The Mori-Tanaka scheme was also used to calculate the thermal expansion of composites. Thermal expansion was taken as eigenstrain, expressed as a function the difference between the thermal expansion coefficients of the matrix and the inclusions [103]. However, if the composite material contains inclusions with eigenstrains other than the eigenstrains that stem from mechanical heterogeneity, the REV stiffness tensor predicted with the Mori-Tanaka scheme may violate symmetry requirements if inclusions have different orientations and shapes [98, 104].

The self-consistent method, initially proposed by Kröner [105], is used when it is not possible to distinguish a matrix phase from inclusion phases, i.e. no phase (or element) is predominant in the composite. This typically happens in polycrystalline media, which can be seen as a mozaïc of minerals which all have comparable volume fractions. Inclusions are assumed to be embedded in an equivalent homogeneous medium which has the same (yet unknown) effective properties as the REV [106]. The self-consistent method was extended to plastically deformed aggregates by Hill [107]. Later, the self-consistent approach was

used to model viscoplastic materials [108] and polycrystals subject to anisotropic damage [11, 109, 110]. The self-consistent scheme was also used to calculate the thermal expansion coefficients of polycrystalline materials [111].

Asymptotic expansions were introduced in a homogenization scheme to formulate a macroscopic model of compacted swelling clays and to correlate macroscopic parameters with microscopic electro-hydrodynamics [112]. Multi-scale homogenization schemes were also employed to predict stiffness changes induced by mineral dissolution in calcite [113].

In this thesis, we use homogenization to understand the fundamental processes that govern the chemo-mechanical behavior of quasi-brittle rocks. We will study salt rock and granite, which are used as model materials to advance the theory of damage and healing mechanics.

Part I

Micro-Macro Damage Mechanics in Salt Rock

Salt rock is a polycrystalline material of interest for geostorage because of its low permeability and because of its potential to self-heal by pressure solution at favorable stress and temperature conditions. It is often assumed that micro-crack propagation and healing lead to isotropic stiffness changes. The goal of this study is to check this assumption and to gain a fundamental understanding of the mechanisms that control the accumulation of damage and irreversible deformation.

In Chapter 2, 2D microstructure images of salt rock are analyzed at several stages of consolidation tests and cyclic compression tests to quantify the evolution of the magnitude and orientation of solidity, coordination, local solid volume fraction and crack volume. The consolidation tests and cyclic compression tests were conducted by our collaborators, Fred Chester, Judith Chester, and Jihui Ding, at Texas A&M University. Solidity characterizes the plastic deformation accumulated at the surface of grains. The orientation of coordination captures the area and orientation of grain-to-grain contacts. The local solid volume fraction is a measure of the packing density around a grain. In both the consolidation and the cyclic compression tests, deformation is controlled by grain rearrangement and not by grain indentation. Almost no crack developed during the consolidation tests, whereas in the cyclic compression tests, wing cracks propagate as a result of sliding cracks. In the consolidation tests, the microstructure becomes organized into horizontal layers of coordinated grains, the orientation distribution of grain indentations is quasi-uniform, and the size of the voids reduces and becomes more uniformly distributed. As a result, salt rock microstructure becomes more homogeneous. The local solid volume fraction increases more in the lateral direction than in the axial direction, which indicates that salt rock becomes much denser laterally under compaction. The oedometer modulus increases. In the cyclic compression tests, grain-to-grain contact areas decrease due to the redistribution of grains and the propagation of inter granular cracks. Grains tend to be reorganized into columns of coordinated grains. Opening-mode wing cracks tend to develop in the axial direction, while sliding cracks propagate preferentially in the lateral direction. The volume of the

wing cracks increases linearly with the axial strain. The lateral components of the fabric tensors of coordination and local solid volume fraction decrease, which results in an increase of the Poisson's ratio.

In Chapter 3, we couple a micromechanical CDM model and an elasto-plastic model to explain the formation of complex patterns of sliding and wing cracks that develop in salt upon confined cyclic axial loading and to quantify the effect of anisotropic damage on stiffness, strength and deformation. Cyclic axial loading tests are performed under a confining stress of 1 MPa on synthetic salt rock generated by thermal consolidation. The stress-strain curves and the microstructure images taken at key stages of the cycles reveal the formation of a complex system of sliding and wing micro-cracks, the orientation of which is loading dependent. We interpret the mechanisms that control the coupled evolution of crack families by a discrete wing crack elastoplastic damage (DWCPD) model. Crack propagation is controlled by mode I and mode II fracture mechanics criteria. Sliding "main" cracks grow if a cohesive frictional criterion is met, while the wing cracks propagate in tension. Displacement jumps at crack faces are related to the deformation of the rock Representative Elementary Volume (REV). The DWCPD model can capture the nonlinear-stress/strain relationship and the degradation of stiffness during the cyclic loading. Simulations show that micro-cracks occur following two stages: (i) Wing cracks initiate and main cracks do not propagate; (ii) Wing cracks and main cracks then propagate simultaneously. Higher friction at the crack faces leads to higher strength and larger lateral dilation. That is why at higher confinement, the initiation of wing cracks is delayed, which results in an increase of strength. Damage accumulates faster in samples that are damaged prior to compression than in the ones that are not. The proposed DWCPD model can be extended to any polycrystalline semi-brittle materials, and can be applied to understand the formation of crack patterns in salt geostorage facilities.

In Chapter 4, we propose a chemo-mechanical homogenization framework to simulate the rate dependent behavior of salt rock observed in cyclic compression tests. A micro-

mechanical model of sliding crack propagation coupled with a pressure solution model is first established to calculate shear displacements at the grain contacts. A Mori-Tanaka homogenization scheme is used to express the REV stress and strain fields as a function of the stress and strain fields at the micro-crack scale. This rate-dependent homogenization model is calibrated against cyclic compression tests conducted by our collaborators at Texas A&M University. The proposed chemo-mechanical homogenization framework captures the rate dependent stiffness degradation and the hysteresis behavior of salt rock. Sensitivity analyses show that thinner sliding planes (i.e. thinner brine films) enhance stiffness reduction and accelerate stress redistributions in the inclusions. Higher roughness angles lead to an increased difference of normal stress on the different segments of the crack plane and to a reduced diffusion path, which both lead to enhanced stiffness reduction and enhanced hysteresis. The larger the volume fraction of the inclusions, the larger the REV deformation and the larger the hysteresis.

CHAPTER 2

FABRIC DEVELOPMENT AND CRACK PROPAGATION IN SALT DURING CONSOLIDATION AND CYCLIC COMPRESSION TESTS

Halite is a polycrystalline material made of bonded crystals, also called grains. Crystal plasticity influences the development of microscopic cracks [114, 115], and inter-granular sliding leads to the degradation of polycrystals' elastic moduli [116, 117, 118, 119]. Macroscopic stiffness and strength in granular materials are also sensitive to the topology of the internal microscopic structure, which defines the fabric [120].

In salt rock, frictional sliding at grain boundaries is the primary accommodation mechanism at room temperature, low confining pressure and high strain rate. Deformation is controlled by the normal and shear stresses at grain boundaries and by the distribution of boundary orientations [121]. The rate of diffusional sliding depends on the shape of the grain boundaries [122]. In the presence of inter-granular fluid films, pressure solution is the predominant creep mechanism. Salt rock local deformation is controlled by the direction of grain-to-grain contacts and by the packing of grain aggregates [123, 124]. Understanding how halite fabric evolves during a variety of loading paths is of foremost importance to predict the long-term behavior of salt rock around storage facilities [125, 126, 127].

In this chapter, we analyze 2D halite microstructure images acquired as several stages of consolidation tests and cyclic compression tests. We calculate the magnitude and orientation distributions of solidity, local solid volume fraction, coordination orientation and crack volume fraction and we define the associated fabric tensors to explain the development of anisotropic mechanical properties. Our methods for analyses are explained in Section 2.1. The distributions of fabric descriptors and crack densities are presented in Section 2.2. In Section 5.3, we interpret the development of opening-mode and sliding cracks in the cyclic compression tests. We conclude this chapter by comparing the evolution of the components

of the fabric tensors to that of halite elastic moduli.

2.1 Materials and Methods

2.1.1 Consolidation tests and cyclic compression tests

Reagent-grade granular salt (high purity 99 wt.%) were subjected to oedometer tests in a hollow cylindrical steel vessel with a 19 mm diameter at a constant temperature of 150 ^{o}C. The granular salt was sieved to separate grains 0.3-0.355 mm diameter. In these so-called " uniaxial consolidation tests", samples were placed in a cell with non deformable lateral boundaries and subjected to a vertical strain applied at a constant rate of 0.034 mm/s. Samples were taken out of the loading cell at porosities 15%, 10%, 5% and 3% and sliced for imaging. These porosities were found by calculating the mass density of the samples at the time they were taken out. Figure 2.1 shows the binary images obtained from a vertical slice located in the longitudinal section of the sample, at mid-height.

Cyclic compression tests were conducted on consolidated salt with an initial porosity of 5% $\pm$0.5%. The confining pressure was 1 MPa. Samples were taken out of the loading cell and imaged for axial strains (ϵ_a) of 0%, 0.8%, 1.8%, 2.8%, 3.8%, and 7.3%, as shown in Figure 2.2. Binary images were obtained from a vertical slice located in the longitudinal section of the sample, at mid-height.

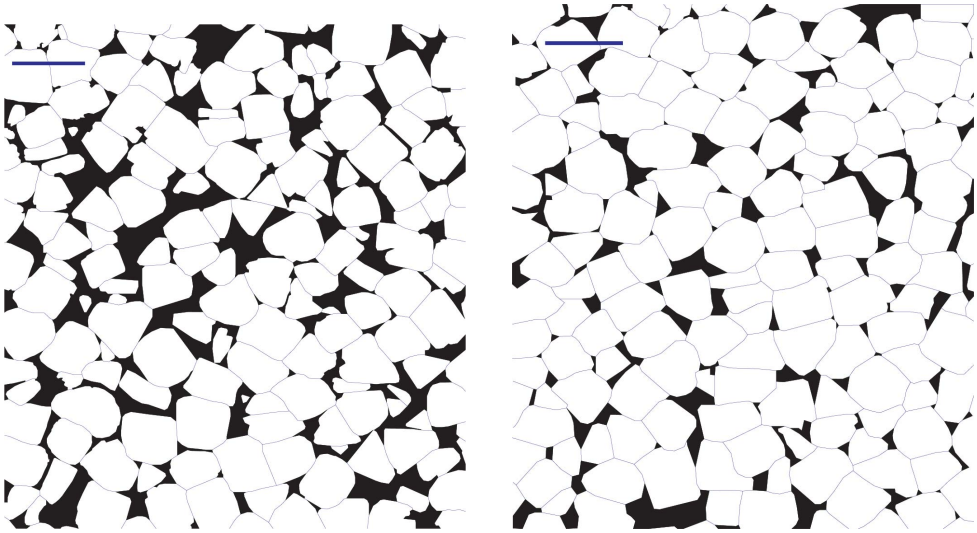

(a) Porosity=15%

(b) Porosity=10%

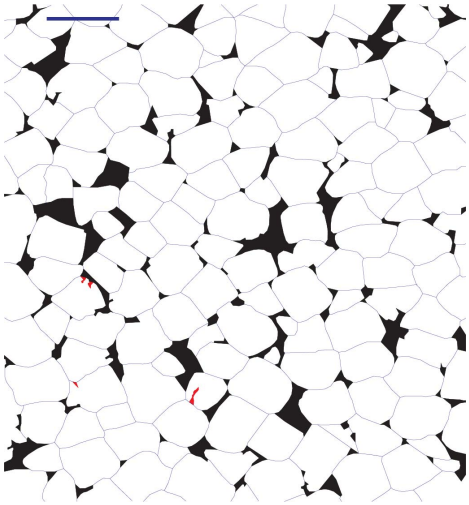

(c) Porosity=5%

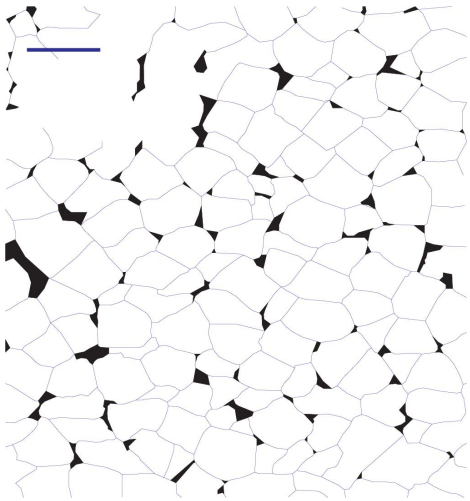

(d) Porosity=3%

Figure 2.1: Binary images of salt microstructure at several stages of consolidation tests. The blue scale bar represents 0.5 mm. The red inserts indicate the presence of intra-granular cracks (see Section 2.1.3).

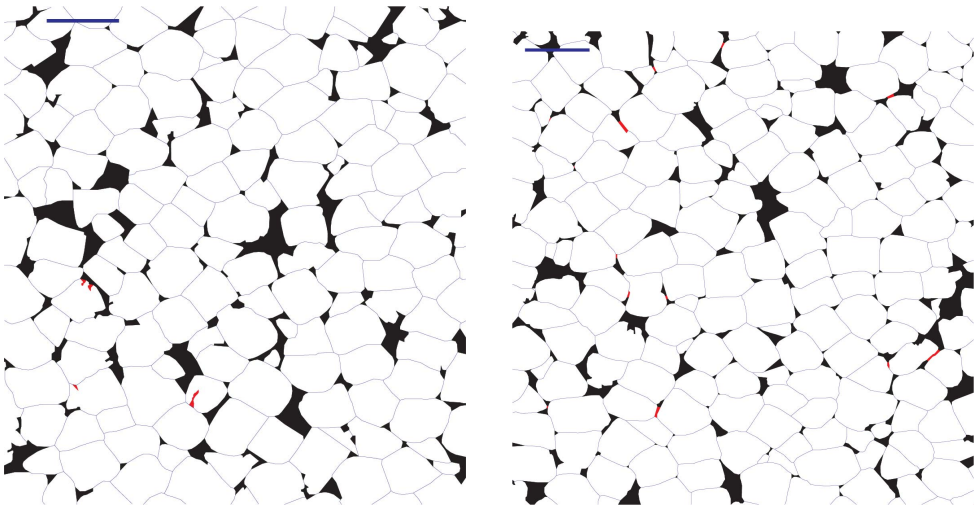

(a) $\epsilon_a = 0\%$

(b) $\epsilon_a = 0.8\%$

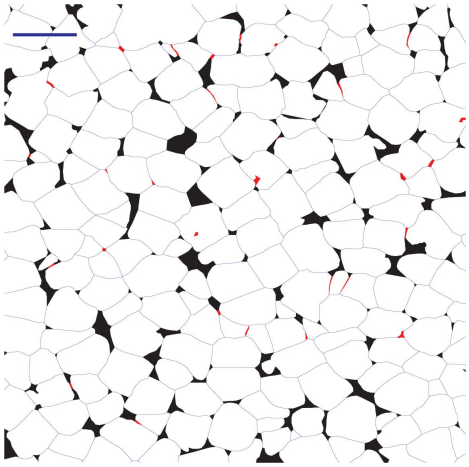

(c) $\epsilon_a = 1.8\%$

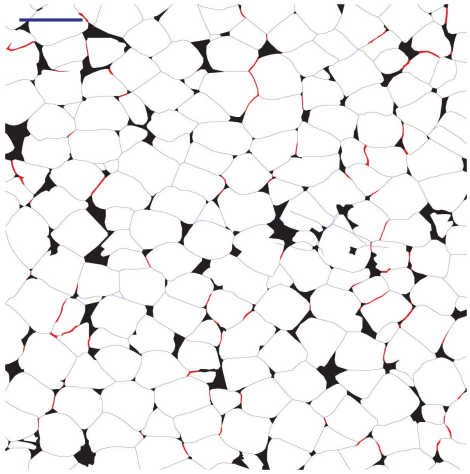

(d) $\epsilon_a = 2.8\%$

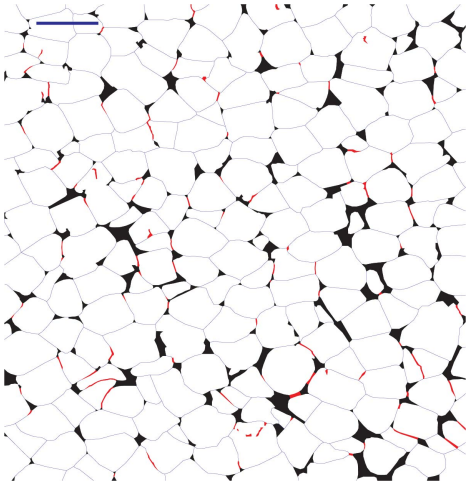

(e) $\epsilon_a = 3.8\%$

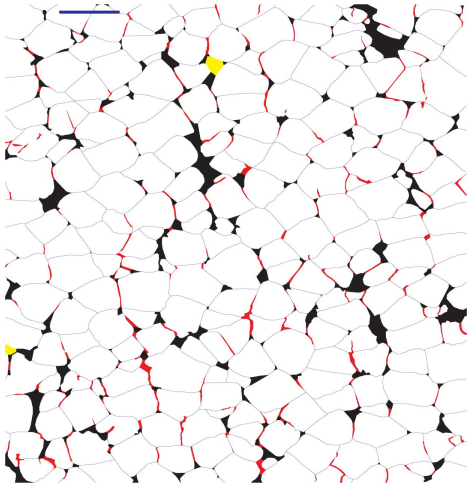

(f) $\epsilon_a = 7.3\%$

Figure 2.2: Binary images of salt microstructure at several stages of cyclic compression tests. The blue scale bar represents 0.5 mm. The red inserts indicate the presence of cracks (see Section 2.1.3). The yellow areas represent grains that were removed by polishing.

2.1.2 Grain morphology

In order to analyze the evolution of grain size and shape during the consolidation and cyclic compression tests, we first process the images to associate an equivalent ellipse to each grain that appears in the images. An equivalent ellipse has the same second-moments of area (respectively to horizontal and vertical axes) as the associated grain in the 2D image. The orientation of a grain is defined as the angle between the major axis of the equivalent ellipse and the horizontal direction (note: the loading direction is vertical).

We seek to explain salt behavior from a higher-order descriptor of grains' contours - called grain solidity. Solidity is usually defined as the ratio between the area of a grain image by the area of the convex hull of the grain. When solidity is close to one, grains have convex shapes. A solidity close to zero reveals a very angular shape or a shape with very rough contours. In the images obtained in this study (Figures 2.1 and 2.2), the lack of convexity stems from indentations that appear at the contour of the grains. Figure 2.3 shows an example of grain with indentations, extracted from a binary image obtained in this study.

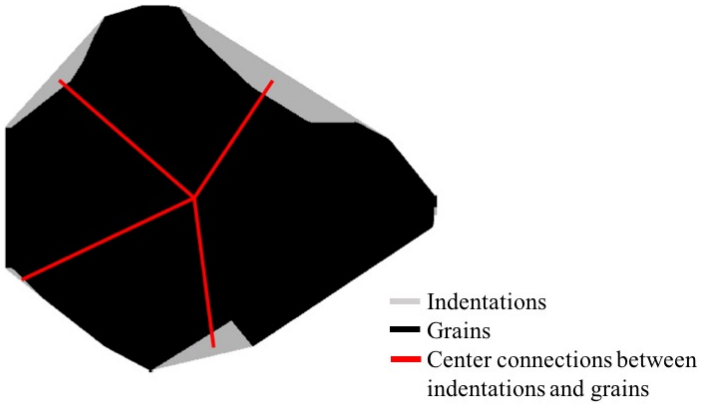

Figure 2.3: Processed image of a grain, showing indentations on the contour. The image was taken at an axial strain of 0%, before the cyclic compression tests.

In order to better understand how grain indentations develop, we define an anisotropic descriptor of solidity. The norm of a solidity vector is the ratio of the area of a grain's 2D

image by the area of its convex hull. The direction of the solidity vector is calculated as follows:

(i) Indentations around each grain are identified by observing the microstructure binary images - see the example shown in Figure 2.3.

(ii) An algorithm calculates the position of the barycenter of each indentation shape, as well as that of the grain. For each indentation, a segment linking the indentation center to the associated grain's center is defined.

(iii) The angle to the horizontal of each segment defined in step (ii) is calculated. Angles are defined over the interval $[0^o;90^o]$ because of the axial symmetry of the tests.

(iv) For each grain, the direction of the solidity vector to the horizontal is the mean of the angles calculated in step (iii), in which each angle is weighted by the area of the associated indentation.

2.1.3 Grain arrangement

Coordination orientation

The coordination number is defined as the number of grain-to-grain contacts at the surface of a given grain. We define a coordination descriptor that also accounts for the area of the contacts, as well as the orientation of the vectors normal to the contacts. The so-called "coordination orientation" is calculated by image analysis, as follows:

(i) The pixels that make the contour of a grain are listed. Pixels that are at the boundary with another grain (named "boundary pixels") are then selected from that list.

(ii) Segments that link the center of the grain to its boundary pixels are defined. The angles formed by these segments to the horizontal are calculated.

(iii) The contour of the grain is divided into 360 angular equal segments, as illustrated in Figure 2.4. For each contour segment within one of the 360 angular segments, the ratio of the number of boundary pixels by the total number of pixels is calculated, which provides a quantitative measure of the support fraction on that segment.

(iv) The coordination orientation of a grain is the average orientation of the angular segments, weighted by their support fraction.

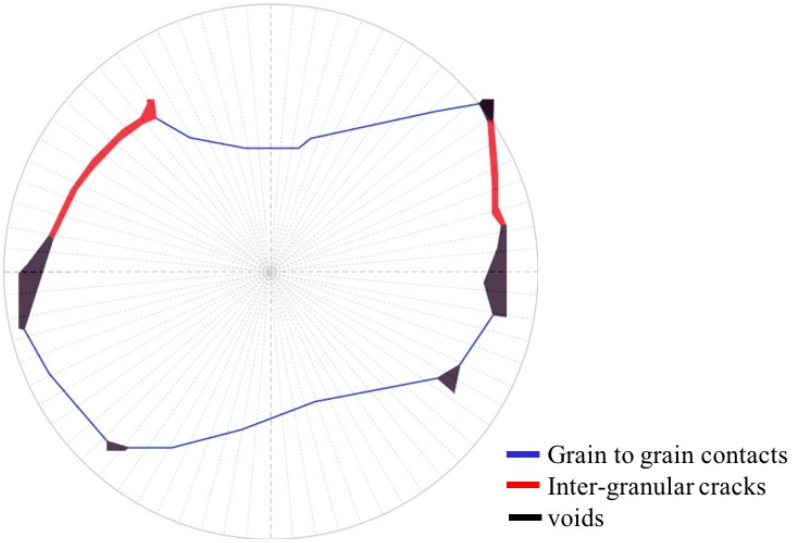

Figure 2.4: The method to calculate the coordination vector of a grain.

Local solid volume fraction

In order to quantify the heterogeneous distribution of pores in the salt sample, we define the Local Solid Volume Fraction (LSVF) vector as follows:

(i) Contact branches, defined as segments linking the centers of two grains in contact, are plotted. A map of polygons is obtained, as shown in Figure 2.5a. Polygon corners are grain centers.

(ii) The solid volume fraction of the domain contained in each polygon is calculated.

(iii) Segments are defined to connect each grain center to the centers of each polygon that overlaps with that grain. The angle between a segment and the horizontal defines the orientation of a polygon relative to a grain. The orientation of the connection is called “direction of the domain polygon”;

(iv) The magnitude of LSVF of a grain is the total solid volume fraction of its domain polygons, as shown in Figure 2.5b. The direction of the LSVF vector is the average of its domain polygons’ directions, using the domain polygons’ solid volume fraction as the weights.

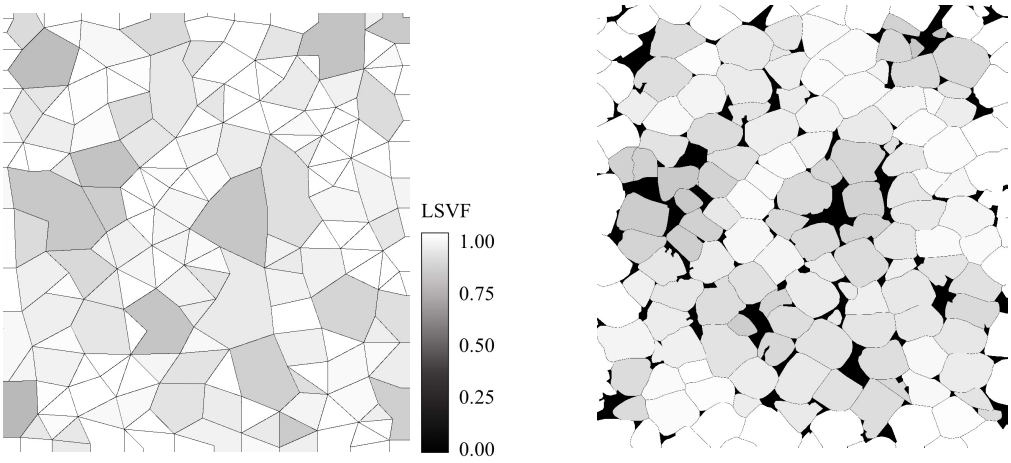

(a) Polygons delimited by contact branches

(b) Grains’ solid volume fraction: average of polygons’ volume fractions

Figure 2.5: The method to calculate grains’ local solid volume fraction. The grey scale illustrates the differences in local solid volume fractions. The images were taken at an axial strain of 0%, before the cyclic compression tests.

Crack propagation during the cyclic compression tests

In the compression cyclic tests, opening mode microscopic cracks were observed. With the increase of axial strain, salt grains re-arranged and inter-granular cracks initiated and propagated along grain boundaries. Intra-granular cracks also occurred, because of stress concentration induced by grain contacts.

2.2 Results

2.2.1 Grain morphology

Grain size and aspect ratio

Figure 2.6 shows the evolution of the probability distribution of the grains' major axes and aspect ratios during the the consolidation tests. Note that the grains' major axes and aspect ratios were defined respectively as the major axes of the equivalent ellipses and as the ratios of the major axis to the minor axis of the equivalent ellipses. The mean major axis of the grains is around 400 μm when the porosity is less than 5%. The aspect ratio of the grains remains stable until the porosity reaches 2%. Figure 2.6a shows that grains with a larger major axis appear when the porosity reaches 2%, i.e., grains become elongated.

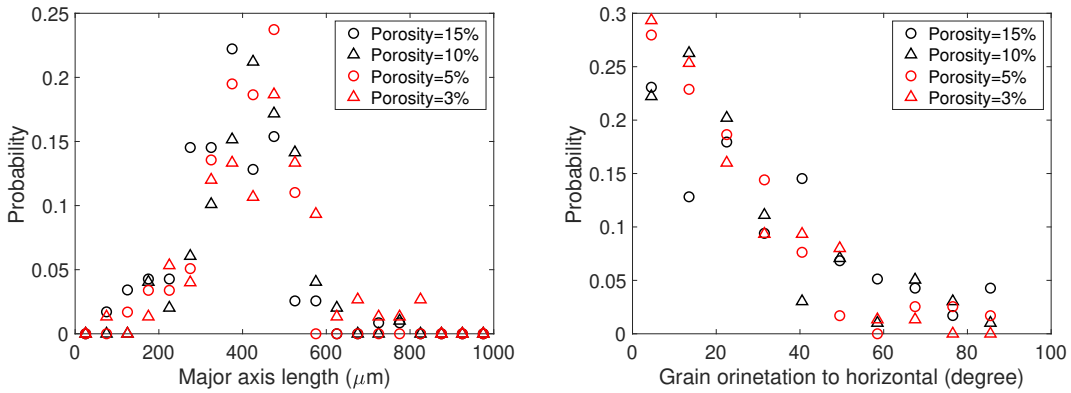

(a) Grains' major axes (b) Grains' aspect ratios

Figure 2.6: Evolution of salt grains' shapes during the consolidation tests.

Figure 2.7 shows the evolution of the probability distributions of the grains' major axes and aspect ratios during the cyclic compression tests. The mean major axis is slightly less than 400 μm, which agrees with the size of the salt grains sieved before consolidation (300-355 μm). The aspect ratio usually ranges from 1 to 2 and few elongated grains are observed. The aspect ratio is not significantly affected by the axial strain.

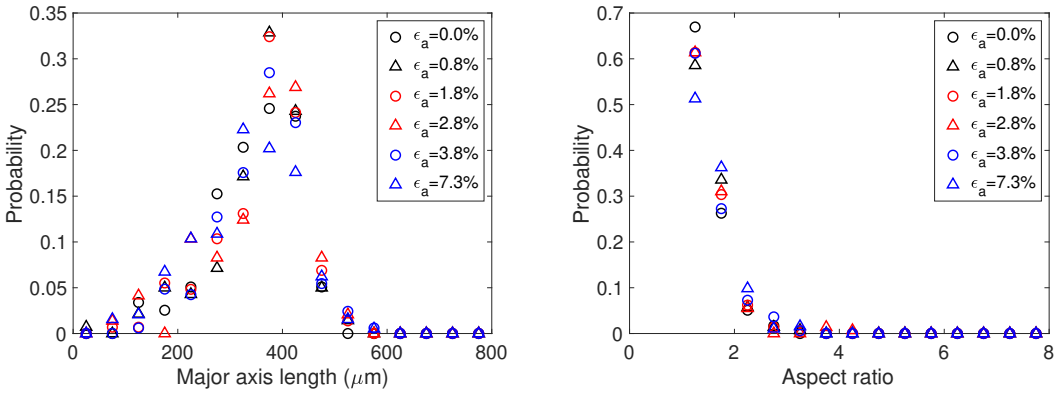

(a) Grains' major axes (b) Grains' aspect ratios

Figure 2.7: Evolution of salt grains' shapes during the cyclic compression tests.

Grain orientation

Figure 2.8 shows the probability distribution of grain orientation during the consolidation tests. Results indicate that the grains tend to rotate towards the horizontal direction under compaction. The influence of grains' deformation cannot be ignored for the samples in the consolidation tests, especially when the porosity of samples is low (i.e. 2%).

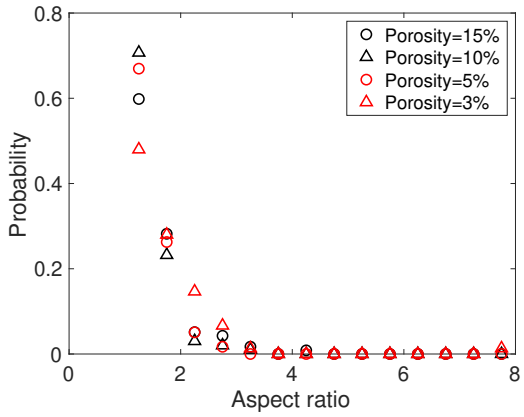

Figure 2.8: Evolution of the orientation of the salt grains during the consolidation tests.

Figure 2.9 shows that there is no significant grain re-orientation during the cyclic compression tests. A comparison between the probability distribution of grains' orientation at a low axial deformation (under 3%) and the probability distribution at an axial deformation of 7.3% indicates a slight increase of the number of grains oriented in directions close to

the horizontal, which was expected, considering that a vertical compression is applied.

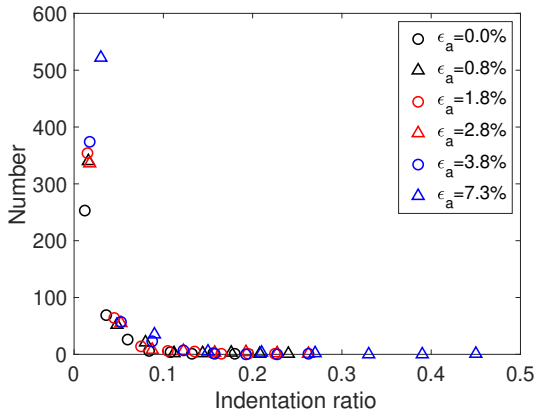

Figure 2.9: Evolution of the orientation of the salt grains during the cyclic compression tests.

Grain solidity and indentations

Compaction triggers grain indentations and grain plastic deformation. In the consolidation tests, the influence of compaction on the orientation of the solidity vector is shown in Figure 2.10a. Solidity can be viewed as an average indicator of grain indentation at the scale of the image processed. Initially, the solidity vector is oriented at an angle of 45^o in average, i.e. the orientation of the solidity vector is uniformly oriented between 0^o and 90^o in the sample. The peak of orientation probability distribution decreases when the porosity decreases. The mean of solidity decreases with the decrease of porosity, see Figure 2.10b.

The distributions of the solidity vectors' orientation and magnitude are shown in Figure 2.11 for the cyclic compression tests. The orientation probability distribution slightly looses symmetry when the axial strain increases. The standard deviation jumps from 16.46 to 19.39 when ϵ_a increases from 1.8% to 2.8%, i.e. the solidity vector starts exhibiting preferential orientations. According to Figure 2.11b, the probability distributions of the magnitude of solidity for the different levels of axial strain are almost super-imposed. When ϵ_a reaches 7.3%, the mean of the solidity magnitude reduces slightly, which indicates that the area of the indentations increases.

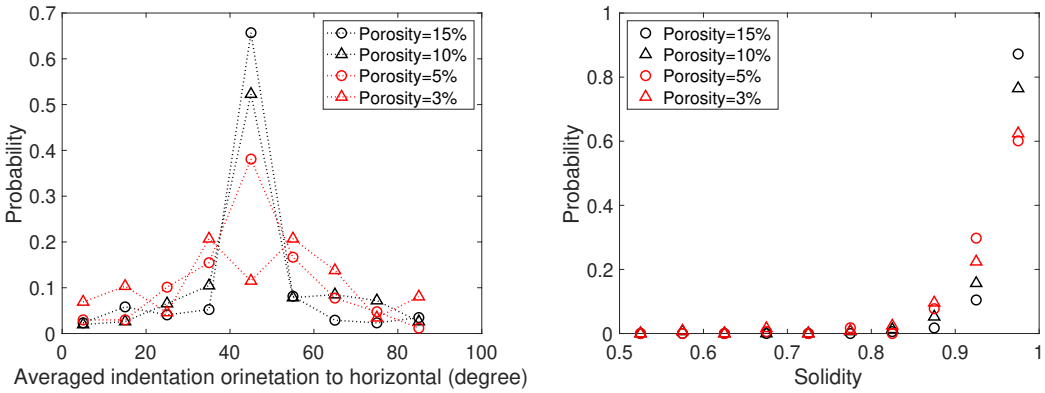

(a) Orientation of the solidity vector (b) Magnitude of the solidity vector

Figure 2.10: Evolution of the solidity vector during the consolidation tests.

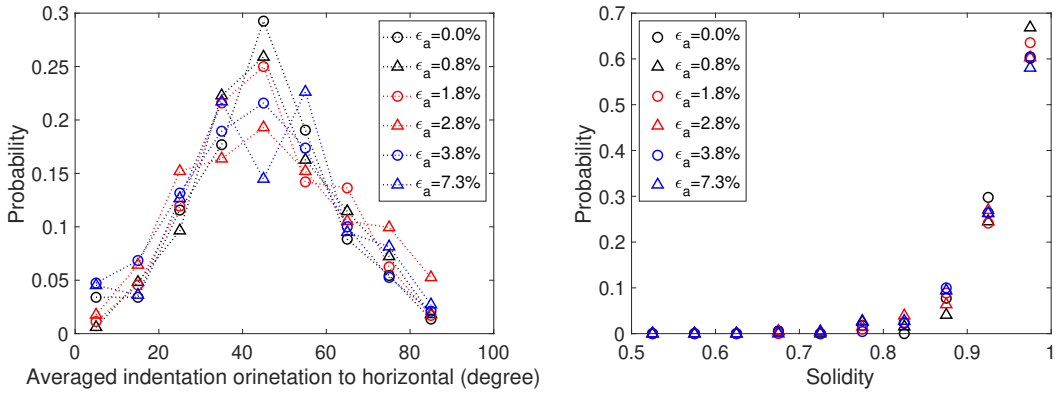

(a) Orientation of the solidity vector (b) Magnitude of the solidity vector

Figure 2.11: Evolution of the solidity vector during the cyclic compression tests.

The probability distribution of indentations' orientations and sizes are presented in Figure 2.12 for the cyclic compression tests. In this figure, the indentation ratio is the ratio of the area of one indentation to the area of the convex hull of the grain. According to Figure 2.12a, indentation orientations are uniformly distributed within the range 0^o to 80^o. Few indentation segments are vertical. For larger axial strains, the standard deviation of the indentation orientation probability is larger, i.e., the distribution is more uniform. Based on Figure 2.12b, larger indentations appear at larger axial strain. The number of indentations increases with the axial strain, which suggests that more indentations induce more plastic deformation. The mean of the indentation ratio remains almost constant when the axial

strain is less than 1.8%, and then increases rapidly. We conclude that grain plastic strains start to accumulate when the axial strain reaches 1.8%.

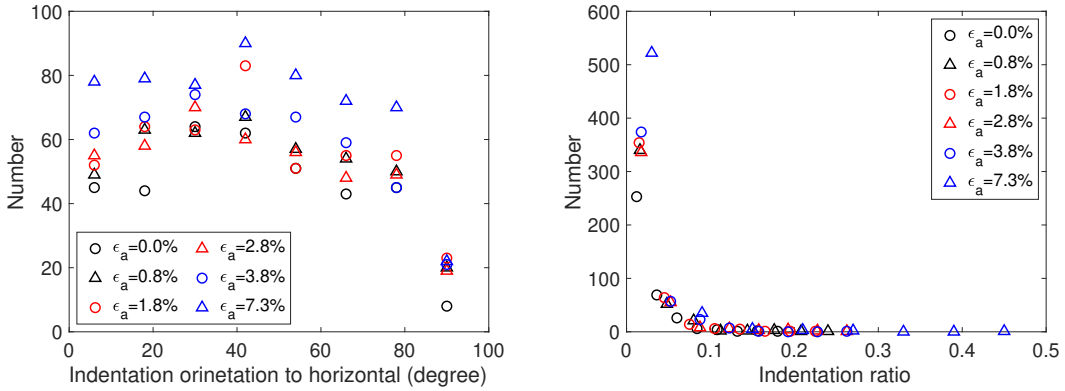

(a) Indentation orientation

(b) Indentation ratio

Figure 2.12: Evolution of the distribution of grain indentations during the cyclic compression tests.

2.2.2 Coordination orientation

The evolution of coordination orientation during the consolidation tests is presented in Figure 2.13. Samples become denser and the total area of grain-to-grain contacts increases. When the porosity is 15%, only about 30% of any grain contour is in contact with other grains. When the porosity reaches 3%, more than 80% of the grain contours is in contact with other grains. At the beginning of the consolidation tests, the axial direction (i.e. 90^o in Figure 2.13) is the dominating grain-to-grain contact direction. Due to the displacement constraint in lateral directions, more lateral grain to grain contacts occur at later stages of consolidation tests, and the coordination orientation becomes almost isotropic.

The evolution of the probability distribution of the coordination orientation during the cyclic compression tests is shown in Figure 2.14. Results show that the support fraction decreases when the axial strain increases. The areas of grain-to-grain contacts reduce because of the redistribution of voids and the propagation of inter-granular cracks. The slope of the coordination orientation curve is steeper under larger axial strain. This observation

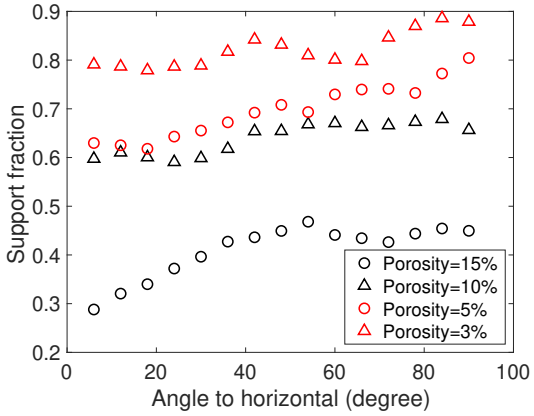

Figure 2.13: Evolution of the coordination orientation in the consolidation tests.

reveals that grains tend to be reorganized into vertical supporting columns, i.e., grain to grain contacts are mainly oriented with a normal parallel to the axial (loading) direction. For an axial strain of 7.3%, less than 40% of the grains are in contact with other grains in sub-horizontal directions (with a coordination angle smaller than 20^o), while nearly 75% of the grains are coordinated vertically. However, the support fraction of the non deformed sample ($\epsilon_a = 0\%$) is smaller than the support fractions of samples under $\epsilon_a = 1.8\%$ and $\epsilon_a = 2.8\%$, which contradicts our interpretation. We will explain this apparent contradiction by analyzing normalized fabric descriptors, to account for the difference between 2D and 3D porosities (see Subsection 2.3.2).

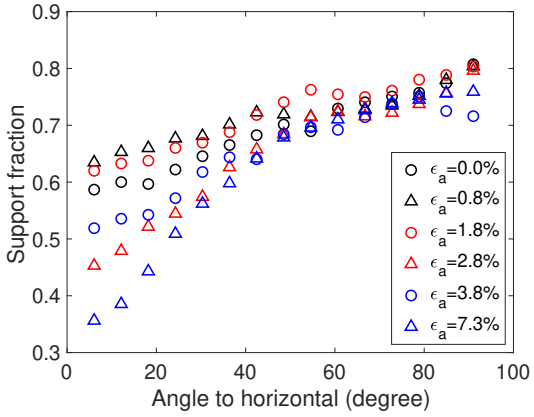

Figure 2.14: Evolution of the coordination orientation in the cyclic compression tests.

2.2.3 Local solid volume fraction

The evolution of the LSVF vector magnitude in the consolidation tests is non-monotonic, as evidenced in Figure 2.15b. Usually, a domain polygon contains an entire pore. The larger the pore, the larger the domain polygon, and the higher the number of grains that overlap with this domain polygon. As a result, the magnitude of the LSVF vector is controlled both by the porosity distribution of domain polygons and by the size of voids. With the decrease of porosity during consolidation, the interval of variations of the LSVF magnitude decreases from 0.25 to 0.13. In other words, the void distribution becomes more uniform. When the porosity of salt rock is 15%, the probability of LSVF orientation (Figure 2.15a) is symmetric about the orientation of 45^o, thus no preferred LSVF orientation is observed. As compression increases, a wider peak forms, indicating that the LSVF becomes more homogeneous in the sample. The peak shifts to the left, from 45^o for a porosity of 15% to 37^o for a porosity of 3%. More voids appear in the axial direction around grains and less voids appear in the lateral direction. In other words, grains are reorganized in layers of horizontally coordinated grains.

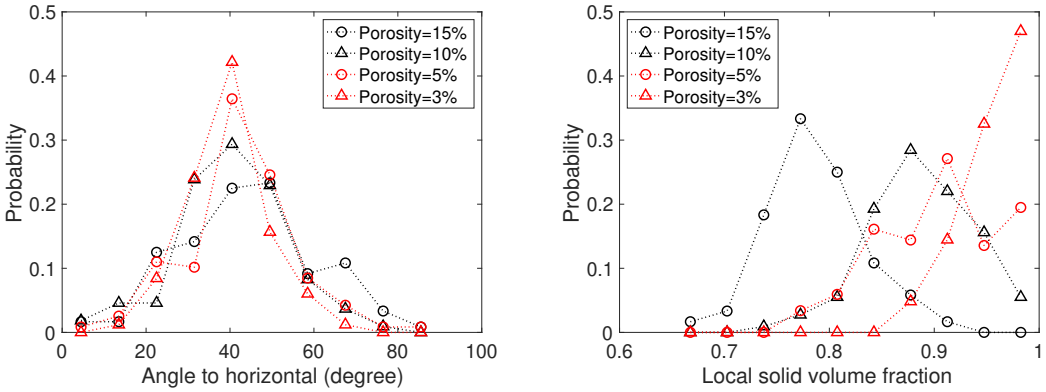

(a) LSVF vector direction (b) LSVF vector magnitude

Figure 2.15: Evolution of the local solid volume fraction (LSVF) in the consolidation tests.

The evolution of the local solid volume of fraction in the cyclic compression tests is shown in Figure 2.16. The magnitude of the peak in Figure 2.16a decreases with the in-

crease of ϵ_a. When ϵ_a is small, a few large and isolated voids are observed, and the LSVF is small. As compression increases, large voids collapse and more small and isolated voids appear. The LSVF increases when ϵ_a increases from 0% to 3.8%. Then, because of the propagation of inter granular cracks, small voids become connected, thus creating large voids. Thus the LSVF starts to decrease. When ϵ_a is small, the porosities of the domain polygons for each grain are relatively uniform, which translates by a peak LSVF orientation angle close to 45^o. When ϵ_a is large, the porosity of the domain polygons for each grain is no longer uniform. The probability of the LSVF orientation angle looses its symmetry. This is particularly visible in the sample with $\epsilon_a = 7.3\%$, for which polygons characterized by a LSVF angle close to 90^o have a higher probability of occurrence. This last observation confirms the hypothesis of grain re-arrangement in the form of supporting columns of vertically coordinated grains.

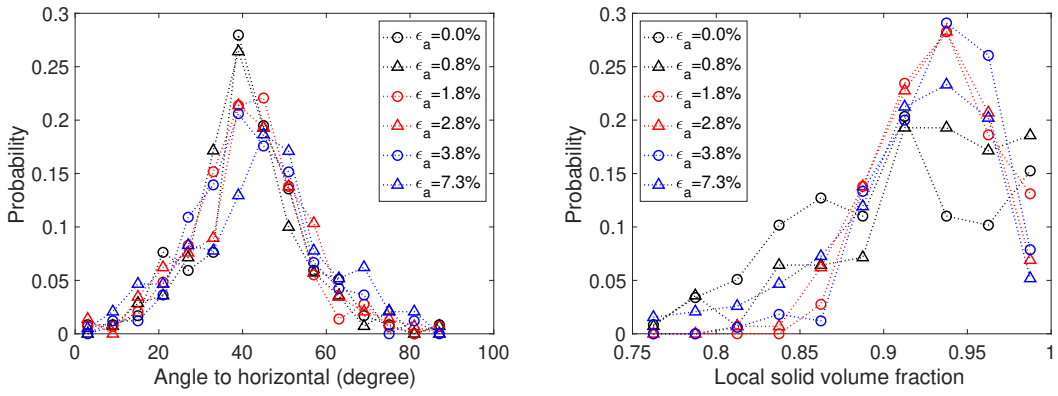

(a) LSVF vector direction

(b) LSVF vector magnitude

Figure 2.16: Evolution of the local solid volume fraction (LSVF) in the cyclic compression tests.

2.2.4 Crack length and orientation

The evolution of the distributions of length and orientation for the cracks identified by image analysis during the cyclic compression tests is shown in Figure 2.17. The cracks initiate at the beginning of the test. Vertical cracks appear first. Cracks in other directions

follow, as shown in Figure 2.17a. As compression increases, both the length and the number of cracks increase (Figure 2.17b). As a result, the change of porosity during the cyclic compression tests is due to changes in pore size and shape and to the formation of opening-mode cracks. As shown in Figure 2.18, the volume of pores decreases rapidly initially. The rate of pore volume reduction stabilizes at a small value when ϵ_a reaches 2%. The volume of opening-mode cracks develops at a slightly increasing rate. When ϵ_a reaches 7%, the opening-mode cracks contribute to more than 20% of the void volume in the sample. Note that the 2D porosity of salt rock obtained by image analysis is slightly larger than the porosity determined by the mass and volume of salt rock in 3D. This fact does not affect the qualitative interpretations that we made on the evolution of cracks, but we will revisit some of our analyses in Subsection 2.3.2 to account for the difference between 2D and 3D porosities.

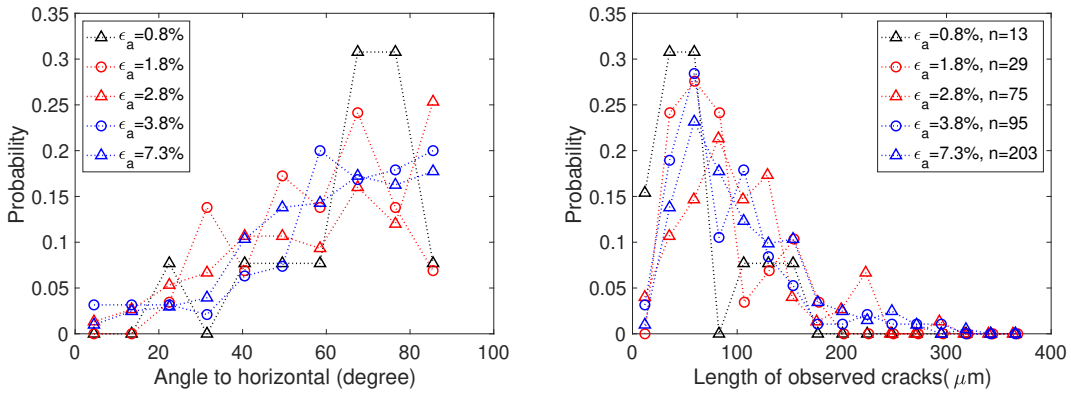

(a) Crack orientations (b) Crack lengths

Figure 2.17: Orientation and length distributions of the cracks observed in the 2D images obtained at several stages of the cyclic compression tests. The number of cracks (n) is given for each loading stage.

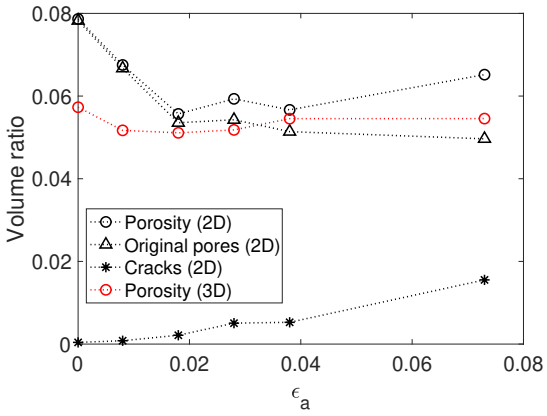

Figure 2.18: Distribution of the void volume when ϵ_a reaches 7% in the cyclic compression tests.

2.3 Discussion

2.3.1 Grain deformation

In order to understand the main factors at the origin of salt deformation during consolidation and compression, we use the 2D solidity vector to calculate the percentage of axial and volumetric deformation that is attributed to grain deformation. The analysis of the results presented in Figure 2.12 shows that the area of the indentations is small compared to that of the grains. Based on this observation, we propose a simple method to estimate the contribution of grain indentation to the deformation of the sample. Let us assume that grains' convex hulls are roughly circular in the 2D images and that indentations are uniformly distributed on the contours of the grains. The relation between the magnitude of the 2D solidity vector, S, and the average depth of the indentations, $\bar{d}$, can then be expressed as:

$$S = 1 - \frac{\sum A_i}{A_s} = 1 - \frac{2\pi R\bar{d}}{\pi R^2} = 1 - \frac{2\bar{d}}{R} \tag{2.1}$$

where A_i is the area of the ith indentation found on the contour of a grain, and A_s is area of the grain's convex hull. The axial strain ϵ_a^g induced by the indentation of the grains can be

expressed as:

$$\epsilon_a^g = -\frac{\bar{d}}{R} \tag{2.2}$$

In the cyclic compression tests, the axial strain induced by grain indentations ϵ_a^g between $\epsilon_a = 0\%$ and $\epsilon_a = 7.3\%$ is found to be equal to 0.451%, which represents only 6.18% of ϵ_a at the final stage of the test (7.3%). The remaining 93.82% is due to grains rearrangements, as discussed in Section 2.2.

Under the same assumption of uniform distribution of indentations, the volumetric strain ϵ_v^g due to the indentation of the grains can be expressed as:

$$\epsilon_v^g = \frac{\delta \sum V_i}{V_s} = \frac{4\pi R^2 \bar{d}}{\frac{4}{3}\pi R^3} = \frac{3\bar{d}}{R} \tag{2.3}$$

where V_i is the volume of the ith indentation of a grain, and V_s is the volume of the grain's convex hull. The volumetric deformation due to grain indentations at $\epsilon_a = 7.3\%$ is found to be equal to 1.251% (shrinkage), while the volumetric deformation of the sample is -1.93% (dilation). This observation implies that the sample's volumetric strain is controlled by grain rearrangement mechanisms, discussed in Section 2.2. For the consolidation tests, the volumetric strain induced by grain indentation at porosity 15%, 10%, 5%, and 3% are respectively 2.64%, 4.97%, 7.12%, and 7.86% of the total volumetric strain of the samples. To summarize, grain indentation is not the controlling mechanism in either consolidation tests or cyclic compression tests.

2.3.2 Normalization of fabric descriptors in the cyclic compression tests

To analyze the evolution of salt microstructure during the cyclic compression tests, samples are sacrified at several stages of the axial strain loading. The initial porosity of the sacrified samples, noted p_i, ranges between 5.11% and 5.73%, as shown in Table 2.1. During the compression tests, the sample dilates (i.e. the volumetric strain ϵ_v increases in absolute value) with the increase of differential stress. According to section 2.2.1, very little changes

of grain's shape and size are observed. Since grain volume changes are negligible, the current porosity of the sample, noted p_c, is calculated from the initial porosity p_i and the current volumetric deformation ϵ_v, as follows:

$$p_c = \frac{\epsilon_v + p_i}{\epsilon_v + 1} \tag{2.4}$$

A discrepancy is noted between p_c and the porosity found by image analysis, noted p_m. In fact, the 3D salt rock sample can be regarded as a stack of 2D microscopic images, in which the thickness of each image is a small constant. 3D porosity can be seen as the mean of the 2D porosites in the stack of images. As we only use the 2D porosity of one microscopic image, a difference between the 2D porosity and the 3D porosity is expected. According to Figure 2.18, the porosity obtained by analyzing 2D images is often larger than the porosity of the 3D sample, calculated by estimating the mass density of the sample. As a result, the support fraction calculated from the 2D image analyses is under-estimated. We propose a normalization method to correct the error made by using 2D porosities in the cyclic compression tests.

Table 2.1: Evolution of volumetric parameters in salt rock during the triaxial cyclic loading test.

ϵ_a	0%	0.8%	1.8%	2.8%	3.8%	7.3%
p_i	5.73%	5.17%	5.11%	5.17%	5.42%	5.38%
ϵ_v	0%	-0.006%	-0.014%	-0.224%	-0.607%	-1.926%
p_m	7.87%	6.75%	5.57%	5.93%	5.67%	6.52%

Based on the discussion presented in Subsection 2.3.1, we consider that the contribution of grain deformation on the deformation of the salt rock sample is negligible. The coordination orientation is normalized by the current porosity p_c for each compression test. The probability of the normalized coordination orientation is shown in Figure 2.19. In samples with ϵ_a equal to 0% and 2.8%, there is a large difference between p_i and p_m, hence the

support fraction increases after normalization. The normalized results confirm the interpretations made in Section 2.2.2: the overall grain-to-grain contact area reduces and the support fractions line up vertically, forming supporting columns of coordinated grains.

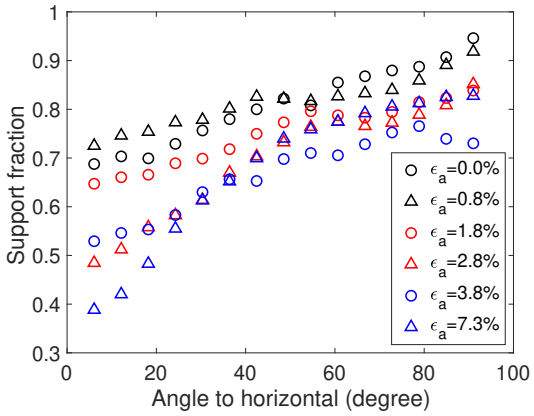

Figure 2.19: Evolution of the coordination orientation after normalization in the cyclic compression tests.

The evolution of the magnitude of the LSVF vector after normalization is shown in Figure 2.20. The trends are similar to those observed in Figure 2.16b. For ϵ_a equal to 1.8%, 2.8%, and 3.8%, curves almost overlap. The distribution of void sizes follows two stages. At the beginning of the test, larger voids collapse, and a significant number of small voids appear. When the axial strain is large, the small voids are connected by inter-granular cracks, and large voids appear again.

2.3.3 Categories of cracks

The cracks observed in the images acquired during the cyclic compression tests can be categorized as intra-granular cracks and inter-granular cracks. The former are defined as cracks that go through only one grain. The latter are defined as cracks that connect to more than one grain. During the compression tests, both opening-mode cracks and sliding cracks are expected to initiate and propagate. However, only opening-mode cracks can be observed in the microscopic images. Based on the wing cracks theory, the sliding cracks are expected to propagate with the occurrence of opening-mode cracks. The observed inter-

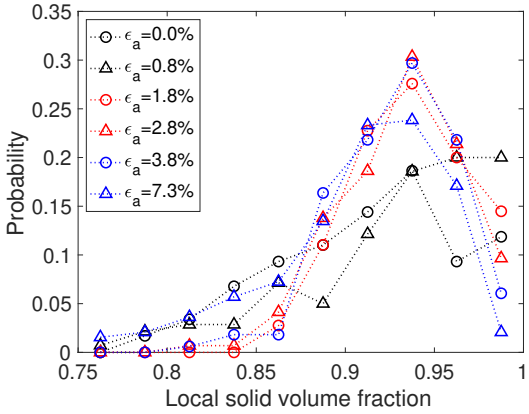

Figure 2.20: Evolution of the magnitude of the local solid volume fraction during the cyclic compression tests.

granular cracks are thus identified as wing cracks, and the sliding cracks are defined as the grain boundaries that connect two neighboring wing cracks. We developed an algorithm that identifies sliding cracks in the two following cases:

(i) One end of a grain boundary is connected to an inter-granular crack, and the other end is connected to a void;

(ii) Each end of a grain boundary is connected to a different inter-granular crack.

We observe very few intra-granular cracks, which are all very short. The orientation and length distributions of the observed inter-granular wing cracks are presented in Figure 2.21, which is in fact very similar to Figure 2.17. The orientation and length distributions of the inter-granular sliding cracks are shown in Figure 2.22. Sliding cracks initiate preferentially at 40^o to the horizontal. With the increase of ϵ_a, the distribution of sliding orientations stabilizes, and sliding cracks propagate along the boundaries of less favorably oriented grains (e.g. grains at $\sim 30^o$, with higher normal stress and lower shear stress at the boundaries). A few vertical sliding cracks develop. According to Figure 2.21b, the length of the sliding cracks is around 200 μm when ϵ_a is small. A larger axial strain leads to longer sliding cracks and a larger range of length distributions. When ϵ_a is equal to 7.3%, the length of sliding cracks reaches 500 μm.

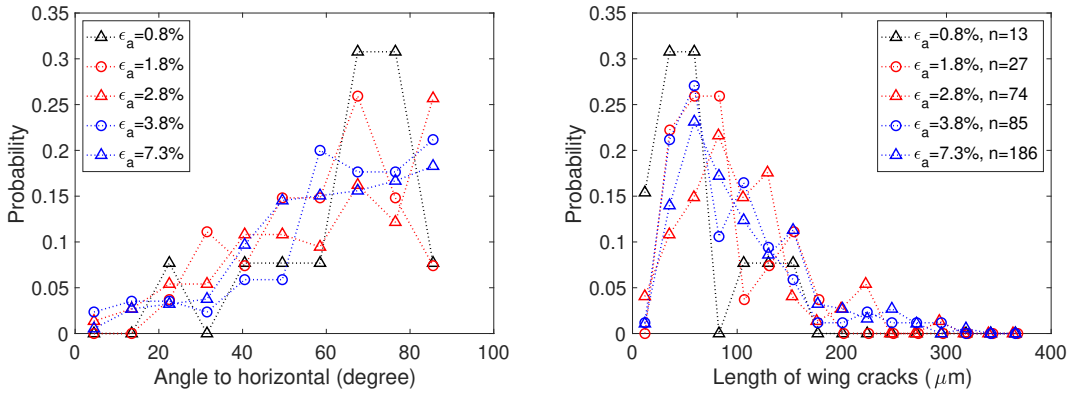

(a) Wing crack orientations

(b) Wing crack lengths

Figure 2.21: Orientation and length distributions of the wing cracks observed in the 2D images obtained at several stages of the cyclic compression tests. n is the number of wing cracks.

2.3.4 Fabric tensors

Fabric tensors are used to describe the evolution of the microstructure in the salt samples. According to [63], the second-order fabric tensor $\bar{\boldsymbol{F}}$ is expressed as:

$$\bar{F}_{ij} = \int_{\Omega} n_i n_j E(\Omega) \mathrm{d}\Omega \qquad (i, j = x, y, z) \tag{2.5}$$

where n_x, n_y, n_z are projections of a unit vector $\boldsymbol{n}$ on the Cartesian reference coordinates; Ω is the whole solid angle corresponding to a unit sphere; $E(\Omega)$ is a probability density function. For 2D analyses, we use the following second-oder fabric tensor $\boldsymbol{F}$:

$$F_{ij} = \int_{\theta=0}^{2\pi} n_i n_j E(\theta) \mathrm{d}\theta \qquad (i, j = x, z) \tag{2.6}$$

$\boldsymbol{F}$ is a symmetric second-rank tensor. The components of $\boldsymbol{F}$ are calculated as:

$$F_{xx} = \frac{1}{N} \sum_{m=1}^{N} f_m \sin^2 \theta_m \tag{2.7}$$

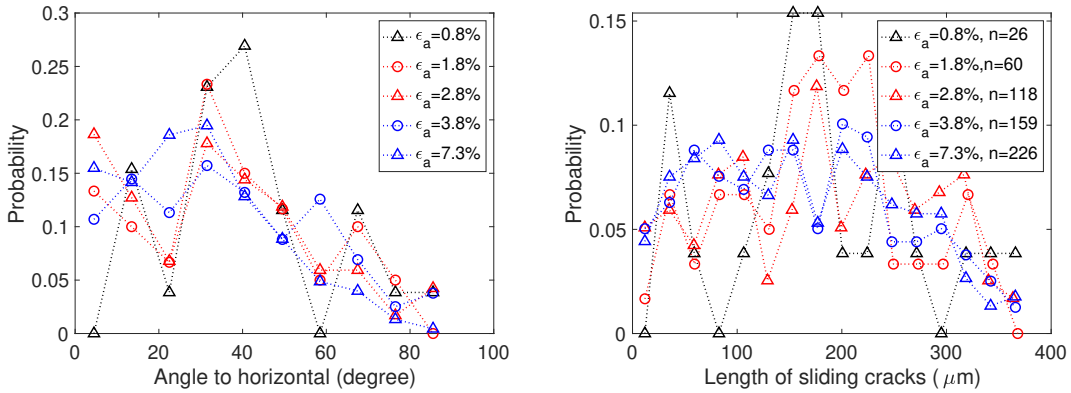

(a) Sliding crack orientations

(b) Sliding crack lengths

Figure 2.22: Orientation and length distributions of the sliding cracks at several stages of the cyclic compression tests. n is the number of main cracks.

$$F_{xz} = F_{zx} = \frac{1}{N} \sum_{m=1}^{N} f_m \sin\theta_m \cos\theta_m \tag{2.8}$$

$$F_{zz} = \frac{1}{N} \sum_{m=1}^{N} f_m \cos^2\theta_m \tag{2.9}$$

where f_m is the magnitude of a fabric descriptor for grain m; θ_m is the direction of that fabric descriptor for grain m. Due to the axial symmetry of the samples and loading conditions, F_{xz} and F_{zx} are close to 0. F_{xx} is the component of the fabric tensor in the lateral direction; F_{zz} is the component of the fabric tensor in the axial direction, and F is the trace of the fabric tensor. In 2D: $F = F_{xx} + F_{zz}$.

The axial and lateral components of the fabric tensors for solidity, coordination orientation, and local solid volume fraction are shown in Figures 2.23 and 2.24, for the consolidation tests and the cyclic compression tests, respectively. In the consolidation tests, the compaction of samples leads to a larger oedometer modulus and a denser packing of salt grains. Solidity decreases due to the inelastic deformation on the grains. Both lateral and axial components of the coordination fabric tensor (C_{xx} and C_{zz}) increase as the porosity of the sample decreases, which indicates that more grain contacts occur at the surface of the

grains. This observation is consistent with the observed increase of the odometer modulus. Due to the denser packing of salt rock, a larger LSVF (L) is observed. The discrepancy between L_{xx} and L_{zz} reveals the development of anisotropy of salt rock: the sample becomes denser in the lateral direction. In the cyclic compression tests, the elastic modulus in the axial direction decreases, while the Poison's ratio increases with the increase of axial strain. Both components of the solidity fabric tensor (S_{xx} and S_{zz}) are stable, and no obvious anisotropic trend is observed in terms of solidity. The trace of the coordination fabric tensor (C) reaches its lowest point at the highest axial deformation, which results in a reduction of the axial elastic modulus. Both the coordination and the LSVF tensors decrease more in the lateral direction than in axial direction, which explains the increase of the Poisson's ratio.

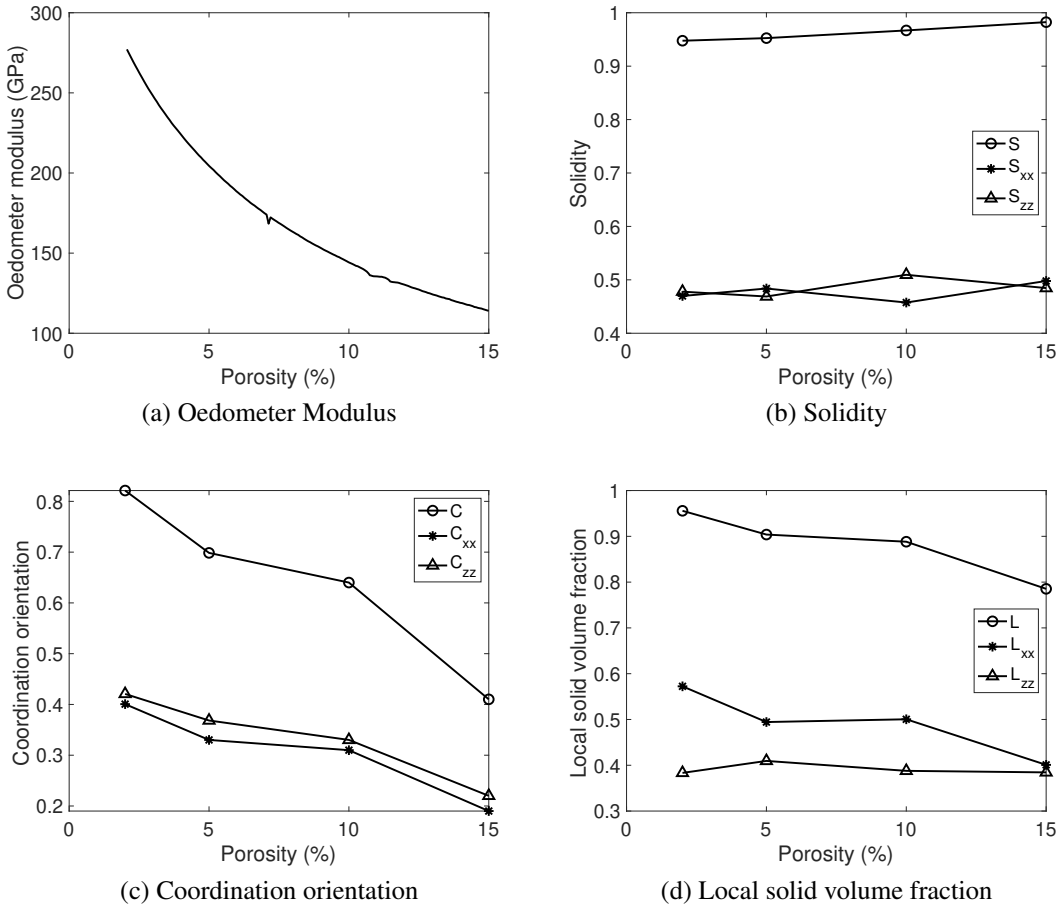

(a) Oedometer Modulus

(b) Solidity

(c) Coordination orientation

(d) Local solid volume fraction

Figure 2.23: Axial and lateral components of fabric tensors in consolidation tests. Notation: F_{xx}, F_{zz}: lateral, axial components of fabric tensor $\boldsymbol{F}$. F: trace of $\boldsymbol{F}$: $F = F_{xx} + F_{zz}$.

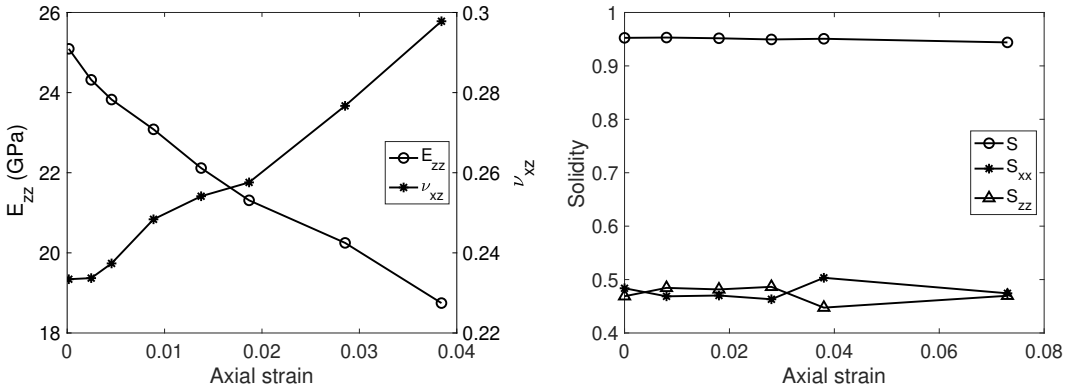

(a) Young's Modulus and Poison ratio

(b) Solidity

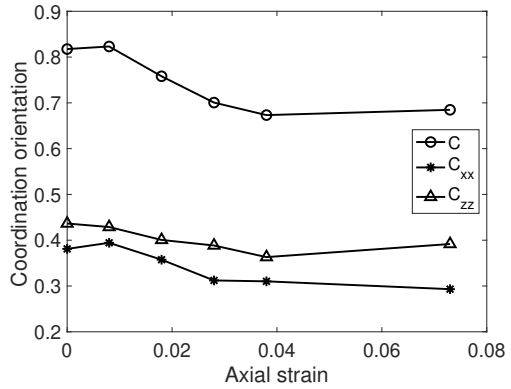

(c) Coordination orientation

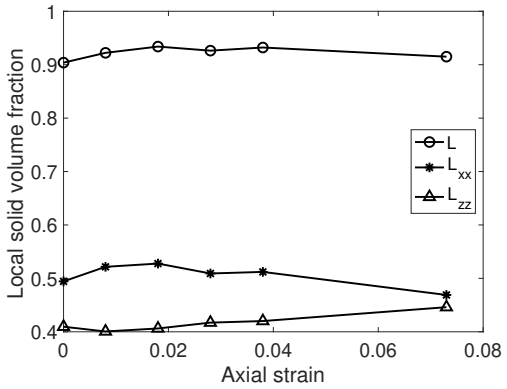

(d) Local solid volume fraction

Figure 2.24: Axial and lateral components of fabric tensors in cyclic compression tests. Notation: F_{xx}, F_{zz}: lateral, axial components of fabric tensor $\boldsymbol{F}$. F: trace of $\boldsymbol{F}$: $F = F_{xx} + F_{zz}$.

2.4 Conclusions

In both the consolidation and the cyclic compression tests, deformation is controlled by grain rearrangement and not by grain indentation. Practically no crack develops during the consolidation tests, whereas in the cyclic compression tests, wing cracks propagate due to the development of sliding cracks.

In the consolidation tests, the contribution of grain indentation to the total deformation of the sample increases as the porosity decreases, but it never exceeds 8% of the volumetric deformation of the sample, even at a porosity as low as 2%. Due to the presence of rigid walls at the lateral boundaries of the sample, lateral grain-to-grain contacts initiate and grow during the consolidation process. The microstructure becomes organized into horizontal layers of coordinated grains. As a result, the orientation distribution of grain indentations is quasi-uniform. The size of the voids reduce and become more uniformly distributed in salt rock. As a result, salt rock microstructure becomes more homogeneous.

In the cyclic compression tests, the changes in grain shape and size are negligible. The deformation of the grains is mainly induced by indentations on the surface of the grains. The number and the area of the indentations increase with the increase of the axial strain, which causes an accumulation of plastic deformation. That being said, only 6.18% of the axial strain of salt rock sample is induced by the deformation of the grains. Large plastic deformation occurs in the axial loading direction and grain rearrangement is the dominant mechanism for the deformation of sample. Due to the redistribution of grains and the propagation of inter granular cracks, grain-to-grain contact areas reduce. The grain to grain contacts are mainly in the axial direction, and a larger local solid volume fraction is observed in the axial direction of grains. These observations indicate that grains tend to be reorganized into vertical columns of coordinated grains. When the axial strain is small, a few large and isolated voids are observed. Due to the differential compressive stress, the larger voids collapse and more small and isolated voids occur. Then, because

of the propagation of the inter-granular cracks, small voids become connected and form large voids, which explains the non-monotonic evolution of the void size distribution. Very few, short intra-granular cracks are noted. Opening-mode wing cracks are observed, which allows identifying grain boundaries where sliding cracks develop. Opening-mode wing cracks tend to develop in the axial direction, while sliding cracks propagate preferentially in the lateral direction. The volume of the wing cracks increases linearly with the axial strain.

The orientation distributions of the fabric descriptors analyzed in this study were used to calculate fabric tensors of solidity, coordination and local solid volume fraction. In the consolidation tests, the local solid volume fraction increases more in the lateral direction than in the axial direction, which indicates that salt rock becomes much denser laterally under compaction. The oedometer modulus increases. In the cyclic compression tests, the lateral components of coordination and local solid volume fraction decrease, which results in an increase of the Poisson's ratio.

CHAPTER 3

DISCRETE WING CRACK ELASTO-PLASTIC DAMAGE MODEL

In this chapter, we couple a micromechanical CDM model and an elasto-plastic model to explain the formation of complex patterns of sliding and wing cracks that develop in salt upon confined cyclic axial loading and to understand the implication of anisotropic damage on stiffness, strength and deformation. In Section 3.1, we summarize the main observations made during an extensive experimental campaign undertaken by our colleagues Fred and Judi Chester at Texas A&M University. Experiments consisted in subjecting synthetic salt rock samples obtained by thermal consolidation to confined cyclic axial loading, and in acquiring microstructure images at key stages of the stress path. In Section 3.2, we formulate a new model, called discrete wing crack elastoplastic damage (DWCPD) model, to explain the fracture patterns observed. A micromechanical model model is proposed to capture the inelastic deformation induced by microscopic cracks. We explain the expression of the Gibbs free energy, damage criteria and flow rules. Then, a plastic damage model is introduced to capture the accumulation of irreversible deformation. In Section 3.3, the DWCPD model is calibrated against the loading test, and the evolution of damage is simulated. In Section 3.4, we discuss the influence of the friction coefficient, the confinement pressure, and the initial damage on the accumulation of damage and stress-strain relationship in salt rock.

List of Symbols

Ψ_s^*	Helmholtz free energy of the REV
G^*	Gibbs energy of the REV
$\overrightarrow{n}, \overrightarrow{l}$	Direction normal to a main crack plane and a wing crack plane
$\boldsymbol{\sigma}, \boldsymbol{\epsilon}$	Microscopic stress and strain tensors of a Representative Elementary Volume (RE

$\boldsymbol{\sigma}^m, \boldsymbol{\sigma}^w$	Stress fields that are applied at main crack faces and wing crack faces
$\sigma_n^m, \boldsymbol{\sigma}_t^m$	Normal stress and the tensor of tangential stress that apply on the faces of the mai
σ_l^m	Net tangential stress that applies on the faces of the main crack in the direction l
σ_n^w	Normal stress that applies on the faces of the main crack
$\boldsymbol{\epsilon}^m, \boldsymbol{\epsilon}^w$	Strain fields on main cracks and wing cracks
$\boldsymbol{\epsilon}^e$	Elastic strain of the matrix
$\boldsymbol{\epsilon}^{ed}$	Recoverable strain induced by the loss of stiffness
$\boldsymbol{\epsilon}^E, \boldsymbol{\epsilon}^p$	Elastic strain and plastic strain of the REV
$\boldsymbol{t}^m$	Traction on a main crack plane
μ, c	Frictional coefficient and cohesion of main cracks
N^m, B^m	Normal and tangential indexes of a main crack
$\beta^m, \boldsymbol{\gamma}^m$	Volume fraction of the normal displacement jumps and shear displacement jumps
s_o, s_1	Normal and shear elastic compliance of cracks
$\overrightarrow{T}$	Shear force applies at the faces of the main crack
V_{REV}	Actual volume of the REV
M_i	Number of cracks in family i
a^m, a^w	Crack lengths of main cracks and wing cracks
ρ^m, ρ^w	Crack densities of main cracks and wing cracks
β^w	Volume fraction of the normal displacement jumps of wing cracks
$\boldsymbol{C}_o$	Elastic stiffness of the matrix
Q	Number of main crack families
$\mathbb{N}_{ijkl}, \mathbb{T}_{ijkl}$	Fourth order tensor operators
f_I, f_{II}	Crack propagation criteria for Mode I and Mode II
K_{Ic}, K_{IIc}	Crack toughness for Mode I and Mode II
K_o, σ_c	Constitutive parameters for toughness
$\boldsymbol{\Omega}$	Macroscopic damage variable of the REV
$\boldsymbol{\Omega}_m, \boldsymbol{\Omega}_w$	Macroscopic damage variable of main cracks and wing cracks

d	Trace of Macroscopic damage variable of the REV
f_p	Plastic yield surface function
g	Plastic potential function
q, p, θ	Deviatoric stress, mean stress, and Lode's angle
J_2, J_3	The second and third stress invariants
e	Cohesion constant of the rock
α_p	Plastic hardening function
m_θ	The parameter controlling the effect of Lode's angle
χ	The parameter controlling the effect of damage
η	The parameter controlling the boundary of the compressive dilation zone
R	The parameter controlling plastic hardening rate
λ, ω	Plastic multiplier and the plastic hardening variable
α_p^o, α_p^m	The plastic yielding threshold and the maximum of the hardening function

3.1 Confined axial loading tests and microstructure observations

Jihui Ding, the Ph.D. student who performed the experimental work at Texas A&M, provided a complete description of the materials, methods, results and interpretations of the tests conducted on salt rock in [128, 129]. Here, we summarize the main results of the experimental campaign in order to present what we aim to explain by the model presented in the following.

3.1.1 Materials and methods

The synthetic salt rock samples used in this study were fabricated through uniaxial consolidation of reagent grade granular halite at the following conditions: grain size ranges between 0.3-0.355 mm; consolidation temperature of 150 °C; maximum axial stress of 75 MPa; displacement rate of 0.034 mm/s. After consolidation, the specimen was a right-

circular cylinder with a diameter of 19.75mm and a length of 42.67 mm, and the bulk porosity of the specimen was 5.6%. The sample was kept dry throughout all stages of this study.

The synthetic salt-rock samples were deformed at room temperature, a confining pressure of 1 MPa, and strain rate of 3×10^{-6} s^{-1}. Axial and radial strains were measured by two rosette strain gauges of 6.35 mm gauge length and 350 Ω resistance. Strain gauges were glued at opposing sides of the sample, and the two strain measurements were averaged to account for sample tilting during deformation tests. Differential force was measured through an internal force gauge that is in direct contact with sample assembly and unaffected by the friction between loading piston and sealing stack. A total of eight unloading-reloading cycles were employed, in addition to initial loading and final unloading. One unloading-reloading cycle was applied in the elastic deformation regime, while the rest of the load cycles were conducted after plastic yielding.

Using repeat experiments, synthetic salt rock samples before, during, and at the end of cyclic loading were extracted for microstructure observation. These samples were epoxy-saturated, cut, and polished to make petrographic sections, and then chemically etched to allow observation of grain-scale features, including grain boundaries and microcracks. The sectioning and etching procedures follow the techniques developed by [130] with only minor modifications. Thin section images were taken from the center portion of the sample using 20x magnification, and stitched together to allow observation of more than 100 grains. On the stitched image, salt grain boundaries were traced and opening-mode microcracks were interpreted based on the following two criteria: (i) There is clear separation between two salt grain boundaries; (ii) The opposing sides of these two salt grain boundaries match well geometrically, which indicates there were previously in contact.

3.1.2 Summary of the results

Figure 3.4 shows the stress-strain behavior during the cyclic axial tests (in red). At room temperature and 1 MPa confining pressure, synthetic salt rock exhibits a ductile mechanical response. The first unloading-reloading cycle nearly fully overlies the initial loading curve, which indicates dominant elastic behavior. After yielding, the sample deforms plastically with slight work hardening. Each unloading cycle is taken to zero differential stress; subsequent reloading does not produce significant hysteresis. The sample behavior first shows slight compaction (positive volumetric strain), followed by continuous dilation (negative volumetric strain). At the end of the test, the sample increases in volume by about 0.6%.

The synthetic salt rock produced from uniaxial consolidation at elevated temperature shows minor intragranular microcracking. Almost all of these intragranular microcracks are associated with fluid inclusions present in salt grains. These fluid inclusions act as stress concentrators and promote microcracking. There is no evidence for separation at grain contacts as all of them are tight, which results from crystal-plastic deformation of salt grains [128]. As shown in Figure 3.1, after cyclic triaxial loading to an axial strain of 7.3%, grain-boundary cracking becomes the dominant brittle deformation mechanism. These microcracks exhibit a preferred orientation that is sub-parallel to the axial loading direction. With further cyclic loading, dilatant grain-boundary microcracks increase in density as well as in separation. These grain-boundary microcracks also display a clear tendency to link with neighboring cracks in the axial direction (Figure 3.1).

3.1.3 Interpretation of the results

In the following, we propose a model to explain the following observed phenomena:

(i) At room temperature and low confining pressure, grain-boundary microcracking is the dominant brittle deformation mechanism;

(ii) Wing cracks linked to sliding cracks propagate along grain boundaries;

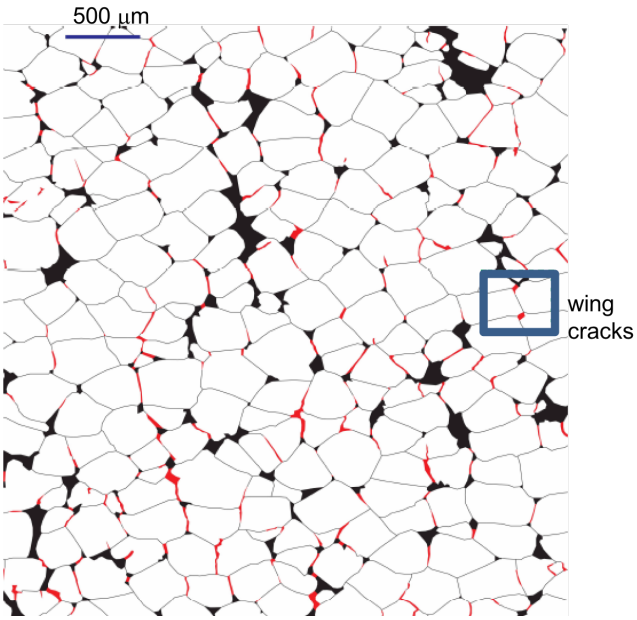

Figure 3.1: Microstructure of experimentally-deformed, granular salt rock after 7.3% axial strain (adapted after [129]).

(iii) Grain-boundary microcracks develop preferably in the loading direction and tend to link with increasing deformation;

(iv) Cyclic loading leads to progressive lengthening of linked crack arrays;

(v) Stiffness degradation is correlated to microscropic inter-granular cracks and grain re-arrangement.

3.2 Theoretical formulation of the discrete wing crack elastoplastic damage (DWCPD) model

3.2.1 The evolution of main cracks

We consider a Representative Elementary Volume (REV) of salt rock made of a homogeneous solid matrix that contains a dilute distribution of penny-shaped cracks, at the tips of which wing cracks propagate. These penny-shaped cracks, called main cracks in the following, can propagate in Mode I and Mode II. In Mode II, we postulate that the slipping of a main crack can trigger the Mode I propagation of wing cracks at its tips, perpendicular

Table 3.1: Deformation modes of main cracks

Mechanism	σ_n^m	$\boldsymbol{\sigma}_t^m$	N^m	B^m
1	≥ 0	$<$ c and has never exceeded c	1	0
2	< 0	$<$ c and has never exceeded c	0	0
3	≥ 0	$\geq$ c or has exceeded c	1	1
4	< 0	$\geq$ c or has exceeded c ; $\parallel \boldsymbol{\sigma}_t^m \parallel + \mu\sigma_n^m > 0$	0	$1 + \mu\sigma_n^m / \parallel \boldsymbol{\sigma}_{ti}^m \parallel$
5	< 0	$\geq$ c or has exceeded c ; $\parallel \boldsymbol{\sigma}_t^m \parallel + \mu\sigma_n^m < 0$	0	0

to the slipping main crack.

We restrict our study to static conditions. Under the assumption that main cracks do not interact, the traction $\boldsymbol{t}^m$ on the faces of the main cracks is induced by the macroscopic stress (noted $\boldsymbol{\sigma}$) applied to the REV [131]. Hence, for each main crack (m), we get:

$$\boldsymbol{t}^m = \overrightarrow{n} \cdot \boldsymbol{\sigma} \tag{3.1}$$

$$\sigma_n^m = \boldsymbol{\sigma} : (\overrightarrow{n} \otimes \overrightarrow{n}) \tag{3.2}$$

$$\boldsymbol{\sigma}_t^m = \boldsymbol{\sigma} \cdot \overrightarrow{n} - (\overrightarrow{n} \cdot \boldsymbol{\sigma} \cdot \overrightarrow{n})\ \overrightarrow{n} \tag{3.3}$$

where $\overrightarrow{n}$ is the direction normal to the main crack plane, σ_n^m is the normal stress that applies on the faces of the main crack (tension stress), and $\boldsymbol{\sigma}_t^m$ is the tensor of tangential stresses that apply on the faces of the main crack (shear stresses).

Here, we introduce a linear frictional crack model (with frictional coefficient μ and cohesion c), in which the main cracks can be subjected to five deformation mechanisms, listed in Table 3.1. N^m and B^m are the normal and tangential indexes, respectively. They are introduced in the expressions of the crack displacements to distinguish the crack propagation micro-mechanisms, as explained in the following.

In mechanism 1, the main crack opens in pure Mode I, without slipping. In mechanism

2, the main crack does not propagate: it remains closed, and does not slip. In mechanism 3, the main crack propagates both in Mode I (tensile opening) and Mode II (slipping). In mechanisms 4 and 5, the main crack is under compressive stress, and does not propagate in Mode I. In mechanism 4, past loading history or current large shear stress led to inter-crystal bond breakage, and the main crack propagates in Mode II, producing frictional shear strain. In mechanism 5, although inter-crystal bonds are broken, slipping does not occur, due to the friction induced by the large normal stress on the crack face. The main crack propagation mechanisms are summarized in Figure 3.2, in which main cracks do not slip in the blue region, while slipping of main cracks occurs in the gray region.

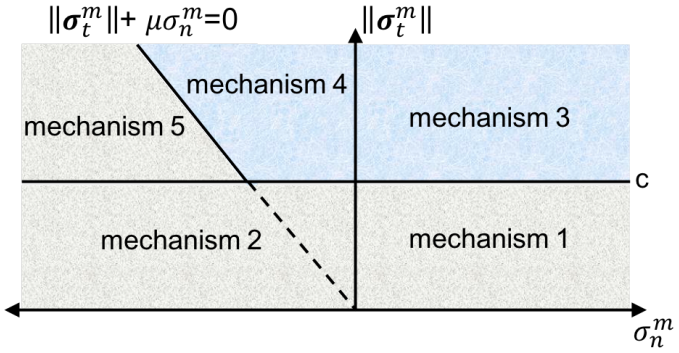

Figure 3.2: The mechanisms of main crack propagation. Blue region: no slipping. Gray region: slipping. Mechanism 1: pure Mode I. Mechanism 3: modes I and II. Mechanism 4: pure Mode II. Mechanisms 2 and 5: no propagation. c is the cohesion at the main crack face. μ is the frictional coefficient. σ_n^m is the normal stress that applies on the faces of the main crack (tension stress). $\boldsymbol{\sigma}_t^m$ is the tensor of tangential stresses that apply on the faces of the main crack.

Main crack deformation is caused by normal and tangential displacement jumps. Main cracks are gathered by families. Since the main cracks are assumed to not interact, the mechanical behavior of the main cracks is that of cracks that are embedded in an infinite elastic medium. In the i^{th} family, all main cracks have the same normal direction $\overrightarrow{n_i}$ and a radius a_i. The volume fraction of the normal displacement jumps β_i^m and the volume fraction of shear displacement jumps $\boldsymbol{\gamma}_i^m$ of the main cracks family i are expressed as follows [5, 83]:

$$\beta_i^m = \rho_i^m s_o N_i^m \sigma_{ni}^m \tag{3.4}$$

$$\boldsymbol{\gamma}_i^m = \rho_i^m s_1 B_i^m \boldsymbol{\sigma}_{ti}^m \tag{3.5}$$

where N_i^m (respectively, B_i^m) is zero when the main cracks do not propagate in Mode I (respectively, do not propagate in Mode II), as explained in Table 3.1. The main crack density ρ_i^m is calculated as:

$$\rho_i^m = \frac{M_i \left(a_i^m\right)^3}{V_{REV}} \tag{3.6}$$

where V_{REV} is the volume of REV and M_i is the number of cracks in family i. The expressions of elastic compliances s_o and s_1 were established by Kachanov [5], as follows:

$$s_0 = \frac{16\left(1-\nu_o^2\right)}{3E_o} \tag{3.7}$$

$$s_1 = \frac{32\left(1-\nu_o^2\right)}{3\left(1-2\nu_o\right)E_o} \tag{3.8}$$

where E_o and ν_o are the Young's modulus and Poisson's ratio of the infinite elastic medium. The average strain induced by the displacement jumps of the main cracks in family i can be then calculated as:

$$\boldsymbol{\epsilon}_i^m = \beta_i^m \overrightarrow{n}_i \otimes \overrightarrow{n}_i + \frac{1}{2}\left(\boldsymbol{\gamma}_i^m \otimes \overrightarrow{n}_i + \overrightarrow{n}_i \otimes \boldsymbol{\gamma}_i^m\right) \tag{3.9}$$

3.2.2 The development of wing cracks

The evolution of wing cracks in solids under compression was studied theoretically [132], experimentally [82], and numerically [133]. Based on the reported observations, we assume that tensile wing cracks initiate at the tips of the main cracks that slip. The shear force that acts on the faces of the main cracks is viewed as the force that drives the propagation of wing cracks. Since salt rock is a polycrystalline material, and salt crystals are typically rhomboids, wing cracks are assumed to propagate in the direction perpendicular

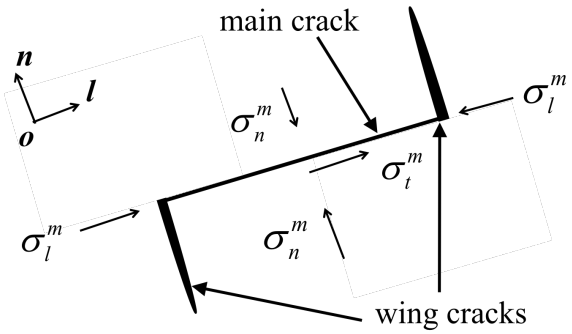

Figure 3.3: Schematic of wing crack propagation. Note: the sketch gives a 2D view, but the proposed model is in 3D. σ_n^m and $\boldsymbol{\sigma}_t^m$ are the normal stress and tangential stress that apply on the faces of the main crack respectively; σ_l^m is the normal stress applies on the faces of the wing crack induced by the stress of the REV.

to the main crack plane, as shown in Figure 3.3. The net tangential stress that applies on the faces of the main crack in the direction $\overrightarrow{l}$ drives the tensile opening of wing crack planes perpendicular to $\overrightarrow{l}$.

The propagation of the wing cracks is triggered by a tensile force, equal to the shear force $\overrightarrow{T}_i$ that applies at the faces of the main crack. The norm of the latter is calculated as:

$$T_i = (a_i^m)^2 \pi B_i^m \parallel \boldsymbol{\sigma}_{ti}^m \parallel \tag{3.10}$$

Note that if B_i^m is equal to zero, the main crack does not slip, therefore $T_i = 0$. The normal stress that applies on the faces of a wing crack of family i is the sum of the projection of the macroscopic stress on the direction normal to the wing crack ($\overrightarrow{l_i}$) and of the tensile stress induced by the main crack shear force:

$$\sigma_{ni}^w = \frac{T_i}{a_i^{w2}\pi} + \boldsymbol{\sigma} : \left(\overrightarrow{l_i} \otimes \overrightarrow{l_i}\right) \tag{3.11}$$

Substituting Eq.3.10 into Eq. 3.11, we have:

$$\sigma_{ni}^w = \left(\frac{a_i^m}{a_i^w}\right)^2 B_i^m \parallel \boldsymbol{\sigma}_{ti}^m \parallel + \boldsymbol{\sigma} : \left(\overrightarrow{l_i} \otimes \overrightarrow{l_i}\right) \tag{3.12}$$

Similar to main cracks, the volume fraction of the normal displacement jumps of a wing crack is obtained as follows:

$$\beta_i^w = \rho_i^w s_o \sigma_{ni}^w \tag{3.13}$$

The strain of the wing cracks in family i is calculated as:

$$\boldsymbol{\epsilon}_i^w = \beta_i^w \overrightarrow{l}_i \otimes \overrightarrow{l}_i \tag{3.14}$$

3.2.3 Micromechanics-based Gibbs free energy

The Helmholtz free energy of the REV (noted Ψ_s^*) is the sum of the elastic deformation energy stored in the matrix and of the elastic deformation energy stored in the displacement jumps of the microscopic cracks. Since the main cracks do not interact, Ψ_s^* it is expressed as follows:

$$\Psi_s^* = \frac{1}{2}\boldsymbol{\epsilon}^e : \boldsymbol{C}_o : \boldsymbol{\epsilon}^e + \frac{1}{2}\boldsymbol{\sigma}^m : \boldsymbol{\epsilon}^m + \frac{1}{2}\boldsymbol{\sigma}^w : \boldsymbol{\epsilon}^w \tag{3.15}$$

where $\boldsymbol{\epsilon}^e$ is the elastic strain of the matrix; $\boldsymbol{C}_o$ is the elastic stiffness of the matrix; $\boldsymbol{\sigma}^m$ and $\boldsymbol{\sigma}^w$ are the stress fields that are applied at main crack faces and wing crack faces, respectively. From equation 3.1, we have:

$$\boldsymbol{\sigma}^m \cdot \overrightarrow{n} = \boldsymbol{\sigma} \cdot \overrightarrow{n} \tag{3.16}$$

Based on Legendre transformation, the Gibbs energy (free enthalpy, G) is expressed as:

$$G^* = \boldsymbol{\sigma} : \boldsymbol{\epsilon}^E - \Psi_s^* \tag{3.17}$$

where $\boldsymbol{\epsilon}^E = \boldsymbol{\epsilon}^e + \boldsymbol{\epsilon}^w + \boldsymbol{\epsilon}^m$ is the REV total elastic strain. Substituting Eq. 3.9, Eq. 3.15, and Eq. 3.16 into Eq. 3.17, we have [134]:

$$G^* = \frac{1}{2}\boldsymbol{\sigma} : \boldsymbol{S}_o : \boldsymbol{\sigma} + \frac{1}{2}\boldsymbol{\sigma} : \boldsymbol{\epsilon}^m + \boldsymbol{\sigma} : \boldsymbol{\epsilon}^w - \frac{1}{2}\boldsymbol{\sigma}^w : \boldsymbol{\epsilon}^w \tag{3.18}$$

According to Eq. 3.9, Eq. 3.14, and Eq. 3.18, the Gibbs energy for Q main micro-crack families of Q different orientations is:

$$\begin{aligned} G^* = \frac{1}{2}\boldsymbol{\sigma} : \boldsymbol{S}_o : \boldsymbol{\sigma} + \frac{1}{2}\sum_{i=1}^{Q} w_i \{ & s_0 \rho_i^m N_i^m \left(\overrightarrow{n}_i \cdot \boldsymbol{\sigma} \cdot \overrightarrow{n}_i\right)\left(\overrightarrow{n}_i \cdot \boldsymbol{\sigma} \cdot \overrightarrow{n}_i\right) \\ & + s_1 \rho_i^m B_i^m [(\boldsymbol{\sigma} \cdot \boldsymbol{\sigma}) : \overrightarrow{n}_i \otimes \overrightarrow{n}_i - \left(\overrightarrow{n}_i \cdot \boldsymbol{\sigma} \cdot \overrightarrow{n}_i\right)\left(\overrightarrow{n}_i \cdot \boldsymbol{\sigma} \cdot \overrightarrow{n}_i\right)] \\ & + 2 s_0 \rho_i^w \boldsymbol{\sigma} : \sigma_{ni}^w \overrightarrow{l}_i \otimes \overrightarrow{l}_i - \rho_i^w s_0 {\sigma_{ni}^w}^2 \} \end{aligned} \tag{3.19}$$

In which we used Bažant's discrete integration scheme, with a discrete set of $Q = 74$ micro-crack families of 74 distinct crack orientations distributed on the unit sphere [71]. The parameters w_i are the weight coefficients for that integration scheme. The total strain of the REV (noted $\boldsymbol{\epsilon}$) can be decomposed into the elastic strain $\boldsymbol{\epsilon}^E$ and the plastic strain $\boldsymbol{\epsilon}^p$ induced by the propagation of microscopic cracks, as follows:

$$\boldsymbol{\epsilon} = \boldsymbol{\epsilon}^E + \boldsymbol{\epsilon}^p = \boldsymbol{\epsilon}^e + \boldsymbol{\epsilon}^{ed} + \boldsymbol{\epsilon}^p \tag{3.20}$$

where

$$\boldsymbol{\epsilon}^E = \frac{\partial G^*}{\partial \boldsymbol{\sigma}} \tag{3.21}$$

$\boldsymbol{\epsilon}^e$ is the elastic deformation of the matrix (which would exist in the absence of cracks under the given stress):

$$\boldsymbol{\epsilon}^e = \frac{1+\nu_o}{E_o}\boldsymbol{\sigma} - \frac{\nu_o}{E_o}\mathrm{tr}\left(\boldsymbol{\sigma}\right)\boldsymbol{\delta} \tag{3.22}$$

$\boldsymbol{\epsilon}^{ed}$ is the additional recoverable strain induced by the loss of stiffness upon the development

of the micro-cracks. Based on Eq. 3.18, 3.21 and 3.20, $\boldsymbol{\epsilon}^e$ and $\boldsymbol{\epsilon}^{ed}$ are expressed as:

$$\boldsymbol{\epsilon}^{ed} = \sum_{i=1}^{Q} w_i \rho_i^m \left(s_1 B_i^m \mathbb{T}_i : \boldsymbol{\sigma} + \frac{1}{2} s_1 \frac{\partial B_i^m}{\partial \boldsymbol{\sigma}} \boldsymbol{\sigma} : \mathbb{T}_i : \boldsymbol{\sigma} + s_0 N_i^m \mathbb{N}_i : \boldsymbol{\sigma} \right) + \sum_{i=1}^{Q} w_i \rho_i^w s_0 \{ \frac{\partial \left(\boldsymbol{\sigma} : \sigma_{ni}^w \overrightarrow{l}_i \otimes \overrightarrow{l}_i \right)}{\partial \boldsymbol{\sigma}} - \sigma_{ni}^w \frac{\partial \sigma_{ni}^w}{\partial \boldsymbol{\sigma}} \} \tag{3.23}$$

where the fourth order operators $\mathbb{N}_{ijkl}$ and $\mathbb{T}_{ijkl}$ are defined as:

$$\mathbb{N}_{ijkl} = n_i n_j n_k n_l \tag{3.24}$$

$$\mathbb{T}_{ijkl} = \frac{1}{4} \left(n_i n_k \delta_{jl} + n_i n_l \delta_{jk} + n_j n_l \delta_{ik} + n_j n_k \delta_{il} \right) - n_i n_j n_k n_l \tag{3.25}$$

When main cracks deform under mechanism 4, $\partial B_i^m / \partial \boldsymbol{\sigma}$ is calculated by Eq. 3.26, otherwise, $\partial B_i^m / \partial \boldsymbol{\sigma}$ is equal to 0. We have:

$$\frac{\partial B_i^m}{\partial \boldsymbol{\sigma}} = \frac{\mu}{\parallel \boldsymbol{\sigma}_{ti}^m \parallel} \frac{\partial \sigma_{ni}^m}{\partial \boldsymbol{\sigma}} - \frac{\mu \sigma_{ni}^m}{\parallel \boldsymbol{\sigma}_{ti}^m \parallel^2} \frac{\partial \parallel \boldsymbol{\sigma}_{ti}^m \parallel}{\partial \boldsymbol{\sigma}} \tag{3.26}$$

3.2.4 Damage criterion and flow rule

Main crack propagation criteria are expressed as:

$$f_{Ii}^m = \sigma_{ni}^m \sqrt{\pi a_i^m} - K_{Ic} \tag{3.27}$$

$$f_{IIi}^m = B_i^m \parallel \boldsymbol{\sigma}_{ti}^m \parallel \sqrt{\pi a_i^m} - K_{IIc} \tag{3.28}$$

for Mode I and II, respectively. K_c represents the hardening of crack toughness; it is expressed as a hyperbolic function of the crack radius [134]:

$$K_c = \frac{a^{3/2}}{\frac{1}{K_o} + \frac{a}{\boldsymbol{\sigma}_c}} \tag{3.29}$$

in which K_o and $\boldsymbol{\sigma}_c$ are constitutive parameters that respectively control the yield point and the peak stress. The values of K_o and $\boldsymbol{\sigma}_c$ in Mode I differ from those in Mode II.

Wing cracks are assumed to propagate in Mode I only, according to the following criterion:

$$f_{Ii}^w = \sigma_{ni}^w \sqrt{\pi a_i^w} - K_{Ic} \tag{3.30}$$

Based on the consistency rule, the radius of cracks of family i is updated as follows:

$$\mathrm{d}a_i = \frac{\frac{\partial f}{\boldsymbol{\sigma}} \mathrm{d}\boldsymbol{\sigma}}{\frac{\partial f}{\partial a_i}} \tag{3.31}$$

in which f denotes the criterion that contributes to the propagation of cracks of family i (f_{Ii}^m, f_{IIi}^m and/or f_{Ii}^w). Note that the radii of the main and wing cracks are calculated separately for each family of cracks (so that each crack family is characterized by a direction, a main crack radius and a wing crack radius). The crack density of crack family i is calculated using Eq.3.6, as follows:

$$\mathrm{d}\rho_i = \frac{3 M_i a_i^2}{V_{REV}} \mathrm{d}a_i \tag{3.32}$$

Note that for each crack family i, we calculate a main crack density (ρ_i^m) and a wing crack density (ρ_i^w). The macroscopic damage variable of the REV ($\boldsymbol{\Omega}$) is defined as the sum of

the crack density tensors of all crack families, as follows:

$$\mathbf{\Omega} = \sum_{i=1}^{Q} \rho_i^m \overrightarrow{n}_i \otimes \overrightarrow{n}_i + \sum_{i=1}^{Q} \rho_i^w \overrightarrow{l}_i \otimes \overrightarrow{l}_i \tag{3.33}$$

3.2.5 Inelastic deformation

The plastic deformation in equation 3.20 (noted $\boldsymbol{\epsilon}^p$) is introduced to account for the inelastic strain that result from crystals' rearrangement and residual geometric incompatibilities at crack faces. A non-associated plastic flow rule is adopted. The plastic yield surface is a quadratic function, adopted in former rock mechanics models [135]:

$$f_p(\boldsymbol{\sigma}, d, \boldsymbol{\epsilon}^p) = q^2 h^2(\theta) + \alpha_p(p - e) \tag{3.34}$$

where q is the deviatoric stress; p is the mean stress; e is a constant describing the cohesion of the rock; α_p is the plastic hardening function; $h(\theta)$ is a function of Lode's angle θ. A simplified expression of $h(\theta)$ can be given as [136]:

$$h(\theta) = 1 - m_\theta \sin(\theta) \tag{3.35}$$

$$\sin(\theta) = -\frac{J_3}{2}\left(\frac{3}{J_2}\right)^{\frac{3}{2}} \tag{3.36}$$

where J_2 and J_3 are the second and third stress invariants, respectively, and m_θ is a material parameter, controlling the effect of Lode's angle. The plastic function α_p couples damage and plasticity, and depends on both on the volumetric part of the damage tensor (d=tr($\mathbf{\Omega}$)) and on the plastic hardening variable (noted ω_p). The expression of α_p is the following:

$$\alpha_p = (1 - \chi d)[\alpha_p^o + \left(\alpha_p^m - \alpha_p^o\right) \frac{\omega_p}{R + \omega_p}] \tag{3.37}$$

in which χ is a material parameter that controls the influence of damage and which can take any value between 0 and 1; α_p^o is the plastic yielding threshold; α_p^m is the maximum value of the hardening function; R determines the plastic hardening rate.

The plastic hardening variable ω_p is defined as the generalized shear strain:

$$\dot{\omega}_p = \sqrt{\frac{2}{3}\dot{\boldsymbol{e}}^p : \dot{\boldsymbol{e}}^p} \tag{3.38}$$

$$\boldsymbol{e}^p = \boldsymbol{\epsilon}^p - \frac{1}{3}\left(\boldsymbol{\epsilon}^p : \boldsymbol{\delta}\right)\boldsymbol{\delta} \tag{3.39}$$

A damage coupled plastic potential is adopted [135]:

$$g(\boldsymbol{\sigma}, d) = qh(\theta) - (1 - \chi d)\eta(p - e) \tag{3.40}$$

where η is a material parameter, controlling the boundary of compressive dilation zone. The increment of plastic strain is calculated as follows:

$$\dot{\boldsymbol{\epsilon}}^p = \dot{\lambda}\frac{\partial g}{\partial \boldsymbol{\sigma}} \tag{3.41}$$

in which $\dot{\lambda}$ is the plastic multiplier. According to the plastic consistency rule, $\dot{\lambda}$ is a positive scalar, and $\dot{\lambda} f_p(\boldsymbol{\sigma}, d, \boldsymbol{\epsilon}^p) = 0$. Substituting Eq. 3.41 into Eq. 3.38, we have:

$$\dot{\omega}_p = \dot{\lambda}\sqrt{\frac{2}{3}\left\{\frac{\partial g}{\partial \boldsymbol{\sigma}} : \frac{\partial g}{\partial \boldsymbol{\sigma}} - \frac{1}{3}\left[\text{tr}\left(\frac{\partial g}{\partial \boldsymbol{\sigma}}\right)\right]^2\right\}} \tag{3.42}$$

When the plastic yield criterion is exceeded ($f_p > 0$), the plastic function α_p is first updated by using the consistency rule applied to the plastic yield function f_p, given in Eq. 3.34. Then, the plastic hardening variable ω_p is obtained from Eq. 3.37 using the updated α_p. The plastic multiplier $\dot{\lambda}$ is then calculated from Eq. 3.40 and Eq. 3.42, with the updated ω_p. Substituting $\dot{\lambda}$ into Eq. 3.41, the plastic strain $\boldsymbol{\epsilon}^p$ is obtained for the current load step.

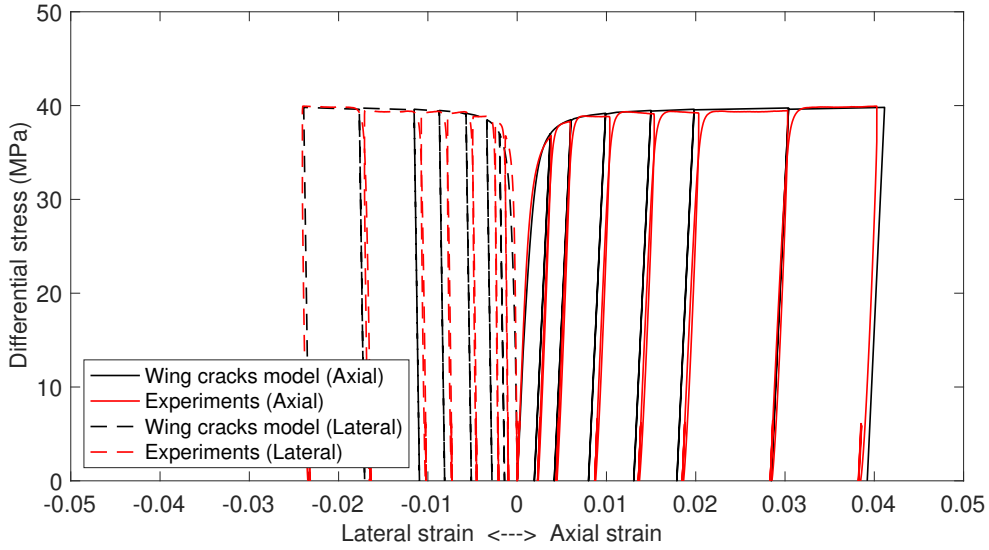

Figure 3.4: stress-strain curve obtained during the confined cyclic triaxial tests: experimental results vs. DWCPD model predictions.

3.3 DWCPD model calibration

We used the stress-strain curves obtained during the confined cyclic axial loading tests presented in Section 3.1 to calibrate the proposed discrete wing crack elasto-plastic damage (DWCPD) model. Reloading was done after unloading, when the differential stress was reduced to 0 MPa. The same confined cyclic loading tests were performed more than 10 times, and the repeatability of the test was confirmed. Figure 3.4 shows the obtained stress-strain curves.

When the differential stress is less than 35 MPa (yielding point), the sample deforms elastically. Hence, we first calibrated the elastic parameters by using the linear portion of the first loading cycle, for stresses lower than 35 MPa. In the subsequent cycles, we noted that main cracks do not propagate when the differential stress is less than 15 MPa, which allowed us to calibrate the yield and frictional parameters. The yielding point is mainly controlled by K_{Ic}, K_{IIc}, and α_p^o. Then, the parameters controlling the ultimate state σ_{Ic}, σ_{IIc}, and α_p^m were calibrated from the strength of the sample. Lastly, we calibrated the plasticity parameters by trial and error, to find the best fit with the experimental stress-

strain curve. The calibrated model parameters are given in table 3.2, in which a_{mo} is the initial radius of the main cracks.

Table 3.2: DWCPD model parameters, calibrated against the cyclic triaxial test.

Elasticity				Plasticity				
E_o	ν_o	e	χ	R	α_p^o	α_p^m	m_θ	η
GPa	$-$	MPa	$-$	$-$	MPa	MPa	$-$	$-$
21	0.32	4	0.5	3.07×10^{-3}	20.25	490	0	-0.79

Friction		Cracks geometry		Damage			
c	μ	a_{mo}	M/V_{REV}	K_{Ic}	K_{IIc}	σ_{Ic}	σ_{IIc}
MPa	$-$	mm	mm^{-3}	MPa/mm	MPa/mm	MPa	MPa
4	0.15	0.022	100	80	344	100	319

According to Figure 3.4, the yielding, hardening, and stiffness degradation of salt rock in the cyclic loading test are captured by the DWCPD model. Upon loading or reloading, cracks propagate only after the differential stress reaches the maximum differential stress ever reached in the loading history. During unloading, the magnitude of the differential stress decreases, and the cracks stop propagating (Eq. 3.27, Eq. 3.28, Eq. 3.30). Based on Eq. 5.8, the REV stiffness depends on crack density, which does not evolve upon unloading, leading to linear unloading paths shown in Figure 3.4, i.e. the hysteresis is not captured by the DWCPD model.

The evolution of damage during the cyclic loading tests is shown in Figure 3.5. The damage tensor is projected on the three directions of space, in which direction 3 is the loading axis and directions 1 and 2 are the so-called lateral directions. We note that Ω_3 is the axial damage component, i.e., the damage that represents an equivalent crack plane normal to the loading axis. Ω_1 and Ω_2 are the lateral damage components, i.e., the equivalent crack planes that contain the loading axis. Note that since the experiment is axis-symmetric, the evolution curves of Ω_1 and Ω_2 overlap. The total damage Ω presented in Figure 3.5a is the sum of the main crack damage Ω_m (Figure 3.5b) and of the wing crack damage Ω_w (Figure 3.5c).

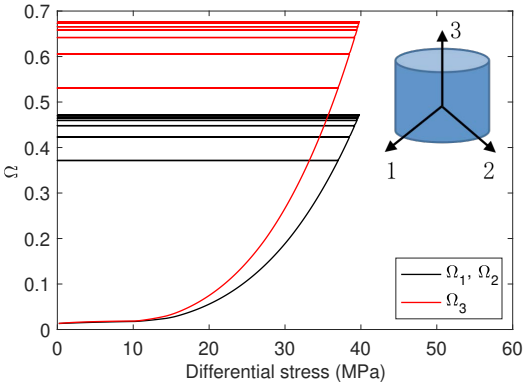

(a) Total damage

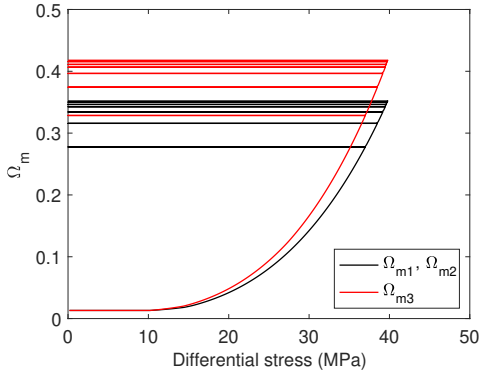

(b) Main crack damage

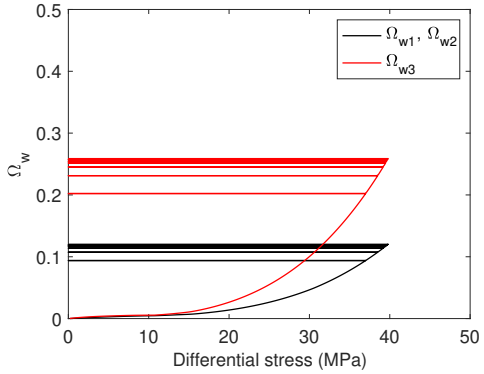

(c) Wing crack damage

Figure 3.5: Evolution of damage during the triaxial cyclic tests (calibration of the DWCPD model). Ω_m is the main crack damage, Ω_w is the wing crack damage, and Ω is the sum of main crack damage and wing crack damage.

The evolutions of Ω_1 and Ω_3 differ, which implies that the sample exhibits an anisotropic behavior after damage initiation (damage-induced anisotropy). Results shown in Figure 3.5 indicate that damage propagates in two phases, as explained in Figure 3.6. In Stage 1, under low differential stress (i.e., under 15 MPa), the main crack damage components remain constant, which means that the main cracks keep their initial radius a_{mo}. By contrast, wing cracks start propagating in Mode I when the differential stress is only a few MPa. Main cracks cannot slip, because of the cohesion and the friction at salt crystal faces. Hence, wing cracks propagate only because of the REV stress. Since the REV is subjected to a compression in direction 3, tensile wing crack propagation mostly leads to lateral damage (Ω_{w1} and Ω_{w2}). Note that Ω_{w3} is not zero, since it is calculated as the projection of the

74 wing crack density tensors on direction 3. In Stage 2, with the increase of differential stress, shear stresses at the faces of the main cracks reach the Mode II crack propagation threshold. Main crack tangential displacement jumps are noted. Main cracks start to propagate in Mode II, predominantly in direction 3 (loading direction). Main crack slipping induces additional wing crack tensile opening, predominantly in direction 3. As a result, in Stage 2, Ω_{m3} increases faster than Ω_{m1} and Ω_{m2} and Ω_{w3} develops faster than Ω_{w1} and Ω_{w2} (see Figure 3.5b and 3.5c). Tensile damage is not observed in main cracks.

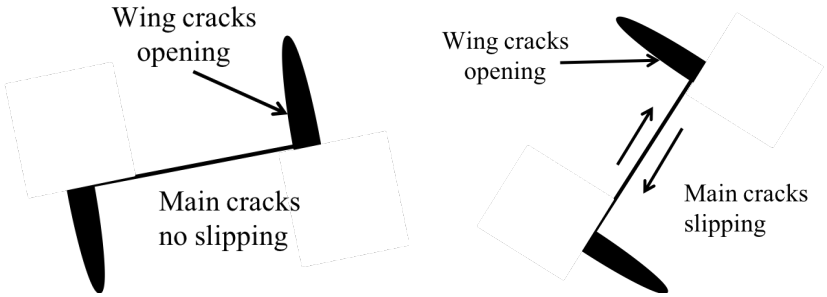

Figure 3.6: Damage propagation process: (1) Wing crack tensile opening; (2) Main crack slipping, inducing additional wing crack opening.

3.4 Sensitivity analyses

3.4.1 Influence of the frictional coefficient at main crack faces

Main cracks only slip when the magnitude of the shear stress exceeds $c + \mu\sigma_n^m$. Here, we present a sensitivity analysis of the frictional coefficient μ and the cohesion c, which control the amplitude of the tangential displacement jumps. Triaxial compression tests are simulated with the same confinement stress as in the calibration simulations (1 MPa). The elastic, damage, and plastic parameters are those listed in Table 3.2. When the axial strain reaches 0.01, we start unloading until the differential stress reduces to 0 MPa.

We perform the simulations with μ equal to 0, 0.2, and 0.4, and c is set to be 4 MPa. Figure 3.7 shows that a larger frictional coefficient leads to larger specimen (REV) strength, because the friction on the faces of the main cracks restricts the propagation of the main

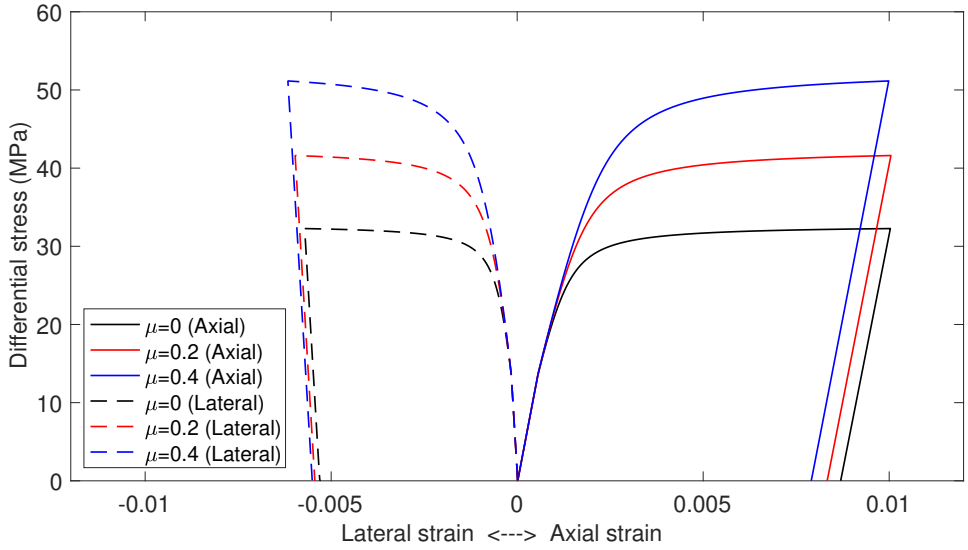

Figure 3.7: Influence of the frictional coefficient at main crack faces (stress-strain curve). μ is the frictional coefficient.

cracks. With a smaller friction coefficient, main cracks undergo larger tangential displacement jumps, hence larger plastic strain ϵ^p, which explains the larger residual strains at lower friction. When the axial strain reaches 0.01, the lateral strain of the sample with $\mu = 0.4$ is 7.8% higher than that of the sample with $\mu = 0$. We note that in general, the higher the friction coefficient, the higher the final lateral strain. In the sample with the higher friction coefficient, crack propagation mainly occurs on the main cracks with orientation close to the axial loading axis (Eq. 3.3 and Eq. 3.28). When the simulations are run to the same total axial strain, larger Ω_{m1} is observed in the sample with higher frictional coefficient, which leads to the higher the final lateral strain. This is because the friction at crack faces leads to important lateral dilation. Figure 3.8 shows that the damage rate is larger for both main and wing cracks when the frictional coefficient is smaller. Like in Section 3.3, the evolution of damage presents two stages, independently of the value of μ. In Stage 1, wing cracks propagate in Mode I because of the loading applied at the external boundaries of the sample, and main cracks do not slip. Therefore, the evolution of damage is independent from the value of the friction coefficient. In Stage 2, main cracks propagate in Mode II and wing cracks rapidly propagate in Mode I. Stage 2 starts at a differential stress of 8 MPa for

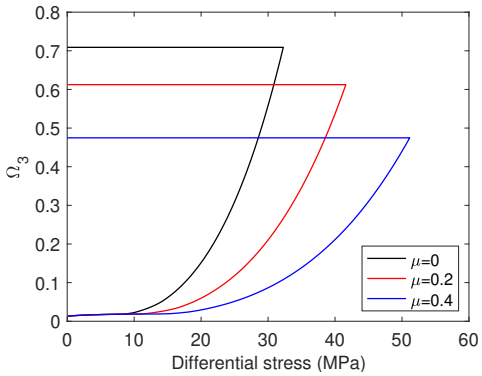

(a) Total damage

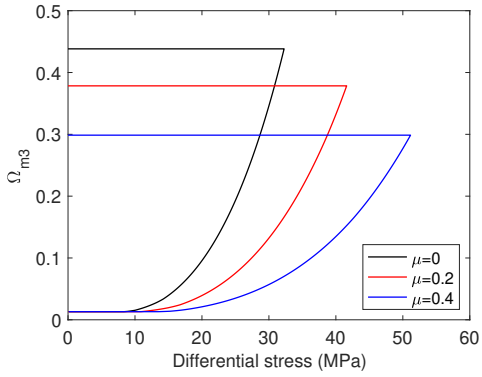

(b) Main crack damage

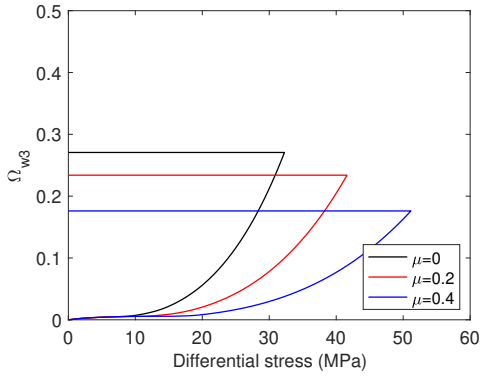

(c) Wing crack damage

Figure 3.8: Influence of the frictional coefficient and the cohesion at main crack faces (damage evolution). μ is the frictional coefficient.

$\mu = 0$, 12 MPa for $\mu = 0.2$ and 15 MPa for $\mu = 0.4$. Hence, a larger friction coefficient delays the propagation of the main cracks, which results in smaller total damage at the end of the unloading phase. Therefore, the evolution of damage is independent from the value of the friction coefficient. In Stage 2, main cracks propagate in Mode II and wing cracks rapidly propagate in Mode I. Stage 2 starts at a differential stress of 8 MPa for $\mu = 0$, 12 MPa for $\mu = 0.2$ and 15 MPa for $\mu = 0.4$. Hence, a larger friction coefficient delays the propagation of the main cracks, which results in smaller total damage at the end of the unloading phase. For example, when the axial strain reaches 0.01, the total axial damage of the specimen with $\mu = 0$ is 0.71, while the axial damage of the specimen with $\mu = 0.4$ is only 0.48. As shown in Figure 3.8b, the difference of final axial main crack damage for μ = 0 (Ω_m = 0.43) and μ = 0.2 (Ω_m = 0.38) is 0.05, and the difference of final axial main

crack damage for μ = 0.2 (Ω_m = 0.38) and μ = 0.4 (Ω_m = 0.30) is 0.08. With the increase of μ, the effect of μ on Ω_m increases. This is because the propagation of the main cracks is controlled by both cohesion and friction, and therefore, slipping is predominantly hindered by the cohesion parameter when the friction parameter is small. As a result, the final main crack damage is not very sensitive to μ when μ is small.

We perform the simulations with c equal to 0 MPa, 8 MPa, and 16 MPa, and μ is set to be 0.15. According to Figure. 3.10, the sample with larger cohesion on the faces of cracks requires higher shear stress to break the bounds between salt crystals, which postpones the development of damage. When cohesion is small, the curves of damage evolution is smooth. With the increase of differential stress, both main crack damage and wing crack damage in samples with a larger cohesion accumulate by steps. When the shear stress on the faces of cracks reaches the cohesion, the bounds are broken following with a sudden increase of main cracks length, which leads to the rapid propagation of wing cracks. Then, the resistance for the tangential displacement of the main crack is only provided by friction, and the damage curves start to converge (i.e. the black line and the red line in Figure. 3.10 are overlapped, when the differential stress reaches 30 MPa). When the cohesion is small, the influence of cohesion on the stress-strain curve is not obvious as shown in Figure. 3.9. Because there is less slipping on the faces of main cracks, the increase of cohesion enhances the strength of salt rock, when the cohesion is large. Due to the rapid crack propagation, strain increases suddenly after breaks the bounds, when the cohesion is 12 MPa (Figure. 3.9).

3.4.2 Influence of the confinement

We now investigate the sensitivity of deformation and damage to the confining pressure. The constitutive parameters are those obtained after calibration, as listed in Table 3.2. Triaxial loading-unloading cycles are simulated with a confinement stress equal to 0 MPa, 5 MPa, and 10 MPa respectively. When the axial strain of the rock reaches 0.01, unloading

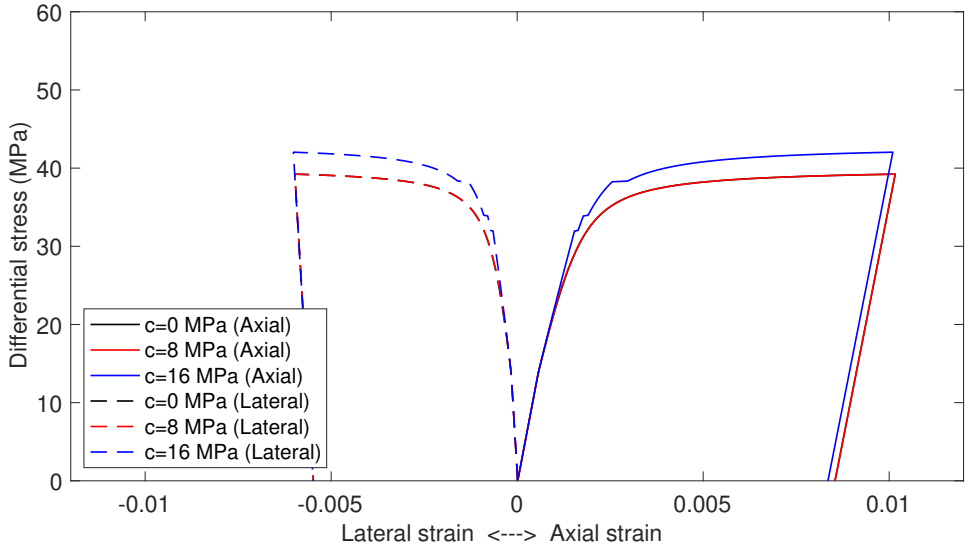

Figure 3.9: Influence of the cohesion at main crack faces (stress-strain curve). c is the cohesion.

begins, until the differential stress gets to 0. Results are presented in Figures 3.11 and 3.12.

According to Figure 3.11, under a confining pressure of 5 MPa, the stress of specimen at 0.01 axial strain is 42.5 MPa, versus 38 MPa without confinement. The residual strain is almost insensitive to the confinement, although we note that the lateral residual strains increase when the confinement decreases. This was expected, since the lateral confinement restricts the lateral strains. Both wing cracks and main cracks propagate faster at low confinement, as shown in Figure 3.12. Since wing cracks propagate in Mode I, a high confinement impedes the initiation of wing cracks. As expected, simulation results indicate that in Stage 1, the initiation of wing cracks are sensitive to the confinement, with a delayed occurrence of damage at high confinement. Here, simulations are strain controlled, and the differential stress reached under the highest loading increases with the confining pressure. As a result, under high confinement, although the initiation of wing cracks is delayed, the damage accumulated because of the wing cracks during the simulated tests increases with the confining pressure. In Stage 2, a high confinement prevents main cracks from slipping. Thus, under low confinement, main cracks initiate earlier and propagate faster, which accelerates the propagation of connected wing cracks. A larger confinement stress

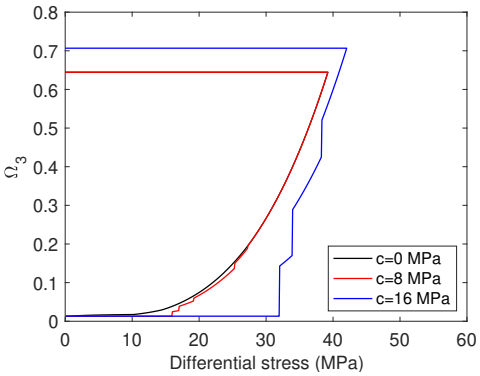

(a) Total damage

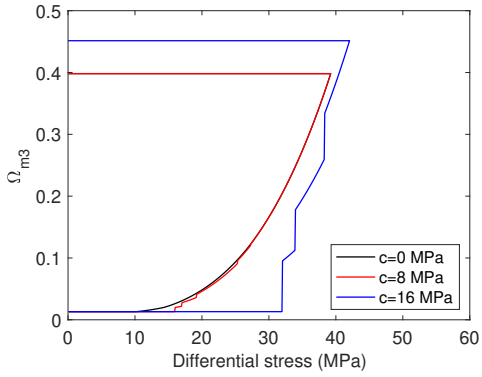

(b) Main crack damage

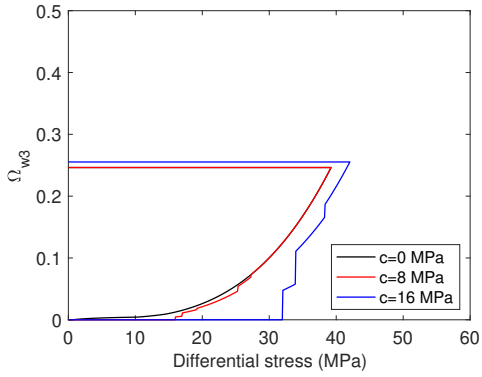

(c) Wing crack damage

Figure 3.10: Influence of the cohesion at main crack faces (damage evolution). c is the cohesion.

induces more slipping and less opening of the main cracks. In all cases, the wing crack damage exceeds the main crack damage when the axial strain reaches 0.01.

3.4.3 Damage evolution in predamaged salt rock

We now study the effect of the initial crack distribution present in the sample on the response of the specimen to the loading-unloading cycles. Constitutive parameters are those listed in Table 3.2. We first simulate an axial tension test, in which the axial stress is incrementally increased up to 2 MPa (in direction 3). Then, we simulate the unloading path from a 2 MPa axial stress to a 0 MPa axial stress. Finally, we simulate a uniaxial compression tests by incrementally applying a 0.01 axial strain. The stress vs. strain curve is shown in Figure 3.13 (O-A-B-C-D). During the tensile loading (OA), damage accumulates

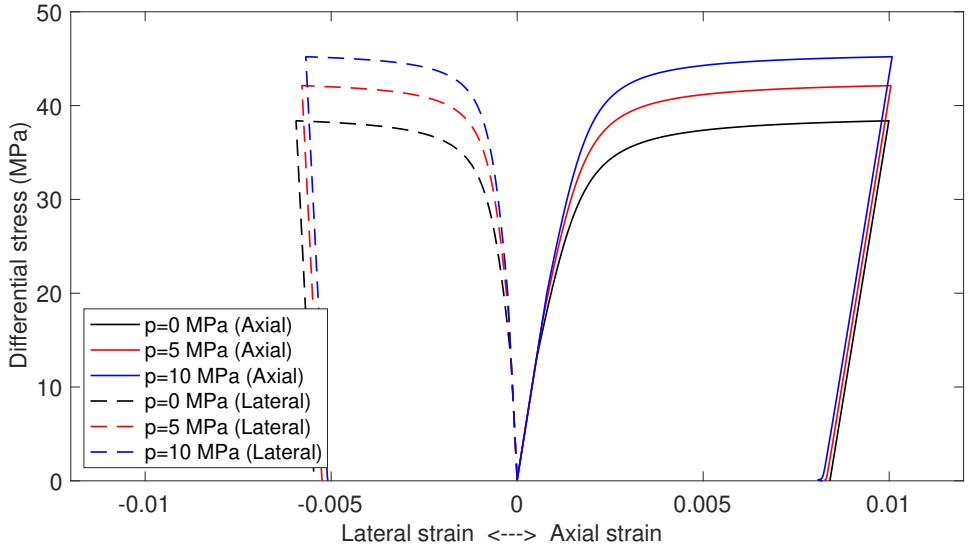

Figure 3.11: Influence of the confinement (stress-strain curve). p is the confinement.

in the sample. Elastic unloading is illustrated by A-B. For comparison, the response to the subsequent compressive loading (B-C-D) is compared the response of a sample that is not subjected to tension prior to the compression (O-C'-D'). As expected, the total accumulated damage obtained in the pre-damaged sample is larger than that in the undeformed sample, and this difference is due to the larger wing crack density developed in the pre-damaged sample. The strength of the pre-damaged sample is also lower than that of the undeformed sample, which is consistent with the observations made and the models proposed by Hoek and Bieniawski [137, 138].

During the uniaxial tension loading phase (O-A), both main cracks and wing cracks propagate in Mode I, predominantly in the loading direction (direction 3). Slight slipping is observed in the main cracks close to the horizontal direction. During the uniaxial unloading phase (A-B), cracks do not propagate. During the uniaxial compression phase (B-C), main cracks only propagate in Mode II. Main cracks are now longer than the initial main cracks of the undeformed sample. Based on Eq. 3.29, the toughness of the main cracks increases with the main crack radius. With the increase of compressive axial stress, main cracks propagate in both the undeformed and the pre-damaged sample, and at the end of

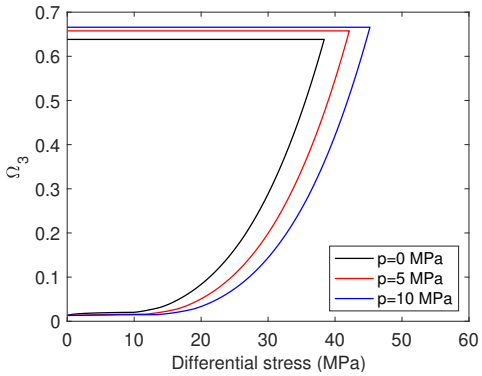

(a) Total damage

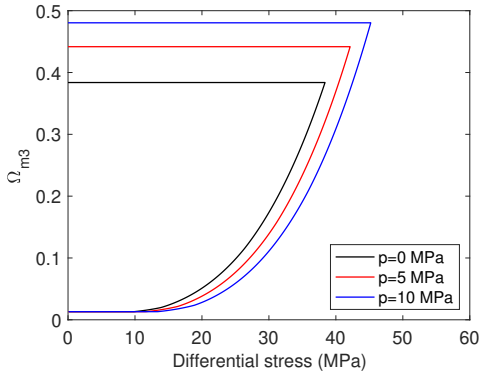

(b) Main crack damage

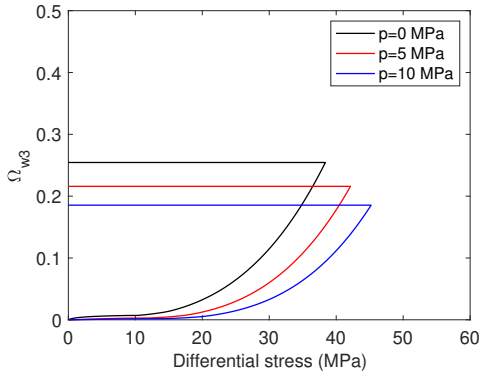

(c) Wing crack damage

Figure 3.12: Influence of the confinement (damage evolution). p is the confinement.

the test simulated, the average main crack length is the same in both samples. The difference between B-C and O-C' in Figure 3.14b is in fact due to the formation of Mode I main crack planes orthogonal to the loading axis during the tension loading phase (OA), applied to create "pre-damage". Very large compressive axial stress is needed to generate a tangential stress component large enough to trigger the slipping of the main crack planes that are nearly orthogonal to the loading direction 3. As a result, when compressive axial stress increases, O-C' gets closer to B-C in Figure 3.14b, but the damage of main cracks in pre-damaged sample is always larger than that in the undeformed sample. Since the development of wing cracks is controlled by the main cracks, the propagation of wing cracks is delayed whenever main crack propagation is delayed. During the tensile loading phase, some main cracks slip in planes that contain the loading axis and tensile wing cracks ini-

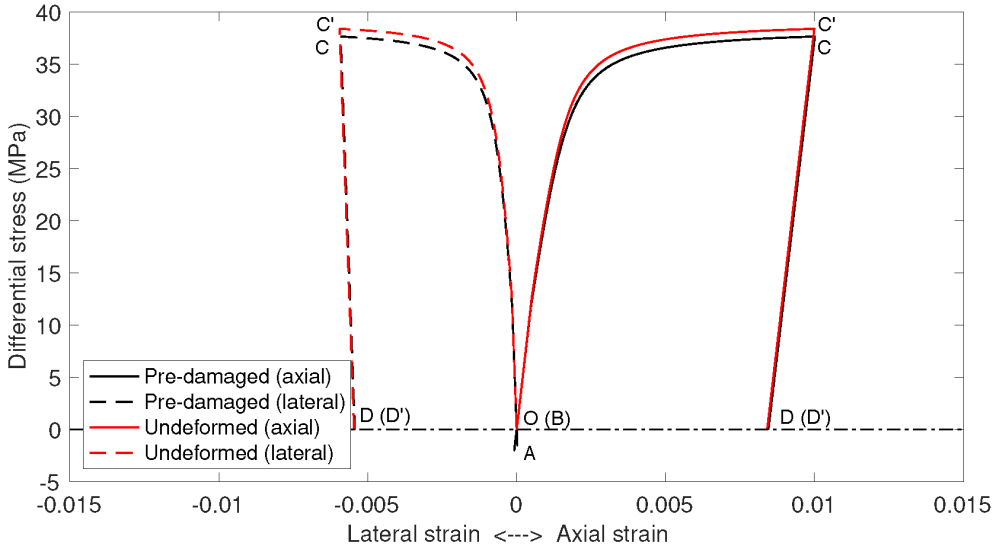

Figure 3.13: stress-strain curve - pre-damaged vs. undeformed salt rock.

tiate and propagate in planes orthogonal to the loading axis. As a result, the pre-damaged sample contains wing cracks and the cumulated damage due to wing cracks remains higher in the pre-damaged sample than in the undeformed sample (see Figure 3.14c).

3.5 Summary

Cyclic axial loading tests were performed under a confining pressure of 1 MPa on synthetic salt rock generated by thermal consolidation. The stress-strain curves and the microstructure images taken at key stages of the cycles revealed the formation of a complex system of sliding and wing micro-cracks, the orientation of which was loading dependent. We formulated a discrete wing crack elastoplastic damage (DWCPD) model to interpret the mechanisms that control the coupled evolution of crack families in salt rock under confined cyclic loading. The macroscopic stress-strain relationship is coupled to the evolution law of damage accumulated by main micro-cracks and associated wing cracks. Wing cracks propagate in Mode I due to slip on the main cracks. The expression of the REV Gibbs free energy is given as a function of the displacement jumps of the main cracks and of the wing cracks. A plastic potential, coupled to the damage induced by the micro-cracks, is intro-

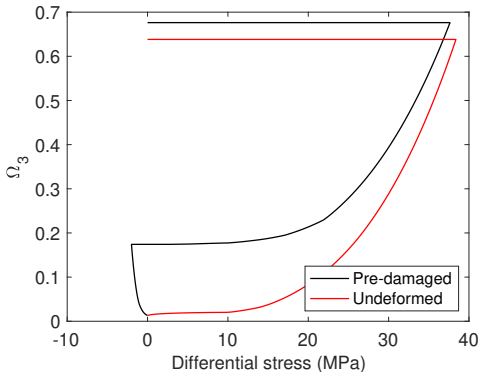

(a) Total damage

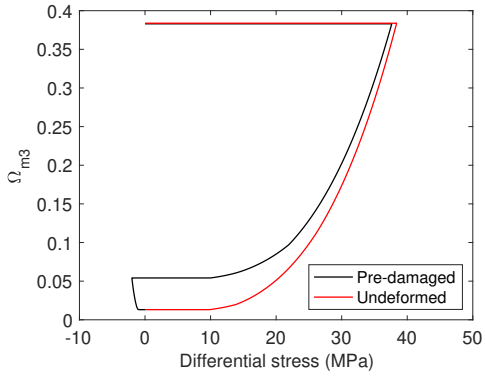

(b) Main crack damage

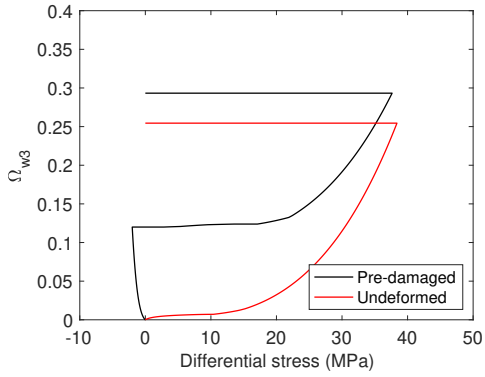

(c) Wing crack damage

Figure 3.14: Damage evolution - pre-damaged vs. undeformed salt rock.

duced to account for the development of irreversible strains. A frictional cohesive model is proposed for the main cracks, which propagate in both Mode I and Mode II. We calibrated the proposed model against the stress-strain curves of the cyclic loading-unloading cycles performed in the laboratory, and we showed that the DWCPD model can successfully capture stiffness degradation, strength reduction and irreversible strain accumulation.

Sensitivity analyses indicate that rock strength decreases when the friction coefficient or the cohesion of the main cracks' faces decreases, when the confining pressure decreases of when the specimen contains cracks prior to loading. Larger inelastic deformation is observed for lower friction or lower confinement. Larger cohesion postpones the initiation of damage. In the example case treated in this study, initial cracks did not seem to influence the final irreversible strains accumulated, because the initial cracks developed in tension

closed under the compression loading phase. Damage accumulated faster in samples that were damaged prior to compression than in the ones that were not.

Interestingly, simulations showed that micro-cracks occur following two stages: (i) Wing cracks initiate and main cracks do not propagate; (ii) Wing cracks and main cracks then propagate simultaneously. Higher friction at the crack faces leads to higher strength and larger lateral dilation. That is why at higher confinement, the initiation of wing cracks was delayed, which resulted in an increase of strength. Another important outcome of this study is the demonstration that salt rock develops damage-induced anisotropy. This is an important finding, because the majority of the constitutive models of salt rock used in geotechnical engineering and in the mining industry assume that micro-crack propagation and healing lead to isotropic stiffness changes. Furthermore, the proposed DWCPD model can be extended to any polycrystalline semi-brittle materials, and can be applied to understand the formation of crack patterns in salt geostorage facilities.

CHAPTER 4

RATE-DEPENDENT CYCLIC MODEL OF SALT ROCK

Loading rate is a significant factor of the mechanical behavior of salt rock [139, 140, 141]. The dependence of salt rock behavior to the loading rate during cyclic loading is usually induced by diffusion. Diffusion can happen within the lattice of crystals, e.g. Nabarro-Herring creep, or along the grain boundaries, e.g. Coble creep [142, 143]. The presence of inter-granular brine enhances pressure solution and accelerates creep and deformation rates [144, 145, 146, 147, 148]. Pressure solution occurs commonly in crystalline media: dissolution occurs at the grain-to-grain contacts that are under high stress, ions are transported by diffusion in fluid films at grain boundaries, and re-precipitate at grain-to-grain contacts that are under low stress. In wet halite (salt rock), pressure solution is the dominating creep mechanism for temperatures below 350 °C, as shown in Fig. 4.1.

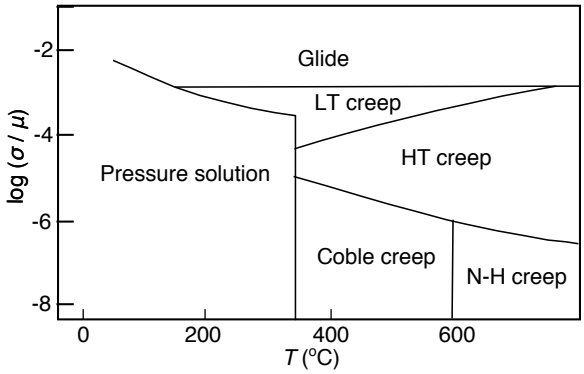

Figure 4.1: Deformation map of damp halite. LT, low temperature; HT, high temperature; N-H, Nabarro-Hering. Adapted from [149]

Diffusion along the grain boundaries leads to local shear displacements at grain contracts, which results in the global deformation of salt rock. The mechanical behavior of diverse and realistic microstructures can be predicted by homogenization, i.e. by upscaling crystal-, bounday- or grain- scale mechanisms to the scale of a Representative Elementary

Volume (REV). In this chapter, a Mori-tanaka homogenization scheme is proposed to simulate the rate-dependent behavior of salt rock during cyclic compression tests conducted at Texas A&M University by our collaborators Drs. Jihui Ding, Fred Chester and Judi Chester. After calibration, sensitivity analyses are presented to evaluate the effects of local diffusion at grain contacts on the macroscopic deformation of salt rock.

List of Symbols

a	Radius of inclusions
$\mathbf{A}_i$	Concentration tensor of the component i
$\mathbf{A}_i^o$	Concentration tensor of the matrix component
α	Angle between the plane of sliding crack and its subsurfaces
b	Length of the subsurface of sliding cracks
β	Volume fraction parameter
c	Thickness of sliding cracks
C	Concentration of minerals (ions) in the fluid
C_o	Reference concentration
C_K, C_G	Parameters for bulk and shear moduli degradation
$\mathbf{C}_{hom}$	Homogenized stiffness of the REV
$\mathbf{C}_i$	Stiffness of the component i
$\mathbf{C}_o$	Stiffness of matrix
γ_c	Shear strain of the inclusion
$\mathbf{D}_{ij}$	Influence tensor
d	Width of the subsurface of sliding cracks
d_c	Tangential displacement at the crack plane
D	Grain boundary diffusion coefficient
δ_{ij}	Kronecker delta
ϵ_i	Local total strain of component i
ϵ_m	Strain field in the matrix

ϵ_v	Volumetric strain of the REV
$\bar{\epsilon}$	Strain of the REV
ϕ_a	Volume fraction of component i
G	Shear modulus
η	Eigenstrain of inclusions
$\mathbf{I}$	Fourth-order identity tensor
J	Diffusion flux along subsurface
K	Bulk modulus
n	Number of components in the REV
N_s	Number sliding cracks counted in the microscopic images
N_b	Number of boundary sections counted in the microscopic images
$\mathbf{n}$	The normal direction of crack plane
θ	Orientation of the sliding crack plane from the horizontal
Q	Number of moles of weathered biotite in the REV
R	Gas constant
S	Thickness of the brine film at the crack surface
σ_i	Local total stress of component i
σ_n	Normal stress applied on the subsurface of sliding cracks
$\bar{\sigma}$	Stress of the REV
$\mathbf{t}$	The tangential direction of crack plane
t	Chemical reaction time
T	Kelvin temperature
ϕ_c	Volume fraction of all the spherical inclusions
φ	Density of sliding cracks
V_d	Dissolution rate at the subsurface
ψ	Angle of revolution of the crack planes around the loading axis
Ω	Molar volume of NaCl

4.1 Observations made during cyclic compression tests

Figure 4.2 below shows the stress/strain response of the consolidated salt rock specimens studied in Chapter 3 during cyclic compression tests conducted at a confining pressure of 1 MPa. The specimens were subjected to seven loading cycles with a maximum axial stress of 75 MPa. These seven loading cycles are named "large loading cycles" in the following.

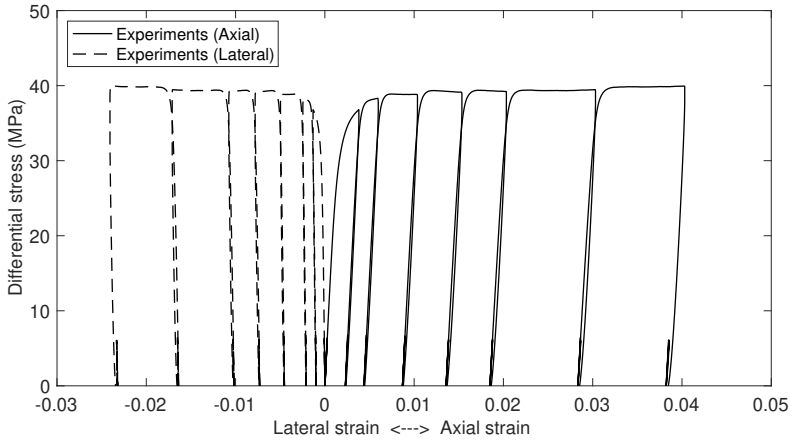

Figure 4.2: Stress-strain curve obtained during cyclic compression tests under a 1 MPa confining pressure. Experimental protocol described in Chapter 3.

Between two large loading cycles, the specimens were systematically subjected to three loading cycles with a maximum axial stress of 6 MPa only. These intermediate cycles (not shown in Figure 4.2) are named "small loading cycles" in the following. For each sequence of three small loading cycles, the first small loading cycle (C1) was applied at a rate of 3 $\times$ 10^{-5} /s, the second small loading cycle (C2) was applied at a rate of 3 $\times$ 10^{-6} /s, and the third small loading cycle (C3) as applied at a rate of 3 $\times$ 10^{-7} /s. The time period between C1 and C2 was 147 seconds, and the time period between C2 and C3 was 538 seconds. Since the maximum axial stress in the small loading cycles was much lower than the yield stress of salt rock (see Figure 4.2), we considered that cracks did not propagate during the small loading cycles, and therefore, that damage accumulated during the large

loading cycles.

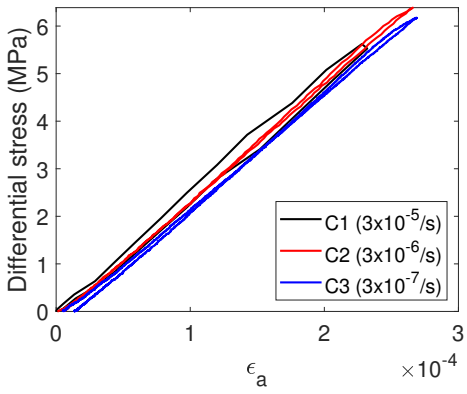

(a) C1-C3 axial stress/strain curve. Permanent axial strain $\epsilon_a = 0\%$

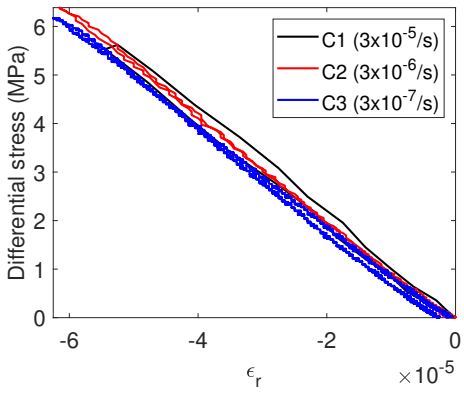

(b) C1-C3 radial stress/strain curve. Permanent axial strain $\epsilon_a = 0\%$

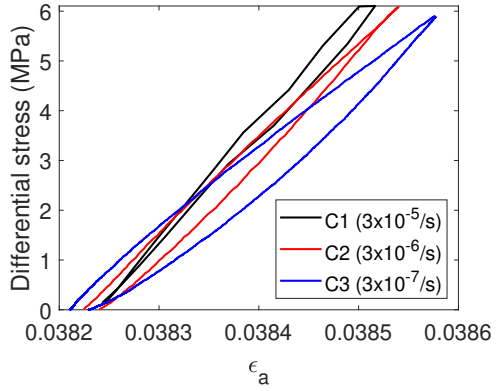

(c) C1-C3 axial stress/strain curve. Permanent axial strain $\epsilon_a = 3.8\%$

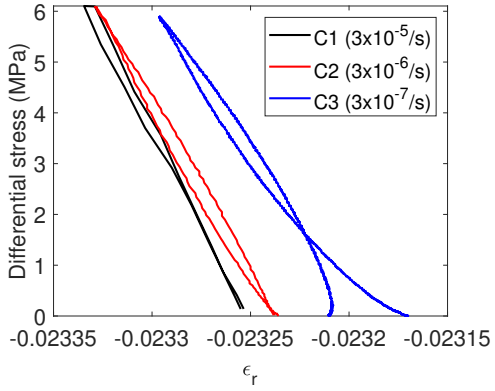

(d) C1-C3 radial stress/strain curve. Permanent axial strain $\epsilon_a = 3.8\%$

Figure 4.3: Plots of differential stress versus axial and radial strain for the first and last small loading cycles. ϵ_a is the axial strain. ϵ_r is the radius strain

During the first set of small loading cycles, the stress/strain curves of C1, C2 and C3 exhibits the same linear elastic behavior (see Figure 4.3.a and Figure 4.3.b). The loading rate does not affect the stiffness and hysteresis properties of the specimens. By contrast, the stress/strain curves obtained during the set of small cycles that followed the last large loading cycle, after a permanent axial strain of 3.8% has been reached, exhibits stiffness degradation and hysteresis (see Figure 4.3.c and Figure 4.3.d). Stiffness degradation and hysteresis are enhanced by low loading rate (i.e. stiffness degradation and hysteresis are

more pronounced during C3 than C2, and more so in C2 than C1).

According to microscopy images taken after each large loading cycles (see Figure 4.4), isolated brine pockets are noted along the grain boundaries at the beginning of the cyclic compression test. After a few cycles, these brine pockets tend to connect because of grain-to-grain sliding. A thin film forms at grain contacts. We hypothesize that this brine film facilitates diffusion along grain boundaries and enhances pressure solution at the grain contacts. In the following, we propose a micro-macro model to test this assumption. We simulate the behavior of salt rock during the small loading cycles and we check that the model can be used to predict the rate dependence of the REV response.

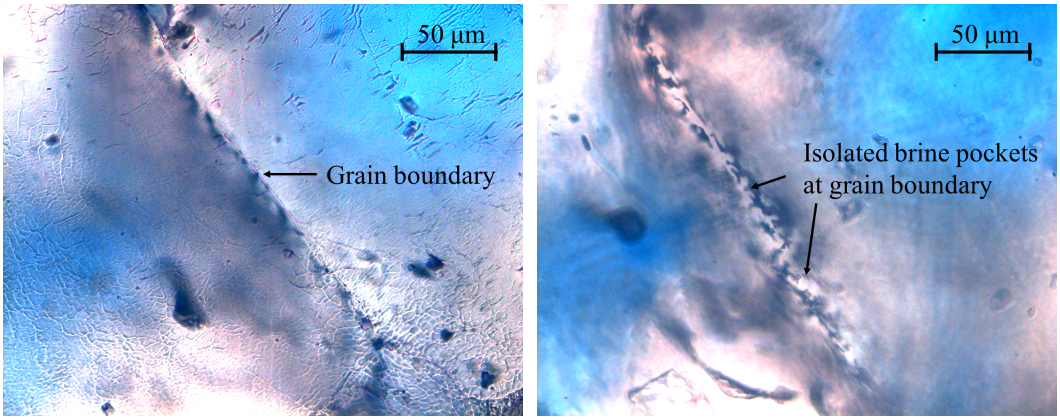

(a) Grain boundary (b) Fluid inclusions

Figure 4.4: Isolated brine pockets along grain boundaries in undeformed consolidated sample (5% porosity) [150].

4.2 Micro-mechancial model of grain boundary sliding driven by pressure solution

4.2.1 Conceptual model

From the observations made in Section 4.1, we assume that the rate-dependent behavior of salt rock is governed by pressure solution on grain boundaries. When subjected to normal stress, salt crystals dissolve at contacts with large contact normal stress. Ions diffuse along fluid films at crystals' boundaries and precipitate at the contacts with less contact stress. Dissolution, diffusion and precipitation happen simultaneously (but at different locations).

Pressure solution thus happens due to the presence of brine films at grain boundaries that are in contact, i.e., brine films contained in sliding cracks. We represent that REV as a solid salt matrix that contains sliding cracks. We model the crack inclusions as spherical volumes that each contain a sliding crack plane. Within one inclusion, the sliding plane is characterized by its orientation in reference to the horizontal (angle θ), so that the REV is viewed as a distribution of oriented spheres embedded in a solid matrix. Additionally, we consider that the sliding planes are rough. Each plane is smooth in two sub-faces with normal direction $\boldsymbol{n}_a$ and $\boldsymbol{n}_b$. In the plane formed by the normal to the plane direction ($\boldsymbol{n}_o$, at an angle 90^o + θ from the horizontal) and the tangential direction $\boldsymbol{t}_o$, the plane can be represented by broken lines. Figure 4.5 provides a visual representation of the REV. The angle formed by two broken lines, ($\boldsymbol{t}_a$ ($\boldsymbol{t}_b$) and $\boldsymbol{t}_o$), in the plane is noted α; it is an indicator of the roughness of the sliding plane. The length of a sliding segment within the sliding plane is noted b, as shown in Figure 4.5. The thickness of the film is noted c. Since the sliding crack plane is embedded in a spherical inclusion, it has a circular shape. We note a its diameter.

The mechanism of pressure solution is explained in Figure 4.6 at the scale of one inclusion. σ_n^1 and σ_n^2 are the projections of the spherical inclusion stress on two segments of the sliding plane. Without loss of generality, we assume $\sigma_n^1 > \sigma_n^2$. The larger normal compressive stress induces a higher chemical potential at crack surface n_1. Mineral dissolves first at the contact surface n_1, diffuses along n_1, and finally precipitates on surface n_2, where the chemical potential is lower. This process happens simultaneously on all the segments n_1 and n_2 of the sliding crack. As a result, the initial crack surface (represented by a red solid line in Figure 4.6) is transformed into another crack surface (represented with an orange dash line). The relation between the two crack surfaces is a translation, which explains the occurrence of shear displacement along the crack plane.

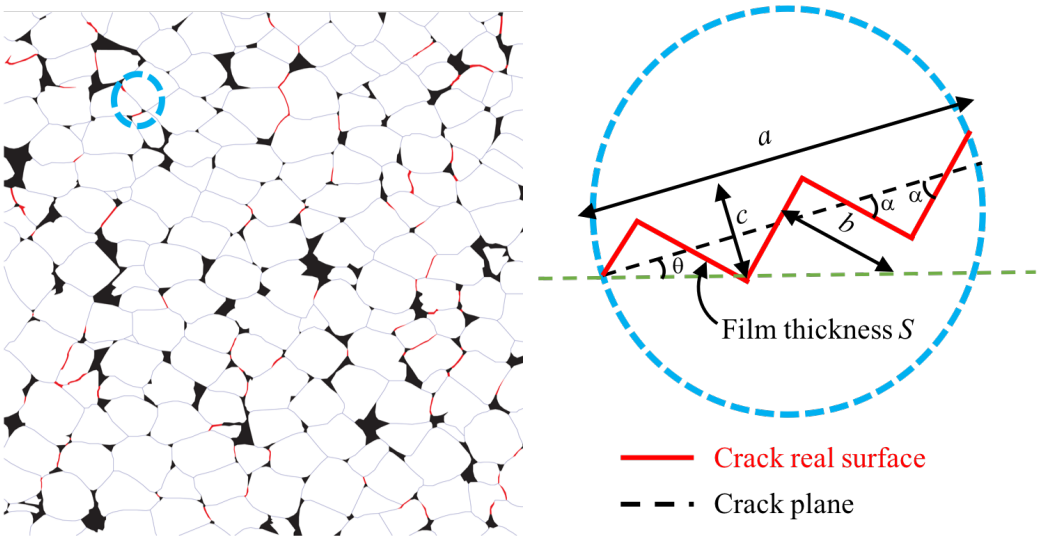

(a) REV of salt rock (b) Spherical inclusion with sliding crack plane

Figure 4.5: The concept of REV in the proposed rate-dependent model of salt rock.

4.2.2 Thermodynamic model

A difference of normal stress at grain contacts triggers an increase of chemical potential μ as follows:

$$\Delta\mu = \Delta\sigma\Omega \tag{4.1}$$

where Ω is the molar volume, and $\Delta\sigma$ is the difference of contact normal stress on the crack surface. The chemical potential μ controls the local concentration of brine; larger chemical potentials lead to higher mineral concentrations, according to the following relation:

$$\mu = RT \ln \frac{C}{C_o} \tag{4.2}$$

where R is the gas constant, T is the Kelvin temperature, C is the concentration of minerals (ions) in the fluid, and C_o is a reference concentration, taken equal to 6.48×10^{-6} mol/mm^3 for salt, following [151]. Differentiating Equation 4.2 with respect to C yields:

$$\frac{\partial\mu}{\partial C} = \frac{RT}{C} \tag{4.3}$$

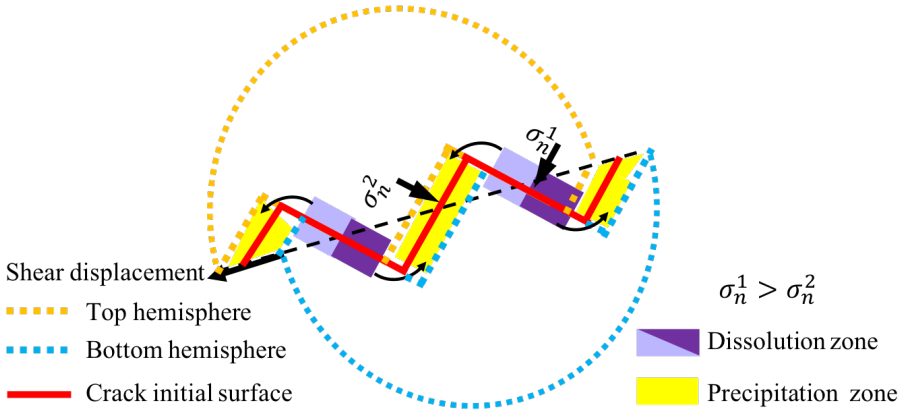

Figure 4.6: Mechanism of shear displacement along a sliding plane filled with brine in a spherical inclusion

According to Fick's first law, the diffusion flux $J(r)$ along a diffusion path at a location r is expressed as follows:

$$J(r) = -D\frac{\partial C}{\partial r} \tag{4.4}$$

where D is the grain boundary diffusion coefficient. With the assumption that $C(r)$ can be taken as a constant C_o [145, 152, 151], Equation 4.3 is substituted into Equation 4.4, which yields:

$$J(r) == -D\frac{\partial C}{\partial \mu}\frac{\partial \mu}{\partial r} = -D\frac{C_o}{RT}\frac{\partial \mu}{\partial r} \tag{4.5}$$

Based on the mass conservation principle, the mass of mineral dissolved at grain contacts is equal to the mass of mineral that diffuses along the crack plane, which can be written as:

$$2dSJ(r) + \frac{2rdV_d}{\Omega} = 0 \tag{4.6}$$

where d is the width of the crack plane, S is the thickness of the brine film at the crack surface, and V_d is the dissolution rate of mineral at the crack surface. Substituting Equation 4.4 and Equation 4.1 into Equation 4.6, we have:

$$\frac{\partial \sigma}{\partial r} = \frac{RTrV_d}{DC_o\Omega^2 S} \tag{4.7}$$

Integrating Equation 4.7 along the diffusion path, the dissolution rate V_d is expressed as:

$$V_d = \frac{8DC_o\Omega^2 S\Delta\sigma}{RTb^2} \tag{4.8}$$

According to the geometry of the cracks shown in Figure 4.5b, the tangential displacement d_c at the crack plane can be determined by the dissolution rate at the crack plane, as follows:

$$d_c = 2V_d t\cos\alpha \tag{4.9}$$

With the assumption of small deformation in inclusions, the shear strain of the inclusion, noted γ_c, is induced by the tangential displacement at the crack plane, and can be expressed:

$$\gamma_c = \frac{2V_d t\cos\alpha}{a} \tag{4.10}$$

where t is the chemical reaction time.

Substituting Equation 4.8 into Equation 4.10 and using the geometric relationship $c = b\sin\alpha$, γ_c is expressed as:

$$\gamma_c = \frac{16C_o\Omega^2}{RT}\frac{DS\cos\alpha\sin^2\alpha\Delta\sigma}{ac^2}t \tag{4.11}$$

In this study, the product of the diffusion coefficient D by the thickness of the brine film S is taken as 2×10^{-10} m^2/s, following [151, 153].

4.3 Homogenization scheme: from sliding cracks to rate-dependent REV behavior

In this section, we formulate a 3D homogenization scheme to account for the influence of shear strain in sliding components on the global deformation of salt rock at the REV scale. For this, we adopt a Mori-Tanaka homogenization scheme [97], in which the stiffness tensor of the REV is deduced from a set of equations that relate the stress and strain fields at the REV scale to those defined in the inclusions and in the surrounding matrix. In the Mori-

Tanaka scheme, the deformation of the homogeneous matrix is not considered equal to that of the REV like in a dilute scheme. The mechanical interactions between the components is accounted for via the matrix. The homogenization scheme is based on Eshelby's theory, which proves that the state of stress in each ellipsoidal inclusion is uniform [91]. In our application of the Mori-Tanaka homogenization scheme, each inclusion is a sphere that contains a sliding plane, and is embedded in a solid matrix that is subjected to boundary conditions that are equivalent to the far field conditions imposed on the infinite medium that the inclusion is embedded in.

The stress and strain fields and the material properties are thus considered uniform in each inclusion. We gather inclusions into families, within which inclusions all have the same sliding plane orientation, and the same sliding plane geometry (c and α). Inclusions of the same family have the same local stress and strain fields. For the i^{th} inclusion family, the local stress σ_i is expressed as a function of the local strain ϵ_i and of the local eigenstrain η_i (i.e. the strain field that would exist in the inclusion in the absence of matrix and inclusions around it). In our study, η_i is induced by the shear displacement along the sliding planes in the inclusions. The in-plane shear component of the second order tensor η_i is equal to the chemical shear strain γ_c. The microscopic stress can be expressed as [154]:

$$\sigma_i = \mathbf{C}_i : \epsilon_i - \mathbf{C}_i : \eta_i \tag{4.12}$$

where $\mathbf{C}_i$ is the fourth-order stiffness tensor for the i^{th} inclusion family, and σ_i, ϵ_i, and η_i are all second-order tensors.

Due to strain compatibility and stress admissibility, the macroscopic strain $\bar{\epsilon}$ (respectively, the macroscopic stress $\bar{\sigma}$) is the volume average of the local strains ϵ_i (respectively, the volume average of the local stresses σ_i) in all inclusions over the REV. The homogenized stiffness $\mathbf{C}_{hom}$ of the REV is the volume average of the local stiffnesses, weigheted

by the inclusion-specific concentration tensor $\mathbf{A}_i$:

$$\mathbf{C}_{hom} = \sum_{i=1}^{n} \phi_i \mathbf{C}_i : \mathbf{A}_i \tag{4.13}$$

where n is the number of inclusion families, plus one (for the matrix) in the REV and ϕ_i is the volume fraction of inclusion family i.

The concentration tensor $\mathbf{A}_i$ is an operator that relates the local strain tensor in the i^{th} inclusion family to the REV strains. Based on Eshelby's theory, the state of stress in each sliding component is assumed uniform and the concentration tensor $\mathbf{A}_i$ can be calculated as follows [107]:

$$\mathbf{A}_i = \mathbf{A}_i^o : \left(\sum_{j=1}^{n} \phi_i \mathbf{A}_i^o \right)^{-1} \tag{4.14}$$

in which $\mathbf{A}_i^o$ is the concentration tensor of the matrix:

$$\mathbf{A}_i^o = [\mathbf{I} + \mathbf{P}_i : (\mathbf{C}_i - \mathbf{C}_o)]^{-1} \tag{4.15}$$

In the Mori-Tanaka scheme, the stiffness of the infinite medium $\mathbf{C}_o$ is equal to the matrix stiffness. $\mathbf{P}_i$ is a fourth-order tensor specific to each inclusion family, its expression is given in [92].

According to Levin's theorem [155], the REV stress $\bar{\sigma}$ is expressed as a function of the REV strain $\bar{\epsilon}$ and of the eigenstrain of each component, as follows:

$$\bar{\sigma} = \mathbf{C}_{hom} : \bar{\epsilon} - \sum_{i=1}^{n} \phi_i \mathbf{C}_i : \eta_i : \mathbf{A}_i \tag{4.16}$$

On the right side of Equation 4.16, the first term ($\mathbf{C}_{hom} : \bar{\epsilon}$) is the linear elasticity relation for a homogeneous medium, while the second term describes how the REV stress is modified by the eigenstrain of each component in the REV.

The strain field in each phase (inclusion family and matrix) is related to the macroscopic

strain field and to the eigenstrains of that phase, as follows:

$$\epsilon_i = \mathbf{A}_i : \bar{\epsilon} + \sum_{j=1}^{n} \mathbf{D}_{ij}\eta_j \tag{4.17}$$

where $\mathbf{D}_{ij}$ is the influence tensor, which accounts for the influence of a phase's eigenstrain on other phases.

Substituting Eq.4.17 into Eq.4.12, using stress admissibility conditions and comparing with Eq. 4.16, the expression of $\mathbf{D}_{ij}$ is given by [154], as follows:

$$\mathbf{D}_{ij} = \Big\{ \delta_{ij}\mathbf{A}_i^o : \mathbf{P}_i - \phi_j \mathbf{A}_i : \mathbf{A}_j^o : \mathbf{P}_j + \left[\mathbf{A}_i : \overline{\mathbf{A}^o : \mathbf{P}} - \mathbf{A}_i^o : \mathbf{P}_i\right] : \left[\overline{(\mathbf{C}_{hom} - \mathbf{C}) : \mathbf{A}^o : \mathbf{P}}\right]^{-1} \\ : \phi_j \left[(\mathbf{I} - \mathbf{A}_j)^T + (\mathbf{C}_{hom} - \mathbf{C}_j) : \mathbf{A}_j^o : \mathbf{P}_j)\right] \Big\} : \mathbf{C}_j \tag{4.18}$$

where δ_{ij} is the Kronecker delta.

4.4 Model calibration

The proposed Mori-Tanaka homogenization model is now calibrated against the results obtained for the sets of small loading cycles with permanent strain 0% and 3.8%, as presented in Section 4.1. We used the density of sliding cracks φ and the distribution of the orientation of sliding cracks obtained by image analysis in Chapter 2, and we calibrated the mechanical properties of the inclusions.

The density of sliding cracks φ is determined as follows:

$$\varphi = \frac{N_s}{N_b} \tag{4.19}$$

where N_s is the number sliding cracks counted in the microscopic images, and N_b is the number of boundary sections counted in the microscopic images. We separate the boundary of a grain into several small boundary segments by the intersections with the boundaries of other grains, N_b is the sum of all the boundary segments. The density of sliding cracks φ

is then used to calculate the volume fraction of all the spherical inclusions, ϕ_c, as follows:

$$\phi_c = \varphi^{\beta} \tag{4.20}$$

where β is a parameter that needs to be calibrated. For simplicity, we assume that all inclusion orientations are represented with the same volume fraction ϕ_c/N_s.

The orientation angle of a crack plane obtained by image analysis in 2D is taken equal to the angle formed by the crack plane with the horizontal in 3D, i.e. θ in Figure 4.5. We assume that the angle of revolution of the crack planes around the loading axis (often noted ψ) is uniformly distributed in the REV. This hypothesis is supported by the fact that: (i) samples were fabricated by consolidating salt aggregates at high temperature, and where statistically identical to one another; (ii) loading conditions and the specimen shape were axis-symmetric. We first sorted the values of θ obtained by image analysis for all the sliding cracks. We divided the interval of variation of the angle θ into ten sub-intervals. In each sub-interval, the mean of θ was calculated. These ten averaged θ were then used to define a distribution of θ in the propose micro-macro model. Ten uniformly distributed values of ψ, ranging from 0^o to 360^o, were used to define the distribution of the revolution angles of the inclusions of the REV. As a result, 100 inclusion families were defined, each having a specific orientation defined by a couple of angles θ and ψ.

We introduce two parameters C_K and C_G to account for the stiffness degradation of the inclusions as a consequence of sliding. The bulk modulus K_i and the shear modulus G_i of the inclusions of family i are calculated as follows:

$$K_i = C_K K_m \tag{4.21}$$

$$G_i = C_G G_m \tag{4.22}$$

where K_m and G_m are bulk and shear moduli of the matrix, respectively.

In the small compression cycles done with a permanent axial strain equal to 0%, few sliding cracks are observed. The stiffness of the salt rock REV is controlled by the stiffness of the matrix. We thus calibrate the bulk and shear moduli of the matrix (K_m and G_m) against the results of the small cyclic compression cycles with a zero permanent strain. In the small compression cycles done with a permanent axial strain equal to 3.8%, very small chemical shear strain occurs in the first cycle C1, because the loading rate is high and the period of time of the loading is small. The deformation of salt rock in C1 is controlled by the modulus reduction parameters C_K and C_G, and the volume fraction of the inclusions, ϕ. ϕ is determined based on the exponent parameter β (Equation 4.20). The geometry of the crack planes and the volume fraction of the inclusion families influence the reduction of stiffness reduction and the development of hysteresis in the three cycles C1, C2, and C3. The parameters controlling the geometry of crack plane include the direction of subsurface α and the thickness of the crack plane, c. The calibrated parameters are listed in table 4.1, and simulations done at the material point with the calibrated model are shown in Figure 4.7 and Figure 4.8.

Table 4.1: Parameters of the rate-dependent micro-macro model of salt calibrated against the results of the small loading cycles at 0% and 3.8% permanent axial strain.

Mechanical properties					Crack geometry	
K_m	G_m	C_K	C_G	β	c	α
GPa	GPa	$-$	$-$	$-$	μm	^{o}
17.0	10.5	0.9	0.6	0.7	4.8	60

When the permanent axial strain ϵ_a is 0%, no sliding cracks develop. Brine is isolated in the inclusions, and there is no brine film on the grain boundary to facilitate the pressure solution process. The simulation results show that the stress/strain curves obtained for the small loading cycles C1, C2 and C3, conducted at different loading rates, are superimposed, which indicates that the effects of chemical reactions are negligible (Figure 4.7). In Figure

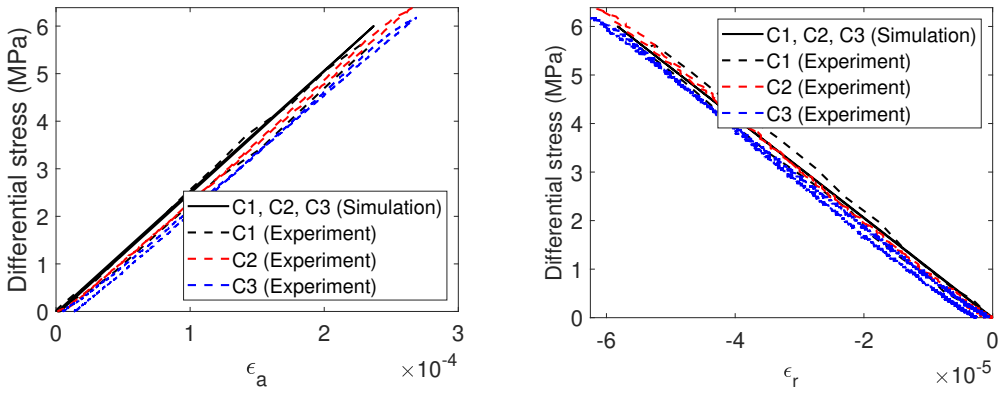

(a) Axial strain (b) Radial strain

Figure 4.7: Model calibration against the results of the small loading cycles at a permanent axial strain ϵ_a = 0%. Solid lines: simulation results. Dashed lines: experimental results.

4.8, we do not calibrate the deformation of salt rock during the intervals between each small loading cycles. In the simulation, each small loading cycle is moved to the corresponding small cycle in the tests. According to Figure 4.8, our model can well capture the stiffness reduction and hysteresis evolution of salt rock, which are observed in the tests.

Figure 4.9a presents the development of local normal contact stress on the segments n_1 and n_2 of a crack surface in one of the inclusion families, during the small loading cycles performed at a permanent axial strain of 3.8 %. Initially, during C1, the compressive normal stress on segment n_1 (σ_n^1) is much larger than the compressive normal stress on segment n_2 (σ_n^2). Then, the difference between σ_n^1 and σ_n^2 decreases. During the unloading phase of C2, σ_n^1 gets equal to σ_n^2 (intersection of the red dashed line and the red solid line in Figure 4.9a). Then, the chemical shear strain γ_c starts to decrease as shown in Figure 4.9b. The loading rate in C3 is 1/10 of the loading rate of C2, and the duration of C3 is 10 times that of C2. γ_c is 2.0 $\times$ 10^{-4} when $\Delta\epsilon_a$ reaches its maximum value in C3, which is only four times of γ_c when $\Delta\epsilon_a$ reaches its maximum in C2 (0.5 $\times$ 10^{-4}). This is because the chemical shear strain rate is controlled by the difference between σ_n^1 and σ_n^2. As a result, during the cyclic compression tests, the chemical strain decreases with the difference between σ_n^1 and σ_n^2.

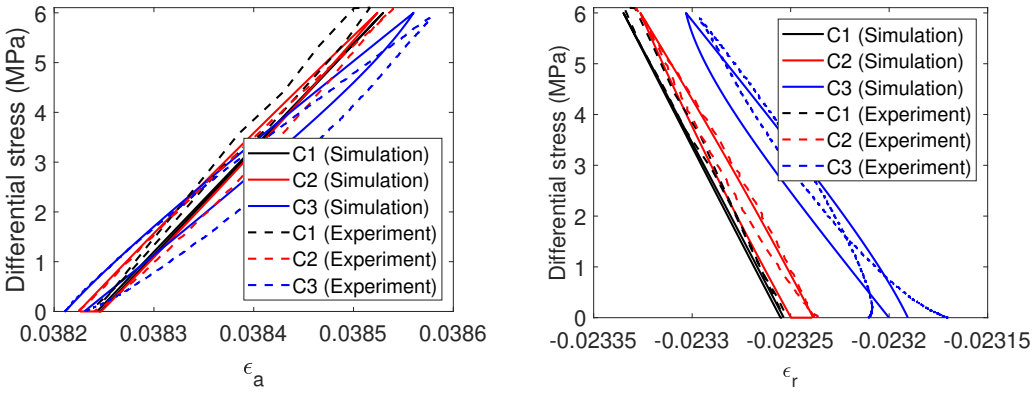

(a) Axial strain

(b) Radial strain

Figure 4.8: Model calibration against the results of the small loading cycles at a permanent axial strain ϵ_a = 3.8%. Solid lines: simulation results. Dashed lines: experimental results.

4.5 Sensitivity analysis

In this section, we investigate how sensitive the deformation of the REV is to the geometry of the crack plane (thickness of crack c and roughness angle α) and to the volume fraction of the inclusion families. The angle between the direction of the crack planes and the horizontal direction is set equal to 60^o. The loading rate is 3×10^{-6} /s. The mechanical properties calibrated above are adopted (see Table 4.1).

According to Figure 4.10, a thinner crack thickness results in larger chemical strain and larger deformation at REV scale, which is consistent with Equation 4.11. A thinner sliding crack provides a shorter diffusion path from the crack plane segment with large normal stress to the crack plane segment with small normal stress. More salt mineral is dissolved at the grain contacts, and the shear displacement increases. When c is larger than 8 μm, hysteresis increases when c decreases, because the dissolution rate is higher at the grain contacts. When c is very small (i.e. c = 2 μm), the stress of inclusions is redistributed very rapidly. As a result, chemical strain develops in the direction opposite to the sliding, and hysteresis reduces.

The influence of the roughness angle α is presented in Figure 4.11. REV deformation

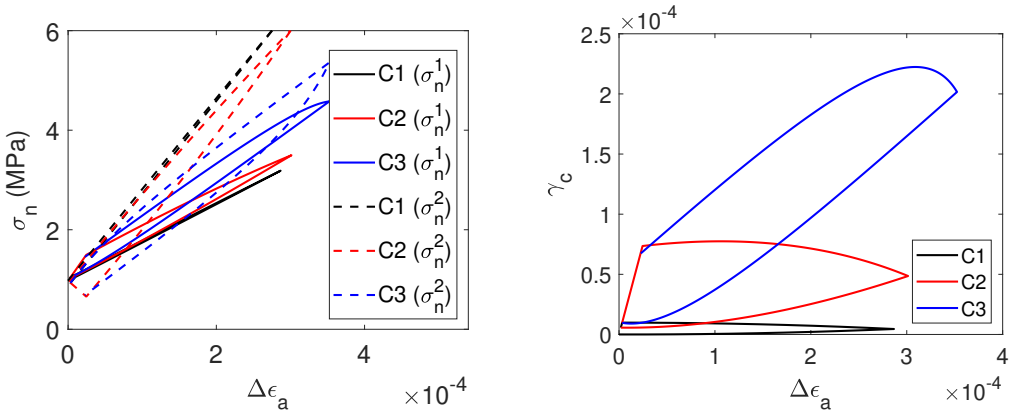

(a) Normal stress on crack segments

(b) Chemical strain

Figure 4.9: Local normal stress and chemical strain in a representative inclusion family. The orientation of crack plane is 25^o

and hysteresis increase with α. When α is larger than 45^o, the influence of α is not obvious. A larger roughness angle α decreases the diffusion path of salt ions, which enhances the shear strain of the inclusions. In addition, the roughness angle α also controls the difference in normal stress $\sigma_n^1 - \sigma_n^2$. When α is very small, the orientations of segments n_1 and segments n_2 are very close (Figure 4.5b). The difference of normal stress becomes negligible, so that the shear strain rate of the inclusion is very small.

Figure 4.12 shows the stress-strain relationship of salt rock with different volume fractions of inclusions. The volume fraction ϕ_c does not influence the local chemical shear strain rate in the inclusions. However, ϕ_c controls the effect of local strains on the macroscopic deformation of the REV, including the elastic strain (Equation 6.35) and the chemical strain induced by pressure solution (Equation 4.16). The larger the volume fraction ϕ_c, the larger the REV deformation and the larger the hysteresis.

4.6 Energy dissipation

The hysteresis and the residual strain observed in the tests indicate that energy is dissipated during the loading and unloading cycles. In this section, we analyze the energy dissipated by pressure solution at sliding crack faces for a loading rate is 3×10^{-6} /s. Figure 4.13a

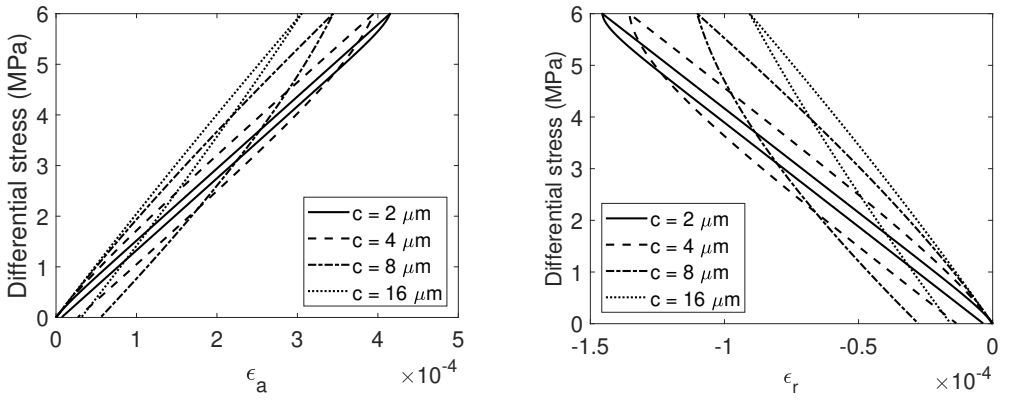

(a) Axial strain (b) Radius strain

Figure 4.10: Influence of crack thickness on stress/strain relationship. The total volume fraction of the inclusions, ϕ_c, is equal to 50%. The roughness angle α is set equal to 60^o.

presents the external work input to the salt rock REV for different sliding cracks thicknesses. The roughness angle α is set equal to 60^o, and the total volume fraction of the inclusions, ϕ_c, is equal to 50%. In each cycle, the specimen is unloaded after the maximum differential stress reaches 6 MPa. Therefore, the maximum external work ever provided to the REV can be calculated by multiplying the maximum axial strain by 6 MPa.

As can be seen from Figure4.13, a smaller crack thickness c is accompanied by a faster pressure solution process at the crack faces, which enhances the local chemical strain and the maximum strain. As a result, the smaller crack thickness c, the larger maximum external work at the REV scale. When c is large ($c >$15 μm), the rate of pressure solution is too small to influence the chemical strain and trigger any hysteresis. When c is small ($c <$ 2 μm), the pressure solution process is so fast that stress is redistributed quasi-instantaneously in the salt REV during the loading. The maximum strain of salt rock is not influenced by pressure solution. Little energy is dissipated during the loading cycle when c is large or small, because hysteresis is negligible.

Figure 4.14a shows the external work provided to the salt rock REV for different volume fractions of sliding inclusions. The roughness angle α was set equal to 60^o. The crack thickness c was set equal to 4.8 μm. Figure 4.14a shows that a higher volume frac-

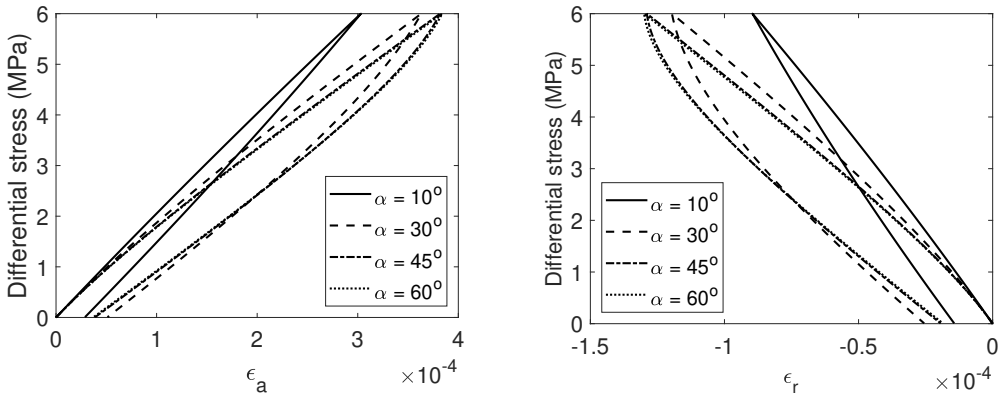

(a) Axial strain (b) Lateral strain

Figure 4.11: Influence of crack subsurface angle on stress/strain relationship. The total volume fraction of sliding inclusions, ϕ_c, is equal to 50%. The crack thickness c was set equal to 4.8 μm.

tion of sliding inclusions magnifies the effects of chemical strain in the inclusions, which facilitates the accumulation of chemical strain at the REV scale. As a result, the both maximum external work and dissipated energy increase with the volume fraction of the sliding inclusions.

To summarize, pressure solution can induce significant hysteresis, which may reduce the efficiency of geological storage facilities that are loaded cyclically, such as Compressed Air Energy Storage (CAES) caverns. From the analysis above, we conclude that CAES is most efficient in undamaged salt rock with only a few sliding cracks, or in salt rock where the pressure solution rate is large (small crack thickness c), or in salt rock where the pressure solution rate is very small (large crack thickness c).

4.7 Conclusions

In this chapter, a chemo-mechanical homogenization framework is proposed to capture the rate-dependent behavior of salt rock during cyclic compression loading. The shear displacement of sliding cracks is related to the mass of salt ions that diffuse along the crack surface. The rate of diffusion is governed by the equations of the pressure solution theory.

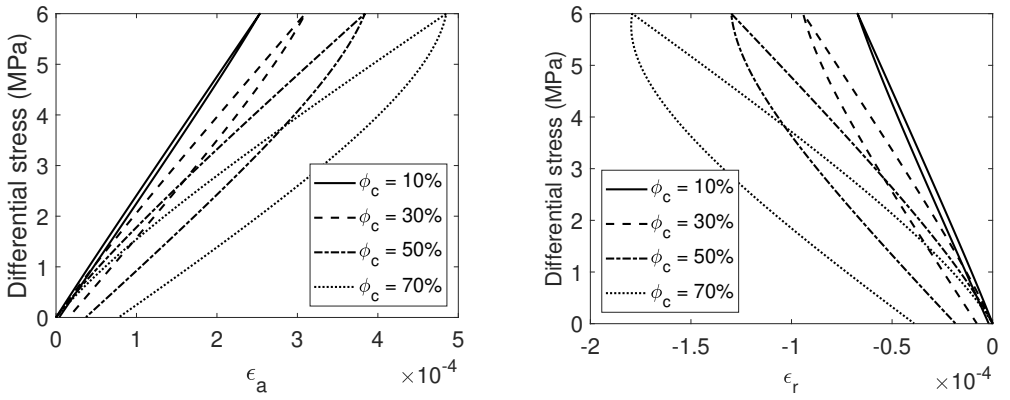

(a) Axial strain (b) Lateral strain

Figure 4.12: Influence of the volume fraction of inclusions on stress/strain relationship. The roughness angle α was set equal to 60^o. The crack thickness c was set equal to 4.8 μm.

The REV is viewed as a solid salt matrix than contains spherical inclusions, which each contain a sliding plane. The sliding plane is endowed with an orientation, a crack thickness and a roughness angle. The inclusions' shear deformation induced by pressure solution define the inclusions' chemical eigenstrain. The relationship between the inclusion-scale stresses and strains and REV scale stresses and strains is established by using Mori-Tanaka homogenization scheme.

This rate-dependent homogenization model is calibrated against cyclic compression tests conducted by our collaborators at Texas A&M University. It is noted that a lower loading rate and/or a larger number of sliding cracks enhances stiffness reduction and hysteresis. Sensitivity analyses show that thinner sliding planes (i.e. thinner brine films) enhances stiffness reduction and accelerate stress redistributions in the inclusions. Higher roughness angles lead to an increased difference of normal stress on the different segments of the crack plane and to a reduced diffusion path, which both lead to enhanced stiffness reduction and enhanced hysteresis. The larger the volume fraction of the inclusions, the larger the REV deformation and the larger the hysteresis) this is because a higher number of sliding cracks amplifies the effects of the local shear strains driven by pressure solution.

The proposed model is the first model that explains the rate dependent behavior of salt.

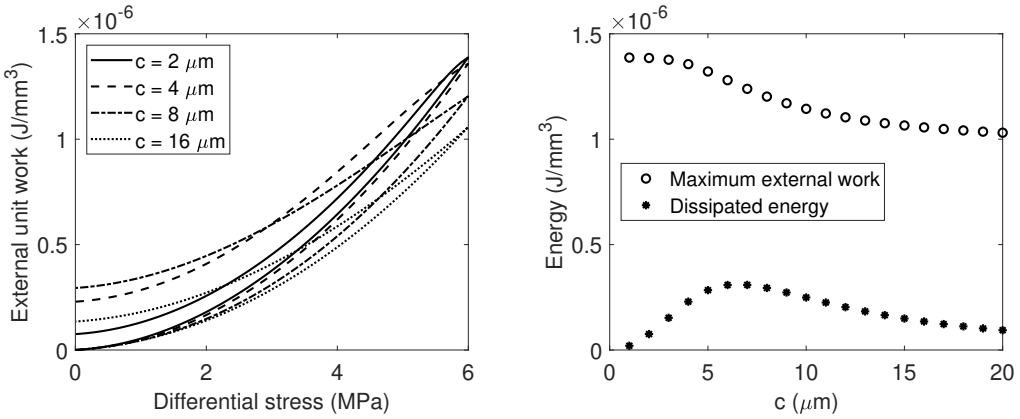

(a) External work (b) Energy dissipation

Figure 4.13: Influence of inclusions' crack thickness on energy dissipation. The roughness angle α is set equal to 60^o. The total volume fraction of the inclusions, ϕ_c, is equal to 50%.

This study sheds light on the design of the geological storage under cyclic unloading, and helps to improve the energy efficiency.

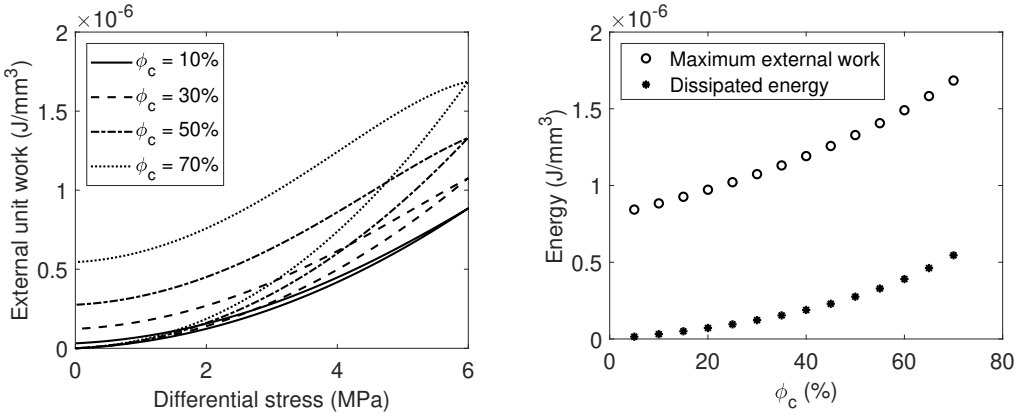

(a) External work

(b) Energy dissipation

Figure 4.14: Influence of the volume fraction of the inclusions on energy dissipation. The roughness angle α was set equal to 60^o. The crack thickness c was set equal to 4.8 μm.

Part II

Micro-Macro Chemo-Mechanical Damage

Bedrock weakening is of wide interest because it influences landscape evolution, chemical weathering, and subsurface hydrology. A longstanding hypothesis states that bedrock weakening is driven by chemical weathering of minerals like biotite, which expand as they weather and create stresses sufficient to fracture rock. In Chapter 5, we build on recent advances in rock damage mechanics to develop a model for the influence of biotite weathering on bedrock damage, which can be thought of as the concentration of micro-cracks in bedrock. We use this model to explore how the abundance, aspect ratio, and orientation affect the time-dependent evolution of damage during biotite weathering. Our simulations suggest that biotite abundance and aspect ratio of biotite have a profound effect on the evolution of bedrock damage during biotite weathering. These characteristics exert particularly strong influences on the timing of the onset of damage, which occurs earlier under higher biotite abundances and smaller biotite aspect ratios. Biotite orientation, by contrast, exerts a relatively weak influence on damage. Our simulations further show that damage development is strongly influenced by the boundary conditions, with damage initiating earlier under laterally confined boundaries than under unconfined boundaries. These simulations suggest that relatively minor differences in biotite populations can drive significant differences in the progression of rock weakening. In this study, we collaborate with Ken L. Ferrier at University of Wisconsin Madison, Nicole West at Central Michigan University, and Dai Sheng Georgia Institute of Technology, and the work is accepted for publication at the Journal of Geophysical Research - Earth Surface with the title ”Mineral weathering and bedrock weakening: Modeling microscale bedrock damage under biotite weathering”.

CHAPTER 5

MICRO-MACRO MODEL OF GRANITE BEDROCK WEAKENING BY BIOTITE WEATHERING

Many weathering profiles contain a layer of fractured, chemically weathered material between bedrock and soil that retains much of the character of the parent bedrock. This layer is variously referred to as saprolite, saprock, or weathered rock (e.g., [156, 157]), and for simplicity in this study we refer to it as saprolite. Understanding the controls on this layer is of wide interest because of its role in landscape evolution (e.g., [158]), nutrient supply (e.g., [159]), landslide hazards (e.g., [160]), and the global carbon cycle [161, 162].

A leading hypothesis posits that saprolite production is dominantly controlled by chemical weathering of Fe-bearing minerals, which expand as they weather and create stresses sufficient to strain and weaken rock under certain mineralogical conditions. Previous studies have investigated this hypothesis using models to compute fracture size from the strain energy generated by mineral expansion, which provide an important constraint on the net change in fracture size after weathering [163, 164, 165, 166, 167, 168, 169]. To date, however, no model has been developed for the transient weakening of bedrock under a continually evolving mineral chemical weathering field, which limits our ability to understand the coevolution of chemical weathering and bedrock weakening.

In the past few years, advances in rock damage theory have improved our understanding of the damage done by mineral chemical weathering. At the same time, advances in numerical modeling have improved the implementation of chemo-mechanical damage processes in coupled thermodynamic models. For example, recently developed hydro-chemo-mechanical models have been used to predict damage in sandstones [170] and rock pillars [171]. Similarly, new thermodynamic models have successfully captured the dissolution of iron-bearing minerals to study the mechanical stability of abandoned mines [172, 173].

An analogous model was applied to explain the reduction of fracture aperture in granites subject to hydrothermal dissolution and precipitation [174]. Subcritical cracking, the primary bond-breaking process for the near surface rock [175], and brittle creep models have been successfully used to predict delayed failure in a variety of lithologies [176, 177, 178] and to simulate borehole spalling and breakout [179]. So far, however, no model accounts for both the effects of chemical reactions on rock stiffness and strength and the effects of fracturing on chemical weathering. The model proposed here provides a first step toward overcoming this limitation.

List of Symbols

a	Long axes of the spheroidal mineral inclusions
$\mathbf{A}_i$	Concentration tensor of the component i
$\mathbf{A}_i^o$	Concentration tensor of the matrix component
α	Damage constitutive parameters
β	Damage constitutive parameters
c	Short axes of the spheroidal mineral inclusions
$\mathbf{C}_{hom}$	Homogenized stiffness of the REV
$\mathbf{C}_i$	Stiffness of the component i
$\mathbf{C}_o$	Stiffness of matrix
$\mathbf{D}_{ij}$	Influence tensor
δ_{ij}	Kronecker delta
ϵ_a	Total strain of inclusions in the direction of long axes
ϵ_c	Total strain of inclusions in the direction of short axes
ϵ_i	Local total strain of component i
ϵ_m	Strain field in the matrix
ϵ_{cc}	Chemical strain of inclusions in the direction of short axes
ϵ_i^c	Local chemical strain of component i
ϵ_v	Volumetric strain of the REV

$\bar{\epsilon}$	Strain of the REV
f_d	Damage criterion
ϕ_a	Volume fraction of component i
g	Gravitational acceleration
h	Depth of the bedrock
$\mathbf{I}$	Fourth-order identity tensor
k_0	Damage initiation threshold
k_1	Damage hardening parameter
K	Ratio between the horizontal and vertical stresses on the bedrock
λ	Lamé constants of the non-damaged matrix
μ	Lamé constants of the non-damaged matrix
n	Number of components in the REV
ν_m	Molar volume of weathered biotite
θ	Orientation of long axis from the horizontal
Q	Number of moles of weathered biotite in the REV
R	Weathering rate of biotite per unit mineral surface area
ρ	Density of bedrock
S	Total biotite surface area within the REV
σ_i	Local total stress of component i
σ_h	Lateral boundary stress applied on the bedrock
σ_v	Vertical stress applied on the bedrock
$\bar{\sigma}$	Stress of the REV
t	Weathering time
t_{tag}	Time until damage initiation
η_i	Chemical weathering strain of component i
$V_{mineral}$	Volume of unweathered mineral
$V^w_{mineral}$	Volume of weathered mineral

V_b	Volume of unweathered biotite
$V_{b,initial}$	Initial volume of biotite
V_b^w	Volume of weathered biotite
Y_d	Damage driving force
Ψ_s	Helmholtz free energy of the REV
Ω	Damage variable

5.1 A chemo-mechanical model of bedrock strain and damage at the REV scale

In the following, we formulate a model for the influence of biotite weathering on strain and damage in a bedrock REV, which is ∼100-1,000 times larger than the modeled biotites by length. We represent the bedrock as a two-phase material consisting of ellipsoidal biotite inclusions embedded in a homogeneous matrix. As we describe below, this representation is useful because it permits calculation of the evolving deformation and damage fields within the REV. The model consists of two sub-models: one for biotite deformation at the crystal scale (Section 5.1.2, which depends on a parameterization for biotite weathering rate in Section 5.1.1), and a Continuum Damage Mechanics (CDM) model for the evolution of damage and stiffness of the matrix (Section 5.1.3). Both models are coupled within a homogenization scheme (Section 5.1.4). Here we give an overview of each part of the model.

5.1.1 Parameterization of biotite expansion during weathering

Our first goal is to capture the behavior of biotite weathering at the crystal scale (∼0.1-1mm). Biotite is an easily weathered sheet silicate that can undergo a number of transformations from unweathered biotite to altered biotite to 2:1 clays (e.g., vermiculite and smectite) to 1:1 clays (e.g., kaolinite and halloysite), depending on the intensity of the weathering environment [19, 180, 181, 182, 164]. During weathering, biotite expands in

the direction normal to its sheets, exerting stress on the surrounding matrix [183, 184].

Biotite expansion can occur by multiple mechanisms. First, interlayer potassium cations can be replaced by hydrated magnesium cations, which thickens a single biotite layer from 10 Å to 14 Å, and induces minimal changes in the layer's lateral dimensions (e.g., [183]). Second, Fe^{2+} cations can be oxidized into Fe^{3+}, producing altered biotite with an expansion of the (001) d-spacing from 10 Å to 10.5 Å [181]. The first of these mechanisms involves the greatest volume expansion and therefore has the greatest potential to damage rock. In this study we thus restrict our attention to this mechanism, following previous studies [164, 165].

To capture the expansion of biotite during weathering, we begin with a parameterization for the production rate of weathered biotite, dQ/dt, within the REV.

$$\frac{dQ}{dt} = RS \tag{5.1}$$

Here Q (mol) is the number of moles of weathered biotite in the REV, R (mol m^{-2} s^{-1}) is the weathering rate of biotite per unit mineral surface area, and S (m^2) is the total biotite surface area within the REV. Since weathered biotite is produced at the expense of unweathered biotite, Q is equivalent to the number of moles of biotite that are lost during biotite weathering.

We adopt a parameterization for R as a decreasing power-law function of time, following empirical observations of biotite weathering [185]:

$$R = 3.001 \times 10^{-5}\, t^{-0.603} \tag{5.2}$$

in which the time (t) is the time since the onset of weathering, expressed in years. This equation is a highly simplified parameterization for biotite weathering that nonetheless captures one of its key characteristics: the decline in reactivity over time. It is beyond the scope of this study to investigate the model's sensitivity to environmental parameters,

but we note that this part of the model could to be modified to do so. Different parameterizations for biotite weathering can be applied here to investigate the model's sensitivity to a variety of factors, including porewater solute concentrations [186], dissolved oxygen concentrations [163], pH [187] and temperature [188].

We use the weathered biotite production rate to calculate the rate of change of the volume of weathered biotite V_w (m^3) in the bedrock REV, which we assign a value of zero at the onset of biotite weathering.

$$\frac{dV_w}{dt} = v_m \frac{dQ}{dt} \tag{5.3}$$

Here v_m is the molar volume of weathered biotite: v_m = 2.10$\times 10^{-4}$ m^3 mol^{-1}. Changes in V_w are calculated by integrating Equation 5.3 over time.

The time-varying value of V_w is useful because it permits the calculation of the evolution of the chemically-driven strain fields in the biotite inclusions (Section 5.1.2), which in turn permits the calculation of the evolution of the bedrock REV's mechanical properties (Section 5.1.4). Since the transformation of biotite into weathered biotite involves minimal changes in the biotite layers' lateral dimensions, the change of volume of the biotite crystals translates into a unidirectional deformation. This deformation, at the crystal scale, occurs independently from the mechanical interactions with the adjacent matrix, and independently from the boundary conditions in the far field.

5.1.2 A crystal-scale model of biotite expansion

We begin the crystal-scale model of biotite expansion by representing biotite crystals as oblate spheroids. This differs from the geometry of biotite crystals in nature, which are closer in shape to rectangular prisms than oblate spheroids. This geometric approximation is useful because it allows us to capture several essential characteristics of biotite weathering and bedrock damage. First, it captures the fact that biotites tend to be relatively flat, thinner in one dimension than in the other two. Second, it allows us to represent biotite

expansion as a change of mineral aspect ratio without changing the mineral's length along its long axis. Third, it permits us to develop an analytical closed formulation based on Eshelby's theory [91] to calculate the spatial and temporal evolution of the rock's strain, stress, and damage fields. This would not be possible if the biotites were represented as rectangular prisms, which would have nonuniform stress and strain fields.

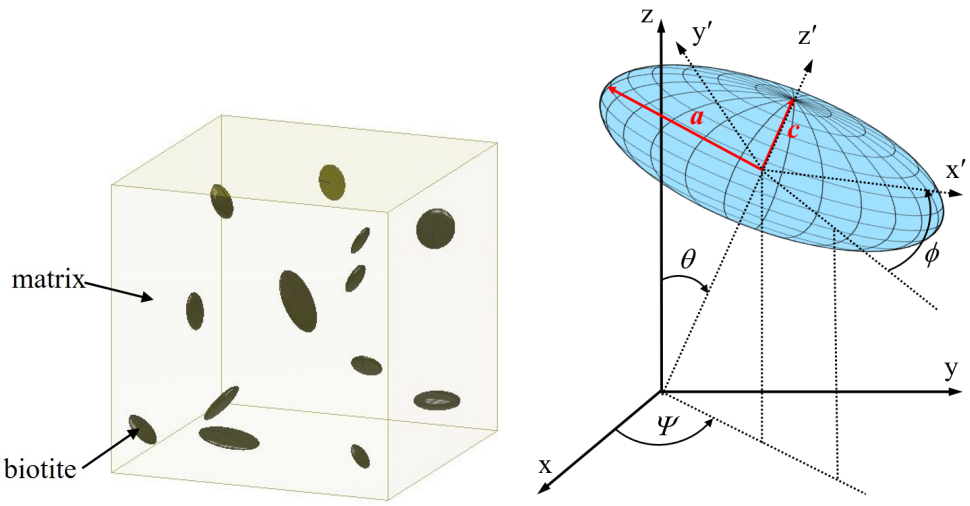

(a) Schematic of the REV (b) Schematic of the inclusion

Figure 5.1: Schematic of the crystal-scale weathering model.

Schematic representations of the biotite inclusion and of the REV are shown in Figure 5.1. We define a and c to be the long and short axes of the spheroidal biotite inclusions, respectively. Note that these definitions of a and c are not the same as the crystallographic a and c axes, which are not directly relevant for our model; instead, the key characteristic here is that biotite weathering drives expansion only in the c direction. During weathering, the modeled biotite inclusions remain oblate spheroids, but their aspect ratio a/c decreases over time due to chemically-driven expansion in the c direction. We assume that a remains constant during weathering, such that the chemically-driven strain in the a-direction (ϵ_{ca}) is 0.

For notational clarity, we distinguish between chemically-driven strain, which is directly generated by biotite expansion, and total strain, which is the combination of chemically-

driven strain and additional strain induced by the mechanical responses of the matrix and the biotites. We denote the chemical strain with the subscript c followed by a second subscript indicating the direction of strain (e.g., ϵ_{ca}), and we denote the total strain by a single subscript indicating the direction of strain (ϵ_a).

The volume of a biotite inclusion increases during weathering from its initial volume $V_{b,initial}$ to the sum of V_w and the remaining unweathered biotite volume, V_b. Since the transformation of a layer of biotite into a layer of weathered biotite increases the layer's thickness by a factor of 1.4, the remaining unweathered biotite volume can be written as $V_b = V_{b,initial} - V_w/1.4$. Use of this expression for V_b permits the chemical strain in the thickness direction, ϵ_{cc}, to be calculated as follows.

$$\epsilon_{cc} = \frac{V_w + V_b}{V_{b,initial}} - 1 = \frac{V_w(1 - \frac{1}{1.4})}{V_{b,initial}} \tag{5.4}$$

In the case of complete biotite weathering, for example, V_w would be $1.4V_{b,initial}$, and ϵ_{cc} would be 0.4. This is the upper limit on ϵ_{cc}.

We are unaware of measurements of the elastic behavior of weathered biotite. Linear elastic moduli of biotite and vermiculite (not weathered biotite) were published in [189] and [190]. Based on this, we assume that weathered and unweathered biotite crystals are linear elastic materials, and that inelastic effects are accounted for via the chemical strain of the inclusion. We consider that the inclusions have an isotropic mechanical behavior, by analogy to the mechanical behavior of salt crystals and amorphous solid crystals such as quartz [191, 153, 192]. The elastic moduli of unweathered and weathered biotite we adopt in this model are reported in Table 5.1. For times in which a biotite crystal is partially weathered, we calculate the elastic moduli of the partially weathered inclusion as the volumetric average of the moduli of the unweathered part of the inclusion (which has a volume of V_b) and of the moduli of the weathered part of the inclusion (which has a volume of V_w). This approximation assumes that the subscale strain field is uniform.

5.1.3 Damage model for the matrix

Biotite weathering results in the volume expansion of inclusions embedded in a rock matrix constrained by far field stresses. The accumulation of chemical eigenstrains in the inclusions results in stress concentrations in the rock matrix around them. If the latter exceeds the strength of the matrix, micro-cracks initiate and the stiffness and strength of the matrix decrease. We model micro-crack propagation with a Continuum Damage Mechanics (CDM) model, in which the damage variable (the scalar Ω) can be thought of as the cracks' volume fraction in the matrix. To ensure the symmetry and positivity of the damaged stiffness tensor, and to ensure that the non-damaged behavior of the matrix is linear elastic, we express the matrix Helmholtz free energy Ψ_s as [193]:

$$\Psi_s = \frac{1}{2}\lambda(\text{tr}\epsilon_m)^2 + \mu\text{tr}(\epsilon_m \cdot \epsilon_m) + \alpha\text{tr}(\epsilon_m)\text{tr}(\Omega\epsilon_m) + 2\beta\text{tr}(\Omega\epsilon_m \cdot \epsilon_m) \tag{5.5}$$

where λ and μ are the Lamé constants of the non-damaged matrix, α and β are damage constitutive parameters and ϵ_m refers to the strain field in the matrix. α and β control the effects of damage on the reduction of λ and μ respectively. In our CDM approach, damage occurs when a damage criterion f_d exceeds a critical value. The damage criterion depends on both the so-called damage driving force, Y_d, and the damage itself [194, 195, 1]. This captures the observation that more energy is required to induce new damage in a more damaged rock than a less damaged rock [196]:

$$f_d = \frac{Y_d}{\sqrt{2}} - (k_0 + k_1\Omega) \tag{5.6}$$

where k_o is the damage initiation threshold and k_1 is a damage hardening parameter. The damage driving force Y_d is calculated from thermodynamic conjugation relationships, as follows:

$$Y_d = -\frac{\partial\Psi_s}{\partial\Omega} = -\alpha\text{tr}(\epsilon_m)\text{tr}(\epsilon_m) - 2\beta\text{tr}(\epsilon_m \cdot \epsilon_m) \tag{5.7}$$

During the initiation and propagation of damage, the consistency conditions hold (i.e., the state of stress is on the elastic/damage boundary, and stays there: $\dot{f}_d = 0$ and $f_d = 0$), which allows calculating the damage rate as follows:

$$\begin{aligned} \frac{d\Omega}{dt} &= 0 && \text{if } \ f_d < 0 \\ \frac{d\Omega}{dt} &= \frac{1}{k_1\sqrt{2}}\frac{dY_d}{dt} && \text{if } \ f_d = 0 \end{aligned} \tag{5.8}$$

5.1.4 A homogenization scheme for bedrock strain and damage at the REV scale

The last component of the biotite weathering model is designed to compute the evolution of the bedrock REV stiffness tensor over time. For this, we used a Mori-Tanaka homogenization scheme [97], which is similar to the homogenization scheme discussed in 4.3. In our application of the Mori-Tanaka homogenization scheme, each biotite inclusion is assigned an aspect ratio and an orientation θ relative to horizontal, and is embedded in a solid matrix of infinite extent (Figure 5.1).

The REV consists of two phases: biotite and matrix. The matrix is a single homogeneous phase, while the biotite phase may contain an infinite number of inclusion orientations and aspect ratios. For simplicity in our simulations, we apply the same aspect ratio and orientation to groups of biotite inclusions, as this facilitates exploration of biotite characteristics on bedrock weakening. To describe the groups of biotite inclusions that share the same aspect ratio and orientation, we introduce the term "inclusion set". We apply the term "component" to each constituent in the REV. In this terminology, the matrix is one component, each biotite inclusion set is a component, and together all components constitute the entirety of the REV.

In the i^{th} component, the local stress σ_i is determined by the local strain ϵ_i and of the local eigenstrain η_i. In this study, η_i is the chemical weathering strain ϵ_{cc_i}, so that we have

[154]:

$$\sigma_i = \mathbf{C}_i : \epsilon_i - \mathbf{C}_i : \eta_i \tag{5.9}$$

where $\mathbf{C}_i$ is the fourth-order stiffness tensor of the i-th phase, and σ_i, ϵ_i, and η_i are all second-order tensors.

The homogenized stiffness $\mathbf{C}_{hom}$ of the REV is the volume average of the stiffness of all components $\mathbf{C}_i$ multiplied by the component-specific concentration tensor $\mathbf{A}_i$, which is given in Equation 6.36 [107]:

$$\mathbf{C}_{hom} = \sum_{i=1}^{n} \phi_i \mathbf{C}_i : \mathbf{A}_i \tag{5.10}$$

where n is the number of components in the REV (i.e., the number of biotite inclusion sets plus one, for the matrix) and ϕ_i is the volume fraction of component i.

In the Mori-Tanaka scheme, the stiffness of the infinite medium $\mathbf{C}_o$ is equal to the matrix stiffness (which depends on damage Ω in the present model). $\mathbf{P}_i$ is a fourth-order tensor specific to each biotite inclusion. The full expression of $\mathbf{P}_i$, given in [92], depends on the orientation and aspect ratio of the ellipsoidal inclusions of component i as well as on the matrix stiffness $\mathbf{C}_o$.

The REV stress $\bar{\sigma}$ is related to the REV strain $\bar{\epsilon}$ and of the eigenstrain of each component [155], as follows:

$$\bar{\sigma} = \mathbf{C}_{hom} : \bar{\epsilon} - \sum_{i=1}^{n} \phi_i \mathbf{C}_i : \eta_i : \mathbf{A}_i \tag{5.11}$$

On the right side of Equation 4.16, the first term ($\mathbf{C}_{hom} : \bar{\epsilon}$) is the linear elasticity relation for a homogeneous medium, while the second term describes how the REV stress is modified by the chemical weathering strain of each component in the REV.

The strain field in each component (noted ϵ_i) is expressed as a function of the macro-

scopic strain field and to the eigenstrains of that component, as follows:

$$\epsilon_i = \mathbf{A}_i : \bar{\epsilon} + \sum_{j=1}^{n} \mathbf{D}_{ij}\eta_j \tag{5.12}$$

where $\mathbf{D}_{ij}$ is given in Equation 4.18.

5.1.5 Resolution algorithm for the homogenization scheme

We use the Mori-Tanaka homogenization scheme to upscale the microscopic stresses and strains in the biotite inclusions and in the matrix to the REV scale. At each time step, the matrix stiffness $\mathbf{C}_o^t$ and the thickness c^t and radius a^t of the biotite inclusions are considered as input variables because they are calculated at the previous time step. The total volume of biotite before the weathering from t to $t + \delta t$ occurs (V_b^t) is obtained from c^t and a^t. In the proposed algorithm (illustrated in Figure 5.2), the volume of weathered biotite V_w^t is first calculated by substituting Eq. 5.1 and 5.2 into Eq. 5.3. Then, the chemical strains $\epsilon_{cc,i}^t$ (i.e., the eigenstrains η_i^t) are updated by using Eq. 5.4, while the stiffness of biotite inclusions $\mathbf{C}_i^t$ is calculated by using a volume average approximation. At the REV scale, the strain concentration tensor $\mathbf{A}_i^t$ and the influence tensor $\mathbf{D}_{ij}^t$ are calculated, based on the shape and stiffness of the inclusions (c^t, a^t and $\mathbf{C}_i^t$). Using $\mathbf{A}_i^t$ and $\mathbf{D}_{ij}^t$, the homogenized stiffness $\mathbf{C}_{hom}^t$ is updated by means of Eq. 6.35. Next, the unknown components of the macroscopic stress $\bar{\sigma}$ and of the macroscopic strain $\bar{\epsilon}$ are calculated with Eq. 4.16, with the given boundary stress and strain conditions. The stresses σ_i^t and the strains ϵ_i^t in each phase are then calculated by using Eq. 4.12 and Eq. 4.17. The matrix damage Ω^{t+1} is updated from the strain of the matrix phase. Ω^{t+1} is then used to update the stiffness of the matrix $\mathbf{C}_o^{t+1}$ for the next time step. Then, inclusion shape parameters c^{t+1} and a^{t+1} are calculated from the strain of each inclusion ϵ_i^t, and their values are stored for the next time step.

To summarize, the model developed in Sections 5.1.1-5.1.4 allows calculating the transient evolution of microscopic damage in bedrock. This is driven by the deformation of

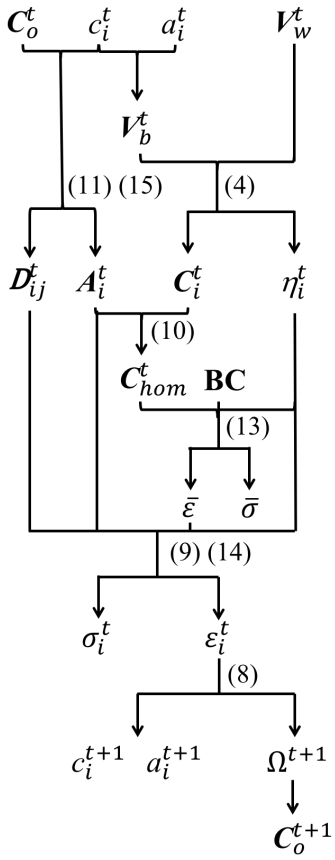

Figure 5.2: Resolution algorithm for the proposed homogenization scheme. See the text for the definitions of the variables in this figure.

biotite inclusions under a biotite weathering rate that decreases over time. This deformation, called eigenstrain, changes the states of stress and strain in the matrix, which in turn influences the state of stress in the biotite inclusions. These stress and strain changes are used to predict the initiation and propagation of damage induced by micro-cracks when the matrix strains (which are related to the matrix energy release rate) exceed a certain threshold.

5.2 Results: Simulation of bedrock damage by biotite weathering

To explore the effects of biotite characteristics (abundance, orientation, and aspect ratio) and boundary conditions on bedrock damage, we conducted a range of simulations with the model presented in Section 5.1. To do this, we simulated bedrock weathering at the

material point, which is at the centroid of the REV and defines our scale of observation. The bulk and shear moduli of biotite, vermiculite and matrix material are listed in Table 5.1 [189, 190]. We adopt values for the matrix similar to those in quartz and feldspar, such that the resulting rock behaves as a mixture of quartz, feldspar, and biotite, similar to a granite [196].

According to [197], the maximum damage threshold above which the proposed CDM model is no longer valid is 0.2 (above this threshold, the model would have to be improved to account for the presence of micro-cracks that interact). We thus stopped the simulations whenever damage grew as high as 0.2.

Table 5.1: Mechanical parameters in bedrock

Biotite		Vermiculite		Matrix					
K_b	μ_b	K_v	μ_v	K_m	μ_m	k_0	k_1	α	β
76700	41600	13824	5300	60700	31300	0.11	2.2	-16000	-31000

K_* and μ_* are respectively the bulk modulus and shear modulus. All parameters are in MPa. [189, 190, 196]

5.2.1 Influence of boundary conditions

During biotite weathering, the evolution of rock damage is influenced by the boundary conditions imposed on the REV because they influence the evolution of stress and strain within the biotites and the matrix. To assess the influence of the boundary conditions on bedrock weakening, we ran a series of simulations with identical biotite characteristics and a range of boundary conditions. In these simulations, biotite abundance is 15% (typical in granite), all biotite inclusions have the same initial aspect ratio $a/c = 3$, and all biotite inclusions are aligned with their long axis (a) oriented at $\theta = 30^\circ$ from the horizontal. The REV thus contains only two components in these simulations: the matrix and one biotite inclusion set.

For the vertical boundary condition, we consider a bedrock REV at depth h subjected to

a vertical stress $\sigma_v = \rho g h$, where ρ is the average density of the overlying material (saprolite and soil) and g is gravitational acceleration (9.8 m s^{-1}). For the horizontal boundary condition, we consider two end-member cases, which we refer to as the proportional stress boundary condition and the oedometric boundary condition (Figure 5.3). In the proportional stress boundary condition, the REV is constrained horizontally by a lateral boundary stress $\sigma_h = K\sigma_v$. Here the lateral boundary stress is proportional to the overburden, and K is the ratio between the horizontal and vertical stresses. In the oedometric condition, the REV is constrained to have zero horizontal displacement at the lateral boundaries. This mimics the boundary conditions in so-called oedometer deformation tests in the laboratory, which in nature would be analogous to exceptionally rigid lateral boundaries. We use the proportional stress and oedometric boundary conditions in the following simulations because they represent two end-member scenarios; it is expected that biotite weathering will have the lowest (respectively highest) influence on matrix damage under the proportional stress (respectively oedometric) boundary conditions.

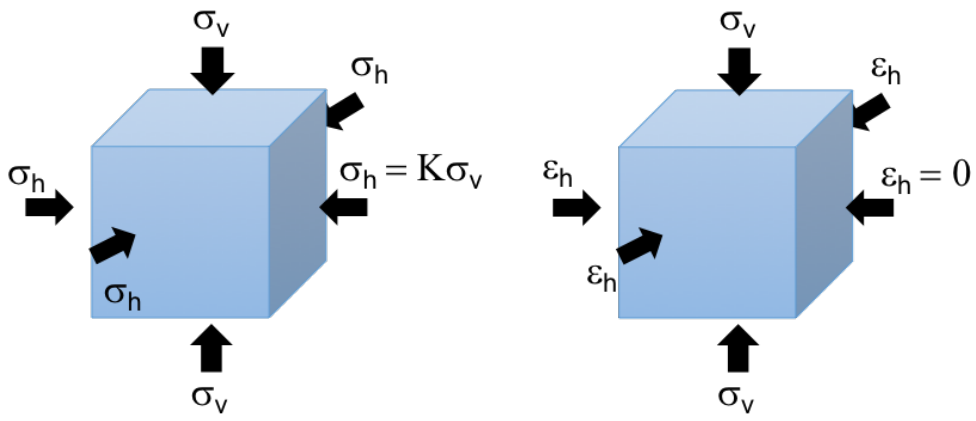

(a) Proportional stress condition (b) Oedometric condition

Figure 5.3: Schematic of the boundary conditions.

Figure 5.4 shows eight simulations that illustrate the sensitivity of bedrock evolution to the boundary conditions. Each simulation shows how strain within biotites (Figures 5.4a and 5.4b) generates strain in the surrounding matrix (Figure 5.4c), which in turn generates

damage (Figure 5.4d). Here, ϵ_c and ϵ_a denote the strains within biotite inclusions in the directions of inclusion thickness c and inclusion radius a, respectively (Figure 5.1). We note ϵ_v the volumetric strain of the bedrock REV.

For each of the proportional stress and oedometric boundary conditions, we conducted four simulations at overburden stresses of σ_v = 19.6, 196, 1,960, and 19,600 kPa. For an overburden density of 2000 kg m^{-3} [198], these correspond to depths of $\sim$1, 10, 100, and 1000 m. In the simulations with the proportional stress conditions, we assign a value of $K = 0.5$ for the stress coefficient [199]. In simulations with the oedometric conditions, lateral boundary stresses are not imposed because they evolve under the constraint of no lateral displacement at the boundary.

The simulations are initialized without eigenstrain in the inclusions and without damage in the matrix. We then calculate the weathering rate and the volume of weathered biotite for each inclusion set at each incremental time step. The strain and stress fields of each component of the REV and of the REV overall are then updated. If the matrix energy release rate exceeds the damage threshold, then the damage of the matrix is updated from the consistency conditions. We stop the simulations when the matrix damage Ω reaches 0.2, which is the critical value above which the continuum assumption underlying our model is no longer valid [200, 197].

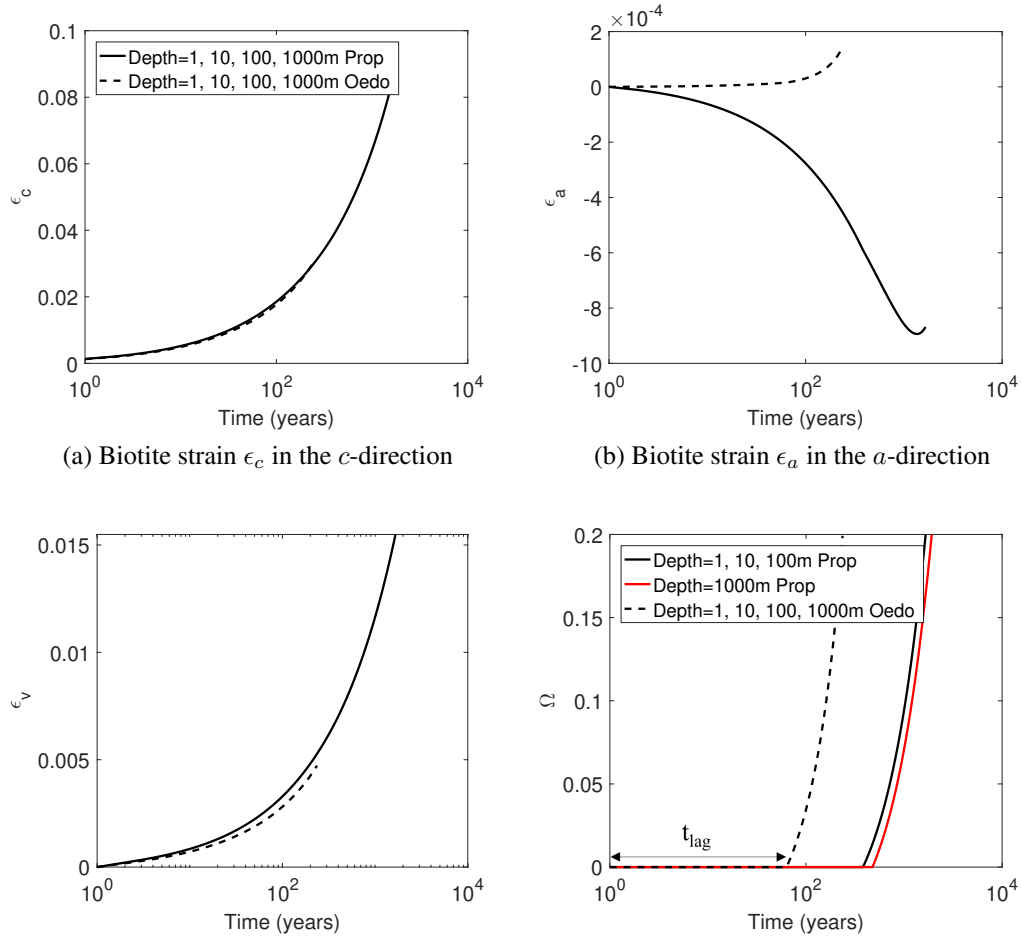

(a) Biotite strain ϵ_c in the c-direction

(b) Biotite strain ϵ_a in the a-direction

(c) Volumetric strain of bedrock REV

(d) Damage in the matrix

Figure 5.4: Influence of boundary conditions on strain and damage: effect of vertical stress. **a.** Biotite strain in the thickness direction c (ϵ_c) increases over time and shows negligible sensitivity to depth and boundary conditions (proportional stress vs. oedometric boundary conditions). **b.** Biotite strain in the transverse direction (ϵ_a) is $\sim$100 times smaller than ϵ_c. It exhibits contraction under the proportional stress condition, expansion under the oedometer condition, and negligible sensitivity to depth. **c.** Volumetric strain in the bedrock REV (ϵ_v) is small ($< 1\%$) and exhibits negligible sensitivity to depth and only minor sensitivity to boundary conditions. **d.** The time until damage initiation is noted as t_{lag}. Bedrock damage (Ω) initiates hundreds of years earlier under the oedometric condition than under the proportional stress condition, and exhibits minor sensitivity to depth. In each simulation, initial biotite abundance was 15%, initial biotite aspect ratio was 3, and the initial orientation of all biotite a-axes were 30° relative to the horizontal.

To further investigate the effects of boundary conditions, we conducted six more simulations under the proportional stress condition and a range of values for the stress coefficient K, which controls the magnitude of the horizontal boundary stresses relative to the vertical boundary stress. In each of these simulations the vertical boundary stress σ_v is set to 196 kPa, roughly equivalent to 10 m of overburden with density 2000 kg m^{-3}.

Figure 5.4 shows that bedrock damage (Ω) initiates hundreds of years earlier under the oedometric boundary condition than under the proportional stress boundary condition, and exhibits minor sensitivity to depth. Figure 5.5 shows that strain and damage are insensitive to the choice of K. All six simulations, with values of K ranging from -1 (lateral tension) to 10 (strong lateral compression), are indistinguishable from one another in Figure 5.5. For comparison, Figure 5.5 also shows one simulation under the oedometric condition (dashed line), in which damage initiates hundreds of years earlier than under the proportional stress boundary condition.

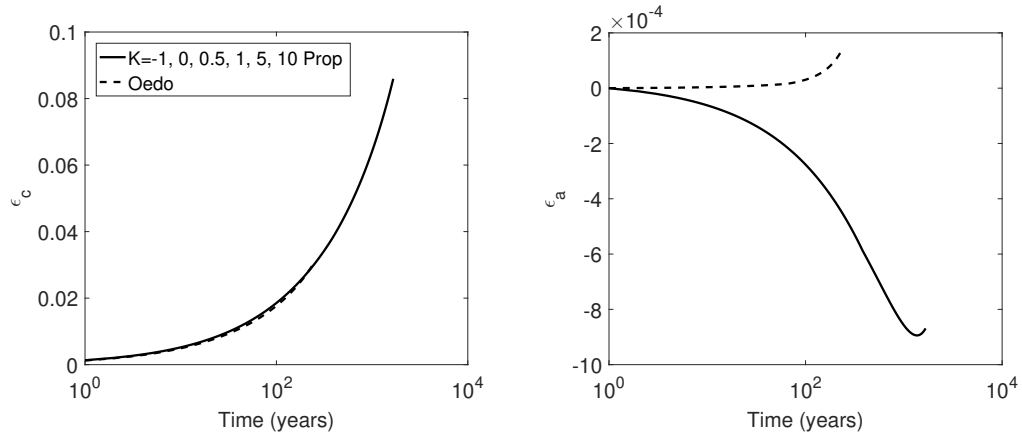

(a) Biotite strain (thickness direction c)

(b) Biotite strain (transverse direction a)

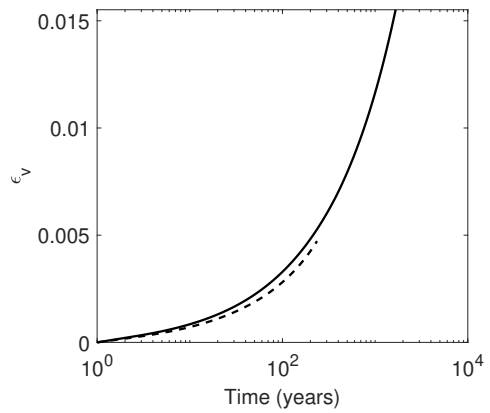

(c) Volumetric strain of bedrock REV

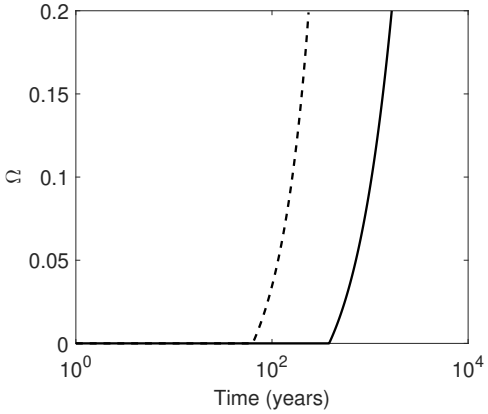

(d) Damage in the bedrock matrix

Figure 5.5: Effect of the stress coefficient (K) on strains and damage under the proportional stress boundary condition. **a.** Biotite strain in the thickness direction (ϵ_c) shows negligible sensitivity to K. **b.** Biotite strain in the transverse direction (ϵ_a) also shows negligible sensitivity to K. **c.** The REV volumetric strain (ϵ_v) is small ($< 1\%$) and exhibits negligible sensitivity to K. **d.** Bedrock damage (Ω) exhibits minor sensitivity to K. In each simulation, the initial biotite abundance was 15%, the initial biotite aspect ratio was 3, and the initial orientation of all biotite a-axes were 30° relative to the horizontal.

5.2.2 Influence of biotite abundance

To illustrate the effects of biotite abundance on bedrock damage, we show the results of three simulations with biotite abundances of 5, 10, and 15% by volume. In each simulation the vertical boundary stress is 196 kPa, equivalent to a depth of 10 m under material with a density of 2000 kg m^{-3}, typical of saprolite. Since strain and damage are relatively insensitive to lateral stresses at that depth (Figure 5.5), K is set to 0.5 in all simulations under proportional stress. The initial aspect ratio of biotite inclusions was set to 3 and all biotite inclusions were aligned at $\theta = 30°$, like in the simulations in Section 5.2.1.

Fig. 5.6 shows the influence of biotite abundance on strains and damage under the proportional stress boundary condition. Figure 5.6a reveals that biotite abundance has only negligible effects on biotite expansion in the direction of biotite thickness, with marginally greater biotite expansion at higher biotite abundance. Radial biotite shrinkage is small ($< 0.3\%$) but grows larger at lower biotite abundances (Fig. 5.6b). Figure 5.6c shows that the REV strain ϵ_v increases with biotite abundance, and Figure 5.6d shows that damage initiates earlier in rocks with higher biotite abundances. The damage accumulation rate does not depend on biotite abundance (i.e., the damage evolution curves are parallel to each other in Fig. 5.6d). For comparison, Figure 5.7 presents an additional set of simulations that show that biotite abundance has similar effects on strain and damage under oedometric boundary conditions. Relative to the proportional stress boundary conditions, the oedometric boundary conditions induce less contraction of ϵ_a, smaller expansion of ϵ_v, and faster evolution of Ω.

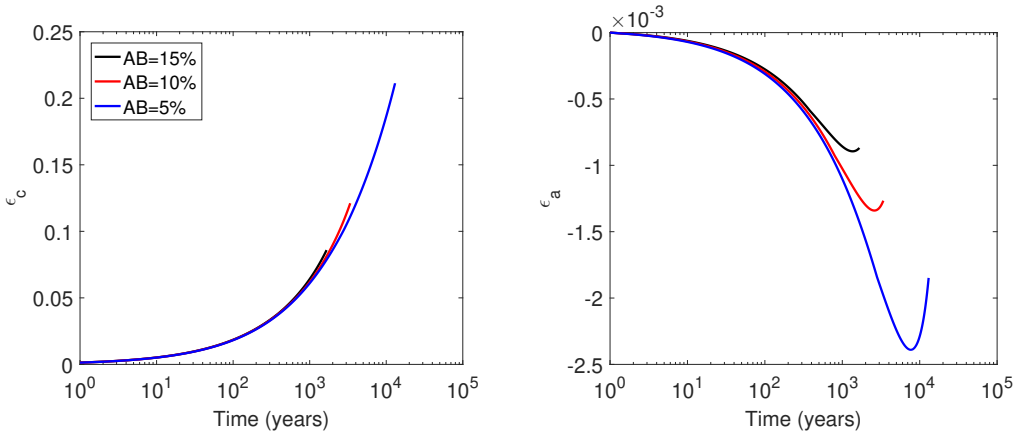

(a) Biotite strain (thickness direction c)

(b) Biotite strain (transverse direction a)

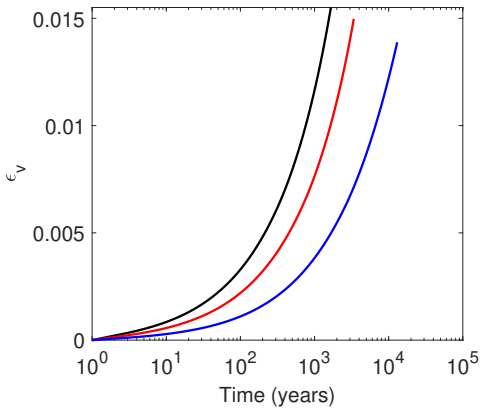

(c) Volumetric strain of bedrock REV

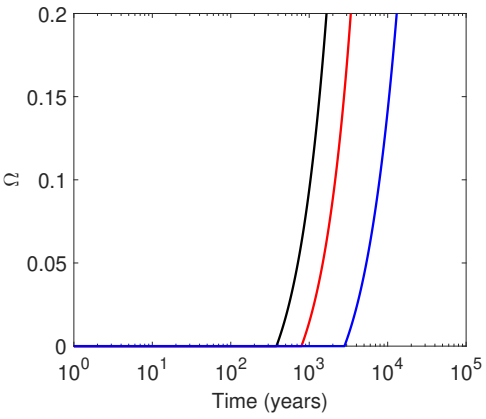

(d) Damage in the bedrock matrix

Figure 5.6: Effect of biotite abundance (AB) on strains and damage under the proportional stress boundary condition. **a.** Biotite strain in the thickness direction (ϵ_c) increases over time and shows negligible sensitivity to abundance until the initiation of damage. **b.** Biotite strain in the transverse direction (ϵ_a) exhibits larger contraction in rocks with lower biotite abundances. **c.** The REV volumetric strain (ϵ_v) increases with biotite abundance. **d.** Bedrock damage (Ω) initiates earlier at higher biotite abundances. In each simulation, the initial biotite aspect ratio was 3, the depth of the bedrock was 10 m, and the initial orientation of all biotite a-axes was 30° relative to the horizontal.

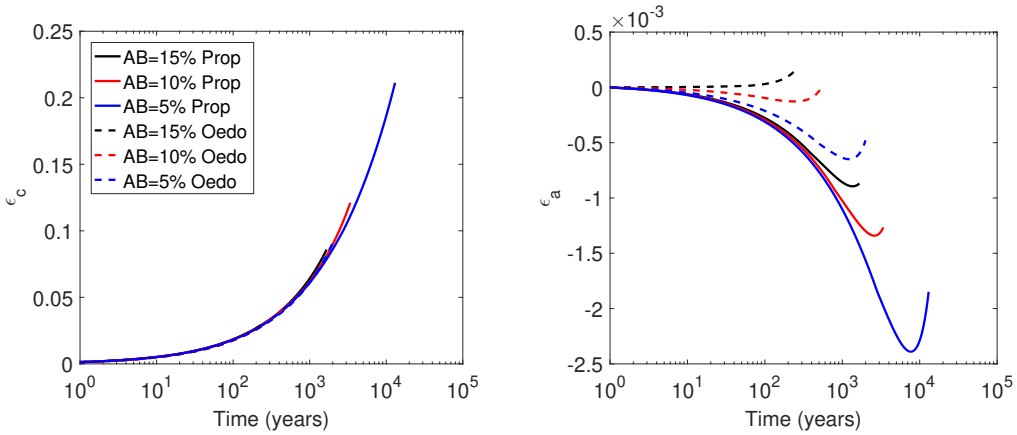

(a) Biotite strain (thickness direction c)

(b) Biotite strain (transverse direction a)

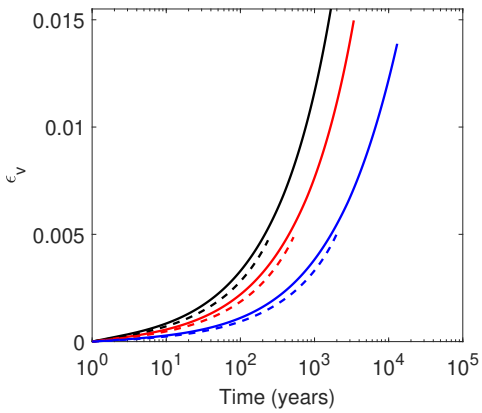

(c) Volumetric strain of bedrock REV

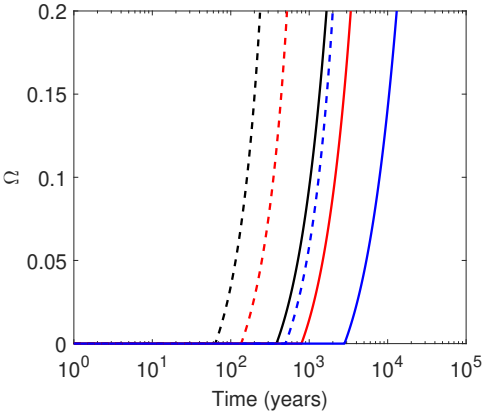

(d) Damage in the bedrock matrix

Figure 5.7: Effect of biotite abundance (AB) on strains and damage under the proportional stress boundary condition ("Prop") and the oedometric boundary condition ("Oedo"). **a.** Biotite strain in the thickness direction c (ϵ_c) increases over time and shows negligible sensitivity to abundance for both proportional stress and oedometric boundary conditions. **b.** Biotite strain in the transverse direction (ϵ_a) exhibits less contraction under oedometric boundary conditions. **c.** The REV volumetric strain (ϵ_v) increases slower under oedometric boundary conditions. **d.** Bedrock damage (Ω) initiates earlier under oedometric boundary conditions. In each simulation, initial biotite aspect ratio was 3, the depth of bedrock was 10 m, the overburden density was $\rho = 2000$ kg m^{-3}, and the initial orientation of all biotite a-axes were 30° relative to the horizontal.

5.2.3 Influence of biotite aspect ratio

The effect of biotite aspect ratio on strains and damage under proportional stress condition is presented in Fig. 5.8. In all simulations, the initial biotite abundance is 15%, biotite inclusions are initially aligned at $\theta = 30°$, and the vertical boundary stress is 196 kPa. We conduct simulations under four scenarios: three in which all biotites share the same initial aspect ratio (either 3, 6, or 9), and one with three equally abundant biotite inclusion sets, one with an aspect ratio of 3 and the other two with aspect ratios of 6 and 9. In the first three cases, the REV contains only two components (matrix and one biotite inclusion set), while in the fourth case, the REV contains four components (matrix and three biotite inclusion sets).

Figures 5.8a and 5.8b show that the deformation of biotite inclusions is almost entirely insensitive to biotite aspect ratio. Figure 5.8c shows that volumetric expansion of the matrix grows larger under smaller biotite aspect ratios before the threshold damage of 20% is reached, though in all cases the volumetric strain is less than 1%. By contrast, Figure 5.8d shows that the time to the initiation of damage is sensitive to biotite aspect ratio, especially for simulations under the proportional stress boundary condition. Figure 5.8d further shows that the simulation with a uniform distribution of aspect ratios (AR = 3, 6, 9) lies between the simulations with AR = 3 and AR = 6, which suggests that inclusions of lower aspect ratio dominate the development of damage in the matrix. For comparison, the influence of biotite abundance under oedometric condition is presented Figure 5.9. Results show that ϵ_c, ϵ_a, ϵ_v, and Ω all exhibit only minor sensitivity to aspect ratio under oedometric boundary conditions. This also shows that damage initiates slightly earlier in rocks with biotite inclusions of smaller aspect ratio under oedometric boundary conditions.

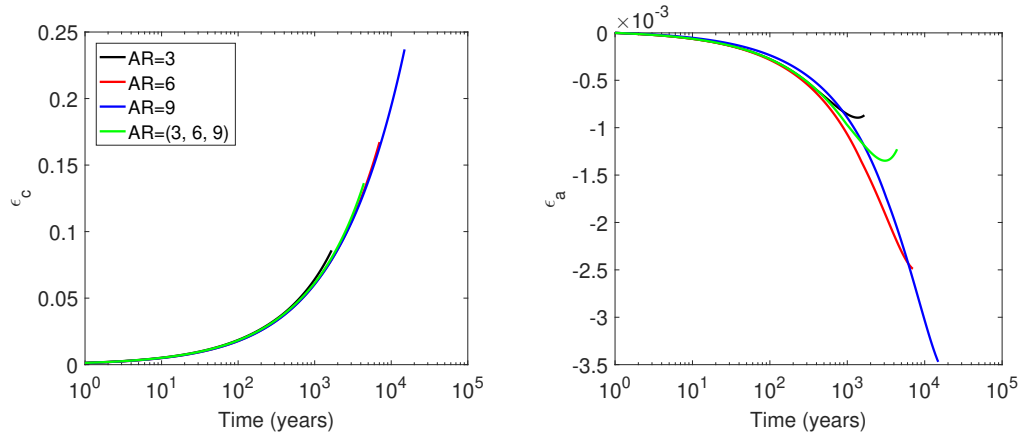

(a) Biotite strain (thickness direction c)

(b) Biotite strain (transverse direction a)

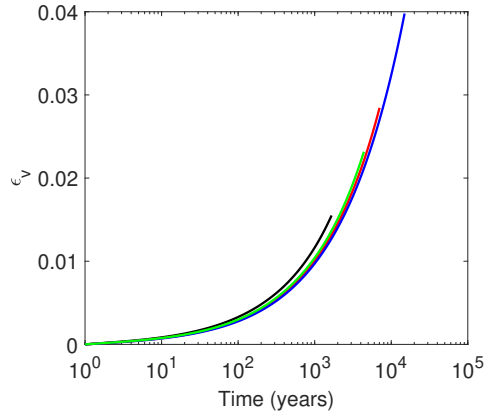

(c) Volumetric strain of bedrock REV

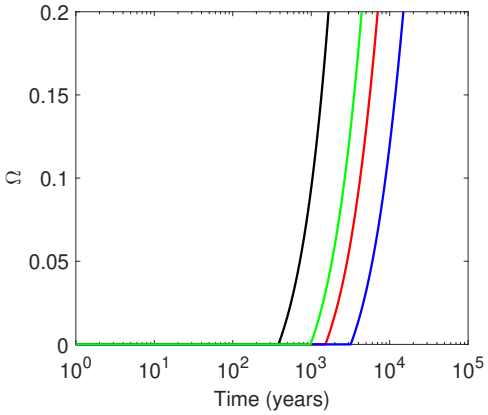

(d) Damage in the bedrock matrix

Figure 5.8: Effect of biotite aspect ratio (AR) on strains and damage. **a.** Biotite strain in the thickness direction (ϵ_c) shows negligible sensitivity to aspect ratio. **b.** Biotite strain in the transverse direction (ϵ_a) exhibits minor sensitivity to aspect ratio. **c.** The REV volumetric strain (ϵ_v) exhibits slightly larger expansion at smaller aspect ratios. **d.** Bedrock damage (Ω) initiates earlier in rocks with biotites with smaller aspect ratios. In each simulation, initial biotite abundance was 15%, the depth of bedrock is 10 m, and the initial orientation of all biotite a-axes were 30° relative to the horizontal.

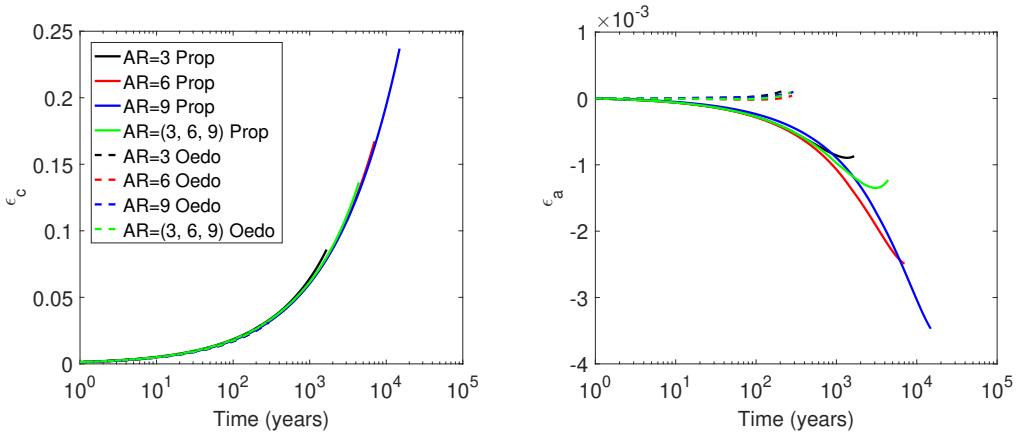

(a) Biotite strain (thickness direction c)

(b) Biotite strain (transverse direction a)

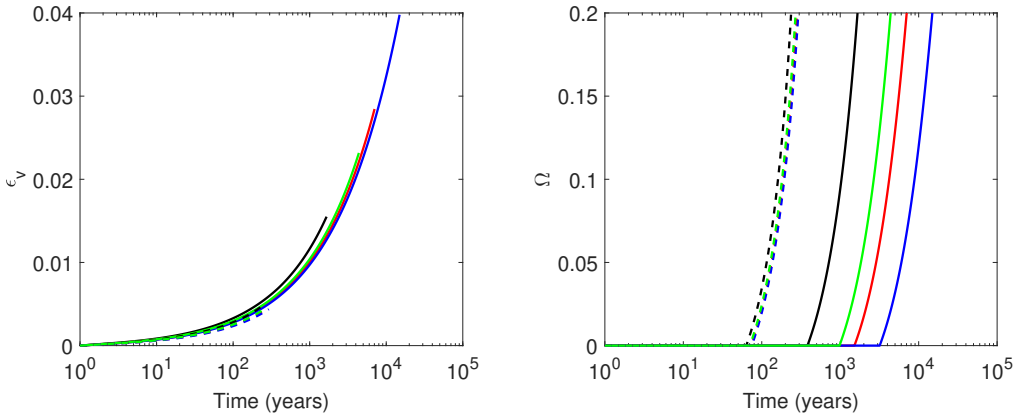

(c) Volumetric strain of bedrock REV

(d) Damage in the bedrock matrix

Figure 5.9: Effect of biotite aspect ratio (AR) on strains and damage under proportional stress and oedometric boundary conditions. **a.** Biotite strain in the the thickness direction c (ϵ_c) shows negligible sensitivity to aspect ratio under both proportional stress and oedometric boundary conditions. **b.** Biotite strain in the transverse direction (ϵ_a) is close to 0 under oedometric boundary conditions. **c.** The REV volumetric strain (ϵ_v) exhibits minor sensitivity to aspect ratio under oedometric boundary conditions. **d.** Bedrock damage (Ω) exhibits negligible sensitivity to aspect ratio under oedometric boundary conditions. In each simulation, initial biotite abundance was 15%, the depth of bedrock was 10 m, the overburden density was $\rho = 2000$ kg m^{-3}, and the initial orientation of all biotite a-axes were 30° relative to the horizontal.

5.2.4 Influence of biotite orientation

The third biotite characteristic we investigated is orientation. To study its effect, we conducted a series of simulations under a range of biotite orientations. In each simulation, the REV contains one set of identical biotite inclusions, which share an initial aspect ratio of 3 and an initial orientation θ of either 0, 30, 45, 60, or 90° (Figure 5.1b). The initial biotite abundance in each simulation is 15%.

The solid lines in Figure 5.10 show that biotite orientation has a negligible effect on the development of strain or damage under the proportional stress boundary condition. In each panel of Figure 5.10, the lines for simulations at all orientations overlap with each other within the width of the plotted line.

To illustrate the sensitivity of damage and strain to biotite orientation, we ran the same simulations under the oedometric boundary condition. In Figure 5.10, the dashed lines show that strain and damage are sensitive to biotite orientation under the oedometric boundary condition, unlike under the proportional stress condition. Figure 5.10d shows that damage initiates earlier under the oedometric boundary condition than under the proportional stress condition, except for the simulation with $\theta = 0°$, which shares almost the same evolution as all proportional stress simulations. This further shows that damage initiates faster at higher values of θ under oedometric conditions than under proportional stress boundary conditions.

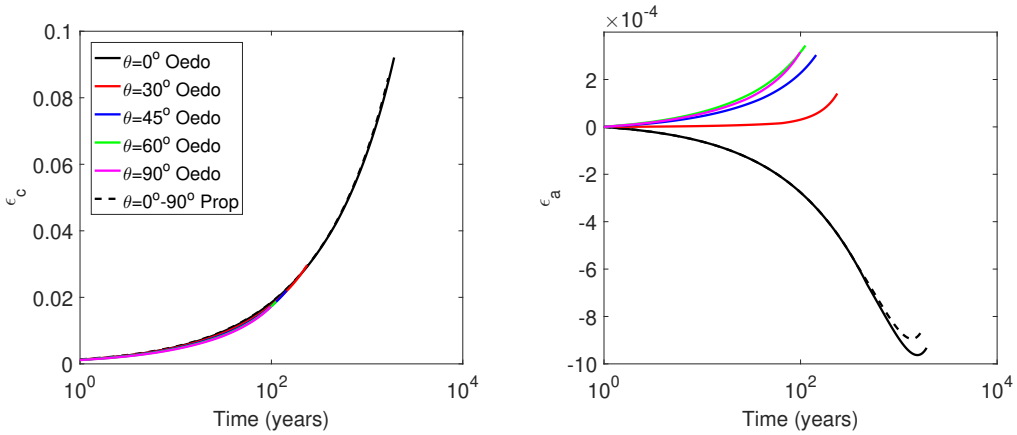

(a) Biotite strain (thickness direction c)

(b) Biotite strain (transverse direction a)

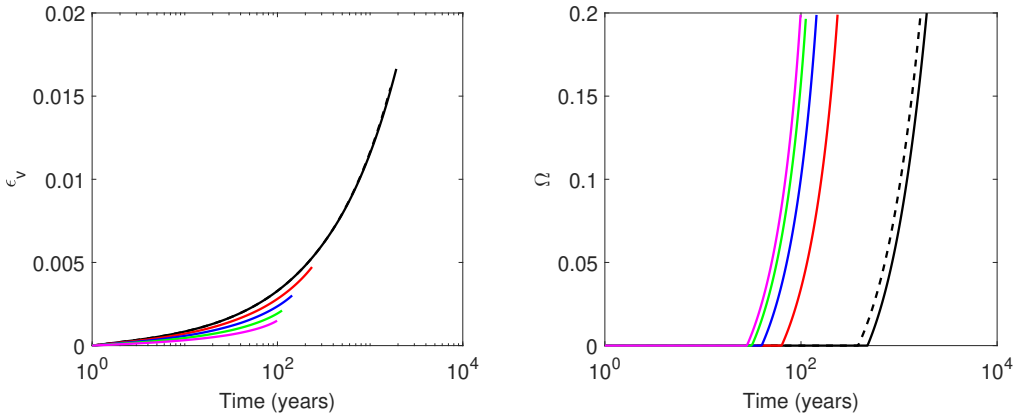

(c) Volumetric strain of bedrock REV

(d) Damage in the bedrock matrix

Figure 5.10: Effect of biotite orientation (θ) on strains and damage. **a.** Biotite strain in the thickness direction (ϵ_c) exhibits minor sensitivity to orientation. **b.** Biotite strain in the transverse direction (ϵ_a) shows negligible sensitivity to orientation under proportional stress boundary conditions, and exhibits larger expansion in rocks with larger θ under oedometric boundary conditions. **c.** The REV volumetric strain (ϵ_v) exhibits minor sensitivity to orientation under the proportional stress boundary condition, and decreases with θ under the oedometric boundary condition. **d.** Bedrock damage (Ω) initiates earlier in rocks with larger θ under the oedometric boundary condition. In each simulation, initial biotite abundance is 15%, the initial biotite aspect ratio is 3, and the depth of the REV is 10 m under overburden with a density $\rho = 2000$ kg m^{-3}.

5.3 Discussion

The simulations in Section 5.2 provide some of the first mechanistic treatments of how biotite expansion affects the transient development of bedrock damage. Despite differences in the initial and boundary conditions between simulations, there are several common behaviors that emerge in all simulations: 1) Biotites thicken monotonically by a large amount (9-20% in $\sim 10^3$ to 10^4 years); 2) Biotites grow or shrink in the transverse direction by a small amount ($< 0.3\%$); 3) The bedrock REV volumetric strain increases monotonically but always remains small ($< 1\%$); 4) After the onset of biotite weathering, no damage occurs for decades to millennia; 5) After damage initiates, it grows rapidly to the upper threshold of 20%, where the continuum approximation breaks down and simulations are terminated. These behaviors are modulated by the boundary conditions imposed on the rock (Figures 5.4-5.5), as well as by biotite abundance (Figure 5.6), aspect ratio (Figure 5.8), and orientation (Figure 5.10).

The time lag between the onset of biotite weathering and the onset of damage, t_{lag} (Figure 5.4d), is one of the key characteristics of the model behavior. Damage occurs when the damage criterion f_d exceeds 0 with the increase of strain in the matrix (Equation 5.6), while the energy release rate controlled by the matrix strain remains below the damage threshold at earlier times during the weathering process. This time lag t_{lag} is of interest because it indicates when micro-cracks start growing in the matrix. It is also the characteristic that is most sensitive to biotite weathering in our simulations, exhibiting a range of roughly two orders of magnitude under a range of biotite characteristics. Figure 5.11 shows that damage initiates earlier at higher biotite abundances (Figure 5.11a), smaller aspect ratios (Figure 5.11b), and, under oedometric boundary conditions, for biotites whose a-axes are oriented at a larger angle compared to the horizontal (Figure 5.11c). Here we discuss why the boundary conditions and biotite characteristics influence the development of damage and strain.

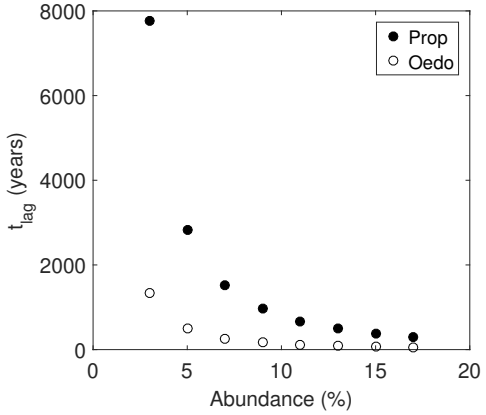

(a) Biotite abundance with biotite aspect ratio = 3 and θ = 30°

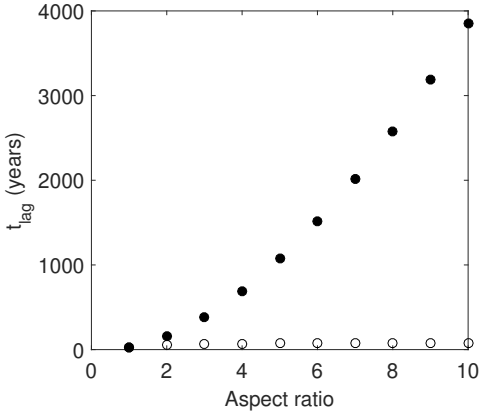

(b) Biotite aspect ratio (a/c) with biotite abundance = 15% and θ = 30°

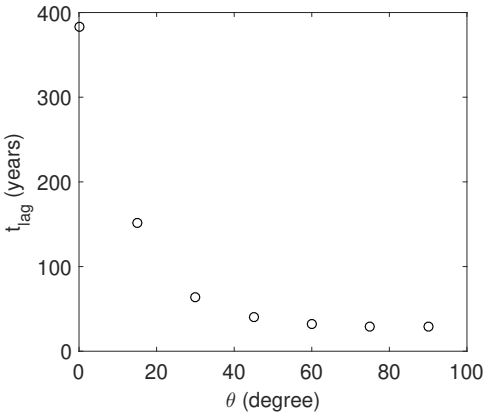

(c) Biotite orientation with biotite abundance = 15% and biotite aspect ratio = 3

Figure 5.11: The effects of boundary conditions and biotite characteristics on damage initiation: simulation results obtained with proportional stress boundary conditions (filled circles), and with oedometric boundary conditions (open circles). In each simulation, the depth of the REV is 10 m with K = 0.5.

5.3.1 Sensitivity to boundary conditions

Our simulations illustrate the sensitivity of damage development to both vertical and horizontal boundary conditions. Figure 5.4d, for example, shows that damage accumulates later in deeper rocks. This is because deeper rocks have larger vertical overburden pressures that more strongly counteract the inclusion strains and matrix stresses that build up due to biotite expansion. At greater depths, damage initiates later because it takes longer for biotite-driven stresses to overcome the overburden stress that inhibits damage. This illustrates the importance of the upper boundary condition that determines the vertical stress on the REV.

The same simulations in Figures 5.4 and 5.5 illustrate the importance of the lateral boundary conditions. For example, in the oedometric boundary conditions simulations in Figure 5.4c, damage initiates after a relatively short time ($<$ 100 years) even though the volumetric strain is still low ($< 0.1\%$). By contrast, in the simulations under proportional stress boundary conditions, damage initiates later (after several hundreds of years) at a time when volumetric strain has grown several times larger ($0.2 - 0.3\%$). This dependence on the lateral boundary condition occurs because the strain in the matrix increases rapidly with the expansion of biotite if the total lateral displacement is fixed. Unless all biotite inclusions are oriented horizontally, the expansion of the biotite inclusions induces a lateral stress in the bedrock REV. Imposing a condition of no lateral displacement on the lateral boundaries of the REV thus induces a compressional strain in the matrix, which results into a tensile difference of principal strains and accelerates the initiation of damage. Under the proportional stress boundary condition, by contrast, the matrix strain build-up is relatively slower, because the REV can expand despite the imposed lateral confinement stress.

One of the most striking results is that the lateral confining stresses under the proportional stress boundary conditions do not have any influence on damage accumulation rates (Figure 5.5). Here, applying a K value as great as 10—where lateral compressive stresses are 10 times the overburden stress—produces only minute differences in damage develop-

ment relative to that in simulations with $K < 1$ (lateral tension). This suggests that bedrock damage during biotite oxidation is divorced from regional or topographic stresses, which are often implicated in fracturing near surface bedrock (e.g., [201, 202, 203, 204]).

5.3.2 Sensitivity to biotite abundance

The biotite characteristic that exerts the strongest control on damage development is abundance. Indeed, biotite abundance has almost as much influence on damage accumulation as the difference between the proportional stress and oedometric boundary conditions. Figure 5.11a shows that biotite abundance has a nonlinear influence on damage development. Increasing biotite abundance by a factor of three from 5% to 15%, for example, decreases the time to the onset of damage by roughly a factor of ten. However, as biotite abundance increases, further increases in biotite abundance induce progressively smaller decreases in t_{lag}.

As described in Section 5.1, the initiation and evolution of damage is determined by the strain of the matrix, which depends on the double dot product of the concentration tensor and the REV strain (Equation 4.17). Because both the concentration tensor and the REV strain tensor are nonlinear functions of biotite abundance (Equations 6.36 and 4.16), biotite abundance has a nonlinear effect on damage development. Physically, this non-linear behavior comes from the non-linear relationship between the weathering rate and the weathered volume of biotite, as well as from the non-linear interaction between the deformation field of the inclusions and that of the matrix.

5.3.3 Sensitivity to biotite aspect ratio

Like abundance, aspect ratio exerts a significant influence on damage development. Our simulations show that biotites with smaller aspect ratios damage rock faster than biotites with larger aspect ratios (Figure 5.11b). This effect is most apparent for the proportional stress boundary condition, in which lateral horizontal stresses are proportional to overbur-

den stresses. Oedometric boundary conditions, by contrast, appear to dampen the influence of biotite aspect ratio (Figure 5.11b).

For a biotite inclusion of a given volume and fixed radius a, the c dimension (thickness) decreases when the biotite aspect ratio a/c increases. It follows that, for a given volume fraction of biotite inclusions in the REV, the number of expandable layers in the biotite inclusions decreases when the aspect ratio increases. As a result, the strain rate of the biotite inclusions also decreases when the aspect ratio increases, such that matrix strains take longer to accumulate under the weathering of biotites with larger aspect ratios. The consequence is that the time lag to the onset of damage increases with aspect ratio.

Figure 5.8 shows that bedrock damage is nonlinearly related to biotite aspect ratio. In this figure, one of the simulations was conducted on bedrock with a mixture of three equally abundant biotite inclusion sets with aspect ratios of 3, 6, and 9. If damage were linearly related to aspect ratio, then the resulting damage would match that in the simulation for biotites with the mean aspect ratio (6), but here it does not. Instead, its damage evolution curve lies between the evolution curves for biotites with aspect ratios of 3 and 6. This implies that damage propagation is dominantly controlled by biotites with small aspect ratios under the proportional stress boundary condition.

5.3.4 Sensitivity to biotite orientation

Figure 5.10 shows that biotite orientation θ influences damage accumulation under certain boundary conditions but not others. Under the proportional stress boundary condition, strain and damage evolve identically under all orientations. By contrast, under the oedometric boundary condition, θ does affect the evolution of strains and damage.

We can gain an understanding for why this occurs by considering the end member orientations $\theta = 0°$ and $\theta = 90°$. First consider the scenario $\theta = 0°$. Here, biotites are aligned horizontally and expand in the vertical direction. Because chemically-driven biotite expansion is perpendicular to the lateral boundaries, it is unaffected by the lateral

boundary condition. As a result, biotite expansion produces identical matrix stresses—and hence identical biotite and matrix strains and damage—under the proportional stress and oedometric boundary conditions.

Now consider the opposite end member scenario of $\theta = 90°$. Here, biotites expand in the horizontal direction. Under proportional stress boundary conditions, the matrix can expand in the the lateral direction, like in the case $\theta = 0°$. The mechanical response of the matrix is thus similar for $\theta = 0°$ and $\theta = 90°$. By contrast, under the oedometric boundary condition, the matrix cannot expand laterally because it is constrained by the fixed horizontal position of the boundary. As a result, compressive strains accumulate in the matrix, which accelerates the initiation of damage.

We can generalize from these end member scenarios to the general dependence of strain and damage on biotite orientation. Under the proportional stress boundary condition, biotite orientation has no effect on strain or damage because rotating the biotite inclusions is equivalent to rotating the tectonic stresses. Stress in the matrix is controlled by inclusions' eigenstrains, and not by the tectonic stresses. Therefore, the orientation of the biotite inclusions has negligible influence on the development of damage in the matrix.

Under the oedometric boundary condition, by contrast, as θ increases, the expansion of biotite leads to progressively larger lateral compressive stress in the matrix because the boundaries inhibit lateral strain. As shown in Fig. 5.10d, this leads to an earlier initiation of damage. Similarly, because increasing θ leads to progressively less confinement in biotite's transverse direction, ϵ_a tends to increase with θ, as shown in Fig. 5.10b. Thus, for all biotite orientations other than $\theta = 0°$, the fixed lateral boundaries under oedometric boundary conditions limit biotite expansion in its thickness direction but promote expansion in its transverse direction. The net result is that deviatoric stresses in the matrix grow faster at higher values of θ, which produces earlier initiation of damage.

5.3.5 Controls on biotite and matrix strains

Figure 5.4b shows that the depth of the REV does not influence the lateral strain of the inclusions (ϵ_a). Instead, ϵ_a increases with the propagation of damage. Under proportional stress boundary conditions, the radius of biotite inclusions decreases during biotite expansion due to the inclusion's Poisson's ratio. Under oedometric boundary conditions, ϵ_a is almost constant, due to the imposed lateral displacements at the REV boundary. Slightly less volume expansion is observed under the oedometric boundary condition in Fig. 5.4c.

Figures 5.4-5.10 show that biotite strain in the thickness direction (ϵ_c) and its rate of change both increase over time. The similarity in the evolution of ϵ_c in all simulations shows that ϵ_c is nearly independent of depth, lateral boundary conditions, or biotite abundance, aspect ratio, and orientation. This implies that ϵ_c is almost entirely controlled by chemically-driven mineral expansion, and that it is almost entirely insensitive to stress in the surrounding matrix. Both weathering expansion and interaction between matrix and inclusions contribute to the development of ϵ_c. Due to the nonlinear influence of the matrix on the biotite inclusions (Equation 4.17), ϵ_c grows non-linearly over time.

5.3.6 Model limitations

The proposed model can successfully be used to predict the initiation of damage in the bedrock and calculate the resulting damaged bedrock mechanical properties as a result of the constrained expansion of weathering biotite crystals. While powerful, we stress that this model's applicability is limited by the assumptions underlying it and the scale at which it is relevant. For example: (i) The Mori-Tanaka homogenization scheme accounts for the volume fraction of the inclusions, but cannot distinguish the offsetting effects of inclusion size from those of inclusion number. Thus, within the REV, it cannot distinguish between many small biotites or a few large biotites, provided they have the same total volume, the same aspect ratio and the same orientation. (ii) Our application of the model is restricted to isotropic inclusions, an isotropic matrix, isotropic damage, and aligned biotite crystals. The

predicted REV stiffness tensor does not always meet the positivity and symmetry requirements when one of the REV components is anisotropic or when the inclusions are either non-uniformly oriented or non-aligned [154]. More work is needed to assess the conditions under which it is reasonable to use the proposed model under non-aligned inclusions or under anisotropic families of cracks in the matrix. (iii) This is a model for microscopic bedrock damage—i.e., the development of micro-scale cracks in the rock—not a model of macroscopic fracturing. Thus it cannot compute the development of the macroscale fracture network. Our restriction of the model in this study to small spatial scales is intentional, because upscaling these processes to model macroscopic fracturing must build on a microscopic damage model such as this one.

Because our model results are confined to microscopic damage, which is defined strictly in our model as a decrease in stiffness, direct comparisons to typically measured parameters in field and laboratory studies of bedrock weathering are also limited. Recent studies have compared measurements in maximum compressive and tensile strengths to fracture densities and chemical mass losses in weathering rock [165, 205]. While these studies reveal correlations between mechanical strength, fracture density, and chemical properties, they are not directly comparable to our model results. However, some qualitative correlations can be made between our model results and these published observations. Tensile and compressive strength tests are commonly used to measure material stiffness, and in granitoid rock, these properties have been shown to correlate with modeled fracture energy density and progression of Fe-oxidation in weathering biotite [165]. Observations described in these studies suggest that progressive oxidation of Fe in biotite contributes to mechanical weakening via microcrack propagation; through which meteoric fluids can further chemo-mechanically weather bedrock once pore space is connected [164, 165, 175]. Observational studies suggest that microcrack propagation initiates once available Fe in biotite is 20%-65% oxidized, which may relate to the lag times predicted in our models between spin up and damage development [165]. Our model results suggest that biotite

aspect ratio and abundance are key drivers to mechanical weakening of granitoid rock during biotite oxidation; however these observations are generally absent from the literature. Our model thus serves to elucidate the role of these mineral grain characteristics in the weakening of weathering rock for future studies.

Our model is driven by a simplified representation of biotite weathering. In nature, several factors can affect the rate of mineral weathering and coevolve along with it. For example, mineral weathering affects the rock's permeability and connected porosity, which in turn affects fluid transport in the rock and pore water solute concentrations, which affect mineral dissolution rates [206, 207, 208]. Chemical weathering triggers the initiation and propagation of cracks, which enhances the porosity of rock, as shown in this study and in [165]. Higher rock permeability facilitates solute transport and increases oxygen availability for weathering. Conversely, secondary mineral precipitation within pore spaces can reduce the conductivity of rock and may create preferential flow paths [209]. Secondary mineral precipitation and solute transport moderate primary mineral chemical weathering rates by regulating the mineral saturation state [210] and reducing the reactive surface area [211]. Redox conditions and concentrations of solutes in the vadose zone play a crucial role in the chemical weathering process [212, 213]. Future studies could explore the couplings between the bedrock weakening modeled in our study and other hydrologic, climatic, and geochemical characteristics by developing a coupled chemo-hydro-mechanical model. Such a model would need to update solute concentrations, hydraulic properties, and oxygen states during the chemical weathering process.

5.4 Conclusions

The primary contribution of this study is the development of a new model for the effects of biotite weathering on the evolution of micro-cracks in bedrock (i.e., damage). Our results suggest that the physical characteristics of biotite crystals—most importantly aspect ratio and abundance—have a profound effect on the evolution of bedrock damage during

biotite weathering. This implies that relatively minor differences in biotite populations between two otherwise similar rock types can drive significant differences in the progression of rock weakening at the microscale. Similarly, this implies that local differences in biotite character could drive differences in damage development within a single pluton. This has compelling implications for a number of weathering processes, wherein some rock volumes experience minimal weathering and are exposed as bare rock at the Earth's surface, while other rock volumes break down into saprolite and soil (e.g., at the Boulder Creek Critical Zone Observatory in Colorado and the Wind River Range in Wyoming; [214, 215]). More broadly, this supports the hypothesis that spatial variations in biotite characteristics can influence the evolution of topography, hydrology, and nutrient supply, consistent with previous studies.

The importance of biotite in bedrock damage motivates future studies of biotite characteristics in bedrock and saprolite at the mineral and field scale. There are many opportunities for progress here. Bedrock biotite abundances are measured relatively infrequently (e.g., [182, 216]), and biotite aspect ratios are not commonly reported in the literature, so the effect of biotite shape on damage generation remains poorly documented. Future field observations of biotite abundance, aspect ratio, and orientation will be needed to test our model results. Our results further motivate upscaling the model from the microscale evolution of bedrock damage to the macroscale evolution of the fracture network, which will permit investigation of biotite's effects at the saprolite scale.

Part III

Micro-Macro Chemo-Mechanical Healing

Mechanical healing is the process by which a damaged material recovers mechanical stiffness and strength. Pressure solution is a very effective healing mechanism, common in crystalline media. In Chapter 6, a chemo-mechanical homogenization model is formulated to predict the long term healing process in geomaterials. The inclusion is a hollow sphere that contains a spherical void located at the intersection of three grain-to-grain contact planes. Pressure solution induces geometric changes, which are used to calculate the viscous strain rate of the inclusion. Sensitivity analyses at the inclusion scale indicate that under uniaxial compression, the healing rate increases significantly when the compressive stress normal to the larger grain-to-grain contact plane is increased. Hill's inclusion-matrix interaction law is used to upscale strains and stresses at the REV scale. Oedometer tests were simulated for specimens containing spherical inclusions with a uniformly distributed contact plane orientations. It was observed that in samples containing inclusions with different initial void sizes, inclusions with larger voids had a negligible healing rate, and were slowing down the overall healing rate of the REV. In samples with uniformly distributed void sizes, the healing rate was faster. In specimens with smaller grain sizes, principal stresses were more widely distributed in magnitude and the healing rate was higher. For uniform void size distributions, the healing rate increased with initial porosity, but the final porosity change did not depend on the initial porosity of the sample. Principal stresses of higher magnitude were noted in the inclusions that were part of REVs of high initial porosity. In Chapter 7, the micro-macro healing mechanics model proposed in Chapter 6 is applied to understand the time-dependent behavior of halite during the storage phase. CO_2 storage in salt rock is simulated with the FEM, assuming constant gas pressure. The initial state is determined by simulating cavity excavation with a CDM model. Simulation results indicate limited healing potential around salt cavities used for CO_2 storage, but it has to be noted that temperature effects were left out in this study. The proposed modeling framework can be used to optimize some microstructure parameters of crushed salt buffers and it can be extended to other self-healing materials.

CHAPTER 6

CHEMO-MECHANICAL HEALING FRAMEWORK FOR SALT ROCK

Self-healing materials gained interest in recent years, due to their long term performance [217, 6, 218]. Healing, the process by which a damaged material recovers mechanical stiffness and strength, can be due to different mechanisms. Voyiadjis [219] distinguished active systems, which are coupled with damage mechanisms [220, 221] and passive systems, which are triggered by external stimulations [222]. Salt rock is an attractive host material for geostorage, because of its favorable creep, permeability, and healing properties. Diffusive mass transfer in salt rock leads to crack rebonding and the recovery of mechanical stiffness, and the transferring rate can be enhanced at a higher temperature [6]. With the aid of brine film, the healing rate in salt rock largely increases. The chemical healing of cracks is driven by surface energy reduction, and the salt recrystallinzation occurs at crack faces [223].

Pressure solution, crystal slip plasticity and grain boundary sliding are three important densification mechanisms in salt, observed under uniaxial loading [224, 225]. The densification rate is largely influenced by crystallographic orientations, crystal boundary orientations, density, temperature and the loading history. In addition, when salt aggregates are saturated and compacted in brine, the densification rate increases rapidly. Larger effective stress and smaller grain size also lead to rapid creep [226]. Under high temperature and large stress, recrystallization can be observed in some highly strained areas, but overall, porosity decreases. During uniaxial creep tests, halite polycrystals become denser and mainly deform because of crystal-to-crystal interactions. In brine-saturated halite polycrystals, deformation is first driven by pressure solution, due to the development of normal stress at the grain contacts. Second, deformation happens because the grain boundaries are lubricated due to the presence of fluid. Third, grain scale cataclasis occurs due to crystal

slip plasticity and grain boundary sliding. When the compressive effective stress is less than -4 MPa, creep is dominated by pressure solution. When the compressive effective stress is larger than -4 MPa (i.e., when the effective stress is less than -4 MPa), plastic related mechanisms, such as dislocation, microcracking and recrystallization, have a significant effect on the deformation of the polycrystal. In this study, we focus on halite under low compressive stress conditions (i.e., between -4 MPa and 0 MPa) and at ambient temperature, in which creep is controlled by pressure solution.

A microphysical model for healing in rocksalt was proposed at the crack scale, taking diffusive mass transfer as the controlling mechanism in the longer term [223]. Deformation measures were conducted at the contact between polished flat lenses immersed in saturated brine, to understand the fundamental pressure solution mechanisms at halite-halite and halite-silica contacts [227]. Phenomenological creep models were formulated to account for effective diffusivity, and calibrated against experiments conducted on rocksalt [228, 229] and calcite [230]. A compaction model that distinguishes dissolution, precipitation and diffusion - dominated creep rates was also proposed for anhydrite, assuming a simple cubic packing of spherical grains [231].

In this chapter, we proposed a homogenization scheme to couple chemical and mechanical microstructure changes in a self-consistent micro/macro model and to predict the mechanical behavior of self-healing materials. We formulate a chemo-mechanical homogenization model to predict time-dependent healing processes in halite, which we consider as a model geomaterial.

6.1 Microscopic chemo-mechanical model

6.1.1 Dissolution at grain contacts in salt rock

When subjected to normal stress, salt crystals dissolve at contacts. Ions diffuse along fluid films at crystals' boundaries and precipitate on pore walls. In the following, we analyze the thermodynamic processes that govern pressure solution at one grain contact. We assume

that flat grain edges that are "in contact" are separated by a thin fluid film [231], as shown in Figure 6.1, which summarizes the main mechanisms of pressure solution mechanisms [147].

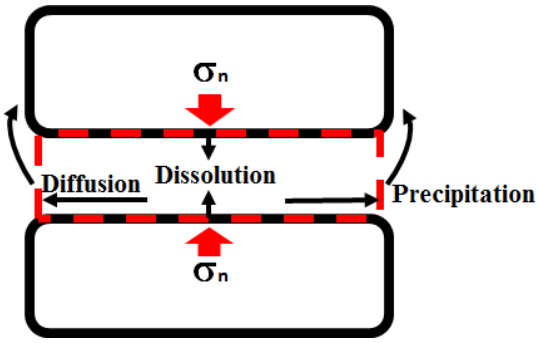

Figure 6.1: Pressure solution mechanisms

Locally (i.e. at the grain scale), an increase of normal effective stress in the solid skeleton changes the difference of chemical potential of the solid constituent of the REV (e.g., halite) in reference to the solute (e.g. brine), as follows:

$$\triangle\mu \approx (\sigma_n - P_f)\Omega \tag{6.1}$$

where σ_n is the normal stress at the grain contact (averaged on the surface of the contact), P_f is the pore fluid pressure, and Ω is the molar volume. The change of chemical potential of the solute can be expressed as a function of the mineral concentration:

$$\triangle\mu \approx R^*T\ln\left(\frac{C}{C_o}\right) \tag{6.2}$$

where C is the concentration of minerals (ions) in the fluid, C_o is a reference concentration, R^* is the gas constant and T is the Kelvin temperature. Assuming a linear dissolution law, common for halite, [232], the expression of the dissolution velocity V_c at the contacts (i.e., at grain scale) is [233]:

$$V_c = \alpha k_+ \Omega \frac{\triangle C}{C_o} \tag{6.3}$$

where α is a parameter describing the influence of grain boundary structure on pressure solution rate (α = 1 for dissolution, α = 0.9 for precipitation), k_+ is the unstressed mineral dissolution rate, which is constant at the reference pressure. At a given contact, dissolution, diffusion and precipitation processes are serial, thus the dissolution velocity at grain contacts is controlled by the slowest of these processes. The expressions for dissolution controlled interface dissolution velocity V_s and precipitation controlled interface dissolution velocity V_p are obtained from Eq.6.1, Eq.6.2 and Eq.6.3, as follows:

$$V_s = \alpha_s k_+ \Omega \left[\exp\left(\frac{\sigma_n^e \Omega d_s^2}{R^* T a_c} - 1 \right) \right] \tag{6.4}$$

$$V_p = \alpha_p k_+ \Omega \left[\exp\left(\frac{\sigma_n^e \Omega d_s^2}{R^* T a_c} - 1 \right) \right] f(\phi^*) \tag{6.5}$$

where σ_n^e is the effective stress on the grain boundary, d_s is the diamter of the grain, a_c is the contact area. $f(\phi^*)$ is a function of porosity ϕ^* and initial porosity ϕ_o^*. Based on the equation of mass conservation, $f(\phi^*)$ equals to $\phi^*/(\phi_o^* - \phi^*)$ [231].

6.1.2 Sphere inclusion model

We upscale the grain-scale pressure solution model to the laboratory sample scale by homogenization. We use a self-consistent scheme, in which inclusions are spherical composites, made of an spherical pore that lies at the intersection of three grain contact planes. The inclusion thus contains a pore and 8 grain fractions, see Figure 6.2a. Noting r_g the radius of the ellipsoidal inclusion, W the thickness of the solid part around the pore contained in the sphere (called wall thickness in the following), and assuming that W is uniform around the pore, the spherical void's dimensions are $2r_g - 2W$. The plane that contains the axes x and y (respectively y and z, x and z) is noted XY (respectively YZ, XZ). Grain contact planes within an inclusion are shown in Figure 6.2b. The Representative Elementary Volume (Figure 6.3) is the volume that contains a representative distribution of inclusion types,

which can be defined in terms of inclusion size, pore size, inclusion orientation (or grain contact plane orientation).

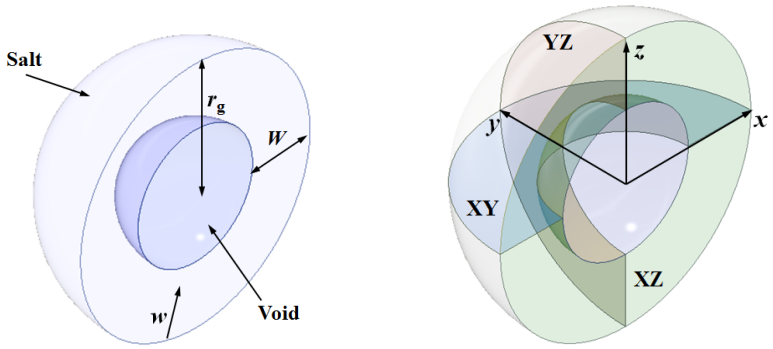

(a) Geometry of the inclusion: hollow soild ellipsoid

(b) Grain contact planes in the inclusion: the pore is at the intersection of three contact planes

Figure 6.2: Schematic of an inclusion

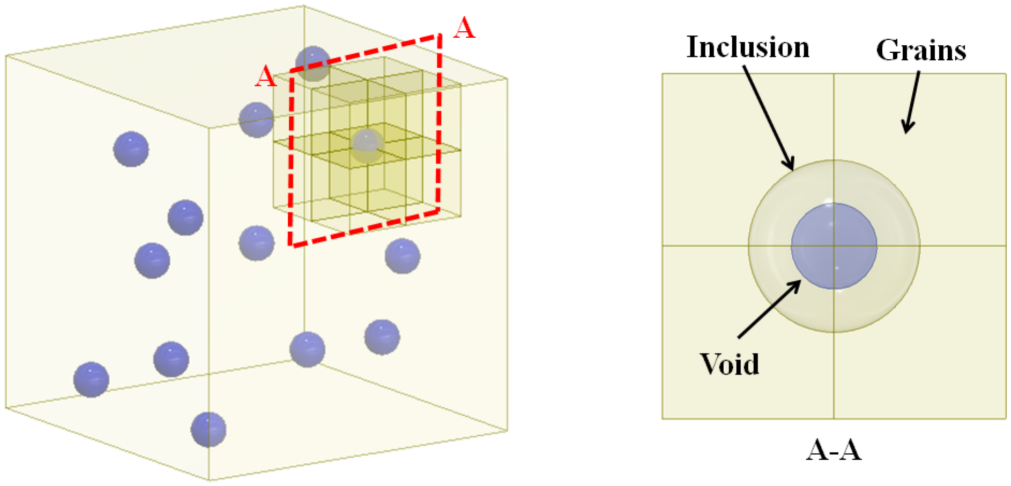

Figure 6.3: REV of salt

At the inclusion scale, under normal stress, the solid mineral is dissolved at contact planes, the solute diffuses along the contact planes towards the pore inside the inclusion, and precipitates at the pore wall. The equation of mass conservation can be written as:

$$J(w)A_{ew} = \frac{2V_c A_{er}}{\Omega} \tag{6.6}$$

Equation 6.6 indicates that the mass of mineral that diffuses radially from the contact planes towards the pore inside the inclusion, through the annulus that has the thickness of the fluid film S and the perimeter of the pore wall $P(w)$, is equal to the mass of mineral that is dissolved at the contact planes. $J(w)$ is the radial diffusion flux at any location along the grain boundary, A_{ew} is the area of the annulus, equal to the product of S by $P(w)$. A_{er} is the area of the contact surface on the plane where dissolution occurs, which has the shape of a ring. We have: $A_{er} = (2r_g - w^2)\pi$

Differentiating Eq.6.2 with respect to C yields $\partial\mu/\partial C = R^*T/C$. Moreover, the radial diffusion flux $J(w)$ is related to the chemical potential μ according to Fick's first law:

$$J(w) = -D\frac{\partial C}{\partial w} = -\frac{DC(w)}{R^*T}\frac{\partial \mu}{\partial w} \tag{6.7}$$

where D is the grain boundary diffusion coefficient. The energy dissipation per unit volume, noted $\dot{\Delta}_w$, is equal to $-J(w)\partial\mu/\partial w$ [152]. The radial energy dissipation increment is thus:

$$d\dot{\Delta}_w = -J(w)\frac{\partial \mu}{\partial w}SP(w)dw \tag{6.8}$$

Under low stress conditions, we assume that the solute concentration $C(w)$ along the grain boundary is equal to that in the pore, C_o [147, 151, 231]. Integrating the radial energy dissipation increment over the distance that goes from a point at the periphery of the inclusion to the pore wall, and using both Eq.6.6 and Eq.6.7, we obtain the expression of the total dissipation $\dot{\Delta}_t^{XY}$ on a contact plane, as follows:

$$\dot{\Delta}_t^{XY} = \int_0^W \frac{2R^*T{V_c^{XY}}^2\pi(2r_g w - w^2)^2}{DC_o S\Omega^2(r_g - w)}dw \tag{6.9}$$

where we took contact plane XY as an example. V_c^{XY} is the dissolution velocity on plane XY in the direction of z axis. Assuming all the work input on the grain boundary is entirely

dissipated by pressure solution, the total dissipation can also be calculated as:

$$\dot{\Delta}_t^{XY} = \sigma_n^{eXY} V_c^{XY} (2r_g W - W^2)\pi \tag{6.10}$$

where σ_n^{eXY} is the normal effective stress on plane AB. Substituting Eq.6.9 into Eq.6.10, the dissolution velocity normal to the contact plane XY is expressed as:

$$V_c^{XY} = \frac{DSC_o\Omega^2\sigma_n^{eXY}\,(2r_g W - W^2)}{R^*T\int_o^W \frac{(2r_g w - w^2)^2}{r_g - w}dw} \tag{6.11}$$

The rate of mineral volume dissolved, $\dot{V}_{XY}$, depends on the dissolution velocity on plane XY and on the area of the contact surface: $\dot{V}_{XY} = (2r_g - W^2)\pi V_c^{XY}$. The dissolution velocity and the rate of volume dissolved on planes YZ and XZ can be obtained in the same way. The chemical viscous strain rate $\dot{\epsilon_x}$, $\dot{\epsilon_y}$ and $\dot{\epsilon_z}$ are obtained from the dissolution velocity on planes YZ, plane XZ and plane XY respectively. The mineral only dissolves on the contact planes. In addition, we assume that the mineral precipitates on the pore wall uniformly. Thus, the change of thickness δW^i at time step t_i can be calculated from the total volume of mineral dissolved and from the pore's surface area A_s^{i-1} at time step t_{i-1}. Diffusion and precipitation processes are illustrated for plane XY in Figure 6.4. We finally obtain:

$$\dot{\epsilon_x} = V_c^{YZ}/r_g \tag{6.12}$$

$$\dot{\epsilon_y} = V_c^{XZ}/r_g \tag{6.13}$$

$$\dot{\epsilon_z} = V_c^{XY}/r_g \tag{6.14}$$

$$\delta W^i = \frac{\dot{V}^i_{XY} + \dot{V}^i_{YZ} + \dot{V}^i_{XZ}}{A^{i-1}_s}\delta t \tag{6.15}$$

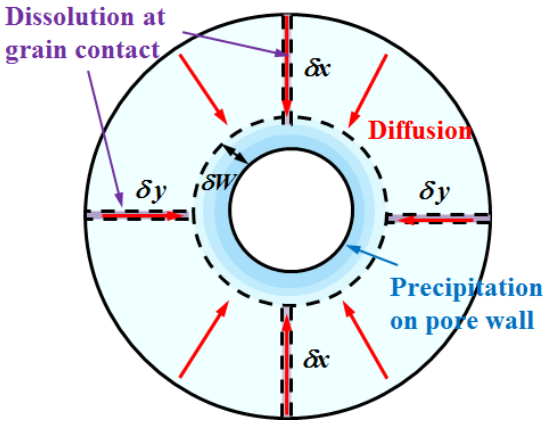

Figure 6.4: Mass transfer governed by pressure solution, in contact plane XY

where δt is the time step.

A creep test is simulated at the inclusion scale under isotropic stress. The inclusion size and the chemical parameters used in the simulations are listed in Table 6.1. Simulation results are presented in Figure 6.5 for isotropic conditions.

Table 6.1: Inclusion parameters in the isotropic and uniaxial creep tests

Initial size		Chemical property		
r_g	W_o	DS	C	Ω
mm	mm	mm^3/s	mol/mm^3	mm^3/mol
0.3	0.05	1×10^{-8}	6.48×10^{-6}	2.7×10^4

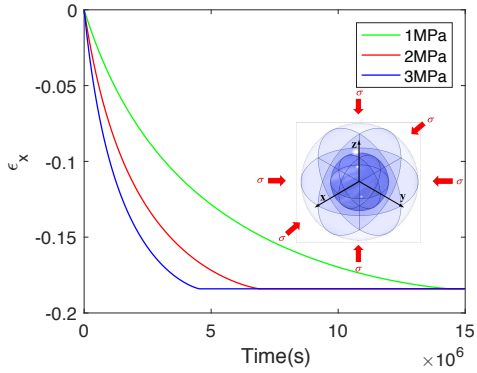

(a) ϵ_x vs. time

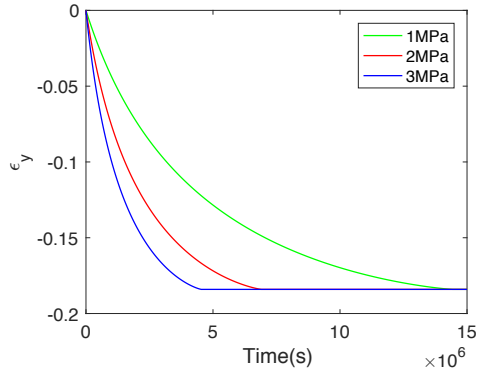

(b) ϵ_y vs. time

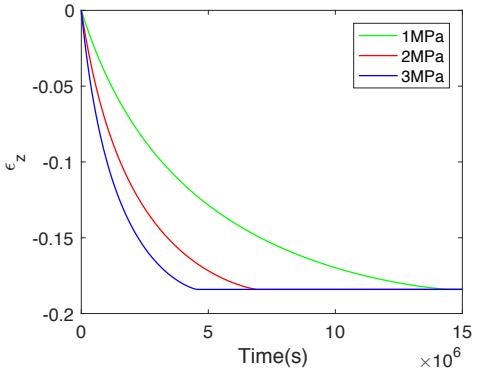

(c) ϵ_z vs. time

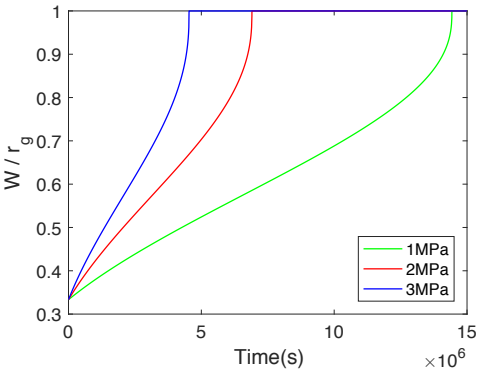

(d) W/r_g vs. time

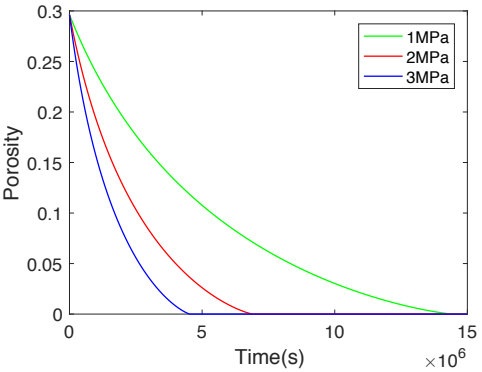

(e) porosity vs. time

Figure 6.5: Evolution of inclusion geometry during an isotropic creep test

Isotropic compressive stress induces dissolution on each contact plane, which leads to a reduction of the dimension of the spherical inclusion perpendicular to each contact plane: ϵ_x, ϵ_y and ϵ_z increase. Because of symmetry of stress condition and inclusion geometry, ϵ_x, ϵ_y and ϵ_z are equal. The solute precipitates at the pore wall. Precipitation stops when the dimensions of the wall is equal to the radius of inclusion: this corresponds to the case when the pore is fully filled with precipitated solid mineral, i.e. when the inclusion is fully healed. When precipitation stops, the inclusion stops deforming and ϵ_x, ϵ_y and ϵ_z reach a plateau. Figure 6.9a, Figure 6.5b, and Figure 6.5c reflect this process and confirm that the healing rate increases with the magnitude of the external stress imposed during the creep test. The time to achieve full inclusion healing is 1.4431×10^7 seconds (107 days), 6.9039×10^6 seconds (80 days) and 4.5374×10^6 seconds (52 days), under under 1 MPa, 2 MPa and 3 MPa, respectively. Since precipitation is assumed to be uniform on the pore wall, the geometry of the fully healed inclusion is determined by the initial dimensions of the inclusion rather than by the external stress conditions. The healing rate does not vary linearly with stress but instead, is influenced by the geometry of the contact, in agreement with Eq.6.16. Figure 6.9c shows that the rate of porosity change decreases over time, which indicates that the highest efficiency of healing is reached at the early stage of the creep test.

The final geometry of the healed inclusion depends on its orientation relative to the direction of major compressive stress. In order to study healing-induced anisotropy, we simulate uniaxial creep tests for various inclusion orientations, defined by three angles ψ (coordinates x′y′z′), θ (coordinates x″y″z″) and ϕ (coordinates x‴y‴z‴), as shown in Figure 6.6. Due to the symmetry of the loading under uniaxial stress conditions, ψ has no influence on the deformation of the inclusion, thus we focus the parametric study on angles θ and ϕ. In total, 13 cases are simulated with different combinations of orientation variables (θ, ϕ), and shown in Figure 6.7. Note that when θ equals to 0, a rotation by an angle ϕ does not influence the strain rate of inclusion. Because of the symmetry of sphere, orientation variables from 0° to 45° are simulated.

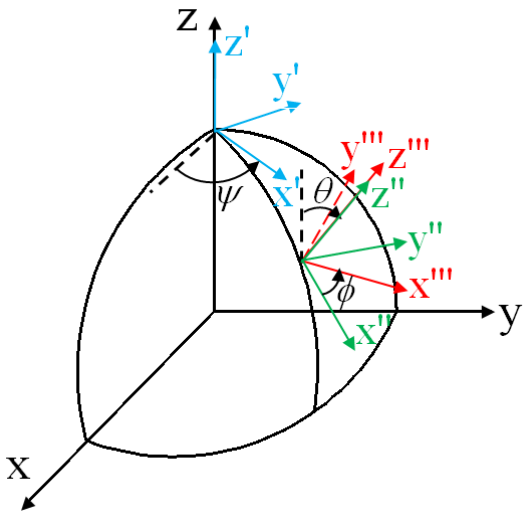

Figure 6.6: System of angles adopted to define the orientation of the inclusion relative to the loading axis in uniaxial creep tests

If $\phi = 0$, the normal to plane XY gets closer to the loading axis z when θ decreases from 45° to 0°, and the dissolution rate in plane XY increases, leading to an acceleration of ϵ_z. According to Figure 6.7a and Figure 6.7b, for non-zero values of ϕ and θ, the dissolution rate in planes YZ and XZ (leading to a increase of ϵ_x and ϵ_y respectively) increases with θ. For a given non-zero value of θ, increasing ϕ increases the dissolution rate in plane XZ (leading to an acceleration of ϵ_y) and decreases the dissolution rate in plane YZ (leading to a deceleration of ϵ_x). For the initial dimensions chosen in this parametric study, Figure 6.7c shows that strain rate $\dot{\epsilon_z}$ is controlled by angle θ. $\dot{\epsilon_z}$ reduces when θ increases, which results in a larger value ϵ_z at the final stage, when healing is complete. ϕ does not influence the strain rate $\dot{\epsilon_z}$ significantly.The evolution of the wall thickness (Figure 6.7d) and of porosity (Figure 6.7e) indicate the efficiency of the healing process. The healing rate decreases over time. For inclusions with different orientations, the trace of given stress matrix is a constant. As the healing speed is controlled by the normal forces on grain planes, the healing efficiency of inclusions with variant orientations is equal.

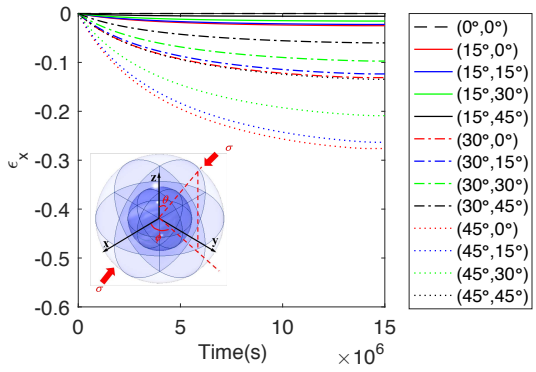

(a) ϵ_x vs. time

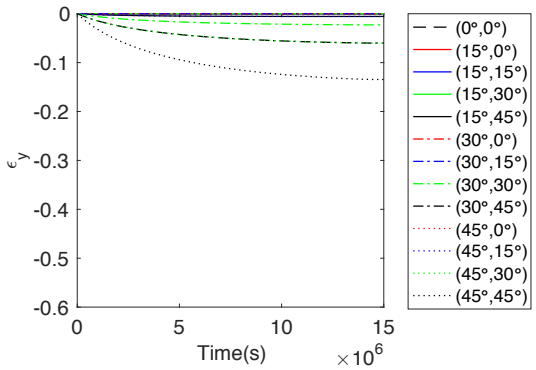

(b) ϵ_y vs. time

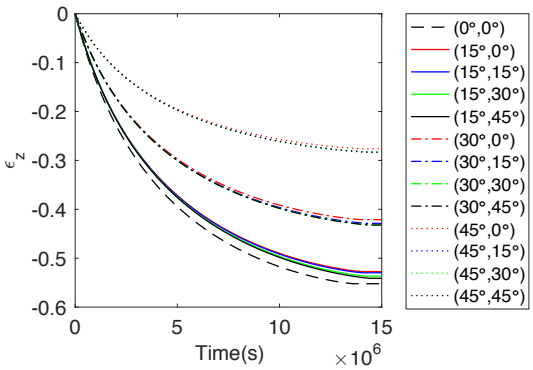

(c) ϵ_z vs. time

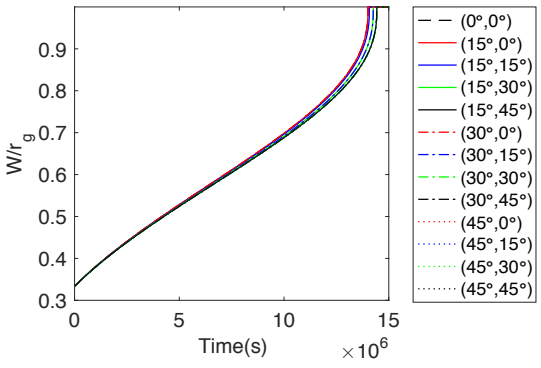

(d) W/a_o vs. time

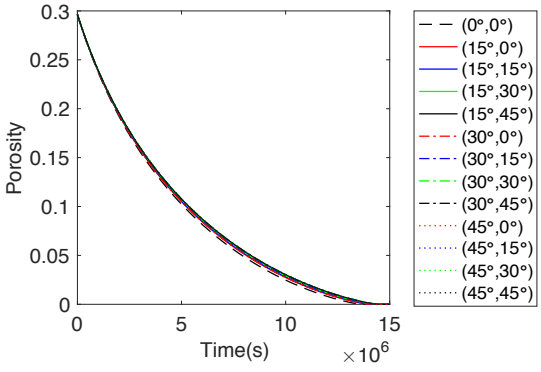

(e) porosity vs. time

Figure 6.7: Evolution of inclusion geometry during a uniaxial creep test

6.1.3 Ellipsoid inclusions

We now replace the inclusions (called cells) by ellispoids in order to account for the anisotropy induced by healing (Figure 6.8a). The axes of an ellipsoid are noted a, b and c. We assume that the voids in the inclusions are also ellipsoidal, and that the thickness of the wall in uniform. We note W the wall thickness. The lengths of the axes of the ellipsoidal void are thus $a-2W$, $b-2W$ and $c-2W$. Like for the isotropic model, we consider three contact planes (AB, AC and BC respectively) which each contain two of the inclusion axes (a and b, b and c, and a and c, respectively). These contact planes separate the ellipsoid into 8 salt grain fractions (Figure 6.8b). The salt diffusion and precipitation processes on plane represented in Figure 6.8c for plane AB.

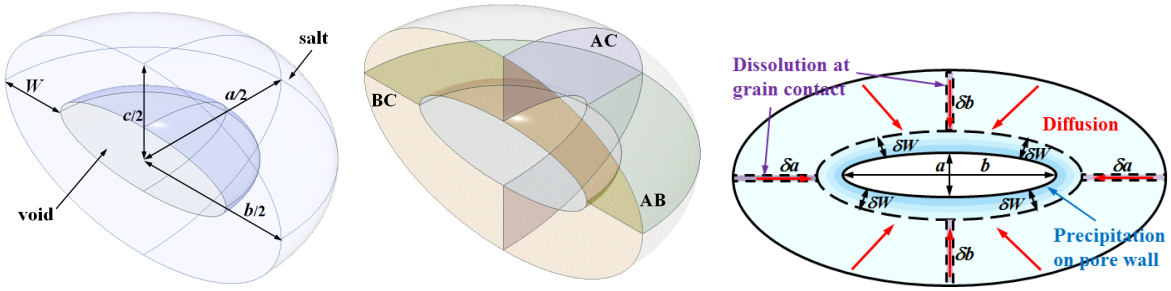

(a) Geometry of a cell (b) Grain contact planes in a cell (c) Pressure solution on plane AB

Figure 6.8: Microstructure of an elliptical elementary inclusion (cell)

The dissolution rate on each boundary plane does not only depend on the normal stress on that contact plane, but also on the dimensions of ellipse. The dissolution velocity in a spherical inclusion (Eq. 6.16) is extended for an ellipsoidal contact surface, as follows:

$$V_c^{AB} = \frac{DSC_o\Omega^2\sigma_n^{eAB}\left(aW+bW-2W^2\right)}{\pi R^* T\int_o^R \frac{\left(aw+bw-2w^2\right)^2}{P(w)}dw} \tag{6.16}$$

The dissolution velocity can be expressed in the same way along planes BC and AC. The incremental change in the dimensions a, b and c are determined from the dissolution rates on plane BC, plane AC and plane AB respectively. Assuming that all the mineral that

is dissolved at the grain boundary precipitates on the void wall uniformly, the incremental wall thickness change δW^i at time step t_i can be calculated from the total volume of mineral dissolved and from the surface area of the void at time step t_{i-1}, noted A_s^{i-1}. To illustrate the effect of chemical healing over time, we simulate the response of a single cell to isotropic stress and uniaxial stress, for various contact plane orientations. As an example, we choose axis lengths typical of salt, with a, b, and c equal to 0.3 mm, 0.25 mm, and 0.2 mm respectively. The deformation of elementary cells is shown in Figure 6.9 and Figure 6.10 for isotropic stress conditions and uniaxial stress conditions, respectively. We use the same chemical parameters and stress conditions as in the isotropic model (Section 6.1.2) .

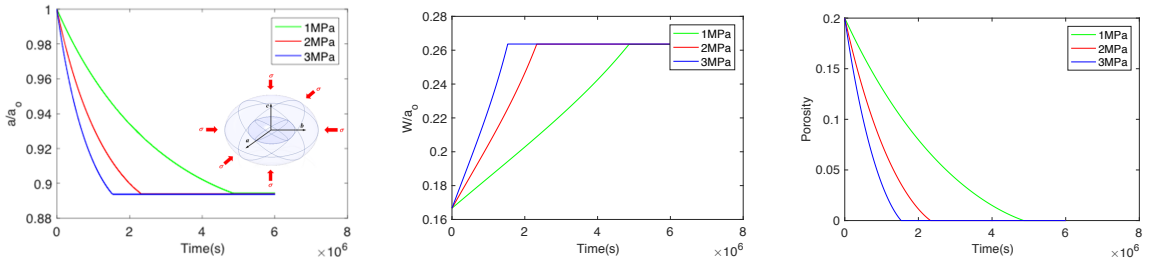

(a) a/a_o vs. time (b) Wall thickness vs. time (c) Porosity vs. time

Figure 6.9: Time-dependent deformation of ellipsoid cells under isotropic stress conditions

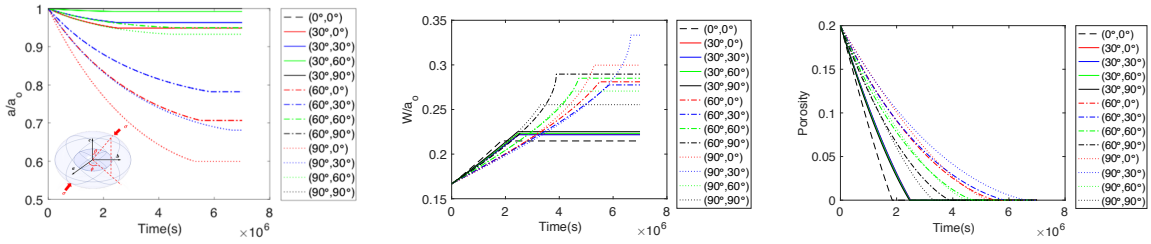

(a) a/a_o vs. time (b) Wall thickness vs. time (c) Porosity vs. time

Figure 6.10: Time-dependent deformation of ellipsoid cells under uniaxial stress conditions. Numbers into brackets indicate angular coordinates (θ, ϕ).

Under isotropic stress conditions, the healing rate is influenced by the magnitude of the external stress. When W reaches either a, b, or c, the void is fully filled by precipitated minerals, and the cell is considered as fully healed. We observe that W (and either a, b or c) reaches a plateau, which marks the time when healing stops. The initial geometry of

the cell dictates the final geometry of the fully healed cell, whereas the stress conditions control the healing rate. In isotropic stress conditions, the healing rate is determined by the direction orthogonal to the ellipsoidal contact plane along which the largest mass of mineral is dissolved, i.e. the plane that has the largest area, i.e. the plane perpendicular to the shortest axis of the ellipsoidal cell. As a result, deformation is the largest in the direction of the shortest axis c, and higher external stress leads to faster healing rate. The evolution of the cell wall thickness in Figure 6.9b and of the cell porosity in Figure 6.9c are good indicators of healing efficiency. The time needed to completely heal the cell under an isotropic stress of 1 MPa (respectively 2 MPa, and 3 MPa) is 4.8329×10^6 seconds (respectively 2.3110×10^6 seconds and 1.5279×10^6 seconds). The healing time are consistent with experiment observation for salt aggregates [226]. The healing rate is not proportional to the external stress, and is also influenced by the contact geometry.

Under uniaxial stress conditions, the healing rate depends on the angle formed by the ellipsoidal axes and the loading axis. The rate of change of length in directions a and b increases with the angle θ. This is because when the components of stress align with directions a and b, a larger stress is exerted on planes BC and AC, leading to larger deformation in directions a and b. Similarly, for a larger angle ϕ, a larger increment of b and smaller increment of a are expected. Healing efficiency can be assessed by observing the reduction of cell porosity in Figure 6.10c. When the stress is parallel to the c axis, the porosity change is the fastest and the increments of a and c are the largest. This is because of the larger grain contact area, which allows more mineral to diffuse to the center void along the grain boundaries. As a result, more mineral precipitates on the void wall. As a result, the cell needs less time to be fully healed. The healing rate decreases when the orientation of stress departs from the orientation of the c axis. For larger values of θ, the healing behavior is very sensitive to the angle ϕ. When θ is small (for example when θ is equal to 30°), ϕ has a negligible influence on the changes of porosity. The healing rate decreases over time; this trend is particularly visible for the cells with low healing efficiency. The longest time

needed to full heal the cell is when θ equals to 90° and ϕ equals to 30°.

6.2 Homogenization Scheme

6.2.1 Averaging method

We consider a Representative Elementary Volume (REV) made of an assembly of hollow ellipsoidal inclusions that have the properties described in Section 6.1. In order to represent the microstructure of a polycrystal such as halite, we assume that there is no dominating phase in the REV composite: each hollow ellipsoid is thought of as an inclusion embedded in a matrix made of all the inclusions present in the REV, and we employ a self-consistent homogenization scheme to determine the relationship between the stress and strain fields of the REV and those of the inclusions. A macroscopic field can be calculated by averaging its microscopic counterpart over the REV. We consider that the REV can contains inclusions of different volumes, porosity and orientation. Accordingly, we introduce the probability of occurrence of inclusion volume V, inclusion porosity Φ and orientations ψ, θ, ϕ. We introduce the solid angle Λ, defined such that $d\Lambda = \sin\theta \mathrm{d}\theta \mathrm{d}\psi$. The probability of the occurrence of orientation(ψ, θ, ϕ) is the product of the probability of occurrence of the solid angle Λ by the probability of occurrence of the spinal rotation angle ϕ. Thus, the probability density function of the inclusion orientation (ψ, θ, ϕ) can be expressed as:

$$\mathrm{d}f(\psi,\theta,\phi) = f(\psi,\theta,\phi)\sin\theta \mathrm{d}\psi \mathrm{d}\theta \mathrm{d}\phi \tag{6.17}$$

The average of probability function $\bar{f}$ (ψ, θ, ϕ) is defined as [109]:

$$\bar{f}(\psi,\theta,\phi) = \frac{1}{\Lambda^*}\int_{\Lambda^*} f(\psi,\theta,\phi)\sin\theta \mathrm{d}\psi \mathrm{d}\theta \mathrm{d}\phi = \frac{1}{8\pi^2}\int_{\psi=0}^{2\pi}\int_{\theta=0}^{\pi}\int_{\phi=0}^{2\pi} f(\psi,\theta,\phi)\sin\theta \mathrm{d}\psi \mathrm{d}\theta \mathrm{d}\phi \tag{6.18}$$

In addition to inclusions' orientation, the inclusion distribution can also depend on the distribution of inclusions' other properties and is given as:

$$\bar{f}(\psi,\theta,\phi) = \frac{1}{\Lambda^*}\int_{\Lambda^*} f(\psi,\theta,\phi) f_1(v_1)\cdots f_n(v_n)\sin\theta \mathrm{d}\psi \mathrm{d}\theta \mathrm{d}\phi \mathrm{d}v_1 \cdots \mathrm{d}v_n \tag{6.19}$$

where v_i can be inclusion size, void size, etc.

Because the inclusion model has three pairwise perpendicular axes of symmetry which intersect at a center of symmetry, the domains of variation of θ and ϕ reduce to the internal [0, π/2]. In transverse symmetric loading conditions (such as in isotropic, uniaxial, and oedometer tests), the model is symmetric about the z-axis at the REV scale, so that the rotation by an angle ψ does not influence the mechanical response of the REV. Thus in the following, ψ is set equal to 0, without losing the generality of the model. Eq.6.19 is rewritten as:

$$\bar{f}(\psi,\theta,\phi) = \frac{2}{\pi}\int_{\theta=0}^{\pi/2}\int_{\phi=0}^{\pi/2} f(\theta,\phi)\text{sin}\theta\text{d}\theta\text{d}\phi \tag{6.20}$$

We derive a close formulation in which we assume that ϕ and θ are uniformly distributed in the internal [0, π/2]. The model can of course be used for other orientation distributions, depending on available microstructure information.

6.2.2 Inclusion-matrix interaction model

Hill's self-consistent method [107] is used to upscale the mechanical behavior of the inclusions at the scale of the REV, which is viewed as a polycrystal. Hill's incremental inclusion-matrix interaction laws relates the increments of stress and strain at the inclusion scale (noted $\delta\sigma_\alpha$ and $\delta\epsilon_\alpha$ respectively for inclusion α) to the increments of stress and strain field of the REV (noted $\delta\bar{\sigma}$ and $\delta\bar{\epsilon}$ respectively), as follows:

$$\delta\sigma_\alpha - \delta\bar{\sigma} = -L^*\left(\delta\epsilon_\alpha - \delta\bar{\epsilon}\right) - \delta L^*\left(\epsilon_\alpha - \bar{\epsilon}\right) \tag{6.21}$$

where L^* is Hill' tensor, which depends on the shape of the inclusion and on the stiffness of the matrix. In the self-consistent method, the matrix is made of the assembly of inclusions present in the REV, and therefore, the stiffness of the matrix is not known *a priori*. Therefore, the resolution of equation 6.21 is iterative. Note that the stress and strain fields in each inclusion is assumed to be uniform, i.e. we assume that pressure-solution produces a

uniform change of stress and strain in the hollow spherical inclusion. Since we present simulations done with uniform distributions of inclusion orientations, the matrix is isotropic. For spherical inclusions embedded in an isotropic matrix, Hill's tensor is expressed as [107, 91]:

$$L^*_{ijkl} = \frac{\mu^*}{4-5\nu}\left[(3-5\nu)\,\delta_{ij}\delta_{kl} + \frac{7-5\nu}{2}\left(\delta_{ik}\delta_{jl}+\delta_{il}\delta_{jk}\right)\right] \tag{6.22}$$

where ν is the Poisson's ratio of the matrix, and μ^* is the shear modulus of the matrix.

We choose an inclusion constitutive model that reflects a linear dependence of the shear and bulk moduli of the matrix (μ^* and k^*) to the porosity of the REV (ϕ^*), and we assume that the Poisson's ratio of the matrix (ν) is a material constant [109]. The matrix shear modulus is expressed as follows:

$$\mu^* = (1-\phi^*)\mu_o\left(\frac{\bar{\sigma}_e}{\bar{\sigma}_o}\right)^n \tag{6.23}$$

where μ_o is the shear modulus of the solid part of the inclusion, and $\bar{\sigma}_e$ is the external global stress. $\bar{\sigma}_o$ and n are model parameters, that need to be calibrated. The decrease of REV porosity induces an increase of the matrix shear modulus μ^*, which results in a change of Hill' tensor L^*. The incremental change of L^* can be expressed as:

$$\delta L^* = \frac{\partial L^*}{\partial \mu^*}\frac{\partial \mu^*}{\partial \phi^*}\delta\phi^* \tag{6.24}$$

6.2.3 Upscaling calculations

r_g is set to be equal to the radius of grains, which is assumed to be uniform in REV. Since we are using a self-consistent homogenization scheme, equation 6.21 is solved iteratively. At time step t_i, what is known from the previous time step t_{i-1} is: the REV stress $\bar{\sigma}^{i-1}$, the local stress of each inclusion, σ_α^{i-1}, the REV strain $\bar{\epsilon}^{i-1}$, the local strain of each inclusion, ϵ_α^{i-1}, the REV porosity ϕ^{*i-1}, the local porosity of each inclusion,$\phi_\alpha^{*\,i-1}$, and the local radius of the void in each inclusion,r_v^{i-1}. In direction z of the loading, the global axial stress at

time t_i is known ($\bar{\sigma}^i_{zz}$ of known value in an oedometer test, $\delta\bar{\sigma}^i_{zz} = 0$ during a creep test). In both oedometer tests and uniaxial creep tests, the other boundary conditions imposed at time t_i are $\bar{\epsilon}^i_{xy} = 0$, $\bar{\epsilon}^i_{yz} = 0$, $\bar{\epsilon}^i_{xz} = 0$, $\bar{\epsilon}^i_{xx} = 0$ and $\bar{\epsilon}^i_{yy} = 0$. The corresponding local stresses and strains in the inclusions can be obtained as follows:

$$\delta\sigma^i_\alpha - \delta\bar{\sigma}^i + L^{*i}\left(\delta\epsilon^i_{\alpha c} + {\mathbb{C}^i_\alpha}^{-1} : \delta\sigma^i_\alpha - \delta\bar{\epsilon}^i\right) + \delta L^{*i}\left(\epsilon^{i-1}_\alpha + \delta\epsilon^i_{\alpha c} + {\mathbb{C}^i_\alpha}^{-1} : \delta\sigma^i_\alpha - \bar{\epsilon}^{i-1} - \delta\bar{\epsilon}^i\right) = 0 \tag{6.25}$$

By definition, the global stress increment $\delta\bar{\sigma}^i$ (respectively the global strain increment $\delta\bar{\epsilon}^i$) is the average of the local stress increments $\delta\sigma^i_\alpha$ (respectively strain increments $\delta\epsilon^i_\alpha$). The variation of a local strain increment $\delta\epsilon^i_\alpha$ is the sum of the chemical strain increment, due to pressure solution (noted $\delta\epsilon^i_{\alpha c}$) and of the elastic local strain increment (noted $\delta\epsilon^i_{\alpha e}$). Using the expression of the dissolution velocity on each dissolution plane, the local chemical strain increment is obtained by calculating the change of inclusion radius induced by pressure solution under local stress σ^i_α and local stress change $\delta\sigma^i_\alpha$, according to the inclusion model explained in Equation 6.16. Now considering that the void inside the ellipsoidal inclusion remains an ellipsoid upon pressure solution, the void radius is updated over time by using Equation 6.15, as follows:

$$\delta r^i_{\alpha v} = -\frac{\dot{V}^i_{XY} + \dot{V}^i_{YZ} + \dot{V}^i_{XZ}}{A^{i-1}_s}\delta t \tag{6.26}$$

After updating the external radius and the pore radius in each inclusion, the variation of local porosity $\delta{\phi^*_\alpha}^i$ and the variation of global porosity $\delta\phi^{*i}$ can be obtained. In the following, we develop the model for spherical inclusions. The Hill's tensor is updated: δL^{*i}, L^{*i} are calculated according to Eq.6.22, Eq.6.23, and Eq.6.24. The porosity damage model employed at the REV scale is also used at the scale of the inclusion, so that the local stiffness tensor $\mathbb{C}^i_\alpha$ is replaced by $(1 - \Phi_\alpha)\mathbb{C}^i_\alpha$. The local elastic strain increment $\delta\epsilon^i_{\alpha e}$ is then calculated as the product of the inverse of the local stiffness matrix ${\mathbb{C}^i_\alpha}^{-1}$ by the local stress increment, $\delta\sigma^i_\alpha$. The algorithm is explained in the flow chart given in Figure 6.11:

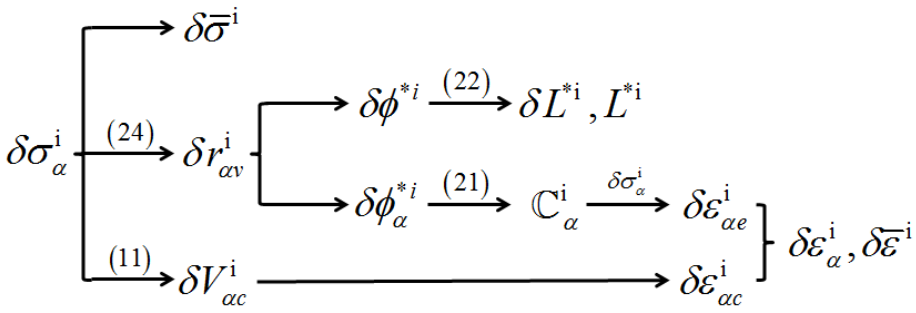

Figure 6.11: Process to update local and global strains from the local stress with the proposed homogenization scheme.

According to the calculation scheme laid out in Figure 6.11, all the unknown variables at time t_i in Eq.6.25 can be regarded as functions of $\delta\sigma_{\alpha}^{i}$. Thus, six components of $\delta\sigma_{\alpha}^{i}$ are unknown for each inclusion, and Eq.6.25 provides six equations. Noting n the number of inclusions in the REV, $6n$ equations have to be solved for $6n$ unknowns at each time step. The Broyden-Fletcher-Goldfarb-Shanno (BFGS) algorithm is employed to solve this system of $6n$ implicit equations. The BFGS algorithm is an iterative optimization method which performs particularly well for solving nonlinear problems [234, 235]. We first obtain a direction $\mathbf{p_k}$, expressed as a function of the approximate Jacobian matrix $\mathbf{B_k}$:

$$\mathbf{p_k} = -\mathbf{B_k}^{-1} f(\mathbf{x_k}) \tag{6.27}$$

Where $f(\mathbf{x_k})$ equals to the left hand side of Eq.6.25, $\mathbf{x_k}$ is a vector that contains the $6n$ components of incremental local stress at iteration step k. $\mathbf{B_k}$ is initialized as the fourth-order identity tensor. Second, the line search method is used to find an acceptable step size α_k in the direction of $\mathbf{p_k}$. Third, the two vectors $\mathbf{s_k}$=$\alpha_k \mathbf{p_k} = \mathbf{x_{k+1}} - \mathbf{x_k}$,and $\mathbf{y_k} = \mathbf{x_{k+1}} - \mathbf{x_k}$ are calculated. Fourth, the matrix $\mathbf{B}$ is updated and used at the next iteration step [236], as follows:

$$\mathbf{B_{k+1}}^{-1} = \mathbf{B_k^{-1}} + \frac{\left(\mathbf{s_k^T y_k} + \mathbf{y_k^T B_k^{-1} y_k}\right)\left(\mathbf{s_k s_k^T}\right)}{\left(\mathbf{s_k^T y_k}\right)^2} - \frac{\mathbf{B_k^{-1} y_k s_k^T} + \mathbf{s_k y_k^T B_k^{-1}}}{\mathbf{s_k^T y_k}} \tag{6.28}$$

The solution of the implicit system of equations converges when $f(\mathbf{x_k})$ is equal to the zero vector. We set the convergence criterion so that the numerical solution $\mathbf{x_k}$ ($\delta\sigma_\alpha^i$) converges when the norm of $f(\mathbf{x_k})$ is smaller than 10^{-12} and the variation between each time step is less than 0.1%. When convergence is reached, $\mathbf{x_k}$ is used to update $\delta\sigma_\alpha^i$. We initialize stress by solving static mechanical balance equations, valid before pressure solution starts. According to Eq.6.21, the corresponding increment of local stress is:

$$\delta\sigma_\alpha^0 = \left(I + \mathbf{L}^{*0}\mathbb{C}_\alpha^{0\,-1}\right)^{-1}\left(\delta\bar{\sigma}^0 + \mathbf{L}^{*0}\delta\bar{\epsilon}^0\right) \tag{6.29}$$

The initial local stress σ_α is calculated as $\sigma_\alpha^0 = \delta\sigma_\alpha^0$. The initial increment of local strain $\delta\epsilon_\alpha^0$ is purely elastic, so $\delta\epsilon_\alpha^0$ equals to $\mathbb{C}_\alpha^{0\,-1}\delta\sigma_\alpha^0$. The initial local strain ϵ_α is initialized as $\epsilon_\alpha^0 = \delta\epsilon_\alpha^0$.

6.3 Model calibration against brine-saturated creep tests

6.3.1 Macroscopic chemical creep of salt rocks and model calibration

Crystal slip plasticity and grain boundary sliding are two important densification mechanisms observed in halite under uniaxial loading [224, 225]. The densification rate is largely influenced by crystallographic orientations, crystal boundary orientations, density, temperature and the loading history. In addition, when salt aggregates are saturated and compacted in brine, the densification rate increases rapidly. Larger effective stress and smaller grain size also lead to rapid creep [226]. Under high temperature and large stress, recrystallization can be observed in some highly strained areas, but overall, porosity decreases. During uniaxial creep tests, halite polycrystals get denser and mainly deform because of crystal-to-crystal interactions. In brine-saturated halite polycrystals, pressure solution first occurs due to the development of normal stress at the grain contacts. Second, the grain boundaries are lubricated, because of the presence of fluid. Third, grain scale cataclasis occurs due

to crystal slip plasticity and grain boundary sliding. When effective stress is less than 4 MPa, creep is dominated by pressure solution. When effective stress is larger than 4MPa, plastic related mechanisms, such as dislocation, microcracking and recrystallization, have a significant effect on the deformation of the polycrystal. In the following, we simulate uniaxial creep tests performed in the laboratory under an axial stress lower than 4 MPa in order to calibrate our micro-macro chemo-mechanical model of pressure-solution.

The volumetric strain curves obtained by Spiers for wet salt aggregates [226] are used to calculate the evolution of brine-saturated halite porosity during uniaxial creep tests. Experimental results obtained under axial stresses of 1.1 MPa and 3.1 MPa are used for calibration. The calibrated model is then compared to the results obtained under an axial stress of 2.1 MPa for verification. The REV is represented by 300 spherical inclusions. The orientations of the grain-to-grain contact plane in the inclusions are uniformly distributed. Due to the geometry adopted for the inclusion, the radius of the inclusion is equal to that of a salt grain. Thus, it is considered uniform in the REV, and equal to 0.1375 mm, according o the experimental data reported in [226]. The initial porosity was 42% in the experiments. Correspondingly, the mean void radius was found to be 0.103 mm. Based on experimental observations [237, 238], we assumed a lognormal distribution for the void radius, with a variance of 0.0001 mm^2. The calibration results are presented in Figure 6.12 and Table 6.2.

Table 6.2: Model parameters found by calibration

Elastic property		Chemical property
n	$\bar{\sigma}_o$	DS
$-$	MPa	mm^3/s
1.035	919	3.75×10^{-8}

Inclusions of different orientations or different initial void radius develop different microscopic principal stresses $\overrightarrow{\sigma}_p$. We represent the 300 minor, middle and major principal stresses on the map shown in Figure 6.13: $\overrightarrow{OT}$ (in the upper right quadrant) represents a tensile principal stress, and $\overrightarrow{OC}$ (in the lower left quadrant) represents a compressive prin-

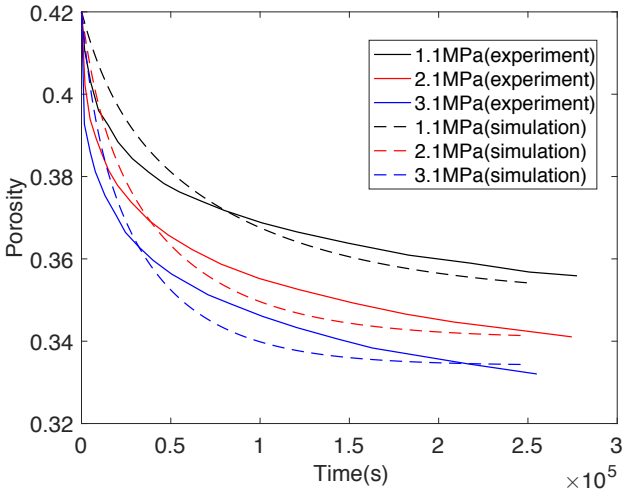

Figure 6.12: Calibration of the model against uniaxial creep tests (tests under 2.1 MPa are used for verification).

cipal stress. α is the angle between the stress eigenvector and the orientation of the loading axis. The principal stresses in the 300 inclusions are shown for the test conducted under an axial stress of 1.1MPa, after 100,000 seconds (27.8 hrs, Figure 6.14) and after 250,000 seconds (69.4 hrs, Figure 6.14a). The dots with a lighter color represent inclusions with smaller voids.

According to Figure 6.14, the major (tensile) principal stresses are oriented close to perpendicular to the loading axis, while the minor (compressive) principal stresses tend to align with the loading axis. The magnitudes of the minor and major principal stresses increase with time. The minor principal stress is nearly zero in some inclusions, while it reaches a value close to 1.5 MPa in some other inclusions. Inclusions with larger initial voids tend to have larger principal stresses. Figure 6.15 illustrates the evolution of local stress as a function of initial void radius and inclusion planes orientation for 10 representative inclusions. Figure 6.15b confirms that before creep starts, the initial state of stress is different in each inclusion, because the inclusions considered have different initial void sizes. After 250,000 seconds, the state of stress is stable in each inclusion. Higher the initial stress, higher the healing rate, lower the inclusion porosity. The compressive principal

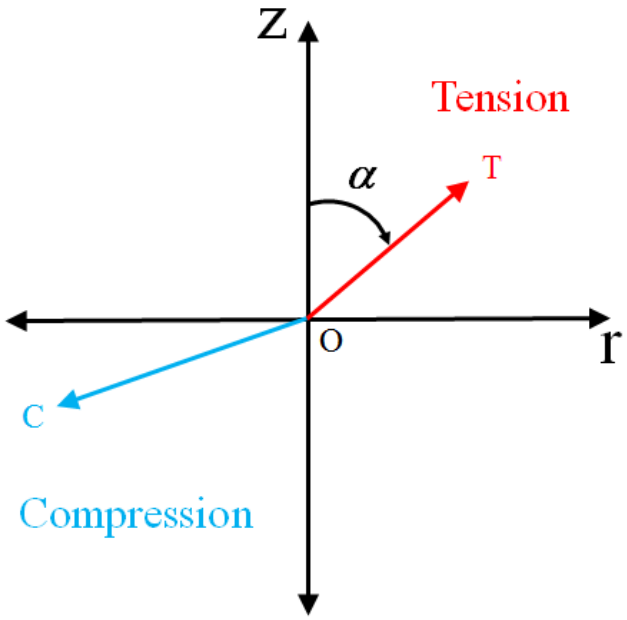

Figure 6.13: Graphical representation of the microscopic principal stresses

stress increases with time for inclusions with small voids, while it decreases for inclusions with large voids. The final compressive principal stress is largely influenced by θ. If θ is close to 0° or 90°, small compressive principal stress is observed.

6.3.2 Sensitivity to the number of inclusions

Sensitivity analyses are performed to determine the minimum number of inclusions that are necessary to consider in the REV. We calibrate our model against oedometer tests performed under axial stresses of 1.1 MPa and 3.1 MPa, for a REV that contains 400 inclusions. We use the calibrated parameters to simulate the oedometer tests for REVs that contain less inclusions, and we find the minimum number of inclusions needed to match the results obtained with 400 inclusions with an acceptable error. Results are presented in Figure 6.16 and Table 6.3. The error made on the estimation of the final porosity is less than 1.00% if the number of inclusions is at least 200. This finding confirms the model calibration presented in Section with 300 inclusions. In the following, we present simulations done with REV of 200 spherical inclusions with a uniform orientation distribution for the

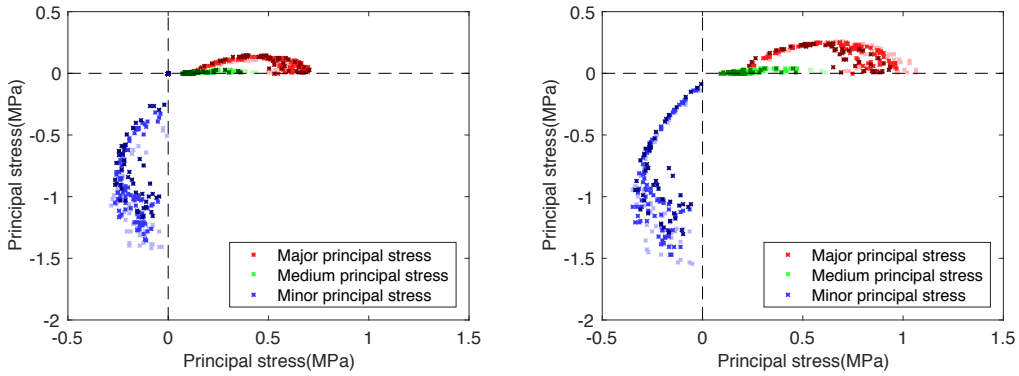

(a) Principal stresses at 100,000s (b) Principal stresses at 250,000s

Figure 6.14: Principal stresses in each inclusion, for a uniaxial creep test under 1.1 MPa.

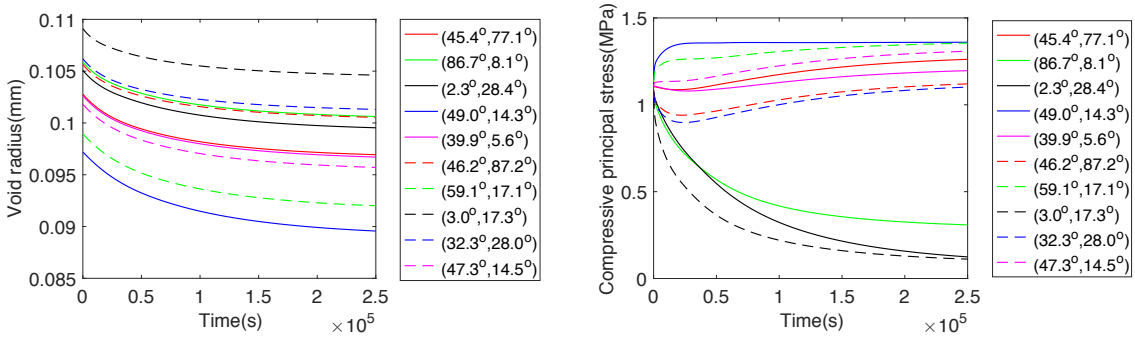

(a) void radius vs. time (b) principal stress vs. time

Figure 6.15: Evolution of the void radius and of the minor compressiver principal stress in 10 different inclusions during the creep test performed under an axial load of 1.1 MPa.

grain-to-grain contact planes. The simulation results with REV of 200 spherical inclusions are stable and consistent with the result of 300 inclusions, which confirms that the number of inclusions is representative.

6.4 Influence of salt fabric on the healing rate and micro-macro creep behavior

We study the sensitivity of the micro-macro model of chemo-mechanical healing to the grain size (which is equal to spherical inclusion size), the initial porosity and the coefficient of variance (COV) of the void radius distribution. The variables used in this parametric study are listed in Table 6.4.

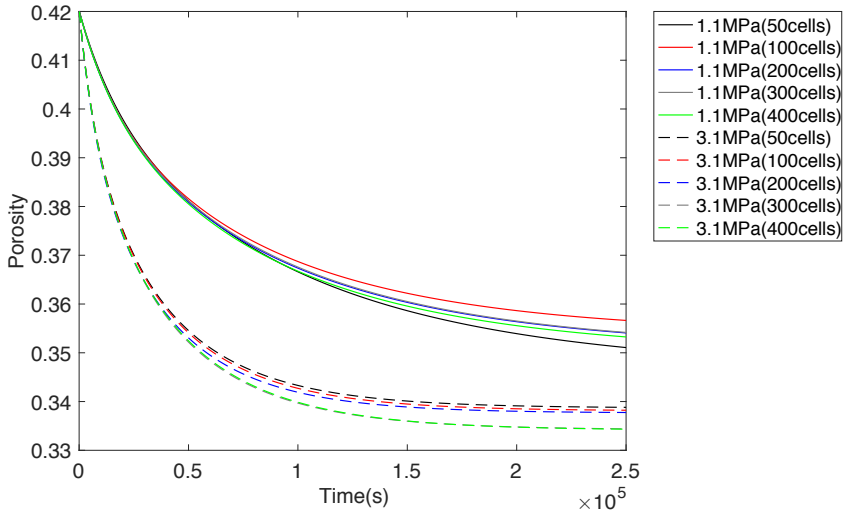

Figure 6.16: Sensitivity analysis on the number of inclusions considered in the REV

Table 6.3: Error made on the estimation of the final porosity, compared to the porosity estimated with 400 inclusions.

Number of cells	50	100	200	300
Error (1.1MPa)	0.62%	0.96%	0.23%	0.26%
Error (3.1MPa)	1.34%	1.16%	1.00%	0.02%

6.4.1 Influence of initial inclusion size

The rate of halite densification is known to be highly dependent on salt grain size. Larger the salt crystals involve less inter-granular cracks in the REV. When salt aggregates are saturated with brine, the size of salt grains not only affects the contact area between grains, but also controls the length of diffusing path. Three cases are simulated, for a grain radius of 0.25 mm, 0.15 mm and 0.05 mm. The porosity of REV is set at 20%, and the COV of the void radius distribution equals to 0.05. An oedometer creep test under 1.1 MPa is simulated. Figure 6.17 shows the corresponding changes of porosity and void radius.

As could be expected from Eq.6.16, a smaller grain radius (or inclusion radius) leads to a larger dissolution rate at the grain boundaries, hence a faster healing rate. Results presented in Figure 6.17a confirm this trend: a smaller grain size results in a faster porosity

Table 6.4: Microstructure parameters used in the sensitivity analysis

Grain's radius(mm)	Initial porosity	COV
0.25	40%	0.1
0.15	20%	0.05
0.05	10%	0.01

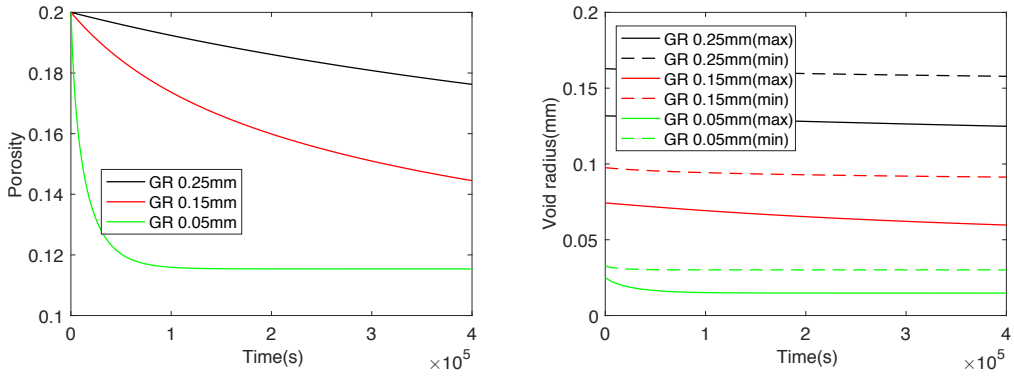

(a) Porosity vs. time

(b) Void radius vs. time

Figure 6.17: Influence of grain size on creep rate

decreasing rate. It is interesting to note that porosity stabilizes to a non-zero value. This is because over time, the macroscopic stress is sustained by less and less inclusions: the inclusions under low stress under go pressure solution at a negligible rate, and therefore, the full healing time cannot be reached during the simulation. Correspondingly, the distribution the void size departs more and more from the initial uniform size distribution. This phenomenon is particularly visible for samples with smaller grains, see Figure 6.17b. When the initial grain radius is 0.05 mm, a minimum void radius is reached, beyond which no further healing is observed. Figure 6.18 shows the microscopic principal stresses in the inclusions, for the three different grain sizes. All the principal stresses are initially compressive, because an oedomenter test is simulated. Then, the major principal stress increases. For small grain sizes, the major and minor principal stresses are widely distributed and the rotation of the principal stresses is significant. Principal stresses do not evolve much once the REV porosity becomes stable.

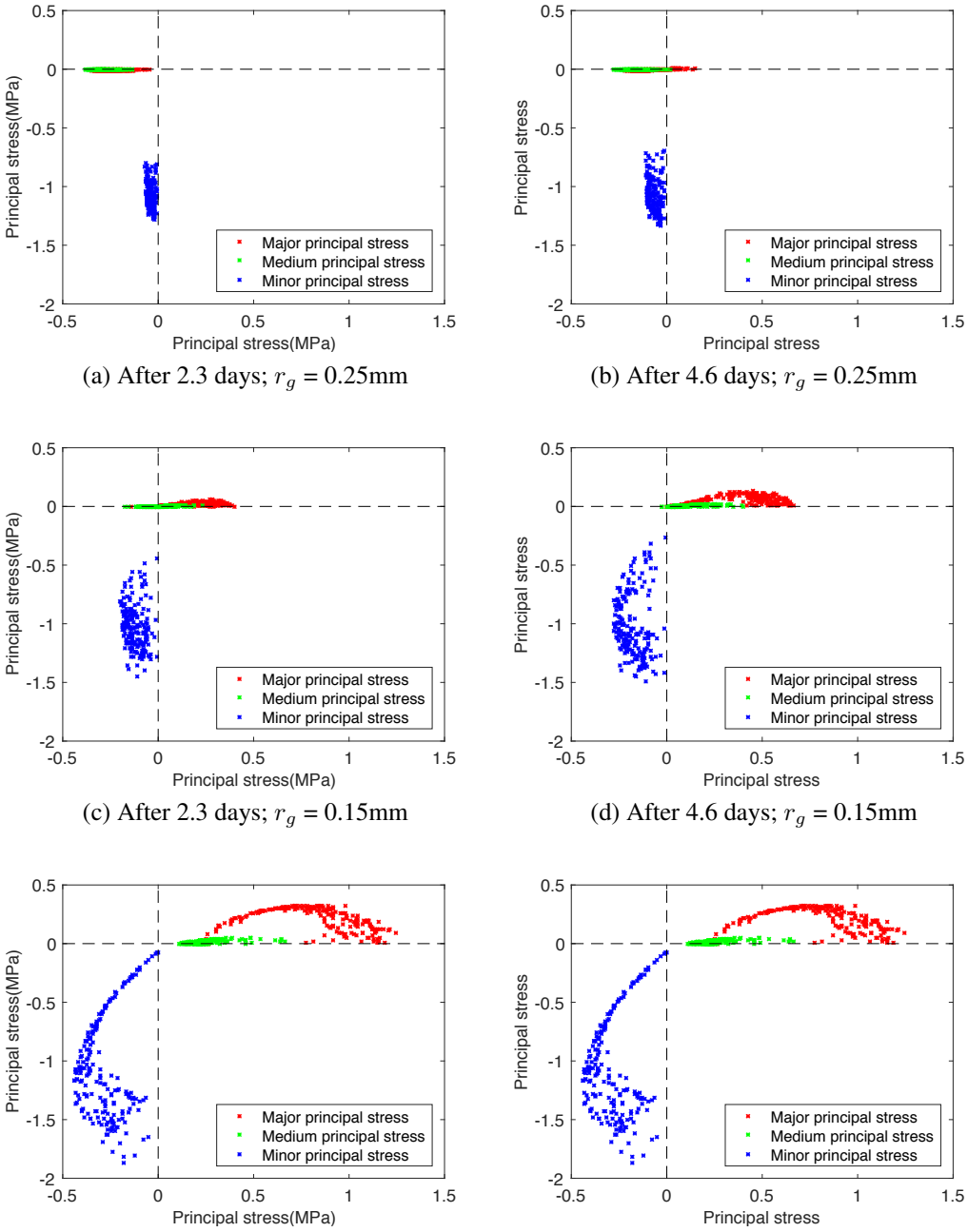

(a) After 2.3 days; $r_g = 0.25$mm

(b) After 4.6 days; $r_g = 0.25$mm

(c) After 2.3 days; $r_g = 0.15$mm

(d) After 4.6 days; $r_g = 0.15$mm

(e) After 2.3 days; $r_g = 0.15$mm

(f) After 4.6 days; $r_g = 0.05$mm

Figure 6.18: Principal stresses obtained during an oedometer test, for different grain sizes.

6.4.2 Influence of initial porosity

Due to its high solubility, salt is easily dissolved in water. Larger void volume in salt rocks usually results in lower stiffness and preferential fluid flow paths. Here, we study the effect of the initial porosity on the deformation of the brine-saturated polycrystal. Oedometer tests under an axial compressive stress of 1.1 MPa are simulated for the a grain radius of 0.15 mm and a void size COV of 0.05, with initial porosities of 40%, 20% and 10%. Figure 6.19 presents the corresponding evolution of the void radius and of porosity. After a test of 4×10^5 seconds, the total porosity decrease is about 5% in all cases. The healing rate of aggregates with higher porosity is very high initially and then slows down, but low porosity leads to stable healing efficiency. Figure 6.20 shows the effect of initial porosity on the distribution of principal stresses in the inclusions. For higher initial porosity, we observe higher major tensile stresses, lower minor compressive stresses and a more significant rotation of principal stress directions over time. For the specimen with the lowest initial porosity, the major tensile principal stress increases rapidly over time, in the radial direction, while the minor compressive stress remains stable.

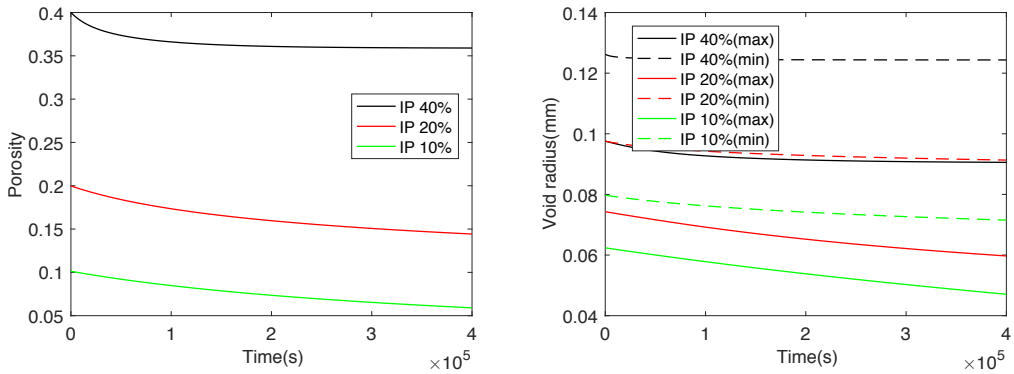

(a) Normalized porosity vs. time

(b) Normalized void radius vs. time

Figure 6.19: Effect of initial porosity on the evolution of porosity and void radius

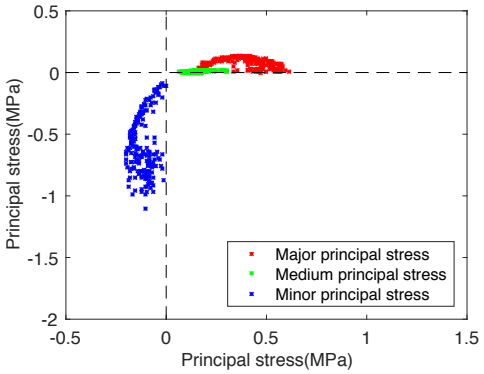

(a) After 2.3 days, initial porosity of 40%

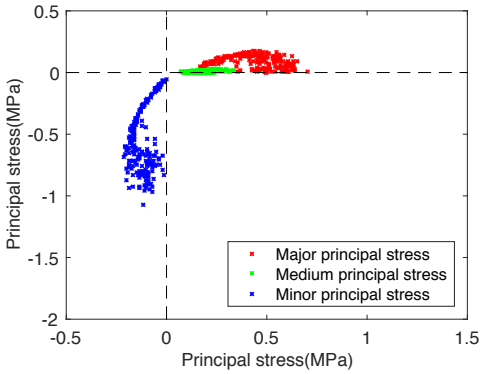

(b) After 4.6 days, initial porosity of 40%

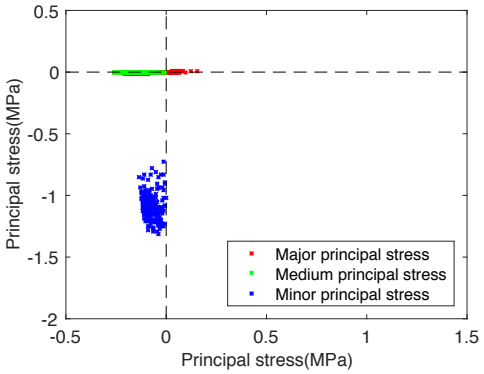

(c) After 2.3 days, initial porosity of 10%

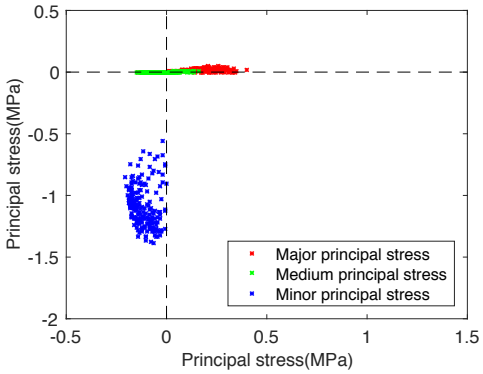

(d) After 4.6 days, initial porosity of 10%

Figure 6.20: Evolution of principal stresses in the inclusions for different initial porosities.

6.4.3 Influence of the variance of the initial void radius distribution

In order to understand the influence of heterogeneous packing on the creep rate, we simulate an oedometer test under 1.1 MPa for specimens of same grain radius (0.15 mm), same initial porosity (20%), but different void size COV. Figure 6.21 shows the corresponding evolution of porosity and void radius during the creep test.

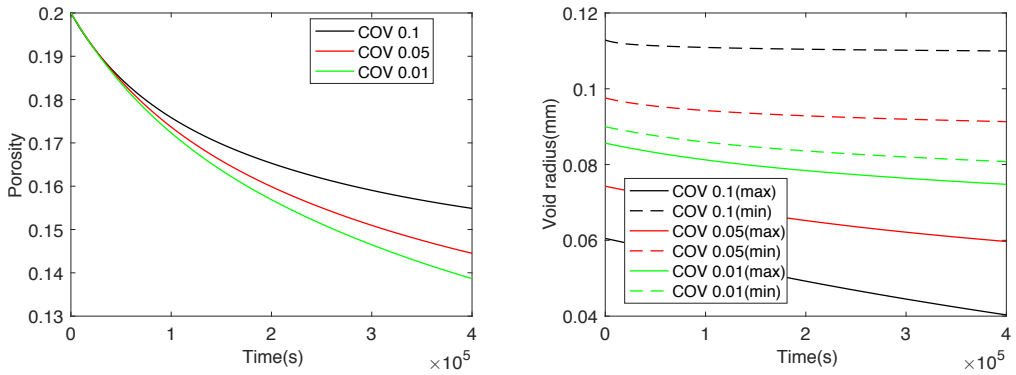

(a) Porosity vs. time (b) Void radius vs. time

Figure 6.21: Influence of the void radius COV on the creep rate

According to Figure 6.21a, the rate of porosity change decreases when the void radius COV increases. This can be explained by the fact that inclusion stiffness increases when the inclusion void size decreases. As a result, inclusions with small voids undergo higher microscopic compressive stress, and heal faster. As healing proceeds in the inclusions that contain smaller pores, the void radius COV increases, which enhances the difference of healing rate between inclusions that contain small pores and inclusions that contain larger pores (Figure 6.21b). Inclusions with large voids never heal completely, which slows down the overall healing rate of the REV. As expected, the distribution of principal stresses is more uniform in a sample that has a smaller void radius COV, see Figure 6.22. Larger tensile stresses and compressive stresses are observed under small void size COV, as shown in Figure 6.22. Low healing rate results in less stress redistribution under large void size COV, and less large tensile stresses and compressive stresses are observed.

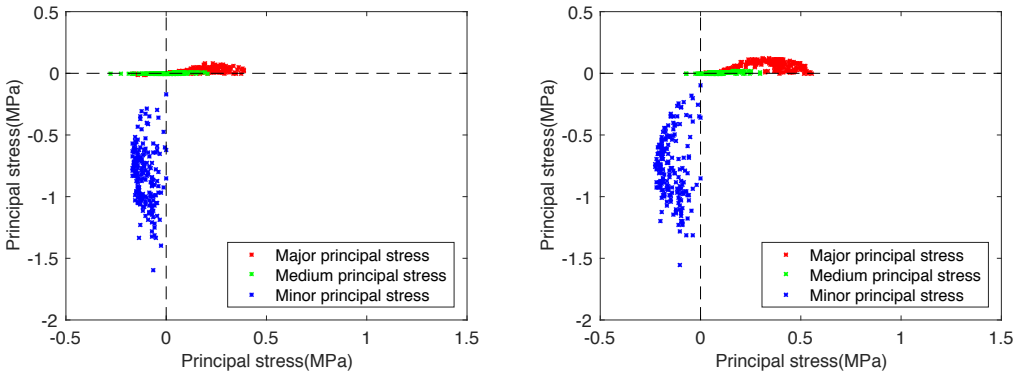

(a) After 2.3 days, COV = 0.1

(b) After 4.6 days, COV = 0.1

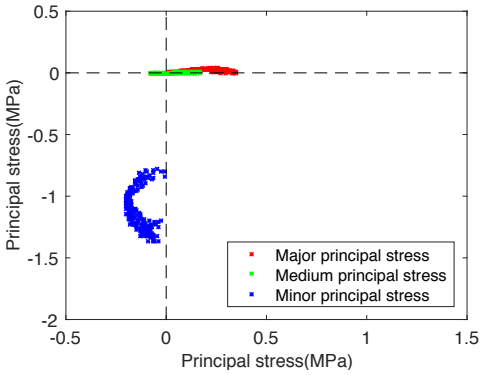

(c) After 2.3 days, COV = 0.01

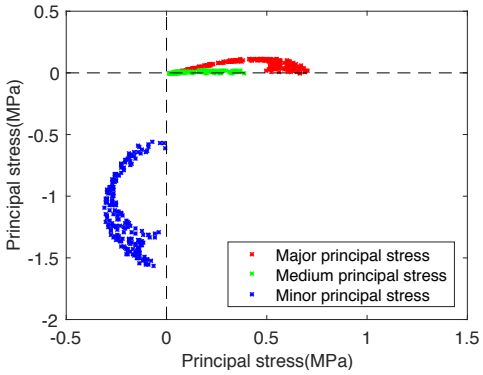

(d) After 4.6 days, COV = 0.01

Figure 6.22: Influence of void radius COV on the evolution of inclusion principal stresses.

6.5 A generalized thermodynamic framework of damage and healing

Thermodynamics is the study of the transformations of all forms of energy involved in the evolution of a system [239]. The two fundamental laws of thermodynamics are energy conservation and the balance of entropy. Thermodynamic analyses were conducted in microporomechanics to predict crack propagation in partially saturated porous geomaterials [154]. A thermo-mechanical CDM model was used to predict the damage and healing in halite [6] under the influence of crack debonding, opening, closure and rebonding. Thermodynamic principles were invoked to derive the constitutive equations from conjugation relationships. In the following, we construct a general thermodynamic framework to model damage and healing with phenomenological variables, in which we account for mass and

energy transfer in a fluid-saturated porous REV endowed with N families of cracks and M families of pores. Pores and cracks are oblate spheroidal inclusions with different shapes and sizes, and pores or cracks that have the same geometry and orientation are considered of the same family.

6.5.1 Helmholtz free energy

Energy is dissipated due to chemical, hydraulic, mechanical and thermal effects, sothe Inequality of Clausius-Duhem (ICD) is expressed as follows [73]:

$$(\boldsymbol{\sigma} : \dot{\boldsymbol{\epsilon}} - S\dot{\tau} - \sum \boldsymbol{\pi}_i : \dot{\boldsymbol{\Phi}}_i + \sum \mu_j^* : m_{cj}^* - \Psi^*) - \frac{q}{\tau} \cdot \nabla\tau \geq 0 \tag{6.30}$$

where Ψ^* is the potential energy of the solid skeleton of the REV; τ is the temperature variation; S is the entropy; $\boldsymbol{\pi}_i$ is the eigenstress in pores of family i, defined as $p_i\boldsymbol{\delta}$; p_i is the pore pressure of pores of family i and $\boldsymbol{\delta}$ is the second-order identity tensor; $\boldsymbol{\Phi}_i$ is a second order tensor, defined as $\phi_i\boldsymbol{\epsilon}_i$, ϕ_i is the volume fraction of pores of family i and $\boldsymbol{\epsilon}_i$ is the strain tensor of pores of family i; μ_{cj} is the chemical potential at cracks of family j; m_{cj} is the number of moles of reacting mineral in cracks of family j; q is heat flow vector.

The potential energy of the solid skeleton (Ψ^*) is defined as:

$$\Psi^* = \Psi + \sum_i^M \boldsymbol{\pi}^i \boldsymbol{\Phi}^i \tag{6.31}$$

where Ψ is the Helmholtz free energy of the solid skeleton. The expression of the potential energy (Ψ^*) is established in terms of global elastic strain $\boldsymbol{\epsilon}^E$, eigenstresses $\boldsymbol{\pi}$, temperature variation τ (state variables), and healing $\boldsymbol{H}$ and damage $\boldsymbol{\Omega}$ (internal variables), as shown in Equation 6.32 below:

$$\Psi^*(\boldsymbol{\epsilon}^E, \boldsymbol{\pi}, \tau; \boldsymbol{\Omega}, \boldsymbol{H}) = \frac{1}{2}\boldsymbol{\epsilon}^E : \mathbb{C}(\boldsymbol{\Omega}) : \boldsymbol{\epsilon}^E + \sum_{i=1}^{n} \boldsymbol{\pi}_i : \boldsymbol{B}_i(\boldsymbol{\Omega}) : \boldsymbol{\epsilon}^E - \boldsymbol{K}(\boldsymbol{\Omega})\tau : \boldsymbol{\epsilon}^E$$
$$- \sum \boldsymbol{\alpha}_j(\boldsymbol{\Omega}) : \boldsymbol{H}_j : \boldsymbol{\epsilon}^E + \sum \sum_{i,j=1}^{n} \boldsymbol{\pi}_j : \boldsymbol{N}_{ij}^{-1}(\boldsymbol{\Omega}) : \boldsymbol{\pi}_i + \sum \sum \boldsymbol{\beta}_{ij} : \boldsymbol{H}_j : \boldsymbol{\pi}_j$$
$$- \frac{1}{2}\frac{C^t(\boldsymbol{\Omega})}{\tau_o}\tau^2 + \sum \boldsymbol{\gamma}_j : \boldsymbol{H}_j\tau + \sum \boldsymbol{\pi}_i : \boldsymbol{\zeta}_i\tau - \sum \sum \frac{1}{2}\boldsymbol{H}_j : \boldsymbol{\eta}_{jq}(\boldsymbol{\Omega}) : \boldsymbol{H}_q \qquad (6.32)$$

where $\mathbb{C}$ is the stiffness tensor homogenized at REV scale; $\boldsymbol{B}$ is the Biot coefficient; $\boldsymbol{N}$ is the Biot modulus; $\boldsymbol{K}(\boldsymbol{\Omega})$ is a second order tensor, defined as $k\alpha_T\phi_s\boldsymbol{\delta}$, α_T is the thermal dilation coefficient, k is the bulk modulus, and ϕ_s is the volume fraction of solid; C is the reduced heat capacity, defined as $C_o^t\phi_s$, and C_o^t is heat capacity of intact solid; α, β, γ, ζ and η are the thermoporoelastic tangent properties.

The definition of the healing variable $\boldsymbol{H}$ depends on the driving mechanism. In the case of pressure solution, the healing variable, noted $\boldsymbol{m}_c^*$, is a second order tensor defined as

$$\dot{\boldsymbol{m}}_{cj}^* = m_{cj}\,\overrightarrow{n}_j \otimes \overrightarrow{n}_j \qquad (6.33)$$

in which $\overrightarrow{n}_j$ is the unit vector normal to the jth crack where m_{cj} moles of mineral react. The force variable that is thermodynamically conjugated to the healing variable, noted $\boldsymbol{\mu}_c^*$, is a tensor that represents the chemical potential of the cracks, as follows:

$$\boldsymbol{\mu}_{cj}^* = \mu_{cj}\,\overrightarrow{n}_j \otimes \overrightarrow{n}_j \qquad (6.34)$$

6.5.2 Hydraulic mechanical coupling

The homogenized stiffness tensor, the Biot coefficient, and the Biot modulus are functions of pores' geometry and of the stiffness of each phase in the porous solid. A modified

Mori-Tanaka homogenization scheme is used to update $\mathbb{C}^{hom}$ [97]:

$$\mathbb{C}^{hom} = \overline{\mathbb{C}\boldsymbol{A}} = \sum_{i=0}^{N+M} \phi_i \mathbb{C}_i : \boldsymbol{A}_i \tag{6.35}$$

with:

$$\boldsymbol{A}_i = \boldsymbol{A}_i^{\infty} \left(\sum \phi_i \boldsymbol{A}_i^{\infty} \right)^{-1} \tag{6.36}$$

$$\boldsymbol{A}_i^{\infty} = \left(I + P^i (\mathbb{C}_i - \mathbb{C}_s) \right)^{-1} \tag{6.37}$$

in which parameters with a 0 subscript refer to the properties of the matrix.

Pore pressure is regarded as the source of eigenstress in the inclusions. According to Pichler [154], the expression of $\boldsymbol{\Phi}_i$ is given as:

$$\boldsymbol{\Phi}_i = \phi_i \boldsymbol{\epsilon}_i \tag{6.38}$$

with:

$$\boldsymbol{\epsilon}_i = \boldsymbol{A}_i : \boldsymbol{\epsilon}^E + \sum \boldsymbol{D}_{ip} : \boldsymbol{\pi}_p \tag{6.39}$$

where $\boldsymbol{D}_{ip}$ is the influence tensor accounting for the effect of the eigenstress of inclusion p on inclusion i. Comparing Equation 6.38 to Equation 6.32, the expressions of the Biot coefficient $\boldsymbol{B}$ and of the Biot modulus $\boldsymbol{N}$ are obtained, as follows:

$$\boldsymbol{B}_i = \phi_i \boldsymbol{A}_i \tag{6.40}$$

$$\boldsymbol{N}_{ip}^{-1} = \phi_i \boldsymbol{D}_{ip} \tag{6.41}$$

6.5.3 Chemical mechanical coupling

Pressure solution at the cracks planes is induced by an increase of contact stress. The projection of the stress field in the solid matrix and of the pore pressure on the crack plane is used to determine the difference between the chemical potential at the crack surface and the chemical potential at the pore walls, as follows:

$$\mu_j = \Omega^*(\boldsymbol{\sigma}_0 + \boldsymbol{\pi}_j) : \overrightarrow{n}_j \otimes \overrightarrow{n}_j \tag{6.42}$$

where $\boldsymbol{\sigma}_0 = \mathbb{C}_0 : \boldsymbol{\epsilon}_0$. Substituting Equation 6.39 and Equation 6.42 into Equation 6.34 and accounting for thermal deformation, the chemical potential tensor $\boldsymbol{\mu}_j^*$ is obtained as follows:

$$\boldsymbol{\mu}_j^* = -\frac{\Omega^*\mathbb{C}_s : B_s}{\phi_s} : \boldsymbol{\epsilon}^E - \sum \frac{\Omega^*\mathbb{C}_s : N_{sp}^{-1}}{\phi_s} : \boldsymbol{\pi}_p + \Omega^* : \boldsymbol{\pi}_j - \boldsymbol{K}\tau \tag{6.43}$$

The expressions of $\boldsymbol{\alpha}$, $\boldsymbol{\beta}$, and $\boldsymbol{\gamma}$ in Equation 6.32 can now be determined from Equation 6.43, as follows:

$$\boldsymbol{\alpha}_j = -\frac{\Omega^*\mathbb{C}_s : B_s}{\phi_s} \tag{6.44}$$

$$\begin{aligned} \boldsymbol{\beta}_{jp} &= -\sum \frac{\Omega^*\mathbb{C}_s : N_{sp}^{-1}}{\phi_s} && \text{if } j \neq p \\ \boldsymbol{\beta}_{jp} &= -\sum \frac{\Omega^*\mathbb{C}_s : N_{sp}^{-1}}{\phi_s} + \Omega^* && \text{if } j = p \end{aligned} \tag{6.45}$$

$$\boldsymbol{\gamma}_j = -\boldsymbol{K} \tag{6.46}$$

6.5.4 Damage evolution

Let us consider that pores are spherical and that cracks have an oblate spheroidal shape. The radius of pores of family i is noted a_{vi}, and the radius of cracks of family j is noted a_{cj}. The damage variable $\mathbf{\Omega}$ is used to quantify energy dissipated by the solid skeleton and is related to the crack density and the void density, as follows:

$$\mathbf{\Omega} = \sum \frac{N_{ci}}{V_{REV}} a_{cj}^3 \overrightarrow{n}_j \otimes \overrightarrow{n}_j + \sum \frac{N_{vi}}{V_{REV}} a_{vi}^3 \boldsymbol{\delta} \tag{6.47}$$

We use a fracture mechanics model to predict the propagation of cracks of radius a_c. The projection of the stress in the solid skeleton on the crack plane is used as the driving force for crack propagation. We assume that cracks initiate and propagate in Mode I (e.g., Equation 3.27). The hardening of crack toughness is expressed as a hyperbolic function of the crack radius (e.g., Equation 3.29).

According to the theory of pressure solution, the mineral is dissolved at grains' contacts (on the crack planes), diffuses along crack planes, and finally precipitates at pore walls. Based on the mass conservation principle, the volume of mineral dissolved at crack contacts is equal to the volume of mineral diffused along the crack plane:

$$2\pi r S J(r) + \frac{2\pi r^2 V_{cj}}{\Omega^*} = 0 \tag{6.48}$$

where $J(r)$ is the diffusion flux, defined in Equation 4.4; V_{cj} is the dissolution rate at crack plane j. Substituting Equation 4.4 into Equation 6.48, the chemical potential μ_j at the jth crack plane is calculated as follows:

$$\mu_{cj} = \int_0^{a_j} \frac{RTV_{cj}r}{C_o \Omega^* DS} \mathrm{d}r \tag{6.49}$$

The number of moles of mineral dissolved at crack plane j, noted $\mathrm{d}m_c j$, is obtained at each

time interval Δt, as follows:

$$\mathrm{d}m_{cj} = \frac{V_{cj}\pi a_j^2 \Delta t}{\Omega^*} \tag{6.50}$$

where we used the fact that the crack plane is circular and we introduced the dissolution rate V_{cj}.

Using Equation 6.49 and Equation 6.50, the relation between the chemical potential μ_j and the number of moles of dissolved mineral $\mathrm{d}m_{cj}$ is established:

$$\mathrm{d}m_{cj} = \frac{2\pi DSC_o \Delta t \mu_{cj}}{RT} \tag{6.51}$$

We assume that the mineral dissolved at crack planes precipitates uniformly on the walls of the spherical pores. The size of pores of family i, noted a'_{vi}, and the volume fraction of pores of family i, noted ϕ'_{vi}, can be updated from the number of moles of dissolved mineral $\mathrm{d}m_{cj}$:

$$a'_{vi} = \sqrt[3]{a_{vi}^3 - \frac{3\Omega^* \sum \mathrm{d}m_{cj}}{4\pi M}} \tag{6.52}$$

$$\phi'_{vi} = \frac{V_{vi} - \frac{\Omega^* \sum \mathrm{d}m_{cj}}{M}}{V_{REV} - \Omega^* \sum \mathrm{d}m_{cj}} \tag{6.53}$$

6.5.5 Calculation procedure

In a strain-controlled simulation, the global elastic strain $\boldsymbol{\epsilon}^E$ is calculated from the total strain $\boldsymbol{\epsilon}$ and the global chemical strain $\boldsymbol{\epsilon}^c$ first. The state variables (i.e. the global elastic strain $\boldsymbol{\epsilon}^E$, the eigenstresses $\boldsymbol{\pi}$, and the temperature variation τ) are input variables at each time step. From the stress of the solid skeleton at the previous time step, the number of moles of dissolved mineral $\mathrm{d}m_cj$ is obtained from Equation 6.42 and Equation 6.51. Then, the sizes of pores are updated based on Equation 6.52 and Equation 6.53.

We assume that the volume change of the REV during the chemical reactions is the sum of the volumes of dissolved mineral at all crack planes. The expression of the macroscopic

chemical strain $\boldsymbol{\epsilon}^c$ is thus obtained as follows:

$$\mathrm{d}\epsilon^c = -\sum \frac{\Omega^* \mathrm{d}m_{cj}}{V_{REV}} \overrightarrow{n}_j \otimes \overrightarrow{n}_j \tag{6.54}$$

The macroscopic chemical strain ϵ^c is used to update the macroscopic elastic strain $\boldsymbol{\epsilon}^E$ iteratively. According to Equation 6.32, the macroscopic REV stress $\boldsymbol{\sigma}$ is calculated at each time step as follows:

$$\begin{aligned}\mathrm{d}\boldsymbol{\sigma} = \mathbb{C}(a) : \mathrm{d}\boldsymbol{\epsilon}^E + \sum \frac{\partial \mathbb{C}(a)}{\partial a_i} : \boldsymbol{\epsilon}^E \mathrm{d}a_i + \sum \mathrm{d}\boldsymbol{\pi}_j : B_j(a) + \sum\sum \boldsymbol{\pi}_j : \frac{\partial \mathbb{C}(a)}{\partial a_i}\mathrm{d}a_i \\ - \sum \tau \frac{\partial \boldsymbol{K}(a)}{\partial a_i}\mathrm{d}a_i - \sum \boldsymbol{\alpha}_j(a) : \mathrm{d}\boldsymbol{m}^*_{cj} - \sum\sum \frac{\partial \boldsymbol{\alpha}(a)}{\partial a_i} : \boldsymbol{m}^*_{cj}\mathrm{d}a_i\end{aligned} \tag{6.55}$$

The expressions of the thermoporoelastic variables in Equation 6.55 are determined according to the method explained in Sections 6.5.1, 6.5.2, and 6.5.3. The calculation algorithm is summarized in Figure 6.23.

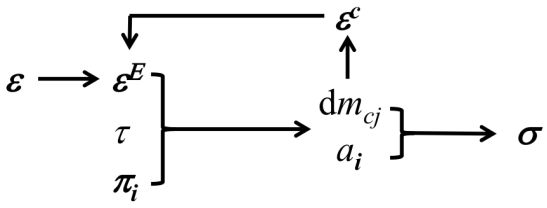

Figure 6.23: Thermodynamic micro-macro model calculation procedure.

6.5.6 Preliminary simulations

The thermo-hydro-chemical-mechanical (THCM) coupled model explained above is used to simulate water-saturated salt rock behavior during oedometer tests. For simplicity, the cracks are assumed to be aligned and perpendicular to the loading direction. The material constants used in the simulation are listed in Table 6.5 [6, 153].

Four loading stages are simulated, as explained in Figure 6.24. In the first stage (S1),

Table 6.5: Parameters used in the THCM model of damage and healing

Mechanical property				Thermal property	
K_m	G_m	K_o	σ_c	α_T	C_o^t
MPa	MPa	MPa/mm	MPa	$1/K$	$J/mm^3/K$
3.8×10^4	1.75×10^4	36	1.0×10^5	1.0×10^{-5}	1.9×10^{-3}

Geometry property				Chemical property		
N	M	ϕ_{co}	ϕ_{vo}	DS	C_o	Ω
$-$	$-$	$-$	$-$	mm^3/s	mol/mm^3	mm^3/mol
21	10	1.5×10^{-3}	2.0×10^{-2}	1.5×10^{-7}	6.48×10^{-6}	2.7×10^4

the magnitude of the compressive axial strain increases from 0 to 0.01 in 100 hours. The pore pressure is 1 MPa, and the temperature is 273 K. In the second stage (S2), the axial strain, the temperature, and the water pore pressure keep constant for 50 hours. In the third stage (S3), the temperature increases from 273 K to 298 K in 50 hours, and the axial strain and water pressure do not change. In the fourth stage, the water pore pressure increases from 1 MPa to 6 MPa in 50 hours without changing the axial strain or the temperature.

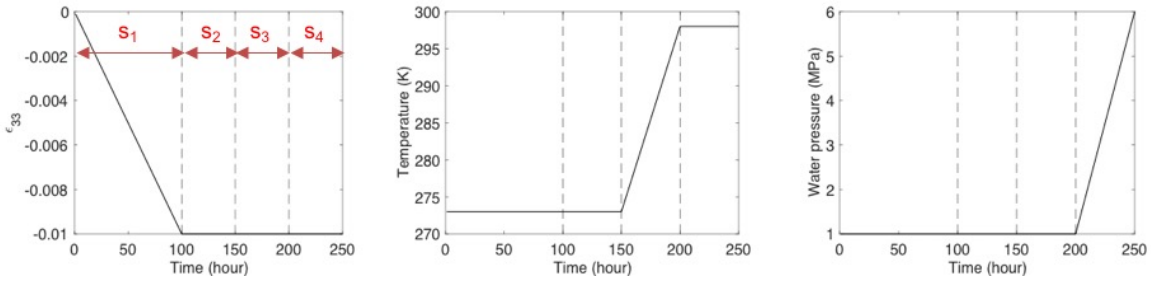

(a) Displacement conditions (b) Thermal conditions (c) Hydraulic conditions

Figure 6.24: THCM loading path

Figure 6.25a highlights the occurrence of healing. Due to pressure solution, mineral precipitates at the pore walls, the radius of voids decreases, and all the damage components decrease. The chemical strain ϵ_c increases time. The total strain ϵ keeps constant from stage 2 to stage 4. The reduction of elastic strain ϵ^E is compensated by the increase of ϵ_c (Figure 6.25b). According to Figure 6.25c, the principal stress in the lateral and axial directions

increases with the compressive axial strain during the first stage. Stress relaxation induced by chemical reactions is observed in both stage 1 and stage 2. In the third stage, salt rock tends to dilate due to the increase of temperataure, which enhances the magnitude of stress. With the increase of water pressure at stage four, the eigenstress in the pore enhances, which results in larger principal stress in both the lateral directions (σ_{11} and σ_{22}) and the axial direction (σ_{33}).

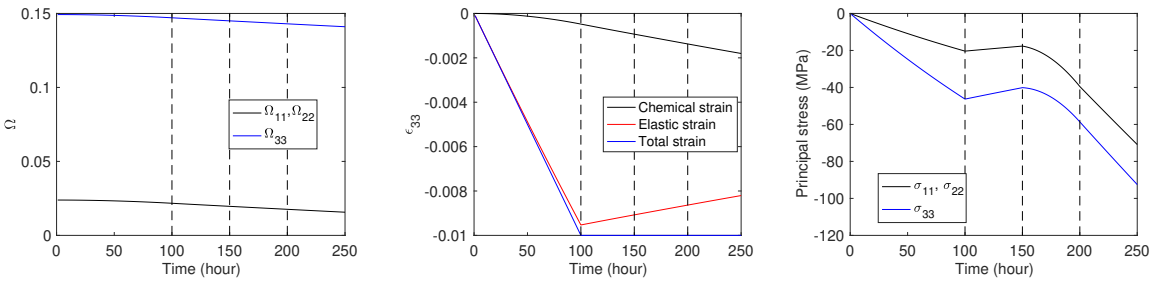

(a) Damage (b) Axial strain (c) Principal stress

Figure 6.25: Simulation results obtained at the material point with the THCM model of damage and healing. Subscript 33 indicates the axial loading direction.

Note that the proposed model has not been calibrated. Parameters used in the simulations were taken from the literature. A rigorous calibration will be required for future studies.

6.6 Conclusion

In this Chapter, we explain a chemo-mechanical self-consistent homogenization scheme that can be used to predict the evolution of stress, strain, porosity and stiffness at both micro- and macro-scale. The inclusion is a hollow sphere that contains a spherical void located at the intersection of three grain-to-grain contact planes. Under compressive stress normal to any of those planes, the solid part of the inclusion dissolves. The solute diffuses towards the pore at the grain-to-grain boundary, and reprecipitates at the pore wall. The resulting changes in the dimensions of the inclusion are used to calculate the viscous strain rate of the inclusion. The healing rate decreases over time. Sensitivity analyses performed

at the inclusion scale under isotropic compressive stress indicate that the healing rate is higher under higher confining stress. Simulations of uniaxial creep tests highlighted the influence of the inclusion orientation relative to the loading axis. In particular, the healing rate increased significantly when the component of compressive stress normal to the grain-to-grain contact plane was increased.

Hill's inclusion-matrix interaction law is used to upscale strains and stresses at the REV scale. Oedometer tests were simulated for specimens containing spherical inclusions with a uniformly distributed contact plane orientations. The REV porosity decreased at a decreasing rate in all cases studied. Inclusions with smaller voids are stiffer, and undergo higher compressive stress. As a result, it was observed that in samples containing inclusions with different initial void sizes, inclusions with larger voids had a negligible healing rate, and were slowing down the overall healing rate of the REV. In samples with uniformly distributed void sizes, the healing rate was faster, because all inclusions contributed to the healing of the REV. As expected, at the inclusion scale, major tensile stresses were mostly radial, and minor compressive stresses were mostly axial. In specimens with smaller grain sizes, principal stresses were more widely distributed in magnitude and the healing rate was higher. For uniform void size distributions, the healing rate increased with initial porosity, but the final porosity change did not depend on the initial porosity of the sample. Principal stresses of higher magnitude were noted in the inclusions that were part of REVs of high initial porosity.

A generalized thermodynamic thermo-hydro-chemo-mechanical framework is proposed to model multiple processes of damage and healing. The macroscopic REV state variables are the elastic strain, eigenstresses and temperature variation, while the internal variables are the healing and damage second-order tensors. The Mori-Tanaka homogenization scheme is adopted to relate the microscopic and macroscopic field variables and to express explicitly the variables that are thermodynamically conjugated to the state and internal variables at the REV scale.

Results obtained in this chapter can guide the design of self-healing materials. For instance, reducing grain size accelerates healing, whereas non-uniform void size distributions decelerates healing. Important lessons learnt in this study also concern the risk of grain (or crystal) breakage. For instance, larger microscopic stresses are noted in samples of high porosity, and in heterogeneous microstructures, grains that are close to smaller voids undergo higher stress.

CHAPTER 7

DAMAGE AND HEALING PROCESS IN A SALT CAVERN

In this Chapter, we use the micro-macro healing model presented in Chapter 6 to investigate the evolution of damage around a salt cavity used for carbon dioxide storage. Simulations are done with the Finite Element Method (FEM). The excavation phase is modeled by assignign a CDM model to the rock mass. In a second phase, elements are assigned the healing model presented in Chapter 6, with an initial porosity equivalent to the damage accumulated after the excavation phase. We simulate the healing processes that occur after CO_2 injection. We study the evolution of net damage and convergence over time, with a particular focus on the effect of the diffusion properties and crystal size of the rock mass.

7.1 FEM modeling of CO_2 storage in a salt cavern

Based on the work of Dusseault [240], the salt cavern is modeled as an oblate spheroid with a vertical axis of 100m and horizontal axes of 150 m. The centroid of the cavern is located at a depth of 1,200m and halite density is taken equal to 2,400 kg/m3. After excavation, the cavern is sealed at a pressure of 15 MPa. The FEM model's dimensions are 1650 m $\times$ 375 m $\times$ 375 m (Figure 7.1). The lateral displacement of salt rock on the boundary is fixed. We used a CDM model (described below) to simulate the excavation phase. In a second stage, the micro-macro healing model presented in Chapter 6 is used with randomly oriented inclusions to simulate the storage phase, by applying a 15 MPa pressure at the cavern wall. The initial value of porosity in the healing simulation phase is set equal to the value of the damage variable Ω^* calculated after the excavation phase. During the storage phase, porosity decreases due to pressure solution, which is expected to increase halite stiffness – a process referred to as "self-healing". An analysis of the sensitivity of the model to mesh size indicates that mesh size may influence the damage value after the excavation phase,

but it has very little effects on the healing process.

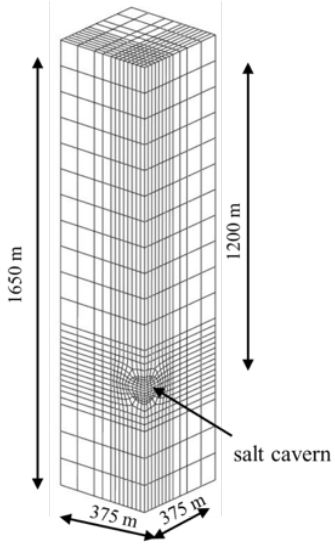

Figure 7.1: Dimensions and mesh of the FEM model

A thermodynamics based CDM model is used to predict excavation damage. At REV scale, the expression of Helmholtz free energy Ψ_s is given as [193, 6]:

$$\Psi_s = \frac{1}{2}\lambda(tr\epsilon)^2 + \mu tr(\epsilon \cdot \epsilon) + \alpha tr(\epsilon) tr(\Omega\epsilon) + \beta tr(\Omega\epsilon \cdot \epsilon) \tag{7.1}$$

where λ_o and μ_o are Lamé constants; α and β are damage material parameters; Ω^* is the dimensionless damage variable, considered as a scalar porosity in the present study. The damage driving force Y_d is expressed from thermodynamic conjugation relationships, as follows:

$$Y_d = -tr(\alpha tr(\epsilon)\epsilon - 2\beta tr(\epsilon \cdot \epsilon)) \tag{7.2}$$

The damage criterion is expressed as:

$$f_d = \frac{|Y_d|}{\sqrt{2}} - C_o - C_1\Omega^* \tag{7.3}$$

where k_o is the damage initiation threshold and k_1 a damage hardening parameter. Dur-

ing the initiation and propagation of damage, the consistency conditions should be satisfied (i.e., f_d = 0 and δf_d = 0). The damage parameters used for the simulation, taken from a prior study [6], are reported in Table 7.1.

Table 7.1: Damage parameters used for the excavation simulation

λ_o	μ_o	α	β	k_o	k_1
Pa	Pa	Pa	Pa	Pa	Pa
2.64×10^{10}	1.75×10^{10}	1.90×10^{9}	-2.64×10^{10}	1000	2.50×10^{5}

7.2 Simulation results

Figure 7.2 shows the distribution of damage around the salt cavern after excavation. The maximum damage observed reaches 9.8% and appears in the middle of sidewall, due to the high compressive principal stress. Damage drops rapidly away from the cavern wall. The size of the damage zone is of the order of the cavern's radius.

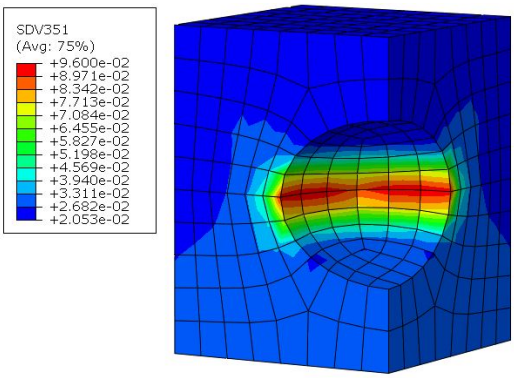

Figure 7.2: Halite damage after excavation

During the storage phase, the REV porosity is calculated from the porosity of the inclusions, and used as the damage variable in the expression of REV stiffness that derives from the expression of the free energy in the CDM model. By so doing, we calculate the evolution of net damage over time, which indicates the amount of damage (or effective porosity) that remains in the rock mass after some healing has occurred. The minimum

(compressive) principal stress distribution around the cavern is represented in Figure 7.3, for DS = 1.75 $\times 10^{-18}$ m^3 and r$_g$ = 0.13 mm. The corresponding evolution of damage at the cavern wall is shown in Figure 7.4. The evolution of cavity convergence is illustrated in Figure 7.5.

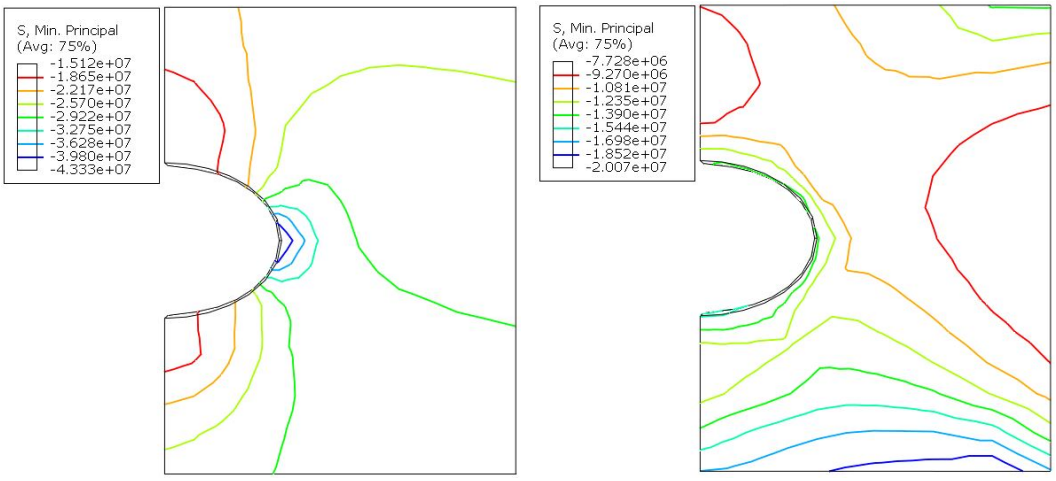

(a) Just after excavation (b) After 100 hours of storage

Figure 7.3: Minimum (compressive) principal stress distribution around the cavity (zone of dimensions 225 m $\times$ 300 m.

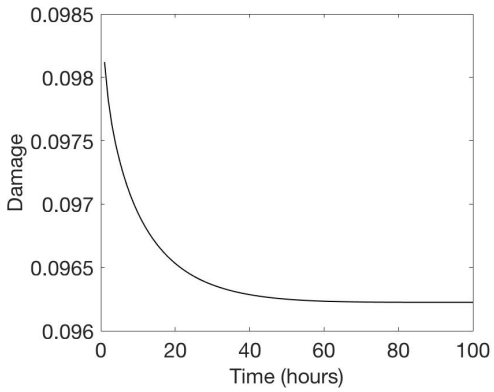

Figure 7.4: Evolution of damage at the cavern wall during the storage phase.

Figure 7.3 clearly shows that the compressive principal stress decreases over time during the storage phase. This is because the dissolution of salt at contact planes triggers negative chemical strains at the inclusion scale. Since halite elements are geometrically constrained, inclusion shrinkage results in tensile stresses at the REV scale, which reduce

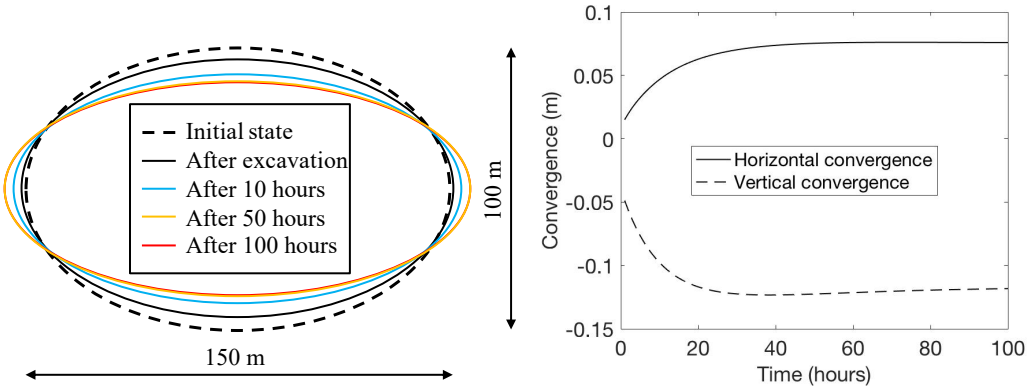

(a) Evolution of the cavity shape (magnified 200 times)

(b) Evolution of horizontal and vertical convergences

Figure 7.5: Evolution the deformation of the salt cavern during storage.

the overall compressive stresses around the cavern. The decrease of compressive stress is particularly visible in the elements with large initial damage in the middle of the sidewall, where the compressive principal stress switches from -43 MPa after excavation to -15 MPa during storage. Figure 7.4 confirms that stress redistribution at the cavern wall is due to healing, i.e., to the reduction of damage, defined here as porosity. Because pressure solution relaxes compressive stress at the contact planes, the dissolution rate decreases over time as salt precipitation occurs at the pore walls. In other words, healing is self-limited. As a result, the healing rate decreases rapidly during the three first days of storage, after which damage reaches a plateau. At the sidewall, damage amounts to 9.8% after excavation, and to 9.6% after four days of storage. Healing thus reduced the maximum damage by 2%. Just after excavation, the vertical convergence is -0.048 m, and the horizontal convergence is +0.015 m (see Figure 7.5). Pressure solution increases convergence, which reaches 1% in both horizontal and vertical directions after four days of storage. Cavern deformation stabilizes when healing reaches a plateau.

7.3 The influence of diffusion efficiency and grain size

Figure 7.6 presents a sensitivity analysis of the parameter DS, which is the product of the diffusion coefficient (D) by the thickness of the fluid films at contact planes (S). Clearly, the healing rate increases with DS, which can be seen as a diffusive efficiency parameter. Physically, pressure solution occurs faster when the diffusion coefficient is higher and/or when the inter-crystalline space is larger. However, DS does not influence the final damage value at the cavity wall, because the rate of pressure solution is independent of the stress redistributions that occur around the cavern (Figure 7.6a). Similarly, a high diffusive efficiency accelerates convergence but does not influence the final shape of the storage facility (Figure 7.6b).

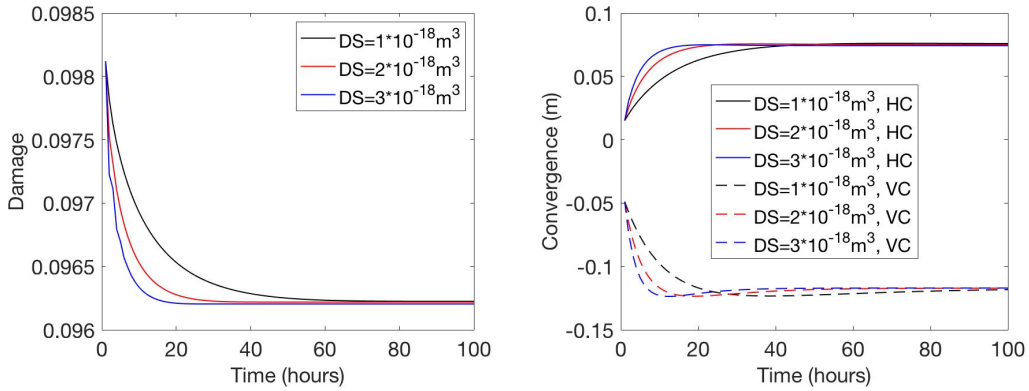

(a) Damage evolution (b) Convergence development

Figure 7.6: Effect of diffusive efficiency on cavern healing.

Figure 7.7 illustrates the influence of the size of the inclusions on salt healing. Inclusion size is equivalent to crystal size and indicates how long the diffusion path is, from high stress dissolution sites to low stress precipitation sites. Larger inclusions imply longer diffusion paths thus lower healing rate. At same initial porosity, larger inclusions also mean fewer inclusions. After 2 days of storage, healing with a crystal size of 0.23 mm is only 50% of the healing obtained with a crystal size of 0.13 mm, and the asymptotic values of damage and convergence are reached after 20 days. The healing rate is negligible with

a crystal size of 1.30 mm, which shows that the healing rate is more sensitive to the crystal size than to the diffusive efficiency.

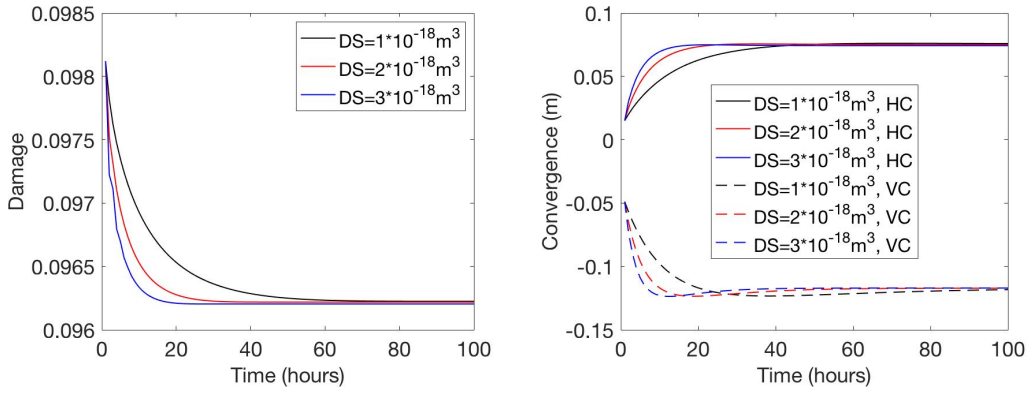

(a) Damage evolution (b) Convergence development

Figure 7.7: Effect of inclusion radius on cavern healing.

7.4 Summary

The micro-macro healing model preented in Chapter 6 was implemented in a FEM package. CO_2 storage in a deep oblate spheroidal salt cavity was simulated. A continuum damage model was used to calculate the damage induced by excavation. The micro-macro healing model was used to simulate the storage phase under constant gas pressure. In real storage conditions, gas pressure increases due to convergence. However, in the present study, convergence was limited to an asymptotic value of 1%, which was not found to influence gas pressure. Under these conditions, numerical calculations showed that only 2% of the excavation damage could be recovered at the sidewall, where damage was the highest. Damage and convergence reached a plateau after four days of storage. The healing rate decreased over time because (i) Salt precipitation at pore walls lengthens the diffusion path of the ions dissolved at high compression stress sites; (ii) Healing results in a stress redistribution around the cavity, reducing compressive stresses, thus limiting the triggering of pressure solution. Higher diffusion coefficients and thicker fluid films could accelerate healing, but

could not change its asymptotic value. A larger crystal size significantly decreased the healing rate.

Simulation results indicate limited healing potential around salt cavities used for CO_2 storage, but it has to be noted that temperature effects were left out in this study. A more comprehensive damage and healing thermo-hydro-mechanical model will be formulated for further analyses. The proposed modeling framework can be used to optimize some microstructure parameters of crushed salt buffers (such as porosity and fluid inclusion distribution) and it can be extended to other self-healing materials.

CHAPTER 8
CONCLUSIONS AND FUTURE WORK

8.1 Main Contributions

In this work, we aim to understand and predict damage and healing processes in rock, by coupling microstructural and poromechanical models. We first performed image analysis on microscopic images acquired in the consolidation tests and cyclic compression tests on salt rock, and proposed fabric descriptors to capture the evolution of fabric. According to the observation of cyclic compression tests, we formulated the discrete wing crack elasto-plastic damage (DWCPD) model to predict the evolution of damage and the development of inelastic strain in salt rock. We explained the degradation of stiffness and the hysteretic behavior observed during cyclic compression tests by a novel chemo-mechanical rate-dependent model. Based on the Mori-Tanaka homogenization scheme, we modeled the accumulation of damage in granite due to biotite weathering. Then, we developed a homogenization scheme to simulate damage and pressure solution - driven healing in salt rock. Finally, we applied a chemo-mechanical homogenization model to predict damage and healing around a salt cavern used for CO_2 storage. Five main contributions to the field of multi-scale geomechanics were made:

1. Fabric descriptors based on image analysis: In order to quantify the evolution of the magnitude and orientation of solidity, coordination, local solid volume fraction and crack volume, 2D microstructure images of salt rock were analyzed at several stages of consolidation tests and cyclic compression tests. Fabric descriptors allowed showing that in both the consolidation and the cyclic compression tests, deformation was dominated by grain rearrangement rather than by grain indentation. In the consolidation tests, with the de-

crease of porosity, plastic deformation accumulates, lateral grain-to-grain contacts initiate and grow, grains are organized into layers, voids' sizes reduce and become more uniformly distributed. In the cyclic compression tests, due to the rearrangement of grains and due to the propagation of inter granular cracks, grains tend to be reorganized into vertical columns of coordinated grains. Voids first collapse into small voids. Then, the isolated small voids become connected and form large voids. The evolution of fabric descriptors correlates with that of the Young's modulus and of the Poisson's ratio of the REV of salt rock.

2. Discrete wing crack elasto-plastic damage (DWCPD) model: We established a novel numerical framework that couples the plastic strain with the damage induced by the initiation and propagation of sliding and wing cracks in salt rock. We found that microscopic wing cracks develop in two stages: (i) Wing crack tensile opening; (ii) Main crack slipping, inducing additional wing crack opening. Results also show that salt rock strength is higher when the friction coefficient and/or the cohesion at crack faces is higher, or when the confining pressure is higher. Interestingly, we also showed that salt rock develops damage-induced anisotropy. This is an important finding, because the majority of the constitutive models of salt rock used in geotechnical engineering and in the mining industry assume that micro-crack propagation and healing lead to isotropic stiffness changes.

3. Rate-dependent model of salt rock: To the best of our knowledge, we proposed the first model to capture the rate-dependent behavior of salt rock under cyclic loading. Our model was calibrated and validated for different loading rates. At low loading rate, stiffness degradation and hysteresis are significantly affected by the development of chemical strain. The accumulation of chemical deformation is accelerated by a higher rate of pressure solution and/or a larger volume fraction of sliding cracks. Higher chemical strains lead to stiffness reduction and larger hysteresis. When the rate of pressure solution is too fast, the stress redistribution happens quasi-instantaneously, which restrains the development of

hysteresis. This model can be applied to guide the design of geological energy storage (i.e. CAES), and improve the efficiency of energy geotechnologies.

4. Micro-macro model of granite bedrock weakening by biotite weathering: We established a homogenization scheme to predict the evolution of damage in bedrock induced by biotite weathering. Our model shows that saprolite production is dominantly controlled by chemical weathering of biotite, which expands as they weather and create stresses sufficient to strain and weaken rock under certain mineralogical conditions. The initiation of damage in the matrix of bedrock is accelerated by larger abundance and smaller aspect ratio of biotite inclusions. This model can be applied to bedrock weakening induced by weathering deformation of any other mineral.

5. Thermodynamic framework for modeling chemo-mechanical healing in salt rock: We presented an original micro-macro framework to simulate salt rock healing driven by pressure solution. A homogenization scheme is first proposed, in which hollow sphere inclusions are traversed by three inter-granular contact planes. Under sufficient normal stress, these planes are subject to dissolution. Precipitation occurs in the inclusion void, which represents a pore. The pore size change is calculated from the mass balance equation of the reacting salt, in which the mass of salt dissolved is a function of the stress normal to the contact planes. Upon calibration, sensitivity analyses done with the proposed model indicate that the healing rate is higher for smaller grain sizes and/or for uniformly distributed void sizes. The healing rate decreases over time because healing redistributes stresses in the REV, such that contact planes in compression are subject to less and less compression as dissolution happens. We implemented the micro-macro model of healing in the FEM for simulating CO_2 storage in a salt cavern. Lastly, a generalized thermodynamic thermo-hydro-chemo-mechanical framework is proposed to model multiple processes of damage and healing in the same, thermodynamically consistent, model.

8.2 Plans for Future Research

The work presented in this thesis can be further improved and applied to other fields. Several topics for future research are listed below.

1. Proposed fabric descriptors can well capture the heterogeneity and anisotropy of salt rock. Despite the correlations made in this thesis, a direct relationship between the evolution of fabric and the macroscopic deformation of rock is still needed. Two methods can be explored to do this: (i) Define fabric tensors based on statistical image analysis, use them as internal variables in a CDM model and establish the evolution laws of these fabric tensors based on phenomenological observations; (ii) Establish a model to predict the evolution of every flaw or feature in the microstructure and use the theory of homogenization to understand how this evolution affects the REV properties.

2. The microscale weakening model of bedrock can be upscaled to investigate the evolution of metric scale fracture networks. The current isotropic phenomenological damage model will have to be updated to simulate the development of anisotropy in bedrock, for example by adopting a micro-mechanical approach. The microscale weakening model can be implemented in FEM. As this microscale model does not account for the coalescence of cracks, cohesive zone element will have to be assigned on the edges of bedrock elements to simulate the development of macroscopic cracks. This multi-scale weathering model will need to be calibrated against triaxial tests and compact tension tests to determine the transition threshold between microscopic damage and macroscopic fracturing. We are planning to use such a multi-scale weathering model to study two Critical Zone Observatories (CZOs): the Luquillo CZO in Puerto Rico and the Southern Sierra CZO in California. Large data sets are available for both of these sites [241, 164]. The model will be used to simulate the local tectonic conditions and to check whether or not weathering processes can change the stress distribution in the bedrock, to the point that it would re-

orient the fractures at the interface with the saprolite layer and influence the evolution of critical zone.

3. The generalized thermodynamic thermo-hydro-chemo-mechanical framework still needs to be calibrated and validated against experimental data. The damage and healing variables will be compared to the evolution of microstructure observed in physical experiments.

4. The weathering model proposed in this thesis is not restricted to granite, and can easily adapted to diorite. The chemo-mechanical homogenization scheme used for granite and salt rock can be extended to other minerals, such as quartz and calcite. More broadly, in addition to its applicability to crystalline media, the modeling approach explained throughout this thesis will be useful to analyze salt recrystallization in concrete. Micro-macro models of damage and healing can also be transferrable to other fields, in biomechanics and biomedical engineering for instance, where the study of hard tissues such as bones and teeth requires a good understanding of damage, poromechanics and possible reparation phenomena.

REFERENCES

[1] J. Lemaitre and R. Desmorat, *Engineering damage mechanics: ductile, creep, fatigue and brittle failures*. Springer Science & Business Media, 2005.

[2] U. Cicekli, G. Z. Voyiadjis, and R. K. A. Al-Rub, "A plasticity and anisotropic damage model for plain concrete", *International Journal of plasticity*, vol. 23, no. 10-11, pp. 1874–1900, 2007.

[3] C. Arson and B. Gatmiri, "Thermo-hydro-mechanical modeling of damage in unsaturated porous media: Theoretical framework and numerical study of the edz", *International Journal for Numerical and Analytical Methods in Geomechanics*, vol. 36, no. 3, pp. 272–306, 2011. eprint: `https://onlinelibrary.wiley.com/doi/pdf/10.1002/nag.1005`.

[4] M. Oda, "Similarity rule of crack geometry in statistically homogeneous rock masses", *Mechanics of Materials*, vol. 3, no. 2, pp. 119 –129, 1984.

[5] M. Kachanov, "Effective elastic properties of cracked solids: Critical review of some basic concepts", *Applied Mechanics Reviews*, vol. 45, no. 8, pp. 304–335, 1992.

[6] C. Zhu and C. Arson, "A model of damage and healing coupling halite thermo-mechanical behavior to microstructure evolution", *Geotechnical and Geological Engineering*, vol. 33, no. 2, pp. 389–410, 2015.

[7] P. Cosenza, M Ghoreychi, B Bazargan-Sabet, and G De Marsily, "In situ rock salt permeability measurement for long term safety assessment of storage", *International Journal of Rock Mechanics and Mining Sciences*, vol. 36, no. 4, pp. 509–526, 1999.

[8] S Kwon and J. W. Wilson, "Deformation mechanism of the underground excavations at the wipp site", *Rock Mechanics and Rock Engineering*, vol. 32, no. 2, pp. 101–122, 1999.

[9] K. S. Chan, S. R. Bodner, and D. E. Munson, "Permeability of wipp salt during damage evolution and healing", *International Journal of Damage Mechanics*, vol. 10, no. 4, pp. 347–375, 2001.

[10] H Mohammadi and S Pietruszczak, "Description of damage process in fractured rocks", *International Journal of Rock Mechanics and Mining Sciences*, vol. 113, pp. 295–302, 2019.

[11] C Zhu, A Pouya, and C Arson, "Comparison between inclusion-matrix modeling and finite element method for viscous damage and fatigue in salt rock", *Mechanics of Materials*, 2016.

[12] J. Silva, T. Worsey, and B. Lusk, "Practical assessment of rock damage due to blasting", *International Journal of Mining Science and Technology*, vol. 29, no. 3, pp. 379–385, 2019.

[13] C. Sun, "Damage zone prediction for rock blasting", PhD thesis, Department of Mining Engineering, University of Utah Salt Lake City, 2013.

[14] C. H. Dowding and A. Rozan, "Damage to rock tunnels from earthquake shaking", *ASCE J Geotech Eng Div*, vol. 104, no. 2, pp. 175–191, 1978.

[15] C. Tang and P. Kaiser, "Numerical simulation of cumulative damage and seismic energy release during brittle rock failure—part i: Fundamentals", *International Journal of Rock Mechanics and Mining Sciences*, vol. 35, no. 2, pp. 113–121, 1998.

[16] S Chaki, M. Takarli, and W. Agbodjan, "Influence of thermal damage on physical properties of a granite rock: Porosity, permeability and ultrasonic wave evolutions", *Construction and Building Materials*, vol. 22, no. 7, pp. 1456–1461, 2008.

[17] Z.-X. Zhang, "Chapter 5 - effect of temperature on rock fracture", in *Rock Fracture and Blasting*, Z.-X. Zhang, Ed., Butterworth-Heinemann, 2016, pp. 111 –133, ISBN: 978-0-12-802688-5.

[18] H. L. Buss, P. B. Sak, S. M. Webb, and S. L. Brantley, "Weathering of the rio blanco quartz diorite, luquillo mountains, puerto rico: Coupling oxidation, dissolution, and fracturing", *Geochimica et Cosmochimica Acta*, vol. 72, no. 18, pp. 4488–4507, 2008.

[19] J. H. Ahn and D. R. Peacor, "Kaolinitization of biotite; tem data and implications for an alteration mechanism", *American Mineralogist*, vol. 72, no. 3-4, pp. 353–356, 1987.

[20] M Thompson and J. Willis, "A reformation of the equations of anisotropic poroelasticity", *Journal of Applied Mechanics*, vol. 58, no. 3, pp. 612–616, 1991.

[21] M. A. Biot, "General solutions of the equations of elasticity and consolidation for a porous material", *J. appl. Mech*, vol. 23, no. 1, pp. 91–96, 1956.

[22] J. R. Rice and M. P. Cleary, "Some basic stress diffusion solutions for fluid-saturated elastic porous media with compressible constituents", *Reviews of Geophysics*, vol. 14, no. 2, pp. 227–241, 1976.

[23] A. Shojaei, A. D. Taleghani, and G. Li, "A continuum damage failure model for hydraulic fracturing of porous rocks", *International Journal of Plasticity*, vol. 59, pp. 199–212, 2014.

[24] C.-F. Tsang, F. Bernier, and C. Davies, "Geohydromechanical processes in the excavation damaged zone in crystalline rock, rock salt, and indurated and plastic clays—in the context of radioactive waste disposal", *International Journal of Rock Mechanics and Mining Sciences*, vol. 42, no. 1, pp. 109–125, 2005.

[25] J. Stormont and J. Daemen, "Laboratory study of gas permeability changes in rock salt during deformation", in *International journal of rock mechanics and mining sciences & geomechanics abstracts*, Elsevier, vol. 29, 1992, pp. 325–342.

[26] K. Fuenkajorn and D. Phueakphum, "Laboratory assessment of healing of fractures in rock salt", *Bulletin of Engineering Geology and the Environment*, vol. 70, no. 4, p. 665, 2011.

[27] C. Martin and G. Lanyon, "Measurement of in-situ stress in weak rocks at mont terri rock laboratory, switzerland", *International Journal of Rock Mechanics and Mining Sciences*, vol. 40, no. 7-8, pp. 1077–1088, 2003.

[28] S. Yuan and J. Harrison, "A review of the state of the art in modelling progressive mechanical breakdown and associated fluid flow in intact heterogeneous rocks", *International Journal of Rock Mechanics and Mining Sciences*, vol. 43, no. 7, pp. 1001–1022, 2006.

[29] D. Krajcinovic and D. Fanella, "A micromechanical damage model for concrete", *Engineering Fracture Mechanics*, vol. 25, no. 5-6, pp. 585–596, 1986.

[30] C. Arson and B. Gatmiri, "Numerical study of damage in unsaturated geological and engineered barriers", *Physics and Chemistry of the Earth, Parts A/B/C*, vol. 36, no. 17-18, pp. 1981–1989, 2011.

[31] A.-S. Chiarelli, J.-F. Shao, and N Hoteit, "Modeling of elastoplastic damage behavior of a claystone", *International Journal of plasticity*, vol. 19, no. 1, pp. 23–45, 2003.

[32] K Hayakawa and S Murakami, "Thermodynamical modeling of elastic-plastic damage and experimental validation of damage potential", *International Journal of damage mechanics*, vol. 6, no. 4, pp. 333–363, 1997.

[33] M. Salari, S Saeb, K. Willam, S. Patchet, and R. Carrasco, "A coupled elastoplastic damage model for geomaterials", *Computer methods in applied mechanics and engineering*, vol. 193, no. 27-29, pp. 2625–2643, 2004.

[34] R. de Borst, J. Pamin, and M. G. Geers, "On coupled gradient-dependent plasticity and damage theories with a view to localization analysis", *European Journal of Mechanics-A/Solids*, vol. 18, no. 6, pp. 939–962, 1999.

[35] J. Lemaitre and R. Desmorat, *Engineering damage mechanics: ductile, creep, fatigue and brittle failures*. Springer Science & Business Media, 2005.

[36] J.-L. Chaboche, "Continuous damage mechanics—a tool to describe phenomena before crack initiation", *Nuclear Engineering and Design*, vol. 64, no. 2, pp. 233–247, 1981.

[37] J. Simo and J. Ju, "Strain-and stress-based continuum damage models—i. formulation", *International journal of solids and structures*, vol. 23, no. 7, pp. 821–840, 1987.

[38] S. Murakami, *Continuum damage mechanics: a continuum mechanics approach to the analysis of damage and fracture*. Springer Science & Business Media, 2012, vol. 185.

[39] S. Miao, M. L. Wang, and H. L. Schreyer, "Constitutive models for healing of materials with application to compaction of crushed rock salt", *Journal of Engineering Mechanics*, vol. 121, no. 10, pp. 1122–1129, 1995.

[40] J. Mergheim and P. Steinmann, "Phenomenological modelling of self-healing polymers based on integrated healing agents", *Computational Mechanics*, vol. 52, no. 3, pp. 681–692, 2013.

[41] G. Z. Voyiadjis, A. Shojaei, G. Li, and P. Kattan, "Continuum damage-healing mechanics with introduction to new healing variables", *International Journal of Damage Mechanics*, vol. 21, no. 3, pp. 391–414, 2012. eprint: `https://doi.org/10.1177/1056789510397069`.

[42] R. K. A. Al-Rub, M. K. Darabi, D. N. Little, and E. A. Masad, "A micro-damage healing model that improves prediction of fatigue life in asphalt mixes", *International Journal of Engineering Science*, vol. 48, no. 11, pp. 966 –990, 2010, Special Issue in Honor of K.R. Rajagopal.

[43] K. Chan, S. Bodner, A. Fossum, and D. Munson, "A constitutive model for inelastic flow and damage evolution in solids under triaxial compression", *Mechanics of Materials*, vol. 14, no. 1, pp. 1–14, 1992.

[44] K. Chan, S. Bodner, and D. Munson, "Recovery and healing of damage in wipp salt", *International Journal of Damage Mechanics*, vol. 7, no. 2, pp. 143–166, 1998.

[45] M. Oda, "Fabric tensor for discontinuous geological materials", *Soils and Foundations*, vol. 22, no. 4, pp. 96–108, 1982.

[46] J. Fonseca *et al.*, "The evolution of morphology and fabric of a sand during shearing", 2011.

[47] J. K. Mitchell, K. Soga, *et al.*, *Fundamentals of soil behavior*. John Wiley & Sons Hoboken, NJ, 2005, vol. 3.

[48] R. Al-Raoush and M. Alsaleh, "Simulation of random packing of polydisperse particles", *Powder technology*, vol. 176, no. 1, pp. 47–55, 2007.

[49] A Hasan and K. Alshibli, "Experimental assessment of 3d particle-to-particle interaction within sheared sand using synchrotron microtomography", *Géotechnique*, vol. 60, no. 5, p. 369, 2010.

[50] I. Cavarretta, "The influence of particle characteristics on the engineering behaviour of granular materials", PhD thesis, Imperial College London (University of London), 2009.

[51] W. C. Krumbein and L. L. Sloss, "Stratigraphy and sedimentation.", Tech. Rep., 1963.

[52] C. Clayton, C. Abbireddy, and R. Schiebel, "A method of estimating the form of coarse particulates", *Geotechnique*, vol. 59, no. 6, pp. 493–501, 2009.

[53] M. A. Taylor, "Quantitative measures for shape and size of particles", *Powder Technology*, vol. 124, no. 1-2, pp. 94–100, 2002.

[54] H. Wadell, "Sphericity and roundness of rock particles", *The Journal of Geology*, vol. 41, no. 3, pp. 310–331, 1933.

[55] R. Al-Raoush and K. A. Alshibli, "Distribution of local void ratio in porous media systems from 3d x-ray microtomography images", *Physica A: Statistical Mechanics and its Applications*, vol. 361, no. 2, pp. 441–456, 2006.

[56] J. Frost and C. Kuo, "Automated determination of the distribution of local void ratio from digital images", *Geotechnical Testing Journal*, vol. 19, no. 2, pp. 107–117, 1996.

[57] C Kuo, "Quantifying the fabric of granular materials: An image analysis approach.", 1995.

[58] C. Thornton, "Numerical simulations of deviatoric shear deformation of granular media", *Géotechnique*, vol. 50, no. 1, pp. 43–53, 2000.

[59] M. Oda, "Co-ordination number and its relation to shear strength of granular material", *Soils and foundations*, vol. 17, no. 2, pp. 29–42, 1977.

[60] S. Palmer and M. Barton, "Porosity reduction, microfabric and resultant lithification in uk uncemented sands", *Geological Society, London, Special Publications*, vol. 36, no. 1, pp. 29–40, 1987.

[61] K. Ken-Ichi, "Distribution of directional data and fabric tensors", *International Journal of Engineering Science*, vol. 22, no. 2, pp. 149–164, 1984.

[62] M. Madadi, O. Tsoungui, M. Lätzel, and S. Luding, "On the fabric tensor of polydisperse granular materials in 2d", *International Journal of Solids and Structures*, vol. 41, no. 9-10, pp. 2563–2580, 2004.

[63] M. Oda and H. Nakayama, "Yield function for soil with anisotropic fabric", *Journal of Engineering Mechanics*, vol. 115, no. 1, pp. 89–104, 1989.

[64] Y. Wang and C. Mok, "Mechanisms of small-strain shear-modulus anisotropy in soils", *Journal of geotechnical and geoenvironmental engineering*, vol. 134, no. 10, pp. 1516–1530, 2008.

[65] K Ventouras and M. Coop, "On the behaviour of thanet sand: An example of an uncemented natural sand", *Géotechnique*, vol. 59, no. 9, pp. 727–738, 2009.

[66] H Horii and S Nemat-Nasser, "Overall moduli of solids with microcracks: Load-induced anisotropy", *Journal of the Mechanics and Physics of Solids*, vol. 31, no. 2, pp. 155–171, 1983.

[67] M. L. Kachanov, B. Shafiro, and I. Tsukrov, *Handbook of elasticity solutions*. Springer Science & Business Media, 2013.

[68] R Courant and D Hilbert, "Methods of mathematical physics. vol. ii. partial differential equations, john willey & sons", *Inc., New York*, 1989.

[69] P. Keast and J. C. Diaz, "Fully symmetric integration formulas for the surface of the sere in s dimensions", *SIAM Journal on Numerical Analysis*, vol. 20, no. 2, pp. 406–419, 1983.

[70] A. McLaren, "Optimal numerical integration on a sphere", *Mathematics of Computation*, vol. 17, no. 84, pp. 361–383, 1963.

[71] P Bažant and B. Oh, "Efficient numerical integration on the surface of a sphere", *ZAMM-Journal of Applied Mathematics and Mechanics/Zeitschrift für Angewandte Mathematik und Mechanik*, vol. 66, no. 1, pp. 37–49, 1986.

[72] S. Levasseur, F. Collin, R. Charlier, and D. Kondo, "A two scale anisotropic damage model accounting for initial stresses in microcracked materials", *Engineering Fracture Mechanics*, vol. 78, no. 9, pp. 1945–1956, 2011.

[73] L. Dormieux, D. Kondo, and F.-J. Ulm, *Microporomechanics*. John Wiley & Sons, 2006.

[74] R. Kilian, R. Heilbronner, and H. Stünitz, "Quartz grain size reduction in a granitoid rock and the transition from dislocation to diffusion creep", *Journal of Structural Geology*, vol. 33, no. 8, pp. 1265–1284, 2011.

[75] V. Lubarda and D Krajcinovic, "Damage tensors and the crack density distribution", *International Journal of Solids and Structures*, vol. 30, no. 20, pp. 2859–2877, 1993.

[76] A. Cauvin and R. B. Testa, "Damage mechanics: Basic variables in continuum theories", *International Journal of Solids and Structures*, vol. 36, no. 5, pp. 747–761, 1999.

[77] D Halm and A Dragon, "An anisotropic model of damage and frictional sliding for brittle materials", *European Journal of Mechanics-A/Solids*, vol. 17, no. 3, pp. 439–460, 1998.

[78] D. Halm and A. Dragon, "A model of anisotropic damage by mesocrack growth; unilateral effect", *International Journal of Damage Mechanics*, vol. 5, no. 4, pp. 384–402, 1996.

[79] B. Budiansky and R. J. O'connell, "Elastic moduli of a cracked solid", *International journal of Solids and structures*, vol. 12, no. 2, pp. 81–97, 1976.

[80] V. Pensée, D. Kondo, and L. Dormieux, "Micromechanical analysis of anisotropic damage in brittle materials", *Journal of Engineering Mechanics*, vol. 128, no. 8, pp. 889–897, 2002.

[81] L. Gambarotta and S. Lagomarsino, "A microcrack damage model for brittle materials", *International Journal of Solids and Structures*, vol. 30, no. 2, pp. 177–198, 1993.

[82] L. Germanovich, R. Salganik, A. Dyskin, and K. Lee, "Mechanisms of brittle fracture of rock with pre-existing cracks in compression", *Pure and Applied Geophysics*, vol. 143, no. 1-3, pp. 117–149, 1994.

[83] W. Jin and C. Arson, "Micromechanics based discrete damage model with multiple non-smooth yield surfaces: Theoretical formulation, numerical implementation and

engineering applications", *International Journal of Damage Mechanics*, vol. 27, no. 5, pp. 611–639, 2017.

[84] F. Lehner and M. Kachanov, "On modelling of 'winged" cracks forming under compression", *International Journal of Fracture*, vol. 77, no. 4, R69–R75, 1996.

[85] D. Gross and T. Seelig, *Fracture mechanics: with an introduction to micromechanics*. Springer, 2017.

[86] W. Drugan and J. Willis, "A micromechanics-based nonlocal constitutive equation and estimates of representative volume element size for elastic composites", *Journal of the Mechanics and Physics of Solids*, vol. 44, no. 4, pp. 497–524, 1996.

[87] *Virtual campus in hydrology and water ressources*, 2016.

[88] W. Voigt, "Ueber die beziehung zwischen den beiden elasticitätsconstanten isotroper körper", *Annalen der physik*, vol. 274, no. 12, pp. 573–587, 1889.

[89] A Reuss and Z Angnew, "A calculation of the bulk modulus of polycrystalline materials", *Math Meth*, vol. 9, p. 55, 1929.

[90] R. Hill, "The elastic behaviour of a crystalline aggregate", *Proceedings of the Physical Society. Section A*, vol. 65, no. 5, p. 349, 1952.

[91] J. D. Eshelby, "The determination of the elastic field of an ellipsoidal inclusion, and related problems", *Proceedings of the Royal Society of London A: Mathematical, Physical and Engineering Sciences*, vol. 241, no. 1226, pp. 376–396, 1957. eprint: `http://rspa.royalsocietypublishing.org/content/241/1226/376.full.pdf`.

[92] T Mura, "Micromechanics of defects in solids (martinus nijhoff, dordrecht, 1987)", *Google Scholar*, p. 1, 1987.

[93] S. Nemat-Nasser and M. Hori, *Micromechanics: overall properties of heterogeneous materials*. Elsevier, 2013, vol. 37.

[94] P Vieville, A. Bonnet, and P Lipiński, "Modelling effective properties of composite materials using the inclusion concept. general considerations", *Archives of Mechanics*, vol. 58, no. 3, pp. 207–239, 2006.

[95] S Lurie, Y Solyaev, and K Shramko, "Comparison between the mori-tanaka and generalized self-consistent methods in the framework of anti-plane strain inclusion problem in strain gradient elasticity", *Mechanics of Materials*, vol. 122, pp. 133–144, 2018.

[96] K. C. Gramoll, A. D. Freed, and K. P. Walker, "An overview of self-consistent methods for fiber-reinforced composites", 1991.

[97] T Mori and K Tanaka, "Average stress in matrix and average elastic energy of materials with misfitting inclusions", *Acta Metallurgica*, vol. 21, no. 5, pp. 571 – 574, 1973.

[98] Y. Benveniste, "A new approach to the application of mori-tanaka's theory in composite materials", *Mechanics of Materials*, vol. 6, no. 2, pp. 147 –157, 1987.

[99] H. Ma, G. Hu, and Z. Huang, "A micromechanical method for particulate composites with finite particle concentration", *Mechanics of Materials*, vol. 36, no. 4, pp. 359–368, 2004.

[100] J. Kim and J.-K. Lee, "A new model to predict effective elastic constants of composites with spherical fillers", *Journal of mechanical science and technology*, vol. 20, no. 11, pp. 1891–1897, 2006.

[101] C. L. Tucker III and E. Liang, "Stiffness predictions for unidirectional short-fiber composites: Review and evaluation", *Composites science and technology*, vol. 59, no. 5, pp. 655–671, 1999.

[102] B. Pichler and L. Dormieux, "Cracking risk of partially saturated porous media—part i: Microporoelasticity model", *International journal for numerical and analytical methods in geomechanics*, vol. 34, no. 2, pp. 135–157, 2010.

[103] P. Lu, "Further studies on mori–tanaka models for thermal expansion coefficients of composites", *Polymer*, vol. 54, no. 6, pp. 1691–1699, 2013.

[104] P. Castañeda and J. Willis, "The effect of spatial distribution on the effective behavior of composite materials and cracked media", *Journal of the Mechanics and Physics of Solids*, vol. 43, no. 12, pp. 1919 –1951, 1995.

[105] E Kröner, "Zur plastischen verformung des vielkristalls", *Acta Metallurgica*, vol. 9, no. 2, pp. 155 –161, 1961.

[106] A Dasgupta and S. Bhandarkar, "A generalized self-consistent mori-tanaka scheme for fiber-composites with multiple interphases", *Mechanics of Materials*, vol. 14, no. 1, pp. 67–82, 1992.

[107] R. Hill, "Continuum micro-mechanics of elastoplastic polycrystals", *Journal of the Mechanics and Physics of Solids*, vol. 13, no. 2, pp. 89 –101, 1965.

[108] G. Weng, "A unified, self-consistent theory for the plastic-creep deformation of metals", *ASME, Transactions, Journal of Applied Mechanics*, vol. 49, pp. 728–734, 1982.

[109] A. Pouya, C. Zhu, and C. Arson, "Micro–macro approach of salt viscous fatigue under cyclic loading", *Mechanics of Materials*, vol. 93, pp. 13–31, 2016.

[110] "Self-consistent micromechanical approach for damage accommodation in rock-like polycrystalline materials", *International Journal of Damage Mechanics*, vol. 0, no. 0, p. 1 056 789 517 747 665, 2017.

[111] R. deWit, "Elastic constants and thermal expansion averages of a nontextured polycrystal", *Journal of mechanics of materials and structures*, vol. 3, no. 2, pp. 195–212, 2008.

[112] C. Moyne and M. A. Murad, "Electro-chemo-mechanical couplings in swelling clays derived from a micro/macro-homogenization procedure", *International Journal of Solids and Structures*, vol. 39, no. 25, pp. 6159 –6190, 2002.

[113] C. Arson and T. Vanorio, "Chemomechanical evolution of pore space in carbonate microstructures upon dissolution: Linking pore geometry to bulk elasticity", *Journal of Geophysical Research: Solid Earth*, vol. 120, no. 10, pp. 6878–6894, 2015.

[114] R. Knipe, "Deformation mechanisms—recognition from natural tectonites", *Journal of Structural Geology*, vol. 11, no. 1-2, pp. 127–146, 1989.

[115] J. T. Fredrich, B. Evans, and T.-F. Wong, "Micromechanics of the brittle to plastic transition in carrara marble", *Journal of Geophysical Research: Solid Earth*, vol. 94, no. B4, pp. 4129–4145, 1989.

[116] M. S. Paterson and T.-f. Wong, *Experimental rock deformation-the brittle field*. Springer Science & Business Media, 2005.

[117] F. M. Chester, "Dynamic recrystallization in semi-brittle faults", *Journal of structural geology*, vol. 11, no. 7, pp. 847–858, 1989.

[118] F Ghahremani, "Effect of grain boundary sliding on anelasticity of polycrystals", *International Journal of Solids and Structures*, vol. 16, no. 9, pp. 825–845, 1980.

[119] C. Zener, "Theory of the elasticity of polycrystals with viscous grain boundaries", *Physical Review*, vol. 60, no. 12, p. 906, 1941.

[120] J Fonseca, C O'Sullivan, M. R. Coop, and P. Lee, "Quantifying the evolution of soil fabric during shearing using directional parameters", *Géotechnique*, vol. 63, no. 6, pp. 487–499, 2013.

[121] F. Chester, "Temperature and rate dependence of friction for faults", *Eos Trans. AGU*, vol. 69, p. 471, 1988.

[122] R Raj and M. Ashby, "On grain boundary sliding and diffusional creep", *Metallurgical transactions*, vol. 2, no. 4, pp. 1113–1127, 1971.

[123] E. Rutter, "Pressure solution in nature, theory and experiment", *Journal of the Geological Society*, vol. 140, no. 5, pp. 725–740, 1983.

[124] C. Spiers, P. Schutjens, R. Brzesowsky, C. Peach, J. Liezenberg, and H. Zwart, "Experimental determination of constitutive parameters governing creep of rocksalt by pressure solution", *Geological Society, London, Special Publications*, vol. 54, no. 1, pp. 215–227, 1990.

[125] J Linckens, G Zulauf, and J Hammer, "Experimental deformation of coarse-grained rock salt to high strain", *Journal of Geophysical Research: Solid Earth*, vol. 121, no. 8, pp. 6150–6171, 2016.

[126] X. Shen and C. Arson, "Simulation of salt cavity healing based on a micro-macro model of pressure-solution", *Petroleum Geoscience*, petgeo2018–094, 2019.

[127] J. Urai and C. Spiers, "The effect of grain boundary water on deformation mechanisms and rheology of rocksalt during long-term deformation", in *Proc. 6th Conf. Mech. Beh. of Salt*, 2007, pp. 149–158.

[128] J. Ding, F. M. Chester, J. S. Chester, C. Zhu, and C. Arson, "Mechanical behavior and microstructure development in consolidation of nominally dry granular salt", 5th symposium of the American Rock Mechanics Association, 2016.

[129] J. Ding, F. M. Chester, J. S. Chester, S. Xianda, and C. Arson, "Microcrack network development in salt-rock during cyclic loading at low confining pressure", American Rock Mechanics Association, 2017.

[130] C. Spiers, J. Urai, G. Lister, J. Boland, and H. Zwart, "The influence of fluid-rock interaction on the rheology of salt rock.", 1st ed. Luxembourg: Commission of the European Communities., 1986.

[131] M. L. Kachanov, "A microcrack model of rock inelasticity part i: Frictional sliding on microcracks", *Mechanics of Materials*, vol. 1, no. 1, pp. 19–27, 1982.

[132] A. Dyskin and R. Salganik, "Model of dilatancy of brittle materials with cracks under compression", *Mechanics of solids*, vol. 22, no. 6, pp. 165–173, 1987.

[133] L. Scholtès and F.-V. Donzé, "Modelling progressive failure in fractured rock masses using a 3d discrete element method", *International Journal of Rock Mechanics and Mining Sciences*, vol. 52, pp. 18–30, 2012.

[134] W. Jin and C. Arson, "Discrete equivalent wing crack based damage model for brittle solids", *International Journal of Solids and Structures*, vol. 110, pp. 279–293, 2017.

[135] J. Shao, Y. Jia, D. Kondo, and A. Chiarelli, "A coupled elastoplastic damage model for semi-brittle materials and extension to unsaturated conditions", *Mechanics of Materials*, vol. 38, no. 3, pp. 218 –232, 2006.

[136] H. Van Eekelen, "Isotropic yield surfaces in three dimensions for use in soil mechanics", *International Journal for Numerical and Analytical Methods in Geomechanics*, vol. 4, no. 1, pp. 89–101, 1980.

[137] E Hoek, Z. Bieniawski, *et al.*, "Fracture propagation mechanism in hard rock", in *1st ISRM Congress*, International Society for Rock Mechanics, 1966.

[138] I Hawkes and M Mellor, "Uniaxial testing in rock mechanics laboratories", *Engineering Geology*, vol. 4, no. 3, pp. 179–285, 1970.

[139] E. Lajtai, E. S. Duncan, and B. Carter, "The effect of strain rate on rock strength", *Rock Mechanics and Rock Engineering*, vol. 24, no. 2, pp. 99–109, 1991.

[140] P. Senseny, F. Hansen, J. Russell, N. Carter, and J. Handin, "Mechanical behaviour of rock salt: Phenomenology and micromechanisms", in *International journal of rock mechanics and mining sciences & geomechanics abstracts*, Elsevier, vol. 29, 1992, pp. 363–378.

[141] K. Fuenkajorn, T. Sriapai, and P. Samsri, "Effects of loading rate on strength and deformability of maha sarakham salt", *Engineering Geology*, vol. 135, pp. 10–23, 2012.

[142] J. Wheeler, "Anisotropic rheology during grain boundary diffusion creep and its relation to grain rotation, grain boundary sliding and superplasticity", *Philosophical Magazine*, vol. 90, no. 21, pp. 2841–2864, 2010.

[143] K. McClay, "Pressure solution and coble creep in rocks and minerals: A review", *Journal of the Geological Society*, vol. 134, no. 1, pp. 57–70, 1977.

[144] M. S. Paterson, "Nonhydrostatic thermodynamics and its geologic applications", *Reviews of Geophysics*, vol. 11, no. 2, pp. 355–389, 1973.

[145] E. H. Rutter and D. Elliott, "The kinetics of rock deformation by pressure solution [and discussion]", *Philosophical Transactions of the Royal Society of London. Series A, Mathematical and Physical Sciences*, vol. 283, no. 1312, pp. 203–219, 1976.

[146] R. Raj, "Creep in polycrystalline aggregates by matter transport through a liquid phase", *Journal of Geophysical Research: Solid Earth*, vol. 87, no. B6, pp. 4731–4739, 1982.

[147] E. H. Rutter, "Pressure solution in nature, theory and experiment", *Journal of the Geological Society*, vol. 140, no. 5, pp. 725–740, 1983. eprint: `http://jgs.lyellcollection.org/content/140/5/725.full.pdf`.

[148] F. K. Lehner, "A model for intergranular pressure solution in open systems", *Tectonophysics*, vol. 245, no. 3-4, pp. 153–170, 1995.

[149] J. Urai, W. Means, and G. Lister, "Dynamic recrystallization of minerals", in *Mineral and rock deformation: laboratory studies*, vol. 36, AGU Washington, DC, 1986, pp. 161–199.

[150] J. Ding, "Grain boundary processes, anelasticity, and test of the effective stress law for semibrittle deformation of synthetic salt-rocks", PhD thesis, Texas A & M University, 2019.

[151] P. Schutjens and C. Spiers, "Intergranular pressure solution in nacl: Grain-to-grain contact experiments under the optical microscope", *Oil & Gas Science and Technology*, vol. 54, no. 6, pp. 729–750, 1999.

[152] F. K. Lehner, "Thermodynamics of rock deformation by pressure solution", in *Deformation Processes in Minerals, Ceramics and Rocks*. Dordrecht: Springer Netherlands, 1990, pp. 296–333, ISBN: 978-94-011-6827-4.

[153] X. Shen and C. Arson, "An isotropic self-consistent homogenization scheme for chemo-mechanical healing driven by pressure solution in halite", *International Journal of Solids and Structures*, vol. 161, pp. 96–110, 2019.

[154] B Pichler and C. Hellmich, "Estimation of influence tensors for eigenstressed multiphase elastic media with nonaligned inclusion phases of arbitrary ellipsoidal shape", *Journal of engineering mechanics*, vol. 136, no. 8, pp. 1043–1053, 2010.

[155] V. M. Levin, "Thermal expansion coefficient of heterogeneous materials", *Mekhanika Tverdogo Tela*, vol. 2, no. 1, pp. 83–94, 1967.

[156] S. P. Anderson, W. E. Dietrich, and G. H. Brimhall Jr, "Weathering profiles, mass-balance analysis, and rates of solute loss: Linkages between weathering and erosion

in a small, steep catchment", *Geological Society of America Bulletin*, vol. 114, no. 9, pp. 1143–1158, 2002.

[157] H. L. Buss, M. C. Lara, O. W. Moore, A. C. Kurtz, M. S. Schulz, and A. F. White, "Lithological influences on contemporary and long-term regolith weathering at the Luquillo Critical Zone Observatory", *Geochimica et Cosmochimica Acta*, vol. 196, pp. 224–251, 2017.

[158] J. L. Dixon, A. M. Heimsath, and R. Amundson, "The critical role of climate and saprolite weathering in landscape evolution", *Earth Surface Processes and Landforms*, vol. 34, no. 11, pp. 1507–1521, 2009.

[159] A. B. Shiels and L. R. Walker, "Bird perches increase forest seeds on Puerto Rican landslides", *Restoration Ecology*, vol. 11, no. 4, pp. 457–465, 2003.

[160] W. A. Lacerda, "Landslide initiation in saprolite and colluvium in southern Brazil: Field and laboratory observations", *Geomorphology*, vol. 87, no. 3, pp. 104–119, 2007.

[161] J. C. Walker, P. Hays, and J. F. Kasting, "A negative feedback mechanism for the long-term stabilization of earth's surface temperature", *Journal of Geophysical Research: Oceans*, vol. 86, no. C10, pp. 9776–9782, 1981.

[162] R. A. Berner, A. C. Lasaga, and R. M. Garrels, "The carbonate-silicate geochemical cycle and its effect on atmospheric carbon dioxide over the past 100 million years", *American Journal of Science*, vol. 283, no. 7, pp. 641–683, 1983.

[163] R. Fletcher, H. Buss, and S. Brantley, "A spheroidal weathering model coupling porewater chemistry to soil thicknesses during steady-state denudation", *Earth and Planetary Science Letters*, vol. 244, no. 1-2, pp. 444–457, 2006.

[164] H. L. Buss, P. B. Sak, S. M. Webb, and S. L. Brantley, "Weathering of the Rio Blanco quartz diorite, Luquillo Mountains, Puerto Rico: Coupling oxidation, dissolution, and fracturing", *Geochimica et Cosmochimica Acta*, vol. 72, no. 18, pp. 4488–4507, 2008.

[165] B. W. Goodfellow, G. E. Hilley, S. M. Webb, L. S. Sklar, S. Moon, and C. A. Olson, "The chemical, mechanical, and hydrological evolution of weathering granitoid", *Journal of Geophysical Research: Earth Surface*, vol. 121, no. 8, pp. 1410–1435, 2016.

[166] A. Navarre-Sitchler, C. I. Steefel, P. B. Sak, and S. L. Brantley, "A reactive-transport model for weathering rind formation on basalt", *Geochimica et Cosmochimica Acta*, vol. 75, no. 23, pp. 7644–7667, 2011.

[167] A. K. Navarre-Sitchler, D. R. Cole, G. Rother, L. Jin, H. L. Buss, and S. L. Brantley, "Porosity and surface area evolution during weathering of two igneous rocks", *Geochimica et Cosmochimica Acta*, vol. 109, pp. 400–413, 2013.

[168] A. Navarre-Sitchler, S. L. Brantley, and G. Rother, "How porosity increases during incipient weathering of crystalline silicate rocks", *Reviews in Mineralogy and Geochemistry*, vol. 80, no. 1, pp. 331–354, 2015.

[169] F. D. A. Reis and S. L. Brantley, "Models of transport and reaction describing weathering of fractured rock with mobile and immobile water", *Journal of Geophysical Research: Earth Surface*, vol. 122, no. 3, pp. 735–757, 2017.

[170] D. Hu, H. Zhou, Q. Hu, J. Shao, X. Feng, and H. Xiao, "A hydro-mechanical-chemical coupling model for geomaterial with both mechanical and chemical damages considered", *Acta Mechanica Solida Sinica*, vol. 25, no. 4, pp. 361–376, 2012.

[171] L. Li, C. Tang, S. Wang, and J Yu, "A coupled thermo-hydrologic-mechanical damage model and associated application in a stability analysis on a rock pillar", *Tunnelling and Underground Space Technology*, vol. 34, pp. 38–53, 2013.

[172] D Grgic, A Giraud, and C Auvray, "Impact of chemical weathering on micro/macro-mechanical properties of oolithic iron ore", *International Journal of Rock Mechanics and Mining Sciences*, vol. 64, pp. 236–245, 2013.

[173] T. Poulet, A. Karrech, K. Regenauer-Lieb, L. Fisher, and P. Schaubs, "Thermal–hydraulic–mechanical–chemical coupling with damage mechanics using ESCRIPTRT and ABAQUS", *Tectonophysics*, vol. 526, pp. 124–132, 2012.

[174] H. Yasuhara, N. Kinoshita, H. Ohfuji, D. S. Lee, S. Nakashima, and K. Kishida, "Temporal alteration of fracture permeability in granite under hydrothermal conditions and its interpretation by coupled chemo-mechanical model", *Applied Geochemistry*, vol. 26, no. 12, pp. 2074–2088, 2011.

[175] M.-C. Eppes and R. Keanini, "Mechanical weathering and rock erosion by climate-dependent subcritical cracking", *Reviews of Geophysics*, vol. 55, no. 2, pp. 470–508, 2017.

[176] N. Brantut, P. Baud, M. Heap, and P. Meredith, "Micromechanics of brittle creep in rocks", *Journal of Geophysical Research: Solid Earth*, vol. 117, no. B8, 2012.

[177] N. Brantut, M. Heap, P. Meredith, and P. Baud, "Time-dependent cracking and brittle creep in crustal rocks: A review", *Journal of Structural Geology*, vol. 52, pp. 17–43, 2013.

[178] I. Stefanou and J. Sulem, "Chemically induced compaction bands: Triggering conditions and band thickness", *Journal of Geophysical Research: Solid Earth*, vol. 119, pp. 880–899, 2014.

[179] M. Schoenball, D. P. Sahara, and T. Kohl, "Time-dependent brittle creep as a mechanism for time-delayed wellbore failure", *International Journal of Rock Mechanics and Mining Sciences*, vol. 70, pp. 400–406, 2014.

[180] D. S. Fanning, V. Z. Keramidas, and M. A. El-Desoky, "Micas", *Minerals in soil environments*, no. mineralsinsoile, pp. 551–634, 1989.

[181] H. Dong, D. R. Peacor, and S. F. Murphy, "Tem study of progressive alteration of igneous biotite to kaolinite throughout a weathered soil profile", *Geochimica et Cosmochimica Acta*, vol. 62, no. 11, pp. 1881 –1887, 1998.

[182] S. F. Murphy, S. L. Brantley, A. E. Blum, A. F. White, and H. Dong, "Chemical weathering in a tropical watershed, Luquillo Mountains, Puerto Rico: Ii. Rate and mechanism of biotite weathering", *Geochimica et Cosmochimica Acta*, vol. 62, no. 2, pp. 227–243, 1998.

[183] E. Bisdom, G. Stoops, J. Delvigne, P. Curmi, and H. Altemuller, "Micromorphology of weathering biotite and its secondary products", *Pedologie*, vol. 32, no. 2, pp. 225–252, 1982.

[184] Y. Takaya, T. Hatta, and Y. Matsukura, "Differential roles of plagioclase and biotite in the early stage weathering of granite: A solid-sided approach combining laboratory experiment and surface analysis", *Zeitschrift für Geomorphologie*, vol. 58, no. 2, pp. 233–249, Jul. 2014.

[185] A. F. White and S. L. Brantley, "The effect of time on the weathering of silicate minerals: Why do weathering rates differ in the laboratory and field?", *Chemical Geology*, vol. 202, no. 3, pp. 479 –506, 2003, Controls on Chemical Weathering.

[186] K Maher, "The dependence of chemical weathering rates on fluid residence time", *Earth and Planetary Science Letters*, vol. 294, no. 1-2, pp. 101–110, 2010.

[187] A. W. Bray, E. H. Oelkers, S. Bonneville, D. Wolff-Boenisch, N. J. Potts, G. Fones, and L. G. Benning, "The effect of ph, grain size, and organic ligands on biotite weathering rates", *Geochimica et Cosmochimica Acta*, vol. 164, pp. 127–145, 2015.

[188] K. L. Ferrier, J. W. Kirchner, and R. C. Finkel, "Weak influences of climate and mineral supply rates on chemical erosion rates: Measurements along two altitudinal transects in the idaho batholith", *Journal of Geophysical Research: Earth Surface*, vol. 117, no. F2, 2012.

[189] D. Moos, J. Dvorkin, and A. J. Hooks, "Application of theoretically derived rock physics relationships for clastic rocks to log data from the wilmington field, CA", *Geophysical Research Letters*, vol. 24, no. 3, pp. 329–332, 1997. eprint: https://agupubs.onlinelibrary.wiley.com/doi/pdf/10.1029/96GL02392.

[190] S. Abidi, Y. Joliff, and C. Favotto, "Impact of perlite, vermiculite and cement on the young modulus of a plaster composite material: Experimental, analytical and numerical approaches", *Composites Part B: Engineering*, vol. 92, pp. 28 –36, 2016.

[191] W. Bosworth, "Strain-induced preferential dissolution of halite", *Tectonophysics*, vol. 78, no. 1-4, pp. 509–525, 1981.

[192] A. A.-C. Guéry, F. Cormery, J.-F. Shao, and D. Kondo, "A micromechanical model of elastoplastic and damage behavior of a cohesive geomaterial", *International Journal of Solids and structures*, vol. 45, no. 5, pp. 1406–1429, 2008.

[193] D. Halm and A. Dragon, "An anisotropic model of damage and frictional sliding for brittle materials", *European Journal of Mechanics - A/Solids*, vol. 17, no. 3, pp. 439 –460, 1998.

[194] H.-S. Yu, *Plasticity and geotechnics*. Springer Science & Business Media, 2007, vol. 13.

[195] G. T. Houlsby and A. M. Puzrin, *Principles of hyperplasticity: an approach to plasticity theory based on thermodynamic principles*. Springer Science & Business Media, 2007.

[196] D. Halm and A. Dragon, "Modélisation de l'endommagement par mésofissuration du granite", *Revue française de génie civil*, vol. 6, no. 1, pp. 21–33, 2002.

[197] W. Jin, H. Xu, C. Arson, and S. Busetti, "Computational model coupling mode ii discrete fracture propagation with continuum damage zone evolution", *International Journal for Numerical and Analytical Methods in Geomechanics*, vol. 41, no. 2, pp. 223–250, 2017.

[198] W. H. Grant, "Weathering of stone mountain granite", *Clays and clay minerals*, vol. 11, pp. 65–73, 1962.

[199] A. da Fonseca and J. e Sousa, "At rest coefficient of earth pressure in saprolitic soils from granite", in *PROCEEDINGS OF THE INTERNATIONAL CONFERENCE ON SOIL MECHANICS AND GEOTECHNICAL ENGINEERING*, AA BALKEMA PUBLISHERS, vol. 1, 2001, pp. 397–400.

[200] C. Arson, "Generalized stress variables in continuum damage mechanics", *Mechanics Research Communications*, vol. 60, pp. 81–84, 2014.

[201] D. J. Miller and T. Dunne, "Topographic perturbations of regional stresses and consequent bedrock fracturing", *Journal of Geophysical Research: Solid Earth*, vol. 101, no. B11, pp. 25 523–25 536, 1996.

[202] J St. Clair, S Moon, W. Holbrook, J. Perron, C. Riebe, S. Martel, B Carr, C Harman, K Singha, *et al.*, "Geophysical imaging reveals topographic stress control of bedrock weathering", *Science*, vol. 350, no. 6260, pp. 534–538, 2015.

[203] M. Slim, J. T. Perron, S. J. Martel, and K. Singha, "Topographic stress and rock fracture: A two-dimensional numerical model for arbitrary topography and preliminary comparison with borehole observations", *Earth Surface Processes and Landforms*, vol. 40, no. 4, pp. 512–529, 2015.

[204] S Moon, J. Perron, S. Martel, W. Holbrook, and J St. Clair, "A model of three-dimensional topographic stresses with implications for bedrock fractures, surface processes, and landscape evolution", *Journal of Geophysical Research: Earth Surface*, vol. 122, no. 4, pp. 823–846, 2017.

[205] L Griffiths, M. Heap, P Baud, and J Schmittbuhl, "Quantification of microcrack characteristics and implications for stiffness and strength of granite", *International Journal of Rock Mechanics and Mining Sciences*, vol. 100, pp. 138–150, 2017.

[206] R. Hellmann and D. Tisserand, "Dissolution kinetics as a function of the gibbs free energy of reaction: An experimental study based on albite feldspar", *Geochimica et Cosmochimica Acta*, vol. 70, no. 2, pp. 364–383, 2006.

[207] K. Maher, C. I. Steefel, A. F. White, and D. A. Stonestrom, "The role of reaction affinity and secondary minerals in regulating chemical weathering rates at the santa cruz soil chronosequence, california", *Geochimica et Cosmochimica Acta*, vol. 73, no. 10, pp. 2804–2831, 2009.

[208] A. F. White, M. S. Schulz, D. V. Vivit, A. E. Blum, D. A. Stonestrom, and S. P. Anderson, "Chemical weathering of a marine terrace chronosequence, santa cruz, california i: Interpreting rates and controls based on soil concentration–depth profiles", *Geochimica et Cosmochimica Acta*, vol. 72, no. 1, pp. 36–68, 2008.

[209] C. Perillo, S. Gupta, E. Nater, and J. Moncrief, "Prevalence and initiation of preferential flow paths in a sandy loam with argillic horizon", *Geoderma*, vol. 89, no. 3-4, pp. 307–331, 1999.

[210] K. Maher, D. J. DePaolo, and J. N. Christensen, "U–sr isotopic speedometer: Fluid flow and chemical weathering rates in aquifers", *Geochimica et Cosmochimica Acta*, vol. 70, no. 17, pp. 4417–4435, 2006.

[211] S. J. Köhler, F. Dufaud, and E. H. Oelkers, "An experimental study of illite dissolution kinetics as a function of ph from 1.4 to 12.4 and temperature from 5 to 50 c", *Geochimica et Cosmochimica Acta*, vol. 67, no. 19, pp. 3583–3594, 2003.

[212] D. M. Rempe and W. E. Dietrich, "A bottom-up control on fresh-bedrock topography under landscapes", *Proceedings of the National Academy of Sciences*, vol. 111, no. 18, pp. 6576–6581, 2014.

[213] C. I. Steefel and K. Maher, "Fluid-rock interaction: A reactive transport approach", *Reviews in mineralogy and geochemistry*, vol. 70, no. 1, pp. 485–532, 2009.

[214] A. M. Heimsath, J. Chappell, W. E. Dietrich, K. Nishiizumi, and R. C. Finkel, "Late quaternary erosion in southeastern australia: A field example using cosmogenic nuclides", *Quaternary International*, vol. 83, pp. 169–185, 2001.

[215] R. S. Anderson, "Modeling the tor-dotted crests, bedrock edges, and parabolic profiles of high alpine surfaces of the wind river range, wyoming", *Geomorphology*, vol. 46, no. 1-2, pp. 35–58, 2002.

[216] K. L. Ferrier, J. W. Kirchner, C. S. Riebe, and R. C. Finkel, "Mineral-specific chemical weathering rates over millennial timescales: Measurements at rio icacos, puerto rico", *Chemical Geology*, vol. 277, no. 1-2, pp. 101–114, 2010.

[217] D. Gardner, A. Jefferson, A. Hoffman, and R. Lark, "Simulation of the capillary flow of an autonomic healing agent in discrete cracks in cementitious materials", *Cement and Concrete Research*, vol. 58, no. Supplement C, pp. 35 –44, 2014.

[218] R. Davies and A. Jefferson, "Micromechanical modelling of self-healing cementitious materials", *International Journal of Solids and Structures*, vol. 113-114, no. Supplement C, pp. 180 –191, 2017.

[219] G. Z. Voyiadjis, A. Shojaei, and G. Li, "A thermodynamic consistent damage and healing model for self healing materials", *International Journal of Plasticity*, vol. 27, no. 7, pp. 1025 –1044, 2011.

[220] E. J. Barbero, F. Greco, and P. Lonetti, "Continuum Damage-healing Mechanics with Application to Self-healing Composites", *International Journal of Damage Mechanics*, vol. 14, no. 1, pp. 51–81, Jan. 2005.

[221] S. R. White, N. Sottos, P. Geubelle, J. Moore, M. Kessler, S. Sriram, E. Brown, and S Viswanathan, "Autonomic healing of polymer composites", *Nature*, vol. 409, no. 6822, pp. 794–797, 2001.

[222] G. Li and N. Uppu, "Shape memory polymer based self-healing syntactic foam: 3-d confined thermomechanical characterization", *Composites Science and Technology*, vol. 70, no. 9, pp. 1419 –1427, 2010.

[223] M. Houben, A. ten Hove, C. Peach, and C. Spiers, "Crack healing in rocksalt via diffusion in adsorbed aqueous films: Microphysical modelling versus experiments", *Physics and Chemistry of the Earth, Parts A/B/C*, vol. 64, no. Supplement C, pp. 95 –104, 2013, Coupled Physical and Chemical Transformations Affecting the Performance of GeoSystems.

[224] D. J. Holcomb and D. H. Zeuch, "Modeling the consolidation of a porous aggregate of dry salt as isostatic hot pressing", *Journal of Geophysical Research: Solid Earth*, vol. 95, no. B10, pp. 15 611–15 622, 1990.

[225] M. Bourcier, M. Bornert, A. Dimanov, E. Héripré, and J. L. Raphanel, "Multiscale experimental investigation of crystal plasticity and grain boundary sliding in synthetic halite using digital image correlation", *Journal of Geophysical Research: Solid Earth*, vol. 118, no. 2, pp. 511–526, 2013.

[226] C. Spiers and R. Brzesowsky, "Densification behaviour of wet granular salt: Theory versus experiment", in *Seventh Symposium on salt*, vol. 1, 1993, pp. 83–92.

[227] S. H. Hickman and B. Evans, "Experimental pressure solution in halite: The effect of grain/interphase boundary structure", *Journal of the Geological Society*, vol. 148, no. 3, pp. 549–560, 1991. eprint: `http://jgs.lyellcollection.org/content/148/3/549.full.pdf`.

[228] C. J. Spiers, P. M.T. M. Schutjens, R. H. Brzesowsky, C. J. Peach, J. L. Liezenberg, and H. J. Zwart, "Experimental determination of constitutive parameters governing creep of rocksalt by pressure solution", *Geological Society, London, Special Publications*, vol. 54, no. 1, pp. 215–227, 1990. eprint: `http://sp.lyellcollection.org/content/54/1/215.full.pdf`.

[229] C. Yang, J. Daemen, and J.-H. Yin, "Experimental investigation of creep behavior of salt rock", *International Journal of Rock Mechanics and Mining Sciences*, vol. 36, no. 2, pp. 233 –242, 1999.

[230] X. Zhang and C. Spiers, "Compaction of granular calcite by pressure solution at room temperature and effects of pore fluid chemistry", *International Journal of Rock Mechanics and Mining Sciences*, vol. 42, no. 7, pp. 950 –960, 2005, Rock Physics and Geomechanics.

[231] A. M. H. Pluymakers and C. J. Spiers, "Compaction creep of simulated anhydrite fault gouge by pressure solution: Theory v. experiments and implications for fault sealing", *Geological Society, London, Special Publications*, vol. 409, no. 1, pp. 107–124, 2015. eprint: http://sp.lyellcollection.org/content/409/1/107.full.pdf.

[232] S. L. Brantley, J. D. Kubicki, and A. F. White, *Kinetics of water-rock interaction*. Springer, 2008, vol. 168.

[233] R. van Noort and C. J. Spiers, "Kinetic effects of microscale plasticity at grain boundaries during pressure solution", *Journal of Geophysical Research: Solid Earth*, vol. 114, no. B3, 2009.

[234] R. Fletcher, *Practical methods of optimization*, ser. Wiley-interscience publication v. 1. Wiley, 1987, ISBN: 9780471915478.

[235] A. S. Lewis and L. O. Michael, "Nonsmooth optimization via bfgs", 2008.

[236] A. Antoniou and W.-S. Lu, *Practical optimization: algorithms and engineering applications*. Springer Science & Business Media, 2007.

[237] M. T. Van Genuchten, "A closed-form equation for predicting the hydraulic conductivity of unsaturated soils", *Soil science society of America journal*, vol. 44, no. 5, pp. 892–898, 1980.

[238] C. Arson and J.-M. Pereira, "Influence of damage on pore size distribution and permeability of rocks", *International Journal for Numerical and Analytical Methods in Geomechanics*, vol. 37, no. 8, pp. 810–831, 2013.

[239] O. Coussy, *Poromechanics*. John Wiley & Sons, 2004.

[240] M. Dusseault, L Rothenburg, S Bachu, *et al.*, "Sequestration of co in salt caverns", in *Canadian International Petroleum Conference*, Petroleum Society of Canada, 2002.

[241] K. L. Ferrier, J. W. Kirchner, C. S. Riebe, and R. C. Finkel, "Mineral-specific chemical weathering rates over millennial timescales: Measurements at rio icacos, puerto rico", *Chemical Geology*, vol. 277, no. 1, pp. 101 –114, 2010.

VITA

Xianda Shen was born on May 21, 1990, in Hangzhou, Zhejiang Province, China. He obtained his Bachelor of Engineering Degree (2012) from Southwest Jiaotong University and Master of Engineering Degree (2015) from Tongji University in China. From August 2015, he started his Ph.D. study under the supervision of Dr. Chloé Arson at the Georgia Institute of Technology. He will receive his Ph.D. degree in December 2019 from Georgia Institute of Technology.